

Time-Resolved Photoluminescence on Perovskite Absorber Materials for Photovoltaic Applications

Florian Staub

Energie & Umwelt / Energy & Environment

Band / Volume 513

ISBN 978-3-95806-503-1

Mitglied der Helmholtz-Gemeinschaft

 **JÜLICH**
Forschungszentrum

Forschungszentrum Jülich GmbH
Institut für Energie- und Klimaforschung
IEK-5 Photovoltaik

Time-Resolved Photoluminescence on Perovskite Absorber Materials for Photovoltaic Applications

Florian Staub

Schriften des Forschungszentrums Jülich
Reihe Energie & Umwelt / Energy & Environment

Band / Volume 513

ISSN 1866-1793

ISBN 978-3-95806-503-1

Bibliografische Information der Deutschen Nationalbibliothek.
Die Deutsche Nationalbibliothek verzeichnet diese Publikation in der
Deutschen Nationalbibliografie; detaillierte Bibliografische Daten
sind im Internet über <http://dnb.d-nb.de> abrufbar.

Herausgeber und Vertrieb: Forschungszentrum Jülich GmbH
Zentralbibliothek, Verlag
52425 Jülich
Tel.: +49 2461 61-5368
Fax: +49 2461 61-6103
zb-publikation@fz-juelich.de
www.fz-juelich.de/zb

Umschlaggestaltung: Grafische Medien, Forschungszentrum Jülich GmbH

Druck: Grafische Medien, Forschungszentrum Jülich GmbH

Copyright: Forschungszentrum Jülich 2020

Schriften des Forschungszentrums Jülich
Reihe Energie & Umwelt / Energy & Environment, Band / Volume 513

D 464 (Diss. Duisburg, Univ., 2020)

ISSN 1866-1793
ISBN 978-3-95806-503-1

Vollständig frei verfügbar über das Publikationsportal des Forschungszentrums Jülich (JuSER)
unter www.fz-juelich.de/zb/openaccess.



This is an Open Access publication distributed under the terms of the [Creative Commons Attribution License 4.0](https://creativecommons.org/licenses/by/4.0/), which permits unrestricted use, distribution, and reproduction in any medium, provided the original work is properly cited.

"I'd put my money on the sun and solar energy. What a source of power! I hope we don't have to wait until oil and coal run out before we tackle that. I wish I had more years left."

Thomas Alva Edison, 1931

Contents

Abstract	1
Zusammenfassung	3
List of publications	5
1 Introduction	7
2 Fundamentals and characterization methods	11
2.1 Photovoltaic performance	11
2.2 Electronic structure of semiconductors	12
2.3 Charge-carrier recombination	16
2.3.1 Radiative recombination	16
2.3.2 Non-radiative recombination	17
2.4 Time-resolved photoluminescence	20
2.4.1 Charge-carrier dynamics	20
2.4.2 Setup and experimental details	23
2.4.2.1 Wavelength calibration	27
2.4.2.2 Intensity calibration	27
2.5 Characterization methods	29
2.5.1 Photoluminescence setup	29
2.5.2 Photothermal deflection spectroscopy	29
2.5.3 Optical pump terahertz probe spectroscopy	31
2.5.4 Thermopower measurements	31
2.5.5 Scanning electron microscopy	32
2.5.6 Atomic force microscopy	32
2.5.7 X-ray diffraction	33

Contents

2.5.8	X-ray photo-electron spectroscopy	33
2.5.9	Profilometer	34
3	Material properties of organic inorganic perovskites	35
3.1	Perovskite crystal structure	35
3.2	Emerging as photovoltaic material	36
3.3	Electronic structure	39
3.4	Sample preparation	42
3.4.1	Perovskite thin films	42
3.4.2	Perovskite single crystals	44
3.5	Morphology of perovskite thin films	45
3.6	Optical properties	47
3.6.1	Absorption coefficient	47
3.6.2	Detailed balance of emission and absorption	48
3.6.3	Band gap characteristics	51
3.7	Electrical properties	54
3.7.1	Doping concentration	54
3.7.2	Charge-carrier mobility	56
4	Time-resolved photoluminescence from perovskite thin films	59
4.1	Charge-carrier recombination processes	59
4.2	Photoluminescence transients in the context of doping	64
4.3	Photon recycling affecting radiative recombination	67
4.4	Lifetimes and internal luminescence quantum efficiency	70
4.5	Charge-carrier diffusion in thin films	75
4.6	Surface passivation and recombination	77
4.7	Fundamental semiconductor properties	86
4.8	Prediction of the implied open-circuit voltage	88
5	Time-resolved photoluminescence from single crystals	93
5.1	Introduction	93
5.2	PDS absorptance of perovskite single crystals	94
5.3	Photoluminescence measurement configurations	96

5.4	Simulations and fundamentals	99
5.4.1	Simulating photoluminescence decays	99
5.4.2	Simulating time-resolved spectral shifts	102
5.5	Time-resolved photoluminescence spectra	104
5.5.1	Findings from modeling experimental data	104
5.5.2	Impacts on spectral time-resolved photoluminescence and transients	110
5.5.2.1	Surface recombination	110
5.5.2.2	Charge-carrier mobility	113
5.5.2.3	Photon recycling	117
6	Photon recycling investigated by time-resolved photoluminescence	123
6.1	Introduction	123
6.2	Experimental design	124
6.3	Morphology of perovskite top layers	127
6.4	Time-resolved photoluminescence	129
6.5	Optical simulations	135
6.6	Photon probabilities and radiative fraction of bimolecular recombination	139
6.7	Possible origin of non-radiative bimolecular recombination	143
7	Conclusion and outlook	147
A	Appendix: Calculating charge-carrier profiles in single crystals	151
A.1	Charge-carrier generation due to pulsed excitation	151
A.2	Diffusive transport and surface recombination	153
A.3	Photon recycling scheme	154
A.4	Bulk recombination	157
B	Appendix: Optical simulation of thin layer stacks	159
B.1	Coherent simulation of flat layer stacks	159
B.2	Incoherent Lambertian light scattering	161
	Abbreviations and symbols	167

Contents

References 173

Acknowledgments 197

Abstract

Time-resolved photoluminescence has become a commonly used tool to mainly determine charge-carrier lifetimes in metal halide perovskites. In this thesis, I investigate photoluminescence transients regarding radiative and non-radiative charge-carrier recombination as well as charge-carrier separation by diffusion. Additionally, I focus on the so-called photon recycling effect. Photon recycling refers to the self-absorption of photons, which have been generated by radiative recombination of excited states, within the absorber material itself. As photon recycling is directly linked with the radiative recombination process, the presence of photon recycling is actually masked and not obvious in photoluminescence transients. Here, I reveal the presence of photon recycling in thin-film perovskites by reporting that the obtained apparent radiative recombination rate can be manipulated by modifying only the optical design of the sample stack; i. e. tuning the probability of photon reabsorption in the absorber layer by altering the light management in the stacks.

Furthermore, perovskite single crystals have been investigated by time-resolved photoluminescence to study the impact of reabsorption in more detail. I show that photon recycling supports the preservation of charge carriers but does not enable efficient charge-carrier transportation over long distances. Spectral shifts observed in the transient measurements are the result of altering reabsorption characteristics as the recombination zone expands over time into the bulk mainly as a consequence of charge-carrier diffusion.

Understanding photon recycling and recombination processes is important for photovoltaic devices as these mechanisms affect the open-circuit voltage. Based only on the findings from time-resolved photoluminescence, I demonstrate how to predict the maximum attainable open-circuit voltage, which the investigated perovskite absorber layer embedded in a solar cell stack could ideally provide. This

Abstract

approach helps to estimate the photovoltaic potential of any absorber layer based on its material quality without the need of fabricating an entire solar cell first.

Zusammenfassung

Zeitaufgelöste Photolumineszenz ist eine häufig verwendete Methode, um Lebensdauern von Ladungsträgern in Metall Halogenid Perowskitverbindungen zu bestimmen. In der vorliegenden Dissertation werden anhand von Photolumineszenz-Transienten die strahlende und nicht-strahlende Rekombination sowie die durch Diffusion bedingte Ladungsträgerseparation untersucht. Zusätzlich wird die Bedeutung des so genannten Photon Recycling Effekt hervorgehoben. Dieser Vorgang beschreibt die Reabsorption von Photonen, die aufgrund von strahlender Rekombination von angeregten Zuständen im Absorbermaterial generiert wurden. Da Photon Recycling als intrinsischer Effekt an den strahlenden Rekombinationsprozess gekoppelt ist, wird dessen Existenz nicht direkt am Verlauf der Transienten erkennbar. In der vorliegenden Arbeit wird gezeigt, dass die gemessene (scheinbare) strahlende Rekombinationsrate durch den optischen Aufbau der untersuchten Schichtstapel manipuliert werden kann; d. h. die Wahrscheinlichkeit, dass entsendete Photonen durch Absorption in der aktiven Schicht wieder in Ladungsträger umgewandelt werden, wird durch die Lichtführung innerhalb des Schichtstapels beeinflusst.

Des Weiteren werden Perowskit-Einkristalle mit zeitaufgelöster Photolumineszenz charakterisiert, um Reabsorption besser verstehen zu können. Es wird aufgezeigt, dass Photon Recycling effektiv eine längere Erhaltung der Ladungsträgerpopulation bewirkt, aber dabei die Ladungsträger nicht effizient über weite Strecken innerhalb der Kristalle zu transportieren vermag. Zeitliche Änderungen der Form der Photolumineszenz-Spektren sind durch Reabsorptionsvorgänge erklärbar, da sich die Rekombinationszone aufgrund von Ladungsträgerdiffusion mit der Zeit ins Volumen des Kristalls ausbreitet.

Rekombination sowie Photon Recycling haben Einfluss auf eine wichtige Kenngröße photovoltaischer Zellen, die offene Klemmspannung. Basierend auf den Er-

Zusammenfassung

kenntnissen aus der zeitaufgelösten Photolumineszenz einer Perowskitdünnschicht, wird eine Methode entwickelt, welche es erlaubt die maximal erreichbare offene Klemmspannung abzuschätzen, welche diese Dünnschicht - eingebettet in einer beispielhaften Solarzelle - idealerweise bereitstellen könnte. Anhand dieser Methode kann das photovoltaische Potential einer beliebigen Absorberschicht bereits anhand ihrer Materialqualität abgeschätzt werden ohne eine vollständige Solarzelle herstellen zu müssen.

List of publications

Publications related to this thesis

F. Staub, H. Hempel, J.-C. Hebig, J. Mock, U. W. Paetzold, U. Rau, T. Unold, and T. Kirchartz. "Beyond Bulk Lifetimes: Insights into Lead Halide Perovskite Films from Time-Resolved Photoluminescence", *Physical Review Applied*, vol. 6, no. 4, p. 044017, 2016.

F. Staub, T. Kirchartz, K. Bittkau, and U. Rau. "Manipulating the Net Radiative Recombination Rate in Lead Halide Perovskite Films by Modification of Light Outcoupling", *The Journal of Physical Chemistry Letters*, vol. 8, no. 20, pp. 5084-5090, 2017.

F. Staub, T. Kirchartz, and U. Rau. "Statistics of the Auger-Recombination of Electrons and Holes via Defect Levels in the Band Gap - Application to Lead-Halide-Perovskites", *ACS Omega*, vol. 3, no. 7, pp. 8009-8016, 2018.

F. Staub, I. Anusca, D. C. Lupascu, U. Rau, and T. Kirchartz. "Effect of Re-absorption and Photon Recycling on Photoluminescence Spectra and Transients in Lead-Halide Perovskite Crystals", *Journal of Physics: Materials*, vol. 3, no. 2, p. 025003, 2020.

Further publications

T. Kirchartz, F. Staub, and U. Rau. "Impact of Photon Recycling on the Open-Circuit Voltage of Metal Halide Perovskite Solar Cells", *ACS Energy Letters*, vol. 1, no. 4, pp. 731-739, 2016.

B. Krogmeier, F. Staub, D. Grabowski, U. Rau, and T. Kirchartz. "Quanti-

List of publications

tative Analysis of the Transient Photoluminescence of $\text{CH}_3\text{NH}_3\text{PbI}_3/\text{PC}_{61}\text{BM}$ Heterojunctions by Numerical Simulations”, *Sustainable Energy Fuels*, vol. 2, no. 5, pp. 1027-1034, 2018.

1 Introduction

Photovoltaics is considered one of the key technologies for providing a sustainable source of electric power. The most common solar cell technology on the market is based on *pn*-junction type (poly-)crystalline silicon. Over the last decades, different material combinations and working principles, e. g. dye-sensitized, organic, and quantum dot solar cells, have also become subject of photovoltaic research. Within the last few years, organic metal halide perovskites have rapidly evolved as promising opto-electronic material class [1, 2] because they provide many beneficial features. Perovskite absorber materials are typically composed of cheap, earth abundant elements like halogens and heavy metals. Substitution of specific elements allows to tune the band gap over a wide range [3, 4], which makes perovskites a suitable counterpart to established photovoltaic materials in tandem solar cells [5–7]. Due to their high absorption coefficients, thin films of some hundreds of nanometers are already sufficient to efficiently "harvest" sun light [8]. Beside savings in material amount, production costs can be hold down because perovskite solar cells can mainly be fabricated from solution at low temperatures and still exhibit high material quality and performance [9, 10]. Exceptionally long charge-carrier lifetimes for solution-processed materials of several microseconds [11] in combination with high luminescence quantum yields [11, 12] allow to easily apply time-resolved photoluminescence as non-destructive tool to study charge-carrier processes in perovskites. First, excess-charge carriers need to be photo-generated by applying a short laser pulse. Shortly after, excited states will recombine over time resulting in a continuous decrease of the charge-carrier concentration until equilibrium conditions are reached again. Recorded photoluminescence transients reflect the charge-carrier decay and are therefore commonly analyzed for estimating charge-carrier lifetimes.

The scope of this thesis is to reveal the multiple processes that charge car-

1 Introduction

riers experience in organic-inorganic perovskite thin films and single crystals by applying time-resolved photoluminescence. Apart from investigating recombination processes, special attention is directed on so called photon recycling. This intrinsic effect describes the reabsorption of photons, which are internally emitted upon radiative recombination of electron-hole pairs, by the absorber layer itself and affects directly e. g. the open-circuit voltage of perovskite solar cells [13]. Due to its dependency on radiative recombination, the impact of photon recycling on photoluminescence transients is masked by overlaying recombination processes and is only revealed by simulations. In the following, the structure of this thesis is presented.

First, **Chapter 2** explains the basic electronic structure of semiconductors and provides an overview of diverse transition processes, i. e. either generation or recombination of excited states. Furthermore, the theory of an important photovoltaic parameter, the open-circuit voltage, which is limited by radiative and especially non-radiative recombination, is covered. Transient photoluminescence is introduced as a powerful tool in more detail to reveal recombination rates but also charge-separation processes.

Chapter 3 gives insight to the emerging class of organo-metal halide perovskites as opto-electronic semiconducting materials. The sample preparation from solution is described and structural, morphological and fundamental material properties are investigated.

In **Chapter 4**, photoluminescence transients are analyzed in detail to understand recombination characteristics in perovskite thin films. I develop a comprehensive model that is additionally able to explain the impact of doping and the photon recycling effect on observed recombination kinetics which shape the measured photoluminescence transients. Furthermore, long charge-carrier lifetimes are revealed, which indicate that solution-processed perovskites exhibit high material quality with low amounts of defects in the bulk and also at the surfaces. Moreover, I demonstrate that - without processing a complete solar cell - the photovoltaic potential in terms of the attainable open-circuit voltage can be predicted for the investigated absorber layer based on the findings from time-resolved photoluminescence.

Chapter 5 focuses on photoluminescence transients obtained from perovskite single crystals. Thick samples are suited to study besides recombination processes

also charge-carrier transport processes like diffusion and photon recycling in more detail. While diffusion is identified as the dominant transport mechanism in the investigated perovskite crystal, photon recycling rather locally supports preservation of charge carriers than their transport. Spectral photoluminescence shifts are detected over time as the recombination zone spreads into the bulk due to carrier transport and, consequently, reabsorption becomes more pronounced.

Lastly, I demonstrate in **Chapter 6** that the observed apparent radiative recombination rate can be manipulated by the optical design of the investigated layer stacks. The rationale behind this observation is given by differences in the reabsorption probability of internally emitted photons, which are tuned by optics. Furthermore, I identify a fundamental limitation of the radiative efficiency, which will limit the maximum attainable efficiency of perovskite solar cells.

2 Fundamentals and characterization methods

2.1 Photovoltaic performance

The operation principle of a solar cell is based on the conversion of sunlight into electrical power. A detailed description of the physics of solar cells can be found elsewhere [14, 15]. Besides the energy conversion efficiency η , important parameters for the photovoltaic operation are derived from the current density - voltage ($j(V)$) characteristic of the illuminated solar cell; e. g. the short-circuit current density j_{sc} at $V = 0$ and the open-circuit voltage V_{oc} when $j = 0$. Typical diode-like $j(V)$ characteristics are shown in Fig. 2.1 for a simulated perovskite solar cell exhibiting different charge-carrier lifetimes τ . It becomes apparent that τ severely controls the attainable open-circuit voltage, while the short-circuit current density remains unaffected to a certain degree. Long lifetimes are obviously favorable in order to achieve high open-circuit voltages and are an indicator of a high quality absorber with a low defect concentration. At open circuit, all photogenerated charge carriers have to recombine eventually and, as a consequence, the net current flow becomes zero. The various mechanisms, that allow charge carriers to recombine, as well as the associated lifetimes play an eminent role in building up V_{oc} as elucidated in Sec. 2.3. As the short-circuit current density mainly emerges from the absorption of the incident spectral irradiance and the collection of photogenerated charge carriers at the electrodes, j_{sc} is only slightly influenced by lifetime. A high solar cell efficiency η necessarily stems from a large j_{sc} and also a large V_{oc} , as apparent from the equation

$$\eta = \frac{P_{\max}}{P_0} = \frac{j_{sc} V_{oc} F F}{P_0}. \quad (2.1)$$

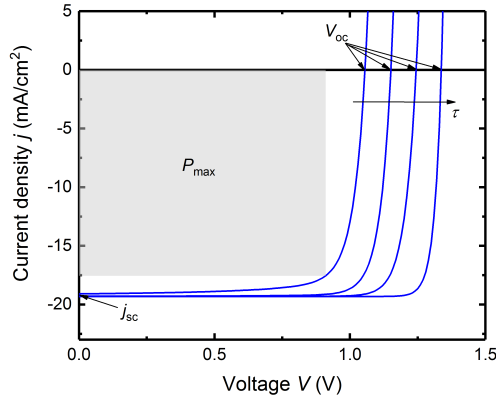


Figure 2.1: Current density - voltage ($j(V)$) characteristics of simulated perovskite solar cells with different charge carrier lifetimes τ under illumination. The short-circuit current density j_{sc} as well as the different open-circuit voltages V_{oc} are indicated. The gray area exemplarily illustrates the maximum attainable power density P_{max} for the cell with the lowest lifetime.

Here, P_{max} denotes the maximum attainable power density of the solar cell (illustrated as gray area in Fig. 2.1) and P_0 indicates the irradiated power per unit area. The fill factor FF describes the ratio between P_{max} and the product of j_{sc} and V_{oc} .

In the present work, I investigate i. a. recombination processes and lifetimes in organic inorganic perovskite films by time-resolved photoluminescence which allows me to draw predictions of the attainable open-circuit voltages.

2.2 Electronic structure of semiconductors

Every semiconductor material exhibits a characteristic band gap E_g , which is defined as the energetic difference between the conduction band minimum (lowest unoccupied state) and the valence band maximum (highest occupied state). The nature of the band gap can either be direct or indirect as shown in Fig. 2.2. In the case of a direct band gap, conduction band minimum and valence band maximum are located

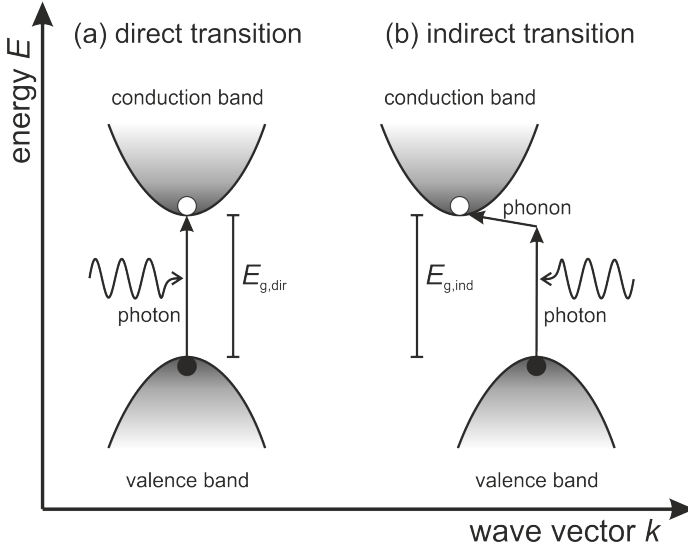


Figure 2.2: Schematic depiction of the excitation processes for a semiconductor with (a) a direct band gap and (b) an indirect band gap. In the case of a direct band gap only the absorption/emission of a photon determines the transition process, whereas for a indirect band gap a phonon is additionally involved to satisfy the conservation of momentum.

at the same position in momentum space, i. e. $\Delta k = 0$. Here, electronic interband transitions are mainly accomplished by absorption or emission processes of photons, respectively, which do not possess considerable momentum. Also phonon-involved interband transitions in direct semiconductors are possible in general but such multiple particle processes are less likely (see Sec. 2.3.2). Therefore, high quality direct semiconductors are typically highly luminescent and, consequently, suited as active materials in e. g. light emitting devices (LEDs). Indirect semiconductor on the other hand exhibit a k -shift of the extrema positions. Thus, besides photons, also momentum carrying quasiparticles like phonons need to be involved to enable interband transition processes. As a consequence, direct semiconductors typically show higher values of the absorption coefficient α than indirect semiconductors.

The transition rate w_{if} for a two level system (initial state with index i at energy E_i and final state with index f at energy E_f) is also known as Fermi's golden rule and a fundamental derivation can be found here [16]. The photon absorption

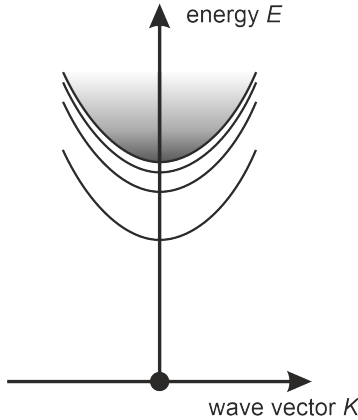


Figure 2.3: Schematic depiction of the exciton in the two-particle picture. The black dot represents the ground state, when the electron is located in the valence band. Parabolae represent different exciton levels.

and emission processes, respectively, are described for a periodic perturbation with frequency ω by

$$w_{\text{if}} = \frac{2\pi}{\hbar} |H'_{\text{if}}|^2 \delta(E_{\text{f}} - E_{\text{i}} \pm \hbar\omega), \quad (2.2)$$

where \hbar is the reduced Planck constant and $|H'_{\text{if}}|^2$ is denoted as transition probability. The delta function δ ensures energy conservation. Transitions between the two levels are only possible if an energy quantum $\hbar\omega$ (e.g. in the form of a photon) is absorbed or released from/to the oscillating field, respectively. The transition matrix element H'_{if} itself is given by

$$H'_{\text{if}} = \int \psi_{\text{f}}^*(\mathbf{r}) H' \psi_{\text{i}}(\mathbf{r}) d\tau =: \langle \psi_{\text{f}} | H' | \psi_{\text{i}} \rangle. \quad (2.3)$$

Here, the quantum mechanical system is described by the Hamiltonian H with perturbation, ψ are the wave functions, and \mathbf{r} is the position vector. When the system consists now of several, continuous states, the recorded luminescence spectra will contain information on the joint density of states weighted by the occupation probability together with the transition matrix elements.

Until now, only band-to-band transitions have been discussed. Beside the

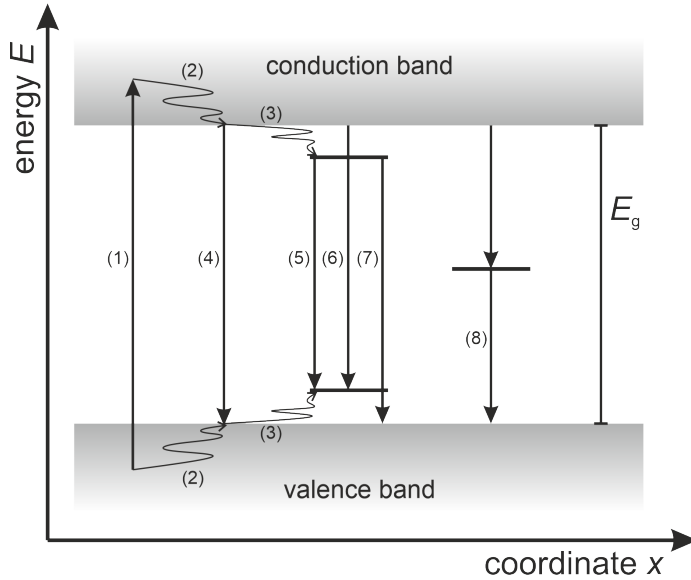


Figure 2.4: Illustration of diverse recombination processes in semiconductors. (1) Generation of an excited state. (2) Thermalization of excited species towards the band edges and (3) into shallow tail states. (4) Band-to-band, (5) tail-to-tail, (6) band-to-tail, and (7) tail-to-band transitions. (8) Recombination process via a deep state according to Shockley-Read-Hall.

valence and conduction bands, discrete states or even bands can exist at energies within the band gap. So called tail states are located in the band gap at the band edges and often appear because of structural disorder in the semiconductor (see also Sec. 3.6.3). Furthermore, Coulomb-bound electron-hole pairs form excitonic states near the band edges, too. As an excitation is formed by two particles, the excitonic energy levels can only be represented in the two-particle picture [17] as depicted in Fig. 2.3. Deep states appear in the middle of the band gap as a result of lattice defects or impurities. These deep states can either be intentionally created by incorporating different elements in the lattice to achieve semiconductor doping, or unintentionally by impure atoms and discontinuities in the crystal lattice (e. g. at the material surface). Figure 2.4 illustrates a multitude of possible transition processes between various states in a semiconductor.

2.3 Charge-carrier recombination

Charge-carrier recombination describes various processes of electron-hole pair annihilation inside a semiconductor. As already shortly stated in Sec. 2.1, the open-circuit voltage can be used a figure of merit to study recombination. Fundamentally, charge carriers in semiconductors can recombine by releasing the excess energy either by emitting photons (radiatively) or releasing phonons (non-radiatively). While radiative recombination processes are unavoidable from a thermodynamic point of view, suppression of non-radiative and defect-related recombination has to be targeted in order to maximize the achievable open-circuit voltage as discussed in the following.

2.3.1 Radiative recombination

In thermal equilibrium, every microscopic process is balanced with its inverse process. This principle called detailed balance is especially important to understand the photovoltaic performance of various types of solar cells and their limitations [18]. The detailed balance principle is illustrated for the emission and absorption process of a black body in Fig. 2.5. The part of black body radiation which is absorbed by an arbitrary body equals the part which is emitted by the same body itself. In Kirchhoff's law [19], this relation is expressed by extrinsic quantities as $\phi_{\text{em}} = A\phi_{\text{in}}$, where ϕ_{em} indicates the emitted photon flux, A is the absorptance of the body and ϕ_{in} is assigned as the incident photon flux. Moreover, van Roosbroeck and Shockley provided a different aspect of the detailed balance approach [20] by linking intrinsic quantities. They found that the internal radiative recombination rate R_{rad} matches the absorption rate $\propto \alpha\phi_{\text{bb}}$ of a body in thermal equilibrium. Here, α is denoted the absorption coefficient and ϕ_{bb} is the black body radiation.

From a thermodynamic perception, radiative recombination as the inverse absorption process cannot be avoided. Consequently, an ideal solar cell is also an ideal LED. In the radiative limit, when radiative recombination is the only present recombination process, the maximum attainable open-circuit voltage $V_{\text{oc}}^{\text{rad}}$ of a solar cell can be derived as [21, 22]

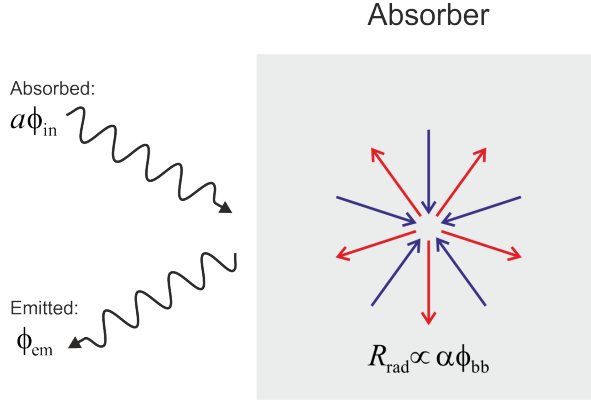


Figure 2.5: Schematic of different facets of the detailed balance between absorption and emission of radiation of a black body absorber in thermal equilibrium. Kirchhoff's law relates the photon emission flux ϕ_{em} to the absorbed fraction of the incident photon flux from the surrounding $A\phi_{in}$. Coming from a rather microscopic perspective, van Roosbroeck and Shockley state that the radiative recombination rate R_{rad} matches the absorption rate $\propto \alpha\phi_{bb}$ of any absorber in thermal equilibrium.

$$V_{oc}^{rad} = \frac{k_B T}{q} \ln \left(\frac{J_{sc}}{J_0^{rad}} \right) = \frac{k_B T}{q} \ln \left(\frac{\int_0^\infty \varepsilon_{in} A(E) \phi_{sun}(E) dE}{\int_0^\infty \varepsilon_{out} A(E) \phi_{bb}(E) dE} \right), \quad (2.4)$$

with J_{sc} being the short-circuit current density, J_0^{rad} is denoted as the radiative saturation current density and ϕ_{sun} is the solar spectrum. Furthermore, ε_{out} and ε_{in} are the étendue of outgoing and incident light, respectively.

2.3.2 Non-radiative recombination

In a real opto-electronic material, beside radiative recombination also non-radiative recombination will take place. As the excitation energy is dissipated during non-radiative recombination as phonons instead of photons, non-radiative recombination processes cannot be directly observed in luminescence spectra. One of the most prominent recombination mechanisms is named after Shockley-Read-Hall (SRH) [24, 25] and their statistics describe the recombination via localized, singly charged states

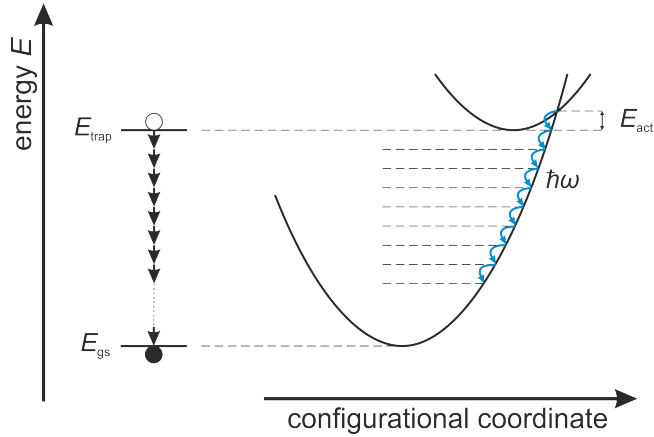


Figure 2.6: Schematic depiction of the non-radiative transition from a deep defect level (E_{trap}) into the ground state (E_{gs}) according to [23]. When overcoming the activation barrier E_{act} , the emission of multiple phonons with energy $\hbar\omega$ accompanies the non-radiative transition process.

in the band gap through multi-phonon emission. Figure 2.6 illustrates this possible process. The respective recombination rate increases with increasing temperature, decreasing band gap and an increasing concentration of deep states, respectively. As these states typically arise from impurity atoms and defects, a suppressed Shockley-Read-Hall recombination rate is an indicator for a rather pure, defect-free and highly crystalline semiconductor material.

During the so called Auger recombination process, the energy gained by recombination of an electron-hole pair, is immediately transferred to an additional electron or hole. In so doing, the involved third charge carrier is ejected deep into its corresponding band. The intra-band relaxation of the carrier back to the band edge is called thermalization and leads to phonon emission, eventually. The Auger effect becomes more efficient for increasing charge-carrier concentrations and also in highly doped semiconductors. Like radiative recombination, Auger-driven recombination is an intrinsic process and as such occurring also in perfect and high quality materials.

Beside the non-radiative Shockley-Read-Hall and Auger recombination pro-

2.3 Charge-carrier recombination

cesses, also direct band-to-band recombination of electron-hole pairs could in principle run non-radiatively through multi-phonon emission. However, direct, non-radiative band-to-band recombination is considered as unlikely, especially in high band-gap materials with low phonon energies [26] as the number of phonons needed to achieve a direct transition strongly influences the multi-phonon transition rate.

As radiative recombination competes with non-radiative recombination, occurring non-radiative recombination causes a reduction in the recorded luminescence intensity. The internal luminescence quantum efficiency Q_i^{lum} states the probability that electron-hole pairs will recombine radiatively

$$Q_i^{\text{lum}} = \frac{R_{\text{rad}}}{R_{\text{rad}} + R_{\text{nrad}}} = \frac{\tau_{\text{nrad}}}{\tau_{\text{rad}} + \tau_{\text{nrad}}}. \quad (2.5)$$

According to Eq. 2.5, Q_i^{lum} can be either expressed in terms of the rates of radiative (R_{rad}) and non-radiative recombination (R_{nrad}) or in terms of the respective carrier lifetimes τ , which can be assigned to the corresponding recombination processes. The internal quantity Q_i^{lum} can be related to an external quantity, the so called LED quantum efficiency Q_e^{LED} . In so doing, the outcoupling efficiency p_e of photons and the probability p_a of parasitic photon absorption have to be taken into account. Hence, Q_e^{LED} which is defined as [27, 28]

$$Q_e^{\text{LED}} = \frac{p_e Q_i^{\text{lum}}}{1 - Q_i^{\text{lum}} (1 - p_e - p_a)} \quad (2.6)$$

contains non-radiative recombination losses, which in turn lower the open-circuit voltage [29–31]. Finally, a relation for V_{oc} can be derived as [27, 28]

$$V_{\text{oc}} = V_{\text{oc}}^{\text{rad}} + \frac{k_B T}{q} \ln(Q_e^{\text{LED}}). \quad (2.7)$$

Consequently, the second term addresses all entropic loss processes, which are connected with parasitic absorption and non-radiative recombination, and result in a further reduction of the attainable open-circuit voltage.

2.4 Time-resolved photoluminescence

Photoluminescence spectroscopy is a non-destructive and sensitive tool to investigate any kind of luminescent transitions in semiconductors. Steady-state photoluminescence, which is recorded during continuous photo-excitation, is commonly used to investigate the electronic structure as discussed in Sec. 2.2, for example the band gap and in general to assess the quality of the semiconductor material by the strength of the luminescence signal. In contrast, time-resolved photoluminescence measures the decay of the luminescence intensity over time after the sample is photo-excited typically by a short laser pulse. The temporal photoluminescence intensity $I_{\text{PL}}(t)$ is dependent on the temporal amount of charge carriers and given by

$$I_{\text{PL}}(t) \propto (n(t)p(t) - n_i^2) = ([n_0 + \Delta n(t)][p_0 + \Delta n(t)] - n_i^2). \quad (2.8)$$

Here, n_i is the intrinsic charge-carrier concentration and the electron and hole concentration are defined as $n(t) = n_0 + \Delta n(t)$ and $p(t) = p_0 + \Delta n(t)$, respectively, with their corresponding equilibrium concentrations n_0 and p_0 . Excess-charge carriers of concentration $\Delta n(t)$ are photo-generated in the sample by the absorption process of the pulsed excitation light. After the pulse has passed, the system strives for equilibrium conditions and excess charges will vanish over time by all kind of recombination events. Consequently, also the photoluminescence intensity as measurable signal will drop according to Eq. 2.8. Ultimately, the observed shape of the luminescence decay gives hints to the various charge-carrier processes like recombination and separation as illustrated in Fig. 2.7 discussed in the following.

2.4.1 Charge-carrier dynamics

In a first simplified attempt to understand charge-carrier dynamics, the charge-carrier profiles are assumed to be flat across the sample at each time during the measurement; i. e. $n(x, t) = n(t)$ and $p(x, t) = p(t)$. Therefore, we first focus only on recombination mechanisms and, additionally, leave out any separation and reabsorption effects. The temporal excess-charge carrier concentration $\Delta n(t)$ can be described by the simplified continuity equation

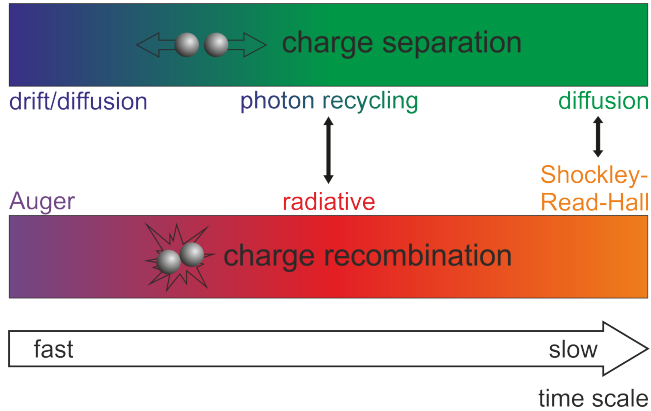


Figure 2.7: Sketch of multiple physical processes which photo-generated charge carriers can undergo during a transient measurement. Various charge-carrier separation and recombination processes may occur on similar time scales and are often interlinked.

$$\frac{d\Delta n(t)}{dt} = -R_{\text{rad}}(\Delta n(t)) - R_{\text{nrad}}(\Delta n(t)). \quad (2.9)$$

The rates $R_{\text{rad}}(\Delta n(t))$ and $R_{\text{nrad}}(\Delta n(t))$ of radiative and non-radiative recombination, respectively, depend on the current excess-charge carrier concentration $\Delta n(t)$ themselves. Types of recombination mechanisms are distinguished by the amount of involved charge carriers and, therefore, show different dependency on the order of $\Delta n(t)$ (see also Sec. 4.1). Consequently, multi-particle recombination processes like Auger and also radiative recombination exhibit high rates at high values of $\Delta n(t)$ and are typically predominant at short times after the excitation pulse. On the contrary, lower order recombination processes like Shockley-Read-Hall become rather critical rather low values of $\Delta n(t)$ and at long times. As the sum of all recombination rates changes during a transient measurement from high values to lower values, excess-charge carriers vanish faster at short times and slower at long times. Consequently, the measured photoluminescence signal according to Eq. 2.8 can exhibit different time-dependent decay behavior. Photoluminescence measures only radiative recombination, however, the shape of its decay is also modified by non-radiative processes, which can later be disentangled amongst each other and from radiative recombination by simulation. In so doing, it is advisable to measure

2 Fundamentals and characterization methods

and compare photoluminescence decays at varying fluences of the excitation light.

Beside charge-carrier recombination, separation of charges can influence time-resolved photoluminescence decays. The charge-carrier concentrations $n(x,t)$ and $p(x,t)$ can spatially vary due to diverse separation effects. As a consequence of any inhomogeneous carrier profile (for example an exponential profile due to Lambert-Beer absorption at $t \approx 0$), there will be regions in the sample of higher internal luminescence strength and others of lower strength. The externally observed luminescence signal is the integral of all local radiative recombination events over the sample dimension d

$$I_{\text{PL}}(t) \propto \int_0^d n(x,t)p(x,t) dx. \quad (2.10)$$

Please be aware that Eq. 2.10 does not consider any reabsorption effects.

Charge carriers can be separated by a drift current due to an applied electrical field, diffusion as a consequence of a concentration gradient, and so called photon recycling. In the first scenario, an electrical field is imposed on a semiconductor, which drives electrons and holes to move in opposing directions. This spatial separation prevents the charge carriers from recombination.

Charge-carrier diffusion is a continuous transport process driven into a net direction by a concentration gradient according to Fick's law. The diffusion current scales directly with the diffusion constant D , which is related to the charge-carrier mobility μ . At short times after the excitation pulse, diffusion will flatten the initially inhomogeneous distribution of the charge-carrier concentrations $n(x,t)$ and $p(x,t)$, which follow a Lambert-Beer like absorption profile. Moreover, an ongoing diffusion current from the bulk to the surfaces will sustain surface (Shockley-Read-Hall) recombination also at later times.

Photon recycling refers to the self-absorption effect of luminescence generated upon radiative recombination, and leads to an effective redistribution of the involved carriers. The effectiveness of photon recycling as charge transport mechanism depends on several factors, e. g. (1) the magnitude of the radiative recombination rate R_{rad} , which indicates how fast charge carriers recombine radiatively; (2) the absorption coefficient $\alpha(E)$ of the semiconductor material specifies the mean travel

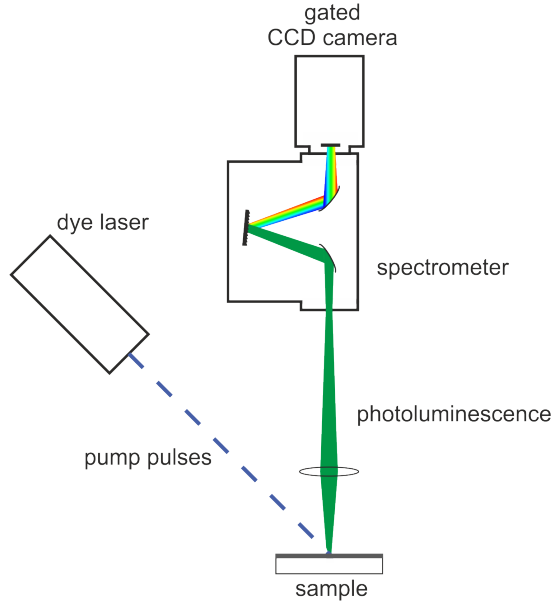


Figure 2.8: Schematic drawing of the time-resolved photoluminescence (TRPL) experiment. The sample is excited by the pulsed beam from a dye laser. The temporal photoluminescence (PL) signal of the sample is coupled into a spectrometer, spectrally resolved due to a grating unit and detected by a gated charged-coupled device (CCD) camera.

length between the location of the recombination event and the position where the internally emitted photon is reabsorbed; (3) the optical design of the sample determines the light path and whether luminescence is preferably internally reabsorbed or rather out-coupled and leaves the sample.

2.4.2 Setup and experimental details

The setup for measuring time-resolved photoluminescence (TRPL) decays is depicted in Fig. 2.8. First, charge carriers are generated within the sample by absorption of pulsed laser light. The excitation source consists here of a dye unit coupled to a nitrogen laser (MNL 200 from LTB), which operates on the principle of transversal excitation at atmospheric pressure. A power switch triggers fast high-current discharging in the laser channel filled with nitrogen gas as gain medium at

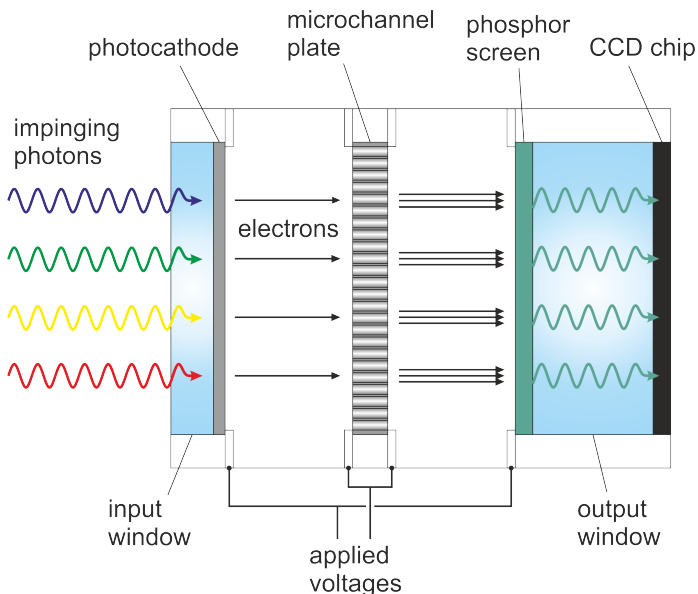


Figure 2.9: Schematic drawing of the image intensifier. A radiation signal impinges onto the photocathode and causes the release of photoelectrons. The electron signal is amplified by transit through the microchannel plate. Subsequently, the free electrons excite a phosphor screen. Ultimately, photons are emitted towards the CCD chip and the radiation signal is detected.

a maximum rate of 20 Hz. The emitted 337.1-nm laser pulses last each for approx. 0.7 ns and exhibit a total energy of $E \geq 100 \mu\text{J}$ each. In turn, a laser dye inside a cuvette is pumped by these ultraviolet (UV) pulses. Due to the already pulsed nature of the pump light, the dyes will emit laser pulses at down-converted, narrow-band photon energies. The laser dyes are typically solid, large organic compounds, which are dissolved in suitable polar liquids. In order to achieve lasing conditions in the dye at a distinct wavelength, the resonator, which holds the cuvette, can be adjusted by a tunable grating unit. The striking advantage of such a laser system is the wide availability of dyes covering basically the entire visible range of the electromagnetic spectrum by their emission [32]. By selecting an appropriate dye, the individual absorption demands of the sample materials can be fulfilled. The laser dyes used in this thesis, Coumarin ($\lambda \simeq 498 \text{ nm}$) and Diphenylstilbene (DPS, λ

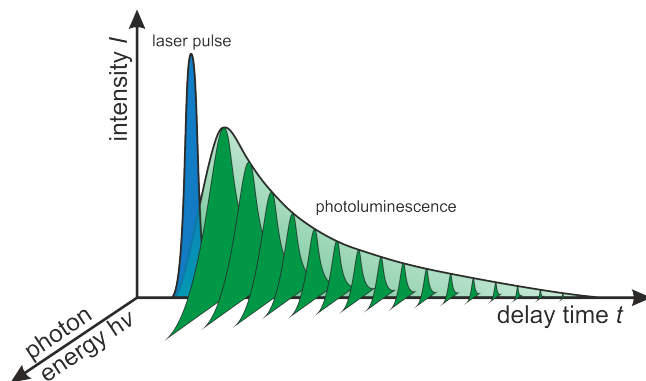


Figure 2.10: Measurement procedure of the time-resolved photoluminescence recorded by a gated camera. While a laser pulse (blue peak) excites the sample, the photoluminescence signal (green shaded envelope) starts to rise first. Eventually, the intensity of the recorded spectra (green filled) will continuously decrease and the photoluminescence signal decays as time goes by.

$\simeq 404$ nm), were purchased from Lambda Physik and Radiant Dyes. A peristaltic pump enables the constant exchange of the dye solution in the cuvette by a flow from a larger reservoir, which helps to decelerate exhaustion effects triggered by UV radiation. Via an optical fiber, the dye laser pulses impinge at an angle of 30° on the sample surface and illuminate a spotsize of approx. 3.4×10^{-3} cm². As a consequence of the excitation process, the sample emits photoluminescence (PL) itself. A fraction of the PL intensity can be focused and coupled into the spectrometer (SPEX 270M from Horiba Jobin Yvon). Edge filters placed in front of the entrance slit of the spectrometer suppress scattered light from the laser. Inside the spectrometer, the PL beam is diffracted by the grating unit (150 lines/mm, 500 nm blaze) and spectrally dispersed. The spectral beam spread is pixel-wise detected as a luminescence spectrum by an intensified charge-coupled device (ICCD) camera (iStar DH720 from Andor Solis). The working principle of the gated camera with image intensifier is shown in Fig. 2.9, which mainly comprises the photocathode, the microchannel plate (MCP), the phosphor screen and the CCD chip. In order to gain amplification of the impinging radiation, the optical signal is first converted into an electronic signal. The photocathode, which is coated onto the inside of the

2 Fundamentals and characterization methods

input window, captures the incident image. Impinging photons within a wavelength range of approx. 200 nm to 900 nm cause the emission of free electrons due to the photoelectric effect. Here, the (Multi Alkali) photocathode material primarily determines the spectral response of the ICCD camera. The generated photoelectrons are drawn by an electric field towards the MCP, which consists of a thin disc with a honeycomb structure of channels, each with a resistive coating. A high potential gradient realized across the channels accelerates photoelectrons. Every time an electron hits the wall of a thin channel during its transit, secondary electrons might be released. The electronic signal gets readily intensified by gains in excess of 10^3 simply by traversing the MCP with multiple impacts on the channel walls. The actual degree of electron multiplication is controlled by the applied voltage across the MCP. Finally, the electron pulses excite a phosphor (P43) screen. The emitted photons at a peak wavelength of approx. 540 nm can be easily detected by the silicon CCD chip consisting of an array of 1024×256 pixels with an effective pixel size of $26 \mu\text{m} \times 26 \mu\text{m}$. Upon illumination, charges proportional to the incident light intensity accumulate in the individual pixels. After pixel-wise readout, images and spectra of the illumination source are obtained. In order to perform time-resolved measurements, the inherently shutter (gate) functionality of the image intensifier is exploited. By reverse poling of the voltages between photocathode and MCP, photoelectrons do not enter the MCP anymore due to the opposing electric field. As a consequence, no signal will be detected. The exact gating times are triggered by a partial signal of the laser dye pulse in combination with applying different delay times between the trigger signal and the actual opening of the gate. This procedure enables recording temporal spectra as schematically depicted in Fig. 2.10. The width of the gate pulse, which allows any PL-related signal to pass the MCP, is typically chosen between 2 or 5 ns depending on the signal strength. The temporal resolution of the gate pulse delay is indicated as precise as 25 ps. To minimize noise and to account for averaging the slightly different energies of individual laser pulses, an integration time of the camera in the range of some seconds was chosen resulting in the accumulation of multiple PL spectra at a given delay time.

2.4.2.1 Wavelength calibration

As seen in Fig. 2.8, the PL signal gets spectrally diffracted by the grating unit of the spectrometer. Thus, only the light of a certain wavelength range impinges on each of the individual vertical camera pixels. In order to calibrate the camera for the correct wavelength setting, the spectral irradiance of either a neon or xenon discharge lamp, which is mounted at the sample position, is recorded for the central grating positions, namely 500 nm and 720 nm. Subsequently, the observed peak patterns are aligned in order to match the respective reference patterns [33] and, in so doing, the wavelength calibration is obtained.

2.4.2.2 Intensity calibration

Before any luminescence signal is detected, it has to run through a set of optical elements. As a consequence, each recorded spectrum represents a convolution of the real luminescence signal and the spectral response of the entire setup. For instance, the transmission through lenses, the grating efficiency and the quantum efficiency of the camera cause a spectral distortion of the initial spectral irradiance of the emitter. In order to correct recorded spectra for the relative intensity, the following procedure is applied as illustrated in Fig. 2.11. First, the spectrum of a halogen lamp (a), which is mounted at the sample position, is recorded. The division of (a) by the known spectral irradiance of the lamp (b) results in a correction curve (c), which takes the spectral response of the setup into account. Any measured PL spectrum (d) is now divided by the correction (c) itself. Because the spectra are often plotted against the photon energy $h\nu$ scale, but the spectral measurement is typically carried out in steps of wavelength $\Delta\lambda$, an additional correction of the spectral shape should be regarded [23]. By differentiating $h\nu$ with respect to λ , I find

$$|d(h\nu)| = \frac{hc}{\lambda^2} |d\lambda|. \quad (2.11)$$

According to Eq. 2.11, when increasing the wavelength by steps of $d\lambda$, the elemental energy interval $|d(h\nu)|$ is not kept constant because it scales with λ^{-2} . In order to maintain the correct relative PL shape of a spectrum plotted against photon

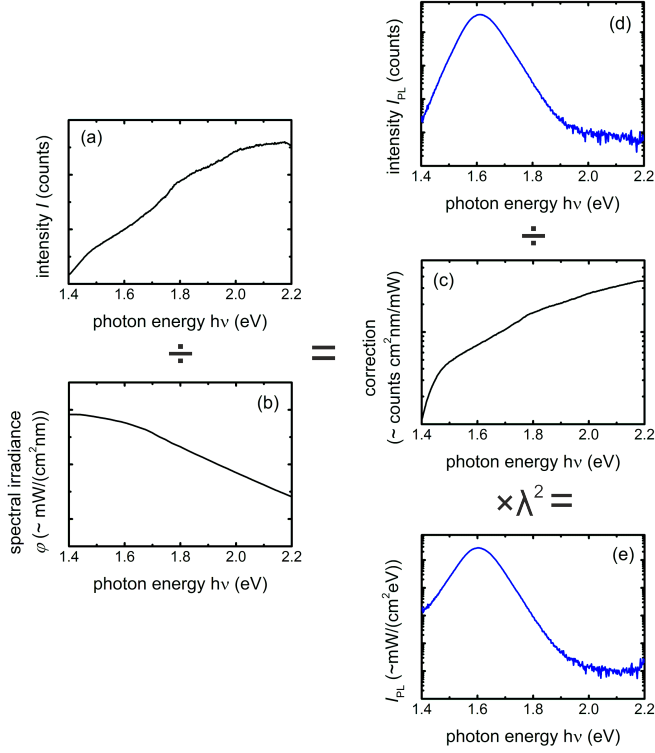


Figure 2.11: Procedure of the intensity calibration of measured PL signals, adapted from [34, 35]. (a) A measured halogen spectrum differs from (b) the known halogen reference due to the spectral response of the entire setup. (c) The calculated correction curve is applied to (d) the measured PL signal in order to obtain (e) the calibrated PL spectrum. The multiplication of the intensity values with λ^2 allows the unit conversion of the y-axis from $\sim \text{mW}/(\text{cm}^2\text{nm})$ to $\sim \text{mW}/(\text{cm}^2\text{eV})$, which is appropriate when spectra are plotted as a function of photon energy.

energy $I(h\nu)$ (e), any measured spectrum $I(h\nu)$ should be corrected by multiplying each value of $I(h\nu)$ by λ^2 .

2.5 Characterization methods

2.5.1 Photoluminescence setup

To measure steady state photoluminescence (PL) spectra, samples are optically excited by continuous wave (CW) solid-state lasers (e. g. Cobolt Samba, wavelength $\lambda = 532\text{nm}$, power output 150 mW) through an microscope (Olympus BX51). The excited area is determined by the Gaussian-shaped laser spot with a full width at half maximum (FWHM) of approx. $1\ \mu\text{m}$. The emitted radiation from the sample is coupled into a spectrometer (iHR320 from Horiba) after filtering the laser scattering by different combinations of notch and edge filters). A more detailed description of the setup can be found elsewhere [34, 35].

2.5.2 Photothermal deflection spectroscopy

Photothermal deflection spectroscopy (PDS) is a highly sensitive technique to obtain the absorptance of thin films. In contrary to conventional methods used to determine absorptance values, PDS does principally not rely on transmission and reflection experiments but measures the thermal state of the sample due to the absorption of radiation. As a consequence of measuring a physical quantity, which is directly proportional to absorptance, a high dynamic range of several orders of magnitude is gained for the absorptance by PDS. The schematic PDS setup is depicted in Fig. 2.12 and measurements were performed by Joseph Klomfaß and Oliver Thimm. The sample is adjusted in a cuvette filled with FC-75 solution. This liquid is a fluorocarbon derivative of tetrahydrofuran ($\text{C}_8\text{F}_{16}\text{O}$), chemically inert towards organic compounds and transparent in the visible wavelength range. A halogen lamp operated at 100 W in combination with an attached spectrometer (270M from Horiba Jobin Yvon) illuminates the sample with monochromatic light. Excited states, which are generated by absorption of radiation, eventually relax back into the ground states in mainly two different ways: (1) radiatively by the emission of photons or (2) non-radiatively by the release of phonons. PDS solely relies on non-radiative recombination of electron-hole pairs. As a consequence thereof, heat is generated in the sample and transferred to the surrounding FC-75 chemical. Thus,

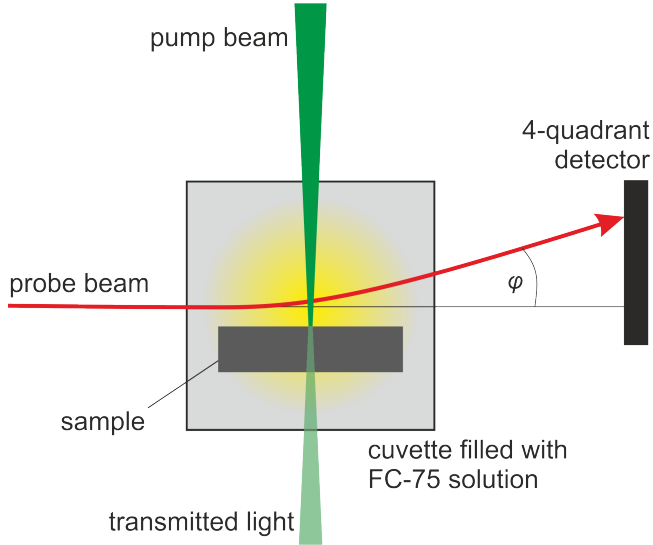


Figure 2.12: Schematic drawing of the photodeflection spectroscopy (PDS) setup. A monochromatic pump beam excites the sample. The absorbed energy is eventually converted to heat and released to the surrounding FC-75 solution. Its refractive index changes as a function of temperature. Therefore, the deflection of a probe beam above the sample is a direct measure of the absorbed power by the sample.

a temperature gradient $\vec{\nabla}T$ establishes in the liquid adjacent to the excitation spot on the sample. Because FC-75 exhibits a temperature-dependent refractive index, $\vec{\nabla}T$ is accompanied by a gradient in refractive index $\vec{\nabla}n_r$. A probe beam from a diode laser (650 nm) is adjusted in parallel and close to the surface of the sample. Due to $\vec{\nabla}n_r$, the probe beam is deflected by an angle φ and detected by a four-quadrant silicon diode. The deflection angle φ is a direct measure of the power of the absorbed light. In order to gain absolute absorptance values, the transmittance and reflectance values are measured. For calculating absorption coefficients without interference fringes, the refractive index and the thickness of the absorbing layer have to be known. For more detailed information about photothermal deflection spectroscopy the reader is directed to Ref. [36–38].

2.5.3 Optical pump terahertz probe spectroscopy

Optical pump terahertz probe (OPTP) spectroscopy is a time-resolved technique which allows studying charge-carrier dynamics in semiconductors and determining charge-carrier mobilities. Samples were investigated with OPTP by Hannes Hempel from Helmholtz-Zentrum Berlin. In the used setup, charge carriers are generated in the sample by excitation of a 403-nm pump pulse of approximately 70 fs full width half maximum. Pulses in the range of (0.3 - 3) THz are used as a probe in transverse mode to monitor excited species. By the applied frequency range, probe energies between a few and some ten meV are covered, which are sensitive to the response of charge quasiparticles like free charge carriers, polarons, and excitons. In organic inorganic perovskites, free electrons with concentration $n(t)$ and free holes with concentration $p(t)$ are probed. The transmitted intensity $E(t)$ of the terahertz probe pulse changes due to absorption by pump-induced free charge carriers. This normalized change $\Delta E/E$ is directly proportional to the conductivity change $\Delta\sigma$ according to

$$\frac{\Delta E(t)}{E} \propto \Delta\sigma(t) = q[\mu_n\Delta n(t) + \mu_p\Delta p(t)]. \quad (2.12)$$

Here, q is the elementary charge and μ_n and μ_p are the mobilities of electrons and holes, respectively. By simulation the exact relation between $\Delta E/E$ and $\Delta\sigma$ based on a transfer-matrix approach, the absolute values of the sum of electron and hole mobility can be gained.

2.5.4 Thermopower measurements

Thermoelectric power measurements are applied to investigate the electronic transport behavior in thin-films and to derive doping concentrations. These measurements were performed by Dr. Jan Mock. The used setup is described in more detail elsewhere [39, 40]. First, coplanar gold contact stripes are thermally deposited on a Corning glass substrate, and a perovskite layer is formed on top (according to Sec. 3.4.1). The sample is brought in contact with two heaters operating at different temperatures in order to achieve a temperature gradient ($\Delta T \approx 10$ K) across the coplanar contact distance (4 mm). As a consequence of ΔT , locally different

2 Fundamentals and characterization methods

amounts of electrons are thermally induced into the conduction band. Due to the gradient in electron concentration, a directional diffusion current establishes. The resulting emergence of a depletion region in the thermodynamic equilibrium is associated with the formation of an electric field, which is experimentally measured as thermoelectric voltage in the end. The interplay between temperature gradient and voltage is known as the Seebeck effect. Furthermore, the ratio between thermoelectric voltage and temperature difference is called Seebeck coefficient $S(T)$. If a thin-film exhibits a high charge-carrier concentration e. g. due to doping, ΔT might cause only a small concentration gradient resulting in a small value of $S(T)$. Therefore, the Seebeck coefficient is a measure of the absolute charge-carrier (doping) concentration of the sample.

2.5.5 Scanning electron microscopy

The used Zeiss (Leo) Gemini 1550 microscope detects secondary electrons emitted from the sample. Surface images are recorded when the electron beam scans over the sample. Here, the microscope exhibits a Shottky field-emission cathode and an in-lens secondary electron detector. The lateral resolution is in the range of ~ 1 nm at a voltage of 20 kV. Measurements are performed in vacuum at a base pressure of 10^{-6} mbar. Scanning electron microscopy (SEM) images were recorded by Pascal Kaienburg, Dr. Benjamin Klingebiel and Jan-Christoph Hebig.

2.5.6 Atomic force microscopy

Atomic force microscopy (AFM) facilitates the mapping of height profiles of surfaces and is conducted with a NANOSTation 300 (S.I.S. GmbH). While the tip of an oscillating cantilever scans over the sample surface, attractive Van-der-Waals forces as well as repulsive Coulomb forces based on the Pauli principle act between the surface and the tip. The resulting deflection of the cantilever is detected as a monochromatic laser beam impinges on a four-quadrant diode after being reflected from the cantilever top. Thus measured height profiles typically exhibit a resolution of $\lesssim 10$ nm. AFM images were recorded by Pascal Foucart. In this work, I have used the software Gwyddion to visualize and analyze surface topographies.

2.5.7 X-ray diffraction

X-ray diffraction (XRD) patterns are obtained to investigate the crystalline structure of perovskite thin films. Here, the used diffractometer (Bruker D8 Advance) operates in the Bragg-Brentano θ - 2θ configuration. The Cu K_α spectral line with a wavelength of 1.54 \AA is used as X-ray source. A detailed description of the working principle and the measurement setup is provided in the dissertation [41] of Dr. Florian Köhler, who conducted the XRD measurements. The perovskite samples are mounted in a sealed plastic dome filled with inert nitrogen to avoid exposure to ambient air and, thus, possible structural changes and degradation during the XRD measurements.

2.5.8 X-ray photo-electron spectroscopy

X-ray photo-electron spectroscopy (XPS system from Scienta Omicron MXPS with XM1000 Al K_α X-ray source at 300 W) is performed to determine the chemical elements and compositions at perovskite surfaces. Survey spectra were collected by Dr. Benjamin Klingebiel in constant analyzer energy (CAE) mode with a path energy of 100 eV, whereas for the high-resolution spectra a path energy of 10 eV is applied. The source analyzer angle is 90° and the takeoff angle of the electrons with respect to the surface normal is 21° . The energy resolution is estimated in a separate measurement to be approx. 0.6 eV from the full width at half maximum of the Au 4f peak. The intensities are determined by measuring the peak areas after subtracting a Shirley-type background and fitting a combination of Lorentzian and Gaussian profiles with a fixed proportion of 30:70 to the experimental data. The fitting procedure was performed in Igor Pro (Wavemetrics) with the help of the XPST plugin (M. Schmid, Philipps University Marburg). Spectra are shifted such that the Pb $4f_{7/2}$ peak (in the formal +2 redox state) is located at a binding energy of $E_b = 138.6 \text{ eV}$ [42]. This procedure eliminates the impact of variations in the work functions of different samples.

2.5.9 Profilometer

The precise determination of film thicknesses is necessary in order to calculate some material parameters, e. g., the absorption coefficient α . Scratching with the sharp tip of tweezers removes the soft perovskite material from the glass substrate. The probe tip of the profilometer (Veeco DEKTAK 6M Stylus Profiler) is brought in direct contact with the sample and scans the topography across the trenches. From the observed difference in the height profile, the film thickness can be evaluated with the precision of some nanometers.

3 Material properties of organic inorganic perovskites

3.1 Perovskite crystal structure

The term "perovskites" generally refers to a broad class of crystalline materials, which exhibit the same structure as calcium titanate (CaTiO_3) [43]. This particular material was named after the Russian Count and mineralogist Lev Perovski by its discoverer Gustav Rose, who spotted the mineral 1839 in the Ural Mountains [44]. The general perovskite structure consists of the chemical formula ABX_3 , where A and B are cations of different sizes and the anion X coordinates to B by forming a BX_6 octahedron (see Fig. 3.1). In organic inorganic perovskites the A-site is typically occupied by organic amine cations like methylammonium (CH_3NH_3^+) or formamidinium ($\text{CH}(\text{NH}_2)_2^+$). A heavy metal cation like Pb^{2+} or Sn^{2+} is located at the B-site and the anion X consists of halide ions like I^- , Br^- and Cl^- or a mixture thereof. The availability of numerous abundant organic as well as metallic ions, which are able to form perovskite structures when combined, enables the creation of materials with unique semiconducting properties [45]. A measure of the ratio of ionic dimensions that are tolerated by the perovskite architecture is given by the Goldschmidt tolerance factor t [46]:

$$t = \frac{r_{\text{A}} + r_{\text{X}}}{\sqrt{2}(r_{\text{B}} + r_{\text{X}})}, \quad (3.1)$$

where r is the radius of the effective ion dimensions of the respective sites as indexed. Most organic inorganic perovskite compounds exhibit tolerance factors in the range of $t \approx 0.8 - 1.1$ [45], whereas an ideal cubic perovskite structure results in $t = 1$.

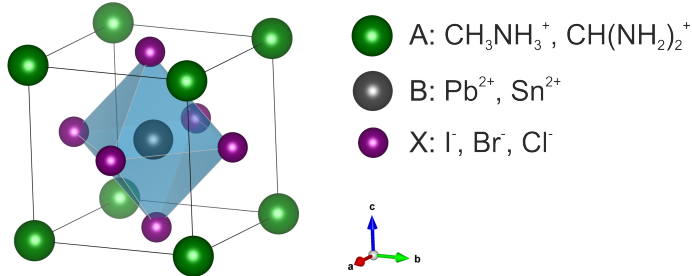


Figure 3.1: Illustration of the cubic organic-inorganic perovskite unit cell with the structure ABX_3 , where A typically displays an organic cation, B denotes a metal ion and X represents a halide ion. The visualization was done with the software tool *VESTA 3* [47].

However, this geometrical packing approach does not take covalent bonding between B and X sites into account and does not allow for a lowering of crystal symmetry. Mismatch of A- and B-sites and tilting of BX_6 octahedral units are the main causes of structural distortions in organic inorganic perovskites [48, 49]. The distortion and the symmetry break get more pronounced for lower temperatures T . Phase transitions are observed upon cooling, evolving from a cubic ($T \gtrsim 330\text{K}$) to a tetragonal ($330\text{K} \gtrsim T \gtrsim 160\text{K}$) and an orthorhombic structure lastly ($T \lesssim 160\text{K}$) [50]. The phase transition temperatures indicated in parentheses are stated for methylammonium lead iodide ($\text{CH}_3\text{NH}_3\text{PbI}_3$). This material composition represents up to now the most common and most investigated organic inorganic perovskite material, which is applied for optoelectronic purposes. In order to understand the exceptional performance of organic inorganic perovskites, it is worth having a brief look at the historic progress of research into its optoelectronic properties.

3.2 Emerging as photovoltaic material

The first synthesis of methylammonium lead halide perovskites and the determination of their crystal structures was accomplished by Weber in 1978 [51]. During the 1990s, Mitzi and coworkers investigated charge transport phenomena in organic inorganic perovskites and fabricated first electronic devices [52–54]. In 1999, the research group of Miyasaka applied perovskites for the first time as absorber materials inside

3.2 Emerging as photovoltaic material

dye-sensitized solar cells yielding power conversion efficiencies of up to 3.8% [55]. This photovoltaic concept relies on a conductive mesoporous scaffold (often titania, TiO_2), which is coated with only a few nanometers of light-absorbing molecules or particles and is immersed under an electrolyte solution. Subsequently, Snaith and coworkers replaced titania by insulating aluminum oxide and still achieved a high conversion efficiency [56]. By doing this, they were able to demonstrate efficient charge transport through methylammonium lead halide perovskites. This discovery paved the way towards high-efficient perovskite solar cells with compact perovskite layers exhibiting thicknesses of hundreds of nanometers [57]. Over the last few years, a better control over perovskite quality and an enhanced alignment of electron and hole transport layers have established new record device efficiencies already reaching 22% by now [58]. The highest efficiencies and open-circuit voltages ($\sim 1.1 - 1.2\text{V}$ for perovskites with a bandgap of 1.6eV [59–61]) can be expected from the *n-i-p* stack starting with a *n*-type conducting material like the commonly used titania on the bottom, covered with a layer of intrinsic perovskite and a *p*-type organic semiconductor on top (often Spiro-OMeTAD: 2,2',7,7'-tetrakis-(N,N-di-4-methoxyphenylamino)-9,9'-spirobifluorene). It shall be noted here, that two main cell architectures, each with specific advantages, are typically applied for perovskite devices. Besides the mesoporous titania approach, which requires a high temperature sintering process ($T > 450^\circ\text{C}$) to form the scaffold, titania can also be employed as flat layer [62]. Here, the planar configuration concept as commonly applied in organic photovoltaics suffers from a typically lower device stability [63, 64] and a distinct appearance of current-voltage hysteresis [65, 66]. However, the planar configuration allows the utilization of a wider field of transport materials by being able to also realize the "inverted" *p-i-n* structure, starting with a *p*-type selective contact at the bottom. In so doing, the hole transport polymer PEDOT (poly-3,4-ethylenedioxythiophene) is most commonly used, while the fullerene derivative PCBM ([6,6]-phenyl- C_{61} -butyric acid methyl ester) is often employed as electron transport material. Devices with the planar *p-i-n* configuration show negligible hysteresis but do not reach the highest efficiencies yet [67, 68].

To put the fast ascent of perovskite photovoltaic development into perspective, gallium arsenide (GaAs) as the best inorganic single-junction absorber reaches nowadays an efficiency of $\sim 29\%$ [58] after starting at $\sim 4\%$ more than 60 years

3 Material properties of organic inorganic perovskites

Table 3.1: Overview of characteristic transport properties of methylammonium lead halide perovskites, crystalline silicon and GaAs. Values are taken from literature [69–72].

Material		Diffusion length (μm)	Carrier lifetime (μs)	Mobility ($\text{cm}^2\text{V}^{-1}\text{s}^{-1}$)	Effective mass (m_0)	Trap density (cm^{-3})
$\text{CH}_3\text{NH}_3\text{PbI}_3$ thin film		0.1 – 1	0.01 – 1	1 – 10	$\sim 0.10 - 0.30$	$10^{15} - 10^{16}$
$\text{CH}_3\text{NH}_3\text{PbI}_3$ single crystal		2 – 8	0.5 – 1	24 – 105	–	$(1 - 3) \times 10^{10}$
$\text{CH}_3\text{NH}_3\text{PbBr}_3$ thin film		0.3 – 1	0.05 – 0.16	30	0.13	–
$\text{CH}_3\text{NH}_3\text{PbBr}_3$ single crystal		3 – 17	0.3 – 1	24 – 115	–	$(0.6 - 3) \times 10^{10}$
Si	e^-	1000	~ 1000	1450	0.19	$10^8 - 10^{15}$
	h^+	600		500	0.16	
GaAs	e^-	7	$\sim 0.01 - 1$	8000	0.063	
	h^+	1.6		400	0.076	

ago [73]. Certainly, the rapid evolution of perovskites as high quality photovoltaic materials has benefited from earlier research of other photovoltaic technologies [69].

While organic inorganic perovskites show exceptional photovoltaic performance, the attraction of this material class stems from multiple aspects. First, perovskite fabrication requires solely low-cost precursor materials which are based on earth-abundant elements. In addition, the huge variety of available organic and inorganic ions facilitates the formation of perovskite materials with unique optical and electrical properties [74]. On top of that, the fabrication process can simply be accomplished from the liquid phase at moderate temperatures around $\sim 100^\circ\text{C}$ with dip and spin coating allowing for cheap processing. Although the fabrication conditions for a solution-based process are not as well-defined as e. g. for vacuum deposition, perovskites can stand up to any comparison with well-established photovoltaic technologies. Table 3.1 summarizes transport characteristics of perovskites and compares them to those of crystalline silicon and GaAs. While carrier lifetimes and effective charge carrier masses (stated here as fraction of the electron rest mass $m_0 \sim 9.1095 \times 10^{-31} \text{ kg}$ [75]) for perovskites are similar to the corresponding prop-

erties of the direct semiconductor GaAs, perovskites have to tolerate lower charge-carrier mobilities and associated diffusion lengths. Crystalline Si exhibits excellent transport properties due to its high purity and indirect band gap.

3.3 Electronic structure

Despite their polycrystalline structure, remarkably long charge-carrier lifetimes can be observed in perovskite thin films (see Table 3.1). The origin of the extended lifetimes and favorable transport characteristics in general is ascribed to the special electronic structure in organic inorganic perovskites. Pb^{2+} exhibits the formal electron configuration $6p^26s^0$, while halides have the configuration np^6 with $n = 3, 4, 5$ in the sequence $\text{Cl}^-, \text{Br}^-, \text{I}^-$. Figure 3.2 depicts the formation of bonding (σ) and anti-bonding (σ^*) hybrid orbitals from atomic lead and iodine orbitals. Surprisingly, the resulting anti-bonding hybrid state between the empty $6s$ -orbital of Pb^{2+} and the dominating halide p -orbital determines the top of the valence band, whereas the non-bonding hybrid state between lead $6p$ - and halide np -orbitals corresponds to the conduction band minimum [76–78]. As lead and iodine are heavy elements, relativistic effects like spin-orbit coupling have to be considered in the formation process of valence and conduction bands [72]. The electronic levels of the organic cation, which occupies the A-site, are situated deep within the valence and conduction bands [79]. Therefore, the impact of the organic cation on the perovskite band structure is negligible. Only a minor effect is observed when substituting the organic A-site cation (methylammonium) by an inorganic cation like Cs^+ as a result of size effects [80]. However, the A-site cations compensate charges of the $[\text{PbI}_6]^{4-}$ octahedrons and, as a consequence, stabilize the perovskite structure.

A semiconductor with anti-bonding states at the valence band maximum often features a tolerance towards defects [84]. Figure 3.3 illustrates calculated energy levels of possible intrinsic point defects in methylammonium lead iodide, including vacancies ($V_{\text{MA}}, V_{\text{Pb}}, V_{\text{I}}$), interstitial ($\text{MA}_i, \text{Pb}_i, \text{I}_i$), cation substitutions ($\text{MA}_{\text{Pb}}, \text{Pb}_{\text{MA}}$) and anti-site substitutions ($\text{MA}_i, \text{Pb}_i, \text{I}_{\text{MA}}, \text{I}_{\text{Pb}}$). Furthermore, the formation energy of the individual defects is indicated. Point defects, which are more likely incorporated in the perovskite structure due a low formation energy, show

3 Material properties of organic inorganic perovskites

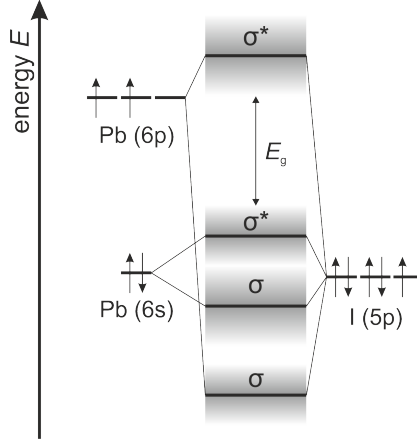


Figure 3.2: Sketch of the bonding diagram formed by the hybridization of lead and iodine atomic orbitals adapted from [76,81]. Bonding/anti-bonding hybrid orbitals are indicated as σ/σ^* . The energy distance E_g refers to the band gap.

only levels with a distance of less than 0.05eV from the band edges. Therefore, they either occur as shallow defects or are situated inside the conduction and va-

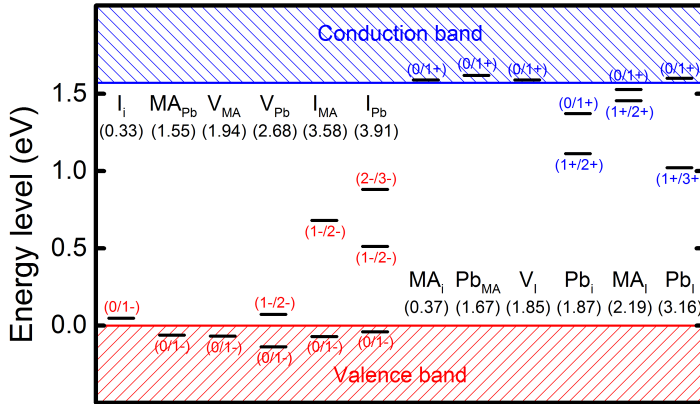


Figure 3.3: Calculated energy levels of intrinsic point defects in methylammonium lead iodide adapted from [82, 83]. The notation M_N refers to a defect where the ion M is located at the lattice position of ion N. Here, V denotes a vacancy and an interstitial site is indexed as i. The respective defect formation energy is shown in parentheses.

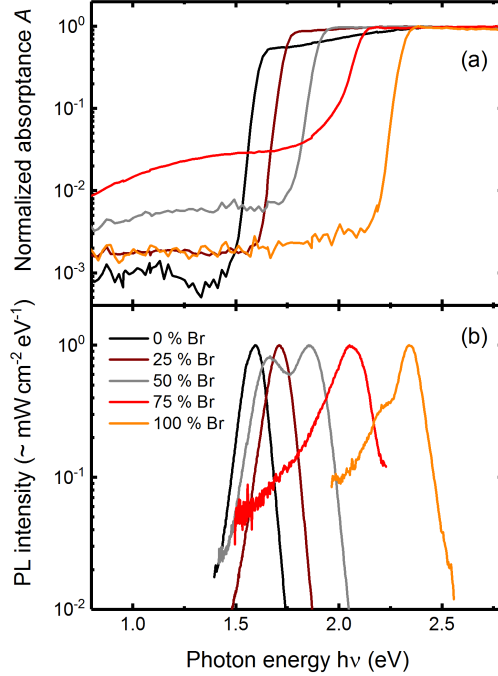


Figure 3.4: (a) Normalized absorbance A from photothermal deflection spectroscopy of perovskite thin-films with different halide compositions. Here, iodine is gradually substituted by bromine. (b) Corresponding photoluminescence (PL) spectra measured with the time-resolved photoluminescence setup at zero delay time with respect to the pump pulse.

lence bands, respectively. In any case, the charge transport will only be marginally hindered by the occurrence of point defects with low formation energies. On the other hand, the remaining defects, which generate deep levels between the bands, exhibit high formation energies. As non-radiative recombination typically relies on deep transition states, the intrinsic defect tolerance allows for long minority-charge carrier lifetimes and explains the achievement of remarkable transport properties in organic inorganic perovskites.

By taking up the earlier fact that the choice of halide element severely influences the position of the valence band maximum, while the position of the bottom of the conduction band is barely altered, the band alignment of perovskites can be

3 Material properties of organic inorganic perovskites

modified. Thus, a continuous band gap grading is achieved by incorporating different amounts of halide elements at the same time [3, 4]. By varying the bromine to iodine ratio as a proof of concept, the band gap is tuned in the range of $\sim 1.6\text{eV}$ (pure iodide perovskite) to $\sim 2.3\text{eV}$ (pure bromide perovskite), as revealed by absorptance and photoluminescence measurements (see Fig. 3.4). Sharp absorption onsets over several orders of magnitude are observed in the normalized absorptance spectra of Fig. 3.4 (a). Some compositions, especially 75 % and 50 % bromide, exhibit relative strong absorption features in their sub-band gap region indicating high structural disorder and the formation of a distinct amount of defect states. A similar trend is seen in the normalized photoluminescence spectra of Fig. 3.4 (b) due to the conjunction of absorption and emission processes. For compositions of 50 % bromide and above, the falling photoluminescence flank towards lower energies significantly smears out. A second apparent peak at lower photon energies may hint at occurring chemical degradation in the case of 100 % bromide and/or a light-induced phase segregation into local bromide-enriched (iodide-depleted) and bromide-depleted (iodine-enriched) domains [4] in the case of 50 % bromide. Anyway, the preparation conditions might not been optimized for the individual perovskite compositions. However, Fig. 3.4 demonstrates the variability of the electronic structure of organic inorganic perovskites.

3.4 Sample preparation

3.4.1 Perovskite thin films

Thin-films of methylammonium lead iodide perovskite are fabricated by the following procedure. First, lead chloride (PbCl_2 , from Alfa Aesar) and methylammonium iodide (MAI: $\text{CH}_3\text{NH}_3\text{I}$, from Dyesol) are dissolved in dimethylformamide (DMF) at a molar ratio of $\text{MAI}:\text{PbCl}_2 = 3 : 1$ (35 wt%). Corning glass substrates (12 mm \times 12 mm) are cleaned with soap (Helmax III), thereafter in an ultrasonic bath of acetone first followed by isopropyl alcohol. After thorough rinsing, the substrates are dried in a nitrogen stream and surface-activated by an oxygen plasma (ZEPTO B plasma laboratory unit from diener electronics) for at least 3.5 min at 50 W. The

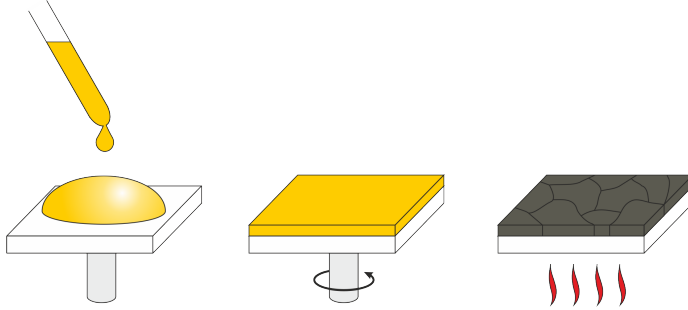


Figure 3.5: Sketch of the manufacturing process of organic-inorganic thin-film perovskites from the liquid phase. The precursor solution is dropped onto the substrate and forms a thin-film by spin-coating. Annealing of the sample results in the transformation into a multi-crystalline perovskite layer.

further procedure is illustrated in Fig. 3.5. Approximately 40 μl of the precursor solution is dropped onto the glass substrate, which is then spin coated inside a nitrogen filled glove box at 3000 rpm for 35 s after a ramp time of 10 s (SpinCoater MB-SC-200 from MBRAUN). A subsequent annealing on a hot plate (typically 90 °C for approximately 2 h) transforms the liquid precursor film into a multi-crystalline layer composed of the typical perovskite structure (see Fig. 3.1) according to the reaction scheme [85]



The amount of chloride which is typically incorporated in the final perovskite structure is vanishingly small ($x \ll 1$) [86–88]. Nevertheless, the perovskite quality benefits from the presence of chloride by a favorable crystallite growth [86] and improved transport characteristics [89]. Due to the off-stoichiometric (from the perovskite formation aspect) molar ratio of MAI:PbCl₂ = 3 : 1, resulting methylammonium chloride compounds or any related products thereof have to vanish by entering the gaseous phase [86].

The annealing step was performed either in nitrogen atmosphere, in ambient air or inside a climate box (890-THC-DT glove box from Plas-Labs), which allows the precise adjustment and control of the moisture content. The best results for per-

3 Material properties of organic inorganic perovskites

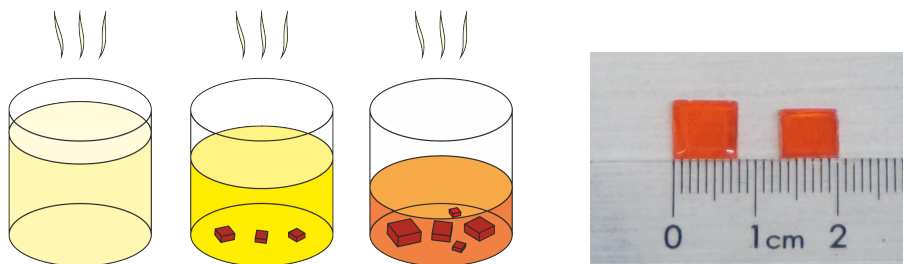


Figure 3.6: Schematic drawing of the procedure to synthesize single crystals (on the left hand side). Continuous solvent evaporation facilitates precipitation and the growth of single crystals inside the over-saturated solution. The picture on the right hand side illustrates the dimensions of the synthesized bromine-containing crystals.

ovskite thin-films showing the longest minority-charge carrier lifetimes are achieved at a low relative humidity of approximately 35 %. The resulting layer thicknesses depend on the chosen fabrication route and are in the range of 300 to 360 nm.

3.4.2 Perovskite single crystals

Single crystals of organic inorganic perovskites have been received from Dr. Irina Anusca from the Institute for Materials Science, University of Duisburg-Essen as well as from Shreetu Shrestha and Ievgen Levchuk from the Department of Materials Science and Engineering, Friedrich-Alexander-University Erlangen-Nuremberg. The synthesis routes are adopted from [90] and [91], respectively. In order to grow pure single crystals of methylammonium lead halides $\text{CH}_3\text{NH}_3\text{PbX}_3$ with $\text{X} = \text{I}, \text{Br}$, methylammonium halide $\text{CH}_3\text{NH}_3\text{X}$ is mixed with the corresponding lead halide PbX_2 at a molar ratio of 1:1 and solved in extra dry γ -butyrolactone (GBA) or dimethylformamide (DMF). During slow solvent evaporation overnight at temperatures of $T \approx 60^\circ\text{C}$, single crystals grow in the over-saturated solutions as depicted in Fig. 3.6. This method facilitates the synthesis of single crystals with dimensions of several millimeters as also apparent from Fig. 3.6. While $\text{CH}_3\text{NH}_3\text{PbBr}_3$ crystals exhibit a cuboid shape with a rather quadratic footprint and appear orange, $\text{CH}_3\text{NH}_3\text{PbI}_3$ crystals form as dodecahedrons (partially rhombo-hexagonal) in black color.

3.5 Morphology of perovskite thin films

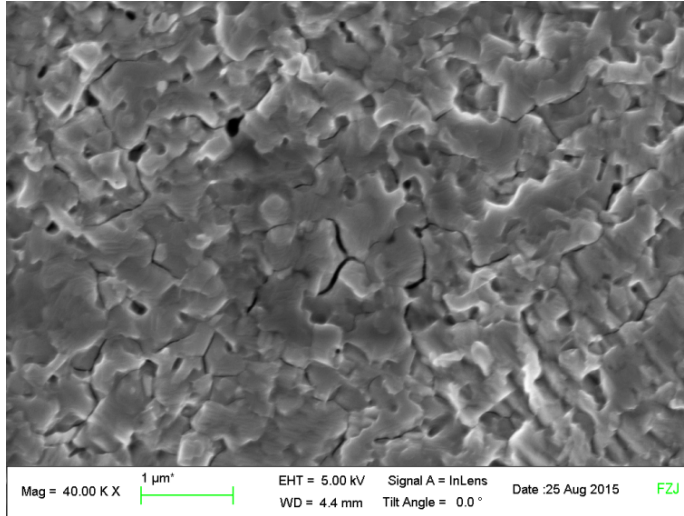


Figure 3.7: SEM image of an uniform polycrystalline methylammonium lead iodide thin film on a glass substrate.

3.5 Morphology of perovskite thin films

Thin films of organic inorganic perovskites are typically composed of polycrystalline structures as they become apparent by scanning electron microscopy (Fig. 3.7). Typical lateral grain dimensions vary between some hundreds of nanometers up to micrometers depending on the choice of substrate and fabrication conditions [92], which affects also the film coverage and the occurrence of pin holes. Besides, only a monolayer of perovskite crystallites can actually determine the film thickness.

In order to further investigate the thin-film crystallinity, X-ray diffraction spectroscopy was used. A resulting XRD spectrum of a methylammonium lead iodide perovskite thin film on glass substrate is depicted in Fig. 3.8 (a). Characteristic Bragg peaks are identified for the series of (002) and (110) reflexes, indicating a polycrystalline material exhibiting a high-ordered tetragonal structure. I fitted Voigt profiles in order to determine the peak positions θ (see red dotted lines in Fig. 3.8 (b) and (c); the red solid line represents the envelope). Bragg reflexes can only be observed for diffraction angles θ , which obey Bragg's law

3 Material properties of organic inorganic perovskites

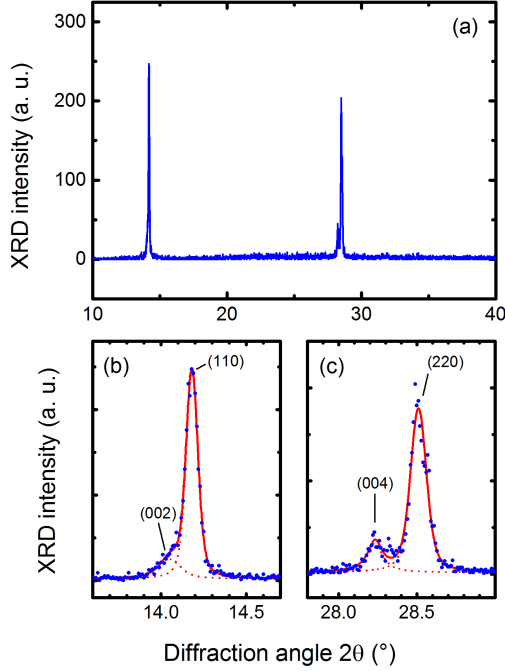


Figure 3.8: X-ray diffraction pattern (a) of a methylammonium lead iodide perovskite thin film on glass substrate. Enlarged sequences with relevant Bragg peaks and corresponding Voigt fits in red are shown in (b) and (c).

$$2d_{hkl} \sin\theta = n\lambda, \quad (3.3)$$

where d_{hkl} denotes the atomic plane distances with respect to the Miller indices hkl , λ is the wavelength of the incident X-ray beam, and n indicates the order of diffraction. From Eq. 3.3 I derive lattice dimensions of $a = (8.84 \pm 0.02) \text{ \AA}$ and $c = (12.61 \pm 0.03) \text{ \AA}$. These parameters are in good agreement with literature results ($a = 8.85 \text{ \AA}$ and $c = 12.44 \text{ \AA}$ at room temperature [93]) from powder X-ray diffraction experiments.

3.6 Optical properties

Light absorption by any semiconductor material is directly related to its respective electronic structure. An ideal photovoltaic absorber would both exhibit a sharp optical absorption onset and full absorption of photons with energies above band gap: $A(E) = 1$ for $E \geq E_g$. While a sharp absorption onset is required to maintain a high open-circuit voltage in a solar cell [8], strong light absorption enables harvesting all available photons above band gap and, thus, maximizing the photocurrent.

3.6.1 Absorption coefficient

In order to understand the optical behavior of perovskite thin films, the absorption coefficient as a measure of the absorption profile is investigated. Figure 3.9 illustrates the absorption coefficient α of methylammonium lead iodide in comparison to established photovoltaic materials exhibiting a direct band gap (CdTe [94], GaAs [94], CIGS [95]) or an indirect one (c-Si [96]). For a solution-processed polycrystalline material, perovskite shows a remarkably steep absorption onset arising over more than five orders of magnitude. The sharp absorption shoulder appears in the immediate vicinity of its reported optical band gap of 1.6 eV [8] and rapidly reaches higher absorption coefficient values than e. g. GaAs. Hence, already some 100 nm thin films of perovskites facilitate adequate light absorption unlike the indirect semiconductor c-Si. As apparent from Fig. 3.9, perovskite features two plateaus in the absorption coefficient, which start to form at about 1.69 eV and 2.51 eV, respectively. A similar feature is not seen for other materials.

The absorption coefficient of perovskite in Fig. 3.9 is derived by stitching together the values obtained by various characterization methods. In the range of strong light absorption $E \gtrsim 2.0$ eV, I used the absorption coefficient values derived by modeling absorbance and transmittance data with the optical spectrum simulator SCOUT [97]. Due to a higher sensitivity in the range of the absorption onset, I applied the absorption coefficient values obtained by photothermal deflection spectroscopy and, additionally, the conversion of an photoluminescence spectrum. In the following section, I elucidate the detailed balance approach of deriving an absorption profile with a high dynamic range from the spectral shape of an emission

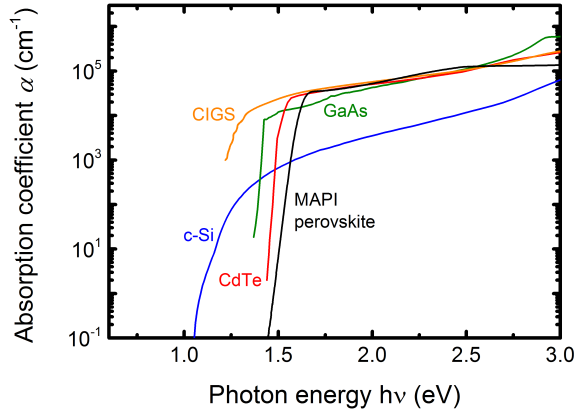


Figure 3.9: Overview of absorption coefficients α for various photovoltaic materials from literature: crystalline silicon (c-Si) [96], cadmium telluride (CdTe) [94], gallium arsenide (GaAs) [94] and copper indium gallium selenide (CIGS) [95]. The values for methylammonium lead iodide (MAPI) perovskite were obtained in the course of this thesis.

spectrum recorded in a quasi equilibrium.

3.6.2 Detailed balance of emission and absorption

Organic inorganic perovskites commonly feature a intense and narrow emission peak, which is slightly homogeneously broadened with a line width of approx. 100 meV probably due to phonon coupling effects [98]. Emission of perovskites is found to be right at the band edge with only little Stokes shift [99, 100]. A photoluminescence spectrum of a perovskite thin film recorded during continuous wave excitation is depicted in Fig. 3.10 (black open circles). The spectral photoluminescence flux $\phi_{\text{PL}}(E)$, which is spontaneously emitted from the sample under non-equilibrium conditions, is linked to the absorptance $A(E)$ according to the generalized Planck's emission law introduced by Würfel [101]:

$$\phi_{\text{PL}}(E) \propto \frac{A(E)E^2}{\exp[(E - \Delta\mu)/(k_{\text{B}}T)] - 1}, \quad (3.4)$$

where $\Delta\mu$ denotes the quasi-Fermi level splitting upon illumination, k_{B} is the Boltz-

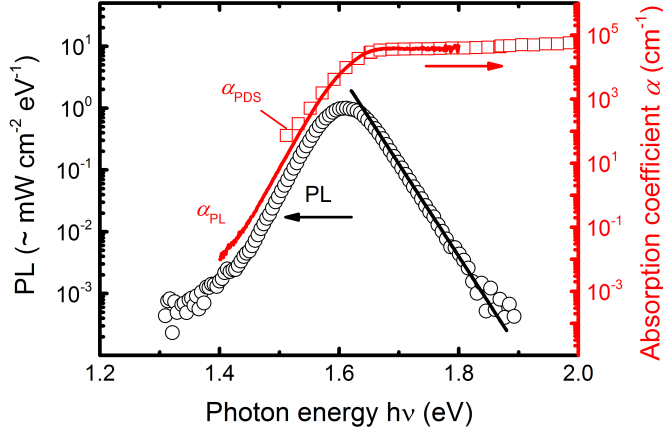


Figure 3.10: Photoluminescence (PL) spectrum of a methylammonium lead iodide perovskite thin film on a glass substrate (black open circles, left y axis). The red solid line represents the corresponding absorption coefficient α_{PL} (right y axis), which is linked to the photoluminescence by detailed balance arguments. Besides, the absorption coefficient α_{PDS} obtained by photothermal deflection spectroscopy is depicted (red open squares) to illustrate the dynamic ranges of the different approaches. Reproduced with permission from [102]. Copyrighted by the American Physical Society.

mann constant and T is the temperature. The Bose-Einstein term can be approximated by a Boltzmann distribution but only for photon energies $E \gg k_{\text{B}}T + \Delta\mu$. In the following, I will now estimate the quasi-Fermi level splitting $\Delta\mu$ in order to find the lower limit of photon energies, which still satisfies the Boltzmann approximation. In Sec. 4.8 I derive an implied open-circuit voltage of $V_{\text{oc}} = 1.28\text{V}$ upon one sun illumination, which is equivalent to $\Delta\mu/q$ with q being the elementary charge. However the excitation intensity applied during the photoluminescence measurement rather corresponds to an intensity of approx. ten suns, I further add $k_{\text{B}}T \times \ln(10) \approx 0.06\text{eV}$ to the one sun equivalent of qV_{oc} . As a consequence, a lower limit of about $E \geq 1.40\text{eV}$ fulfills the requirement according to $E - \Delta\mu \gtrsim 60\text{meV} \gg k_{\text{B}}T$.

When I apply the Boltzmann approximation, the generalized Planck's emission law simplifies to

3 Material properties of organic inorganic perovskites

$$\phi_{\text{PL}}(E) \propto A(E)E^2 \exp[-E/(k_{\text{B}}T)] \exp[\Delta\mu/(k_{\text{B}}T)]. \quad (3.5)$$

Now, $\Delta\mu$ does not affect the spectral shape of the emission spectrum anymore. The constant exponential term containing $\Delta\mu$ only determines the absolute alignment of the spectral photon flux. Based on Eq. 3.5, the sample temperature can be determined from the falling photoluminescence edge towards high photon energies. As the absorptance A approximately stays constant in the higher energetic photon range due to the mentioned plateau in the absorption coefficient, the high energy part of the emission reflects mainly the occupation statistics given by the Boltzmann term. Here, I determine a sample temperature of $T \approx 321$ K under continuous illumination by fitting $E^2 \exp[-E/(k_{\text{B}}T)]$ to the high energetic edge (black line in Fig. 3.10).

Only the relative shape of $A(E)$ can be extracted by the detailed balance approach of Eq. 3.5 from the measured emission flux, which is typically not available in absolute values. However, the derived absorptance from the photoluminescence measurement can easily be adjusted in the high energetic range to the absolute absorptance values obtained by other spectroscopy measurements. In order to calculate the absorption coefficient from the absorptance of the thin film, I apply the relation [103]

$$A(E) = \frac{(1 - R_{\text{f}}(E))(1 - \exp[-\alpha(E)d])(1 + R_{\text{r}}(E)\exp[-\alpha(E)d])}{1 - R_{\text{f}}(E)R_{\text{r}}(E)\exp[-2\alpha(E)d]}, \quad (3.6)$$

which takes a Lambert-Beer absorption profile with multiple reflections between front and rear layer surfaces with the respective measured reflection coefficients $R_{\text{f}}(E)$ and $R_{\text{r}}(E)$ into account but disregards interference effects. Here, the perovskite layer thickness was determined as $d = (311 \pm 10)$ nm. Reorganizing Eq. 3.6 reveals $\alpha_{\text{PL}}(E)$, which is depicted in Fig. 3.10 as red solid line. With this detailed balance approach, precise and ultralow absorption coefficients over several orders of magnitude can be gained [104], which significantly prolong the dynamic range of absorption coefficients obtained by photothermal deflection spectroscopy (red open squares in Fig. 3.10). Accurate data of the absorption coefficient especially below

the band gap energy allows for deriving fundamental semiconductor properties as elucidated later on in Sec. 4.7.

3.6.3 Band gap characteristics

In this section, the band gap of organic inorganic perovskites is investigated in terms of its special character which facilitates direct as well as indirect transitions. While for a direct band gap, the absorption coefficient α shows a square-root dependence on the difference between photon energy $h\nu$ and direct band gap energy $E_{g,\text{dir}}$ [105]:

$$\alpha_{\text{dir}} h\nu \propto \sqrt{h\nu - E_{g,\text{dir}}}, \quad (3.7)$$

for an indirect band gap, the dependence becomes rather quadratic and also phonons with energy E_{phon} are involved in an indirect transition [105]:

$$\alpha_{\text{ind}} h\nu \propto (h\nu - E_{g,\text{ind}} - E_{\text{phon}})^2. \quad (3.8)$$

The energy of longitudinal optical phonons in methylammonium lead iodide perovskites is estimated to be $E_{\text{phon}} \approx 15 \text{ meV}$ [106, 107], which is even below the available thermal energy at room temperature.

Figure 3.11 illustrates the spectral product of absorption coefficient α and photon energy $h\nu$. By fitting the different dependencies of $h\nu$ based on Eq. 3.7 and 3.8 to the experimental data (black open circles), I highlight the distinct direct and indirect band gap character of organic inorganic perovskites. In accordance to literature reports [108, 109], the absorption edge seems to be mostly dominated by an indirect contribution (red dashed line) with a band gap of $E_{g,\text{ind}} \approx 1.56 \text{ eV}$. However, this finding implies that the radiative recombination in perovskites mainly evolves from indirect transitions [109]. On the one side, an indirect band gap just slightly below a direct one helps to achieve longer radiative lifetimes, which will improve charge collection. On the other side, a lower positioned indirect band gap does not allow for an increase in open-circuit voltage [109]. The direct transition shows its impact at photon energies higher than $E_{g,\text{dir}} \approx 1.65 \text{ eV}$ (red solid line), while the contribution of the indirect band gap is held constant at the same time.

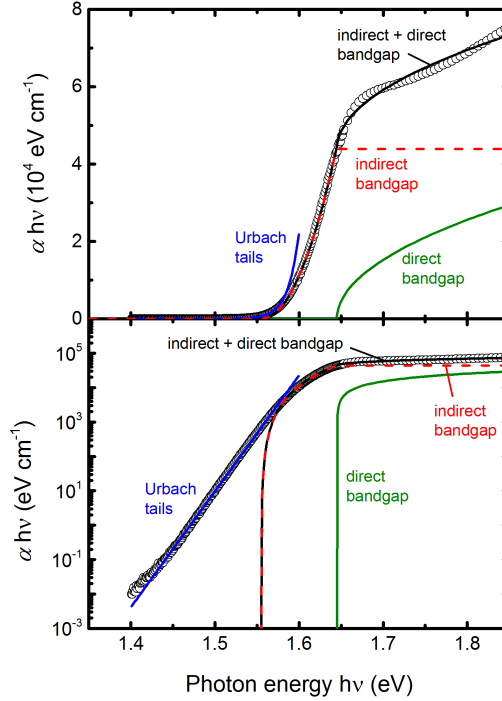


Figure 3.11: Product of absorption coefficient α and photon energy $h\nu$ (black open circles) as a function of $h\nu$ on a linear (top) and semi-logarithmic scale (bottom). Several fits illustrate the character of the band gap for perovskites: direct gap (green line) and indirect gap (dashed red line). The sum of indirect and direct band gap contribution is depicted as black line. Additionally, Urbach tails are indicated by the blue line.

It is apparent from Fig. 3.11, that the absorption coefficient is always dominated by the indirect contribution. Furthermore, a steep exponential absorption onset is found. Such a rapid onset identifies a quite low density of absorption tail states, which are considered to evolve from structural disorder [110–112]. An Urbach energy E_0 can be attributed to the so called Urbach tail according to the relation [110]

$$\alpha \propto \exp\left(\frac{E}{E_0}\right). \quad (3.9)$$

Here, I derive a low Urbach energy of $E_0 \approx 14$ meV, which indicates only small

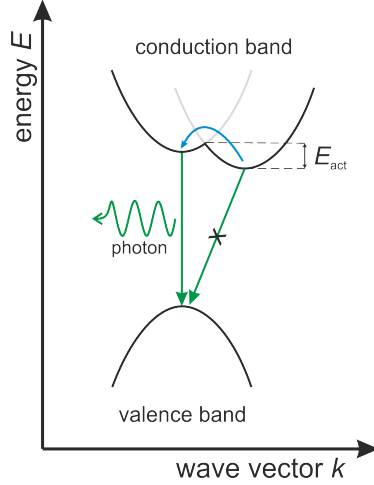


Figure 3.12: Band diagram of organic inorganic perovskite proposed by Hutter *et al.* [114]. An indirect band gap is located slightly below a direct band gap. The indirect transition from the conduction band minimum into the valence band maximum requires besides a momentum change by the participation of a phonon also a spin-flip of the electron. Thus, this spin-forbidden, typically non-radiative process runs much slower [115] than the direct radiative transition from the local conduction band minimum. In order to enable direct transitions, electrons in the conduction band minimum have to overcome an energy barrier first with an activation energy E_{act} of about 25 – 75 meV [114, 116, 117].

disorder-related broadening [8, 113]. The obtained Urbach energy of perovskite is in good agreement with reported values of $E_0 = 15 \text{ meV}$ [8], even smaller than CIGS ($\sim 25 \text{ meV}$), comparable to c-Si ($\sim 11 \text{ meV}$) and only slightly higher than GaAs ($\sim 8 \text{ meV}$).

The origin of the different band gap characteristics of organic inorganic perovskites lies in the so called Rashba band splitting: strong spin-orbit coupling associated with heavy elements like lead and iodine and the structural inversion asymmetry in orthorhombic and tetragonal phases give rise to the Rashba effect, which lifts the spin degeneracies in the valence and conduction bands near the band gap [118, 119]. As a consequence, "inner" and "outer" bands with opposite spin textures are formed. As the valence and conduction bands are mainly contributed by halides and lead, respectively, the bands undergo different Rashba splitting [120]. Hence, it is not

surprising that conduction band minimum and valence band maximum are located at different points in k -space. The formed indirect band gap for recombination lies shortly below the direct one as schematically depicted in Fig. 3.12. This finding directly affects recombination in organic inorganic perovskites [114,120]. Once charge carriers are photo-generated in the conduction band, they will rapidly thermalize towards the band extrema as phonon-induced relaxation rates are many orders of magnitude faster than the electron-hole recombination rate [118,121,122]. For large Rashba splitting and at low temperatures, the majority of free charge carriers will be situated at the band extrema. Due to the spin and momentum mismatch, the recombination rate between the respective band extrema is quite slow resulting in effective screening of charge carriers. Consequently, charge-carrier lifetimes are prolonged [118,123]. Faster direct transitions are only enabled after thermal activation of charge carriers ($\approx 25 - 75$ meV [114,116,117]) and momentum transfer by the participation of phonons [114,123]. In summary, organic inorganic perovskites combine the advantageous features of a direct and an indirect semiconductor, namely strong photon absorption of the former and long lifetimes of the later [118].

3.7 Electrical properties

3.7.1 Doping concentration

Doping of semiconductors affects charge-carrier transport due to its potential impact on minority-charge carrier lifetime, conductivity, and mobility through charge-carrier scattering at impurities. Therefore, doping becomes an important parameter for the analysis of transient photoluminescence decays [102]. Basically, the chosen perovskite processing route may show a tremendous impact on the attained self-doping of thin films [82,124]. By changing the stoichiometric ratio of the precursor materials (MAI:PbI₂) significantly, doping concentrations ranging between $\sim 10^{14}$ cm⁻³ and $\sim 10^{19}$ cm⁻³ have been reported [125]. In accordance with the calculated defect levels shown in Fig. 3.3, MA⁺- and I⁻-rich/Pb²⁺-poor compositions result into p -type doping (most likely by Pb²⁺ vacancies and/or I⁻ interstitials), while MA⁺- and I⁻-poor/Pb²⁺-rich films are rather n -type (most likely by I⁻ va-

cancies and/or Pb^{2+} interstitials) [82, 124, 125]. Additionally, the annealing conditions and temperature affect the doping because some components like MAI become volatile at elevated temperatures [125]. For these reasons, thermoelectric power measurement were conducted to derive the doping concentration in perovskite thin films, which helps to interpret time-resolved photoluminescence data [102]. Heating with an applied temperature gradient of 30 K results in an actual temperature gradient of approximately 10 K across the coplanar contact distance of 4 mm. A positive Seebeck coefficient (thermoelectric power) of $S = 1042 \mu\text{V}/\text{K}$ is determined in nitrogen atmosphere for an average sample temperature of 335 K. The positive sign of S identifies holes to be the dominant carriers for charge transport in perovskite thin films. While assuming charge carriers to scatter dominantly at ionized defects, the Seebeck coefficient for a non-degenerated semiconductor is derived as [126, 127]

$$S(T) = -\frac{k_{\text{B}}}{q} \left(\frac{4F_3(\mu^*(T))}{3F_2(\mu^*(T))} - \mu^*(T) \right), \quad (3.10)$$

where k_{B} is the Boltzmann constant, q denotes the elementary charge, $\mu^*(T)$ is the reduced Fermi energy at temperature T and the Fermi-Dirac integral $F_j(x)$ is given as

$$F_j(x) = \frac{1}{\Gamma(j+1)} \int_0^\infty \frac{u^j \text{d}u}{1 + e^{u-x}} \quad (3.11)$$

with Γ being the gamma function. After solving Eq. 3.10 for $\mu^*(T)$, a hole concentration $p(T)$ is derived by

$$p(T) = N_{\text{v}}(T) F_{1/2}(\mu^*(T)). \quad (3.12)$$

Here, the density of states in the valence band N_{v} is assumed to be $N_{\text{v}} \approx 1.5 \times 10^{15} \text{T}^{3/2} \text{cm}^{-3} \text{K}^{-3/2}$ based on the values derived in the following Sec. 4.7. From Eq. 3.12 a moderate doping concentration of $p \approx 3 \times 10^{15} \text{cm}^{-3}$ is found. Previous findings from other techniques, like Hall measurements [125] and electron-beam-induced current profiles [128], are in good agreement with the value presented here and highlight the almost intrinsic nature of stoichiometrically grown organic inorganic perovskites. The value of the doping concentration is needed for the

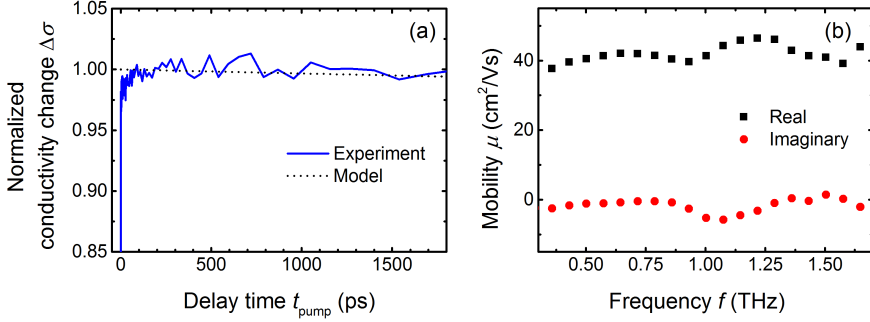


Figure 3.13: Optical pump terahertz probe spectroscopy measurements of a $\text{CH}_3\text{NH}_3\text{PbI}_3$ perovskite film [102]. (a) Measured normalized conductivity change $\Delta\sigma$ of the sample over delay time t_{pump} (blue line). The black dotted line represents the modeled conductivity change. (b) Real (black squares) and imaginary parts (red circles) of the derived complex mobility μ for different probe frequencies f at 1 ns after photoexcitation. The real part accounts for the sum of electron and hole mobility. Reproduced with permission from [102]. Copyrighted by the American Physical Society, 2016.

analysis of transient photoluminescence curves in Chap. 4 in order to distinguish between high and low level injection conditions.

3.7.2 Charge-carrier mobility

Optical pump terahertz probe spectroscopy provides intra-grain charge-carrier mobilities, which help to interpret transient photoluminescence data. Figure 3.13 (a) indicates that the measured pump-induced conductivity (blue line) stays constant within the first two nanoseconds after photo-excitation. This finding is in contrast to optical pump terahertz probe transients of many other established thin-film photovoltaic materials like Cu_2SnS_3 [129], $\text{Cu}_2\text{ZnSn}(\text{S},\text{Se})_4$ [130], and microcrystalline silicon [131]. Typically, a fast decay on the pico- to nanosecond timescale is observed, which is caused by charge-carrier recombination. Here, no conductivity decay can be resolved within the timeframe of the optical pump terahertz probe measurement (2ns), hinting at constant charge-carrier concentrations due to low recombination rates. Figure 3.13 (b) shows the derived complex mobility, which accounts for the

sum of electron and hole contributions, measured by optical pump terahertz probe spectroscopy at a delay time of 1 ns. As the real part of the mobility stays constant ($\sim 40 \text{ cm}^2 \text{ V}^{-1} \text{ s}^{-1}$) over the entire frequency range, it can be extrapolated to the same DC value. The observed dip in the imaginary mobility at about 1 THz was previously assigned to the coupling of THz radiation to a phonon mode [132]. I assume equal electron and hole mobilities of $\sim 20 \text{ cm}^2 \text{ V}^{-1} \text{ s}^{-1}$ on the base of similar predicted effective masses for electrons and holes [70] and assuming similar scattering times. The charge-carrier mobility values derived from optical pump terahertz probe measurements are similar to previously reported values [125, 133] (see also Tab. 3.1 for comparison). Most organic semiconductors, which can also be fabricated by solution-based processes, typically exhibit significantly lower mobilities of $10^{-2} \text{ cm}^2 \text{ V}^{-1} \text{ s}^{-1}$ and below [134, 135]. In the context of being solution-processed materials, mobilities on the order of $\mu \approx 10 \text{ cm}^2 \text{ V}^{-1} \text{ s}^{-1}$ in organic inorganic perovskite films appear to be high due to the absence of scattering centers as a consequence of the defect tolerance discussed in Sec. 3.3. As its inorganic lead halide framework is mostly responsible for the semiconducting properties, one should rather compare perovskites with conventional inorganic photovoltaic materials on the other hand. In this perspective, mobilities in perovskites come out to be rather modest (see Tab. 3.1). Electron-phonon scattering is posited to be limiting the charge-carrier mobility in "soft" organic inorganic perovskites [136].

4 Time-resolved photoluminescence from perovskite thin films

In this chapter, I investigate various recombination mechanisms that shape photoluminescence transients of perovskite thin films. By developing a model that also includes doping and photon recycling in the films, I gain precise recombination parameters from analyzing transients. Based on the derived long charge-carrier lifetimes, which are not only an indicator of a high quality absorber material but, as I show, also imply excellent passivation of surface defects, I am able to provide an estimation of the attainable open-circuit voltage without the need of fabricating an entire solar cell. This physical property helps to predict the photovoltaic potential of any semiconducting material.

4.1 Charge-carrier recombination processes

Charge carriers in organic lead halide perovskites undergo various recombination processes. In order to reveal those mechanisms, I applied time-resolved photoluminescence measurements on thin-films deposited on glass. Figure 4.1 (a) shows the spectral luminescence decay for an excitation fluence of $11 \mu\text{J}/\text{cm}^2$ as a contour plot. Here, the time axis t is adjusted in a way that the maximum photoluminescence signal is detected at $t = 0$. The depiction of Fig. 4.1 (a) is chosen that every data point of each spectrum is normalized to the one value showing the highest absolute intensity. There is still photoluminescence detectable at delay times of $t > 1\mu\text{s}$, which provides the first hint of remarkably long lifetimes and low defect densities in solution-processed organic inorganic perovskites. In Fig. 4.1 (b), each spectrum is normalized to the respective values of the one luminescence spectrum with the

4 Time-resolved photoluminescence from perovskite thin films

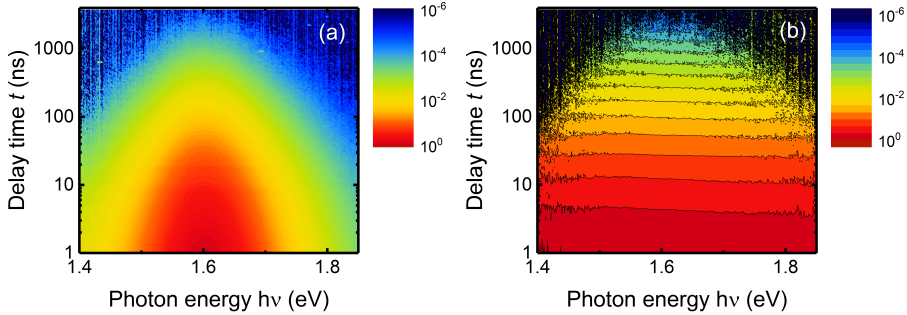


Figure 4.1: Different normalizations applied to the spectral photoluminescence decay of a perovskite thin film recorded for an excitation fluence of $11 \mu\text{J}/\text{cm}^2$. Every data point in (a) is standardized to the one value showing the maximum absolute photoluminescence intensity. The data in (b) is spectrally normalized to the respective values of the one photoluminescence spectrum with the highest overall intensity.

highest overall intensity (at $t = 0$). This depiction facilitates the observation of any spectral changes during the measurements. However, the appearance of the straight horizontal lines seen in the contour plot indicates that the shape of the spectra does not significantly change and only their intensity drops over time. Thus, the processes that charge carriers undergo during the time-resolved measurements do not alter the spectral profiles and spectrally independent recombination rates can be expected. For analyzing the transient data, it is therefore more convenient to integrate all measured spectra over photon energy and plot the gained photoluminescence intensity signals as a function of delay time t . Normalized photoluminescence transients of the perovskite thin film are shown in Fig. 4.2 for different excitation fluences ranging over more than two orders of magnitude ($\phi_{\text{exc}} = 85 \text{ nJ}/\text{cm}^2 - 11 \mu\text{J}/\text{cm}^2$). The higher the excitation intensity is chosen, the faster the photoluminescence signal decays initially. Eventually, each transient ends up turning into a single-exponential decay at longer times. The distinct decay dynamics are investigated in detail later on (see Sec. 4.2).

Upon photo-excitation, the only species generated in $\text{CH}_3\text{NH}_3\text{PbI}_3$ perovskites will be free charge carriers with concentration Δn , because the determined values for exciton binding energies of only $\sim 2 - 16 \text{ meV}$ [71, 137–139] are smaller than the

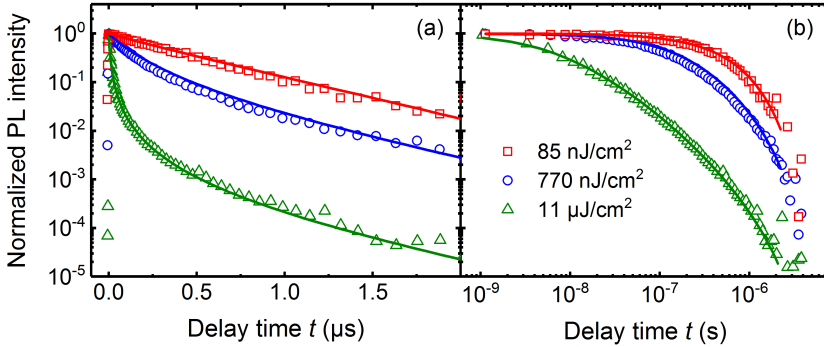


Figure 4.2: Normalized photoluminescence decays from measurements (open symbols) of a $\text{CH}_3\text{NH}_3\text{PbI}_3$ perovskite film for different excitation fluences (85 nJ/cm^2 , 770 nJ/cm^2 , $11 \mu\text{J/cm}^2$). The data in (a) is plotted on a semi-logarithmic scale, while a double-logarithmic depiction is chosen in (b). Solid lines represent global fits including radiative and trap-assisted recombination and Auger recombination. Adapted with permission from [102]. Copyrighted by the American Physical Society, 2016.

available thermal energy at room temperature. The respective excess-charge carrier densities $\Delta n(0)$ in the absorber layer are derived from the corresponding excitation fluences ϕ_{exc} according to

$$\Delta n(0) = \frac{(1 - R)A\phi_{\text{exc}}}{h\nu d}. \quad (4.1)$$

Here, R and A are the sample's reflectance and absorptance, respectively. The photon energy of the monochromatic excitation source is denoted as $h\nu$ and d represents the layer thickness. Equation 4.1 assumes that the excitation pulse is infinitesimally short (Dirac delta function) and no recombination takes place in the sample during the illumination process. Furthermore, excess-charge carriers are considered to exhibit a homogeneous distribution across the layer thickness. An immediate flat charge-carrier profile is an appropriate assumption for perovskite thin films, as discussed in Sec. 4.5 later on. Besides, absorbed photons are believed to be transformed into excess-charge carriers with a quantum efficiency of 1.

At first, I consider charge-carrier recombination only in the bulk and leave out

4 Time-resolved photoluminescence from perovskite thin films

the effect of surface recombination, which is discussed separately in Sec. 4.6. The excess-charge carrier density $\Delta n(t)$ at any delay time t after the excitation pulse is described by the continuity equation [102]

$$\frac{\partial \Delta n}{\partial t} = -R + G^{\text{int}} = -k^{\text{ext}}(np - n_i^2) - \frac{np - n_i^2}{\tau_p n + \tau_n p} - C_n n (np - n_i^2) - C_p p (np - n_i^2). \quad (4.2)$$

Here, R denotes the sum of all recombination rates, G^{int} is the internal generation rate due to reabsorption of radiation in the absorber layer (see also Sec. 4.3), k^{ext} is the externally obtained bimolecular recombination coefficient, τ_n and τ_p are the Shockley-Read-Hall lifetimes for electrons and holes, C_n and C_p are the Auger coefficients for electrons and holes. The electron n and hole concentrations p in Eq. 4.2 are defined as $n = n_0 + \Delta n$ and $p = p_0 + \Delta n$, respectively, with the corresponding equilibrium concentrations n_0 and p_0 . The intrinsic charge-carrier concentration is denoted with index i and is neglected in the following analysis because the non-equilibrium established throughout the course of the transient measurement leads to $n, p \gg n_i$. The bimolecular recombination coefficient k^{ext} in the first recombination term on the right hand side of Eq. 4.2 stems from radiative band-to-band recombination of free electrons and free holes with the externally observed radiative recombination coefficient $k_{\text{rad}}^{\text{ext}}$ (see also Sec. 4.3) and a non-radiative component with coefficient k_{nrad} . The existence of such a non-radiative quadratic decay channel is demonstrated in Chap. 6 but revealing its origin still remains a task for future investigation.

In order to obtain the temporal excess-charge carrier concentration $\Delta n(t)$, which is needed to simulate the photoluminescence transients, the explicit continuity equation from Eq. 4.2 can only be solved numerically. The resulting photoluminescence signal $I_{\text{PL}}(t)$ originates from radiative recombination and is obtained as

$$I_{\text{PL}}(t) = k_{\text{rad}}^{\text{ext}} ([n_0 + \Delta n(t)][p_0 + \Delta n(t)] - n_i^2). \quad (4.3)$$

As the decrease of Δn involves the sum of radiative recombination and non-radiative recombination of varying kinds, time-resolved photoluminescence itself con-

4.1 Charge-carrier recombination processes

tains the information on the total recombination processes.

When I simulate time-resolved photoluminescence decays numerically according to Eq. 4.2 and 4.3, the assumed doping concentrations show a tremendous impact on the attained recombination parameters, which is discussed in more detail in Sec. 4.2. In the present case, good fits are achieved for doping concentrations $\lesssim 4 \times 10^{16} \text{ cm}^{-3}$, whereas the values of the recombination parameter alter significantly. Thus, unambiguous fitting results are achieved only when the doping density of the sample is measured separately. In Sec. 3.7.1, moderate p -type doping of $p_0 \approx 3 \times 10^{15} \text{ cm}^{-3}$ was determined. Keeping the doping concentration in the simulations fixed to that value and neglecting n_0 and n_i , I fit the normalized time-resolved photoluminescence decays in Fig. 4.2 (a) and (b) globally according to Eq. 4.2 and 4.3 by the method of least squares. The resulting recombination parameters are listed in Table 4.1 and are in agreement with previously reported values [133, 140, 141]. For the sample investigated here, the higher order Auger recombination influences the time-resolved photoluminescence curves only for high level injection conditions, when $\Delta n \gg p_0, n_0$ holds. Therefore, I can provide only the sum of the individual Auger coefficients $C = C_n + C_p$ instead of values for each carrier type. The majority-charge carrier lifetime τ_p has a much higher uncertainty than the minority-charge carrier lifetime, because τ_p affects the photoluminescence transients only slightly during a short time interval (see also Fig. 4.4).

Based on this set of the derived recombination parameters, I can also model the measured normalized conductivity transient $\Delta\sigma(t)$ in Fig. 3.13 based on the equation

$$\Delta\sigma(t) = q[\mu_n n(t) + \mu_p p(t)]. \quad (4.4)$$

Here, q is the elementary charge and $n(t)$ and $p(t)$ are the temporary electron and hole concentration, respectively. The electron μ_n and hole mobility μ_p are determined to be $\sim 20 \text{ cm}^2 \text{ V}^{-1} \text{ s}^{-1}$ each (see Sec. 3.7.2). The simulated normalized conductivity change $\Delta\sigma(t)$ is indicated in Fig. 3.13 as blue line and predicts the measured optical pump terahertz probe trace.

Table 4.1: Bulk-recombination parameters obtained from modeling time-resolved photoluminescence decays for a fixed p -type doping concentration of $p_0 = 3 \times 10^{15} \text{ cm}^{-3}$: The external bimolecular recombination coefficient $k^{\text{ext}} = k_{\text{rad}}^{\text{ext}} + k_{\text{nrad}}$, the minority- and majority-charge carrier lifetimes τ_n and τ_p from Shockley-Read-Hall recombination, as well as the Auger recombination coefficient $C = C_n + C_p$. The commonly stated lifetime τ_{mono} , which is obtained in the monoexponential time-resolved photoluminescence regime at long times, is in excellent agreement with the minority-charge carrier lifetime τ_n .

k^{ext} (cm^3s^{-1})	$(4.78 \pm 0.43) \times 10^{-11}$
τ_n (ns)	511 ± 80
τ_p (ns)	871 ± 251
C (cm^6s^{-1})	$(8.83 \pm 1.57) \times 10^{-29}$
τ_{mono} (ns)	508 ± 29

4.2 Photoluminescence transients in the context of doping

The different decay dynamics observed during a transient photoluminescence measurement (see Fig. 4.2) are dominated by the currently prevalent recombination processes, which can change in the course of the measurement and/or are experienced for different excitation fluences. In order to understand the different transient curves, I accept some simplifications for Eq. 4.2, which allow me to derive an analytical solution for the excess-charge carrier density $\Delta n(t)$. Namely, in the case that the higher order Auger processes become insignificant because lower order (linear and quadratic) effects represent the predominant recombination mechanisms (i. e. at excitation fluences up to approx. $\sim 5 \mu\text{J}/\text{cm}^2$), I find for a p -type doped semiconductor

$$\Delta n(t) = \left[(\tau_{\text{mono}} k^{\text{ext}} + \Delta n^{-1}(0)) e^{\frac{t}{\tau_{\text{mono}}}} - \tau_{\text{mono}} k^{\text{ext}} \right]^{-1} \quad (4.5)$$

to be a possible solution. Here, I define a monomolecular lifetime τ_{mono}

$$\tau_{\text{mono}} = (k^{\text{ext}} p_0 + 1/\tau_{\text{SRH}})^{-1}, \quad (4.6)$$

4.2 Photoluminescence transients in the context of doping

which is either limited by a monomolecular contribution deduced from bimolecular recombination as a consequence of doping with concentration p_0 or the effective lifetime τ_{SRH} of the trap-assisted Shockley-Read-Hall mechanism. First, I consider the photoluminescence transients at high excitation fluences and for times $t \ll \tau_{\text{mono}}$. For short times, I can apply the Taylor expansion to the exponential term $\exp(t/\tau_{\text{mono}}) \approx 1 + t/\tau_{\text{mono}} + \dots$, which I cut here after the first order. Inserting this approximation into Eq. 4.5 yields the expression

$$\Delta n(t) \approx \frac{\Delta n(0)}{k^{\text{ext}} \Delta n(0)t + 1}, \quad (4.7)$$

when relatively high excitation fluences are applied, i. e. leading to $\Delta n(0) \gg (k^{\text{ext}} \tau_{\text{mono}})^{-1}$. The photoluminescence transient is derived as

$$I_{\text{PL}}(t) = k^{\text{ext}} \Delta n(t)^2 \propto (k^{\text{ext}} \Delta n(0)t + 1)^{-2} \quad (4.8)$$

according to Eq. 4.3 when $\Delta n(t)$ is significantly larger than p_0 . This excitation condition is known as high level injection (HLI). Consequently, for the applied restrictions (short times and high excitation fluences) the time-resolved photoluminescence curves ideally follow a powerlaw decay since Eq. 4.7 and 4.8 become completely independent of the influence of monomolecular recombination. Such fast decays are experimentally seen in Fig. 4.2.

On the contrary, for low excitation fluences leading to $\Delta n(0) \ll (k^{\text{ext}} \tau_{\text{mono}})^{-1}$ or for times $t \gg \tau_{\text{mono}}$, respectively, the excess-charge carrier density becomes

$$\Delta n(t) \propto e^{-\frac{t}{\tau_{\text{mono}}}}. \quad (4.9)$$

As a consequence, the photoluminescence signal during low level injection (LLI) conditions follows in this case a mono-exponential decay

$$I_{\text{PL}}(t) = k^{\text{ext}} p_0 \Delta n(t) \propto e^{-\frac{t}{\tau_{\text{mono}}}}, \quad (4.10)$$

when monomolecular processes provide the predominant recombination events. An exponential photoluminescence decay is also confirmed for experimental data in

4 Time-resolved photoluminescence from perovskite thin films

Fig. 4.2 for either low excitation fluences or after longer times. It becomes apparent that the exponential photoluminescence decay is either limited by doping or trap-assisted recombination according to Eq. 4.6 and the long-term lifetime τ_{mono} does not necessarily reflect solely Shockley-Read-Hall statistics, as it is in contrast unreservedly accepted in the literature so far. In any case, both the doping concentration p_0 and Shockley-Read-Hall related recombination parameters cannot be independently identified at the same time from modeling luminescence transients. Therefore, I advice to measure the doping concentration separately in order to derive precise monomolecular recombination parameters. Here, as the doping concentration ($p_0 \approx 3 \times 10^{15} \text{ cm}^{-3}$) in the present sample is rather low, the long-term decay is exclusively affected by trap-assisted recombination. Hence, the mono-exponential lifetime $\tau_{\text{mono}} = (508 \pm 29) \text{ ns}$ determined from a fit in the monoexponential time-resolved photoluminescence regime is identical to the minority-charge carrier lifetime $\tau_n = (511 \pm 80) \text{ ns}$ revealed based on the recombination model.

Moreover, I show in Fig. 4.3 what range of relative photoluminescence intensities and excess-charge carrier concentrations is covered by the experimental data. Here, I assign an actual excess-charge carrier density (lower x -axis) to the transient data (time scale depicted on upper x -axis, which relates to the highest excitation fluence only) by fitting the recombination model based on Eq. 4.2 and 4.3 to the experimental data. Photoluminescence transients recorded for different excitation fluences (open symbols) merge into each other and can simply be stitched together. This observation confirms that the time-resolved photoluminescence decays of perovskite thin films are well described by the presented model (black solid line) and are only affected by recombination. The transient data follows the trend of Eq. 4.3: the photoluminescence intensity scales with Δn^2 (see Eq. 4.8) for high level injection conditions (HLI, $\Delta n \gg p_0 \gg n_0, n_i$), whereas in the low level injection regime (LLI, $p_0 \gg \Delta n \gg n_0, n_i$), the photoluminescence signal is rather proportional to Δn (see Eq. 4.10). The dotted vertical line in Fig. 4.3 indicates the measured doping concentration ($p_0 \approx 3 \times 10^{15} \text{ cm}^{-3}$) and, thus, marks the center of the transition region between low and high level injection.

4.3 Photon recycling affecting radiative recombination

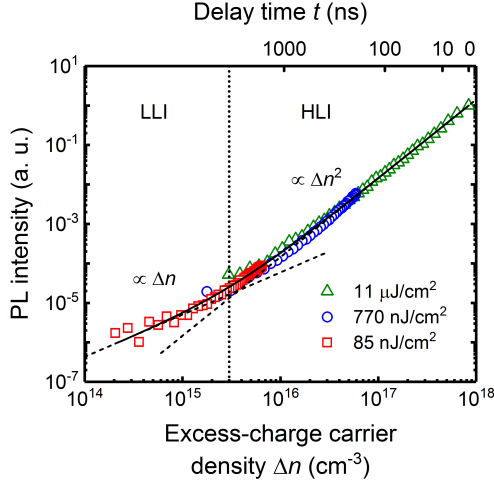


Figure 4.3: Normalized photoluminescence intensity as a function of the injected excess-charge carrier density Δn derived from solving the continuity equation. Open symbols represent experimental data for the indicated excitation fluences. The solid line shows the best fit from simulation. Furthermore, dashed lines illustrate regions where low level injection (LLI, $\Delta n \ll p_0$) and high level injection (HLI, $\Delta n \gg p_0$) conditions hold, respectively. Here, the dotted black line displays the measured doping concentration p_0 . Furthermore, the time axis relevant to the highest excitation fluence is indicated on top. Adapted with permission from [102]. Copyrighted by the American Physical Society, 2016.

4.3 Photon recycling affecting radiative recombination

Due to the large energetic overlap of luminescence emission with the absorption profile [100, 142, 143] (see also Fig. 3.10), photons spontaneously generated with the intrinsic radiative recombination rate $R = k_{\text{rad}}^{\text{int}} np$ are reabsorbed by the absorber layer itself with probability p_r . This process is commonly referred to as photon recycling and is of particular importance for absorber materials operating close to the radiative limit. As the perovskite layer is illuminating itself, photon recycling causes a quasi-immediate internal generation of electron-hole pairs with the rate

4 Time-resolved photoluminescence from perovskite thin films

G^{int} resulting in

$$-k_{\text{rad}}^{\text{int}}np + G^{\text{int}} = -(k_{\text{rad}}^{\text{int}} - p_r k_{\text{rad}}^{\text{int}})np = -k_{\text{rad}}^{\text{ext}}np. \quad (4.11)$$

As a consequence, I find that the apparent, externally observed, radiative recombination coefficient $k_{\text{rad}}^{\text{ext}}$ is reduced compared to the internal radiative recombination coefficient $k_{\text{rad}}^{\text{int}}$ by the average number of photon recycling events $1/(1-p_r)$ before the luminescence leaves the sample. Thus, the intrinsic parameter $k_{\text{rad}}^{\text{int}}$ is

$$k_{\text{rad}}^{\text{int}} = \frac{k_{\text{rad}}^{\text{ext}}}{(1-p_r)}. \quad (4.12)$$

The lifetime τ of any recombination process R is defined as $\tau = \Delta n/R$. Therefore, the reduced $k_{\text{rad}}^{\text{ext}}$ compared to $k_{\text{rad}}^{\text{int}}$ causes the apparent, external radiative lifetime to appear substantially longer than the internal radiative lifetime, which is a known phenomenon from GaAs based devices [144].

In order to quantify the amount of photon recycling, which is necessarily needed to derive the correct internal coefficient $k_{\text{rad}}^{\text{int}}$, I have to consider the fate of any photon generated inside the absorber layer, i. e. outcoupling and, thus, leaving the sample with probability p_e , parasitically absorption by any adjacent material (e. g. metal back reflector and transport layers in a solar cell stack) with probability p_a and reabsorption by the absorber layer itself with probability p_r , such that

$$p_e + p_a + p_r = 1. \quad (4.13)$$

While p_r is not easily calculated, the probability of outcoupling for a solar cell with active cell area S_{cell} can be calculated as the ratio of the outgoing photon flux J_0^{rad}/q to the integral internal radiative recombination $\int_0^d R_0^{\text{rad}} dx$ in the layer of thickness d [28]

$$p_e = \frac{J_0^{\text{rad}}/q}{\int_0^d R_0^{\text{rad}} dx} = \frac{\varepsilon_{\text{out}} \int_0^\infty A(E) \phi_{\text{bb}}(E) dE}{\int_0^\infty 4\pi S_{\text{cell}} dn_r^2(E) \alpha(E) \phi_{\text{bb}}(E) dE}, \quad (4.14)$$

with A being the absorptance and n_r being the refractive index of the perovskite

4.3 Photon recycling affecting radiative recombination

film (see Sec. 3.6.2 and Fig. 4.6 (a)) and α being the absorption coefficient (see Sec. 3.6.1). Furthermore, ϕ_{bb} denotes the spectral black body radiation defined as

$$\phi_{\text{bb}}(E) = \frac{2E^2}{h^3 c^2} \frac{1}{\exp[E/(k_{\text{B}}T)] - 1}, \quad (4.15)$$

where h is Planck's constant, c is the speed of light in vacuum, k_{B} is the Boltzmann constant and T is the temperature of the sample, which I set to $T = 300\text{K}$. The étendue ε_{out} of outgoing light stated in Eq. 4.14 measures the "spread out" of light rays propagating through a surface element dS_{cell} into a medium of refractive index $n_{\text{r,out}}$ and are confined to a solid angle $d\Omega = \sin\theta d\theta d\varphi$ according to

$$d\varepsilon_{\text{out}} = n_{\text{r,out}}^2 dS_{\text{cell}} \cos\theta d\Omega, \quad (4.16)$$

where θ is defined as the polar angle and φ denotes the azimuthal angle. As the investigated organic inorganic perovskite film of thickness $d = (311 \pm 10)\text{nm}$ is coated on a transparent glass substrate, photons can escape the sample from both sides to be released into air ($n_{\text{r,out}} = 1$) each as hemispherical flux, which is accounted for by assuming an outgoing étendue of $\varepsilon_{\text{out}} = 2\pi S_{\text{cell}}$. Consequently, I find an outcoupling probability of $p_{\text{e}} \approx 0.055$. Furthermore, I expect that parasitic absorption can be neglected for this type of sample and $1 - p_{\text{e}}$ matches the probability of reabsorption $p_{\text{r}} \approx 0.945$. On average, $1/(1 - p_{\text{r}}) \approx 18$ recycling events are required before a random photon generated in the absorber is able to escape the film.

From time-resolved photoluminescence measurements I can only obtain the total externally observed bimolecular recombination coefficient $k^{\text{ext}} = (4.78 \pm 0.43) \times 10^{-11} \text{cm}^3 \text{s}^{-1}$, which is the sum of a non-radiative part k_{nrad} and an external radiative component $k_{\text{rad}}^{\text{ext}}$. Now, I will anticipate findings, which are later discussed in detail in Chap. 6, where I derive an internal radiative fraction $\kappa \approx 0.66$ defined as

$$\kappa = \frac{k_{\text{rad}}^{\text{int}}}{k^{\text{int}}} = \frac{k_{\text{rad}}^{\text{int}}}{k_{\text{rad}}^{\text{int}} + k_{\text{nrad}}}. \quad (4.17)$$

Combined with Eq. 4.12, the overall external and internal bimolecular recombination coefficients are thus linked by the equation

Table 4.2: Diverse bimolecular recombination coefficients, i. e. the externally observed $k^{\text{ext}} = k_{\text{rad}}^{\text{ext}} + k_{\text{nrad}}$, which is typically obtained from modeling time-resolved photoluminescence decays and contains an non-radiative component k_{nrad} and an externally observed radiative part $k_{\text{rad}}^{\text{ext}}$. The latter bases on the internal radiative coefficient $k_{\text{rad}}^{\text{int}}$ after modification by photon recycling. Lastly, the internal bimolecular recombination coefficient is analogously defined as $k^{\text{int}} = k_{\text{rad}}^{\text{int}} + k_{\text{nrad}}$.

	k ($10^{-11} \text{ cm}^3 \text{ s}^{-1}$)
k^{ext}	4.78 ± 0.43
k^{int}	12.7 ± 1.1
k_{nrad}	4.32 ± 0.39
$k_{\text{rad}}^{\text{ext}}$	0.46 ± 0.04
$k_{\text{rad}}^{\text{int}}$	8.38 ± 0.75

$$k^{\text{ext}} = k^{\text{int}}(1 - \kappa p_r). \quad (4.18)$$

The values of the diverse definitions of the bimolecular recombination coefficient are ultimately listed in Tab. 4.2.

4.4 Lifetimes and internal luminescence quantum efficiency

Based on the revealed rates R_i of individual recombination processes, I address bulk charge-carrier lifetimes $\tau_{\text{bulk},i}$ to each recombination process i defined as

$$\tau_{\text{bulk},i} = \frac{\Delta n}{R_i - G_{\text{int}}}. \quad (4.19)$$

Additionally, I derive the overall effective bulk lifetime τ_{bulk} according to

$$\frac{1}{\tau_{\text{bulk}}} = \sum_{i=1}^N \frac{1}{\tau_{\text{bulk},i}}. \quad (4.20)$$

The derived lifetimes are depicted in Fig. 4.4 (a) and depend strongly on the

4.4 Lifetimes and internal luminescence quantum efficiency

excess-charge carrier density Δn and, thus, on the illumination intensity. For low level injection conditions, the lifetime τ_{SRH} (orange curve in Fig. 4.4 (a)) of the Shockley-Read-Hall process is limited by the minority-charge carrier lifetime τ_n and also restricts the effective lifetime (black curve) for moderate excess-charge carrier densities. Here, the overall external bimolecular lifetime (blue curve) is fixed to $(k^{\text{ext}}p_0)^{-1}$ as indicated. With increasing excess-charge carrier density, τ_{SRH} rises with an inflection point located at the doping concentration $p_0 \approx 3 \times 10^{15} \text{ cm}^{-3}$, while the lifetimes of higher order recombination mechanisms drop progressively. The effective lifetime τ_{bulk} becomes first restricted by bimolecular recombination before trimolecular, Auger recombination becomes the limiting mechanism at even higher excess-charge carrier densities. During high level injection conditions, the sum of minority- and majority-charge carrier lifetimes define τ_{SRH} , the bimolecular lifetime is given by $(k^{\text{ext}}\Delta n)^{-1}$ and the Auger lifetime (purple curve) is expressed as $(C\Delta n^2)^{-1}$.

4 Time-resolved photoluminescence from perovskite thin films

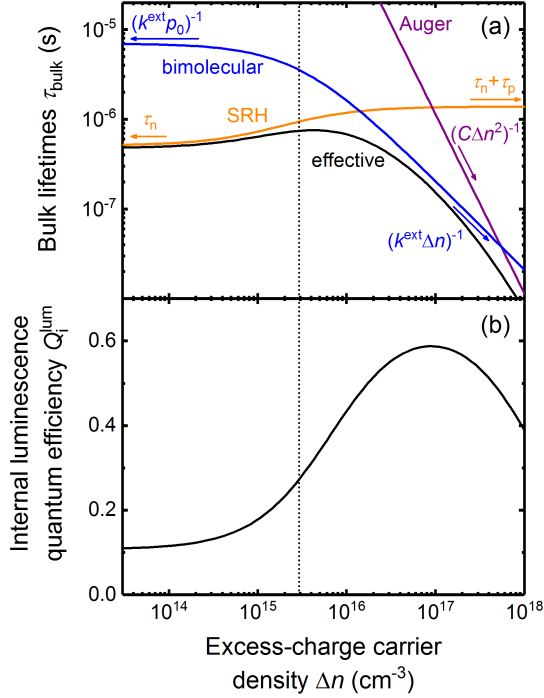


Figure 4.4: (a) Bulk lifetimes τ_{bulk} of individual recombination processes as a function of the excess-charge carrier density Δn , namely Shockley-Read-Hall (SRH), Auger and bimolecular (radiative and non-radiative) recombination. The black solid curve refers to the effective bulk lifetime τ_{eff} . Furthermore, the vertical dotted line marks the excess-charge carrier density $\Delta n \approx 2.9 \times 10^{15} \text{ cm}^{-3}$ found in the absorber layer upon illumination with one sun. (b) Internal luminescence quantum efficiency Q_i^{lum} derived as the ratio of the internal radiative recombination rate R_{rad} to the sum of all recombination rates $R = R_{\text{rad}} + R_{\text{nrad}}$. Adapted with permission from [102]. Copyrighted by the American Physical Society, 2016.

From a photovoltaic aspect, the effective charge-carrier lifetime τ_{eff} in the absorber layer upon one sun illumination is of particular interest for the performance of a solar cell. Therefore, I derive the excess-charge carrier concentration Δn generated upon steady-state illumination of one sun intensity in the next step. On

4.4 Lifetimes and internal luminescence quantum efficiency

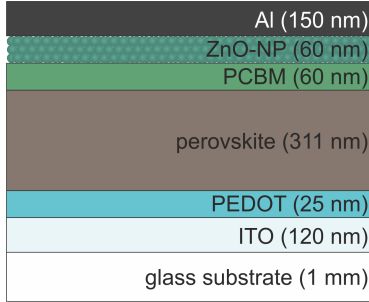


Figure 4.5: Illustration of the hypothetical cell stack with the individual layers and thicknesses (not to scale) as indicated.

that account, I use the numerical device simulator Advanced Semiconductor Analysis (ASA) [145] in order to calculate the external optical generation rate G^{ext} in the perovskite absorber layer embedded in a hypothetical but common device stack (see Fig. 4.5): glass (1 mm)/ITO (120 nm)/PEDOT (25 nm)/perovskite (311 nm)/PCBM (60 nm)/ZnO-NP (60 nm)/Al (150 nm). The simulation is based on a transfer matrix method (TMM) and takes interference effects into account. Optical data (refractive indices n_r and extinction coefficients k) are obtained from modeling transmittance and reflectance of corresponding single layers of the applied materials with the software SCOUT [97], respectively. Figure 4.6 shows these material-dependent parameters. Upon steady-state illumination at open circuit and assuming flat band conditions, the obtained generation rate $G^{\text{ext}} \approx 3.9 \times 10^{21} \text{ cm}^{-3} \text{ s}^{-1}$ matches the recombination rate. Solving for Δn yields an excess-charge carrier density of $\Delta n \approx 2.9 \times 10^{15} \text{ cm}^{-3}$ at one sun conditions, which is indicated in Fig. 4.4 as a vertical black dotted line. At one sun conditions, I derive an effective charge-carrier lifetime of $\tau_{\text{eff}} \approx 740 \text{ ns}$, which is an astonishingly high value for a solution-processed solar cell material.

Based on internal volume parameters, namely the pure radiative ($R_{\text{rad}} = k_{\text{rad}}^{\text{int}} np$) and the overall non-radiative recombination rate $R_{\text{nrad}} = k_{\text{nrad}} np + np / (\tau_n p + \tau_p n) + C(n^2 p + np^2)$, the internal luminescence quantum efficiency Q_i^{lum} is defined as

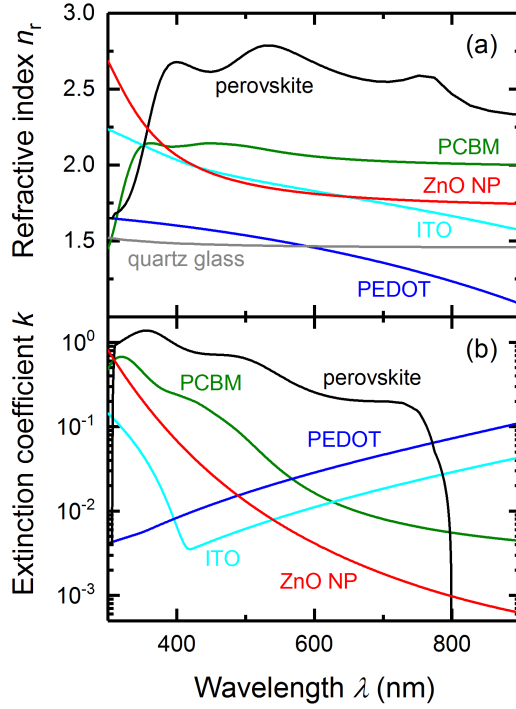


Figure 4.6: Optical constants of a variety of materials employed as thin layers in a flat solar cell stack as a function of wavelength: (a) refractive index n_r and (b) extinction coefficient k .

$$Q_i^{\text{lum}} = \frac{R_{\text{rad}}}{R_{\text{rad}} + R_{\text{nr}}}, \quad (4.21)$$

which is illustrated in Fig. 4.4 (b) as a function of the excess-charge carrier density Δn . Non-radiative Shockley-Read-Hall processes prevent high internal luminescence quantum efficiencies at low level injection conditions. At one sun illumination, charge carriers recombine radiatively with a quantum yield of $Q_i^{\text{lum}} \approx 0.27$. This value is of particular interest for estimating the implied open-circuit voltage as discussed in Sec. 4.8. Due to the bimolecular nature, radiative recombination becomes more essential in the range of higher excess-charge carrier densities. Therefore, Q_i^{lum}

risers gradually when proceeding towards higher excitation intensities. Eventually, Q_i^{lum} gets limited to a maximum value of about 0.6 at $\Delta n \approx 9 \times 10^{16} \text{ cm}^{-3}$ because of the significant non-radiative bimolecular component, which allows only for an intrinsic radiative fraction of bimolecular recombination of $\kappa \approx 0.66$, and the increasing influence of non-radiative Auger recombination. The latter mechanism is the cause that Q_i^{lum} drops in the ultra high level injection regime.

4.5 Charge-carrier diffusion in thin films

As briefly mentioned before, shortly after the excitation process a homogeneous charge-carrier distribution establishes across the layer thickness as illustrated in Fig. 4.7. Here, I assume that the excess-charge carriers are initially exponentially distributed based on a Lambert-Beer absorption profile with the absorption coefficient $\alpha = 1.25 \times 10^5 \text{ cm}^{-1}$ at the wavelength $\lambda = 498 \text{ nm}$ of the pulsed excitation source. For the simulation according to the diffusion equation, I take a charge-carrier mobility of $\mu = 20 \text{ cm}^2 (\text{Vs})^{-1}$ and reflecting boundary conditions into account while I neglect recombination. As seen in Fig. 4.7, a nearly homogeneous distribution profile is already established after one nanosecond, which is even shorter than the applied integration time ($\sim 2 - 5 \text{ ns}$) of the camera. In the context of recombination, harmonizing of the excess-charge carrier profile will happen only marginally faster. Admittedly, the recombination rates scale up for locally increased excess-charge carrier densities Δn but the effective bulk charge-carrier lifetime τ_{bulk} is always at least one order of magnitude higher than the found diffusion time of approx. 1 ns (see Fig. 4.4). Therefore, as redistribution of charge carriers occurs on a fast time scale than recombination events, it is legitimate to assume an immediate homogeneous excess-charge carrier density right from the beginning of a time-resolved photoluminescence measurement of an organic inorganic perovskite thin-film. However, for thick samples like single crystals, the effect of charge-carrier diffusion on the luminescence transients becomes severe and has to be implemented in the simulation of time-resolved photoluminescence decays as I show in Chap. 5.

Furthermore, I evaluate the distance that an arbitrary minority-charge carrier can travel driven by diffusion before it recombines upon the conditions present at

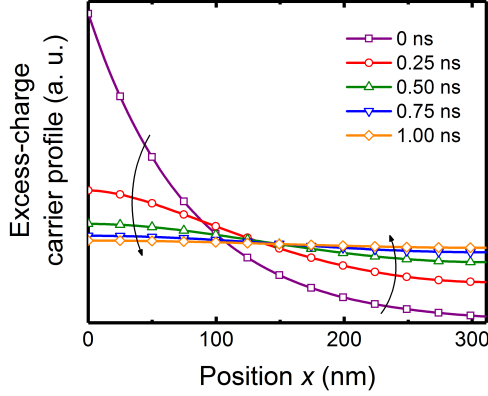


Figure 4.7: Simulation of the flattening of an initially exponential excess-charge carrier profile as the result of charge-carrier diffusion. Here, I use an absorption coefficient of $\alpha = 1.25 \times 10^5 \text{ cm}^{-1}$ and a charge-carrier mobility of $\mu = 20 \text{ cm}^2 (\text{Vs})^{-1}$.

one sun illumination. This distance enables the identification of possible transport limitations, which affects the working mechanism and may restrict the overall efficiency of a solar cell, and is denoted as the diffusion length of minority-charge carriers L_d

$$L_d = \sqrt{D\tau_{\text{eff}}}, \quad (4.22)$$

where τ_{eff} refers here to the effective bulk lifetime at one sun illumination ($\tau_{\text{bulk}} \approx 740 \text{ ns}$). The diffusion constant D can be expressed in terms of the derived charge-carrier mobility $\mu = 20 \text{ cm}^2 (\text{Vs})^{-1}$ according to the Einstein-relation as

$$D = \frac{\mu k_B T}{q}, \quad (4.23)$$

where $k_B T$ denotes the thermal energy and q is the elementary charge. Consequently, I find a charge-carrier diffusion length of $L_d \approx 6 \mu\text{m}$, which substantially exceeds typical thin-film absorber thicknesses of a few hundredths of nanometers. Thus, transport limitations in such high quality perovskite layers can be excluded.

4.6 Surface passivation and recombination

Until now, I have only considered recombination in the volume of the perovskite absorber layer and left out the effect of defects located at the surfaces of the absorber layer in the form of e. g. dangling bonds and uncoordinated atoms. To account for non-radiative recombination implemented by surface defects, I introduce an additional Shockley-Read-Hall recombination rate \tilde{R}_s , which reads in the case of electrons being the minority-charge carriers [146]

$$\tilde{R}_s = \frac{\Delta n_s(p_0 + \Delta n_s)}{\frac{\Delta n_s}{S_p} + \frac{p_0 + \Delta n_s}{S_n}}. \quad (4.24)$$

Here, Δn_s denotes the local excess-charge carrier concentration at the surfaces. The surface recombination velocities S_n and S_p for electrons and holes, respectively, are a measure of how fast charge carriers recombine via localized surface defects and are drained from the volume of the absorber layer to the surfaces by diffusion. For the assumption that the volume contains significantly less defects than the surfaces, the local excess-charge carrier concentration Δn_s at the surfaces will always be lower than in the bulk due to sustained surface recombination. As the p -type doping found in the examined sample is rather low, Δn_s for high excitation fluences might be still larger than the doping concentration p_0 . When I additionally assume equal surface recombination velocities for electrons and holes $S_n = S_p = S$, Eq. 4.24 simplifies

$$\tilde{R}_s = \xi S \Delta n_s, \quad (4.25)$$

where ξ varies between 0.5 – 1 depending on the prevalent injection level in the sample ($\xi = 0.5$ for high level injection conditions and $\xi = 1$ for low level injection conditions). For simplicity, I assume $\xi = 1$ in the following calculations. As \tilde{R}_s denotes the number of charge carriers recombining per surface area and time, I rather transform Eq. 4.25 into a volume-related recombination rate R_s by taking the absorber layer thickness d into consideration

$$R_s \approx \xi \frac{S}{d} \Delta n_s = \frac{\Delta n}{\tau_s}. \quad (4.26)$$

4 Time-resolved photoluminescence from perovskite thin films

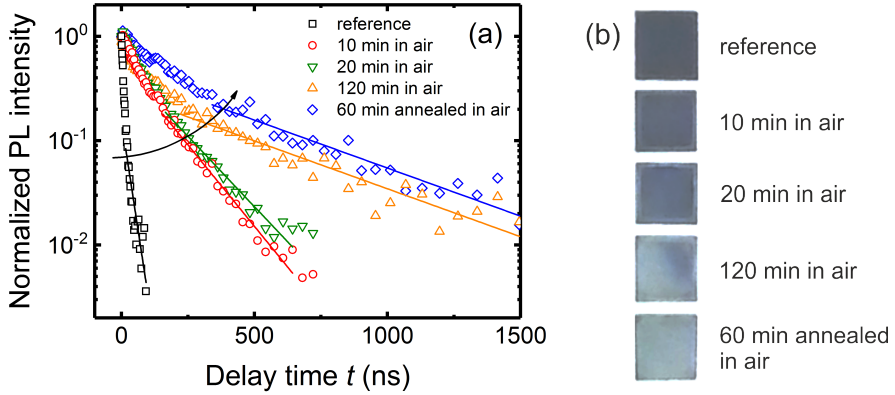


Figure 4.8: (a) Normalized photoluminescence decay (open symbols) for perovskite thin-films with different dwell times in ambient air (relative humidity $RH \approx 50\%$, ambient temperature $T \approx 26^\circ\text{C}$, excitation fluence $\phi_{\text{exc}} \approx 0.7 \mu\text{J}/\text{cm}^2$). Mono-exponential fitting (solid lines) of the long-term decays allows for the determination of minority-charge carrier lifetimes. Pictures of the respective samples are shown in panel (b).

This step allows me to assign the recombination rate R_s to the bulk charge-carrier concentration Δn instead of its surface equivalent Δn_s , and also the lifetime τ_s , which is related to surface recombination. In the presence of a severe amount of surface defects, the overall effective Shockley-Read-Hall lifetime $\tau_{\text{SRH,eff}}$ can be exclusively dominated by surface recombination instead of trap-assisted recombination in the bulk

$$\frac{1}{\tau_{\text{SRH,eff}}} = \frac{1}{\tau_s} + \frac{1}{\tau_{\text{SRH}}}, \quad (4.27)$$

where τ_{SRH} is the lifetime assigned to Shockley-Read-Hall recombination in the volume of the absorber. Therefore, in order to facilitate the determination of desired bulk recombination parameters from photoluminescence transients, the impact of surface recombination has to be minimized. Historically, the control over surface chemistry for various semiconductors and photovoltaic technologies has become an uttermost important strategy of improving material quality and solar cell performance [147–150]. Figure 4.8 (a) shows that a treatment of perovskite thin films in

4.6 Surface passivation and recombination

Table 4.3: Minority-carrier lifetimes for perovskite thin-films with different dwell time in ambient air derived from the exponential time-resolved photoluminescence decays in Fig. 4.8. Additionally, the relative lifetime gains in terms of the reference value are indicated.

	minority-carrier lifetime	relative gain
reference	(26 ± 6) ns	1.0
10 min in air	(139 ± 13) ns	5.3 ± 2.0
20 min in air	(161 ± 6) ns	6.2 ± 2.3
120 min in air	(472 ± 33) ns	18.2 ± 6.9
60 min annealed in air	(471 ± 32) ns	18.1 ± 6.9

ambient air (relative humidity $RH \approx 50\%$, ambient temperature $T \approx 26^\circ\text{C}$) exhibits a remarkable trend on the long-term decay of photoluminescence transients. Here, I processed thin films inside a nitrogen filled glovebox, including spin-coating as well as annealing steps, and, subsequently, exposed them to ambient air for different dwell times $t = (0 - 120)$ min. Additionally, one sample was annealed in ambient air for $t = 60$ min. The minority-charge carrier lifetimes derived from mono-exponential fits (see straight lines in Fig. 4.8 (a)) of the time-resolved photoluminescence decays are listed in Table 4.3 and improve by a factor of 18 ± 7 with increasing exposure time in ambient air compared to the reference sample, which is not exposed to air at all. Despite the change of the visual impression of perovskite samples from originally glossy to eventually matt during the exposure (see also Fig. 4.8 (b)), the absorptances measured by photothermal deflection spectroscopy remain unaffected by the treatment (see Fig. 4.9). The latter finding indicates that the perovskite bulk material quality is maintained as the well resolved sub-band gap characteristics are virtually identical, which are associated with structural disorder and the presence of defect states in the bulk. Additionally, no apparent shifts in the absorption onset are identified. For these reasons, I assume that the change in the visual impression of the samples can be attributed to recrystallization processes of the polycrystalline films to a varying extent. However, as the bulk properties in terms of impurities and defects turn out to be unchanged, air exposure seems to modify the surface chemistry of polycrystalline perovskite films by reducing surface defect states and possibly passivating defect-rich grain boundaries. As a consequence, I attribute the

4 Time-resolved photoluminescence from perovskite thin films

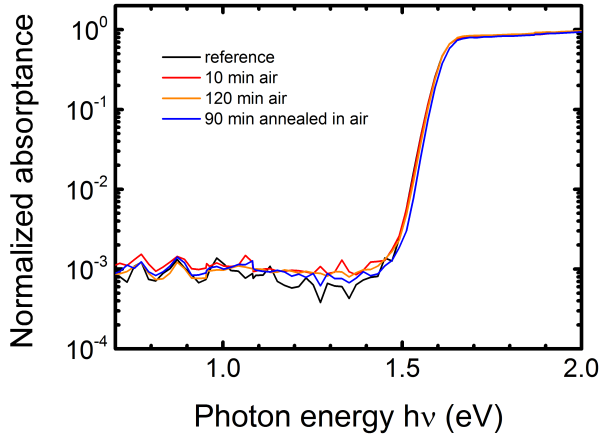


Figure 4.9: Normalized photothermal deflection spectroscopy absorbances for perovskite thin-films with different dwell times in ambient air.

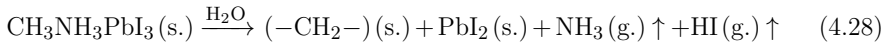
improved minority-charge carrier lifetimes upon air exposure exclusively to an enhancement of the surface lifetime τ_s , which in turn leads to an improved effective lifetime $\tau_{\text{SRH,eff}}$ based on equal bulk Shockley-Read-Hall lifetimes τ_{SRH} according to Eq. 4.27. Hence, surface recombination typically limits the attainable effective lifetime $\tau_{\text{SRH,eff}}$ in perovskite thin films and neutralizing surface defects is essential in order to be able to derive bulk properties from photoluminescence transients. Here, the surface passivation effect is attributed to moisture, which partly solvates methylammonium and, thus, causes a "self-healing" of perovskite surfaces by a reduction in trap state density as speculated in the literature [151]. Oxygen alone does not exhibit the same beneficial passivation effect [151, 152]. Besides the passivation effect attained by residual lead iodide [153] and the influence of moisture [151], respectively, also ligand passivation of perovskite surfaces is achieved by applying various Lewis bases like pyridine [154, 155] and trioctylphosphine oxide [11], which are assumed to act as electron donors for under-coordinated Pb atoms.

In order to gain a deeper understanding of the different surface chemistry, I show X-ray photoelectron spectroscopy (XPS) measurements in Fig. 4.10 of perovskite films annealed in a moisture-containing environment (blue line, $RH \approx 35\%$) and in dry nitrogen (red line), respectively. Both survey scans reveal the existence

4.6 Surface passivation and recombination

of all the elements expected for $\text{CH}_3\text{NH}_3\text{PbI}_3$ perovskite and closely resemble with the exception that additional peaks are identified and some are more pronounced for the film exposed to moisture. Figure 4.11 shows a selection of high resolution XPS scans for various peaks. The prominent differences between the samples are the occurrence of additional Pb $4f_{7/2}$ and Pb $4f_{5/2}$ peaks, which are denoted with (B) in Fig. 4.11 (a) and are not resolved in panel (f). The change in binding energy E_b relies on a chemical shift due to a different chemical bonding environment of lead atoms and indicates that lead exists in different phases at the surface of the perovskite film exposed to moisture. Furthermore, chlorine peaks $2p_{3/2}$ and $2p_{1/2}$ are only identified when the perovskite film is treated with humidity (see Fig. 4.11 (e)). Additionally, the oxygen $1s$ peak in Fig. 4.11 (d) is more pronounced than in panel (i) due to the uptake of water molecules during the exposure of the film to moisture.

Moreover based on the intensity of the individual elemental peaks, I deduce the stoichiometric composition of perovskite with respect to lead ($4f$ (A) peaks) at the surface resulting in $(\text{CH}_3\text{NH}_3)_{1.15}\text{PbI}_{3.33}$ for the film annealed in dry nitrogen and $(\text{CH}_3\text{NH}_3)_{0.78}\text{PbI}_{2.49}$ for the film annealed in moisture atmosphere. While in the former perovskite composition, lead located at the surfaces is over-coordinated and, thus, forms possible recombination centers, lead in the latter composition appears to be rather under-coordinated. However, perovskite decomposes in a humid environment according to the proposed reaction scheme [156, 157]



and solid (s.) residuals like lead iodide and hydrocarbons remain on the surface while other resulting compounds are volatile (g.). Therefore, I propose that a fraction of lead in the form of Pb^{2+} (found as Pb (A) peaks) is actually chemically bound as PbI_2 or even PbCl_2 instead of being entirely incorporated in the perovskite structure as assumed for the previous estimation of the stoichiometric composition at the surface. The obtained surface passivation effect in the presence of moisture is believed to stem from a thin residual layer of lead halides covering the perovskite grain surfaces and boundaries due to a local degradation of perovskite material [153]. Based on the smaller band gap of perovskite compared to the surrounding lead halides, an

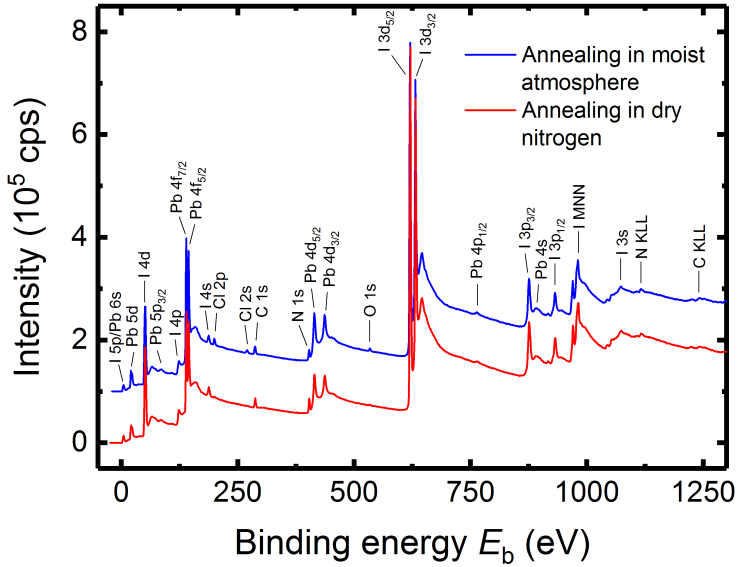


Figure 4.10: X-ray photoelectron spectroscopy spectra of two perovskite thin films, where the blue line and the red line represent a perovskite sample annealed inside a climate box in a moist atmosphere (relative humidity $RH \approx 35\%$) and inside a glovebox filled with nitrogen, respectively.

energy barrier for charge carriers towards the interface is building up. The resulting band alignment is believed to expel charges from the perovskite surface leading to suppressed surface recombination [153]. It shall be noted here, that excessive exposure to high humidity levels damage perovskite films due to severe degradation by destabilizing the perovskite structure. The chemical reaction 4.28 promotes the formation of hydrocarbons, which could explain the increased intensity found from the carbon 1s orbital in Fig. 4.11 (c) compared to (h).

Now, I will address the issue of the additional lead peaks (B) found for the perovskite film exposed to a humid atmosphere (see Fig. 4.11 (a)), which are shifted towards lower binding energies. Typically, a decrease in binding energy is caused by a reduced electrostatic shielding e. g. as a consequence of the addition of valence electron charge. Here, I find the Pb $4f_{7/2}$ and $4f_{5/2}$ peaks to be located at $E_b \approx$

4.6 Surface passivation and recombination

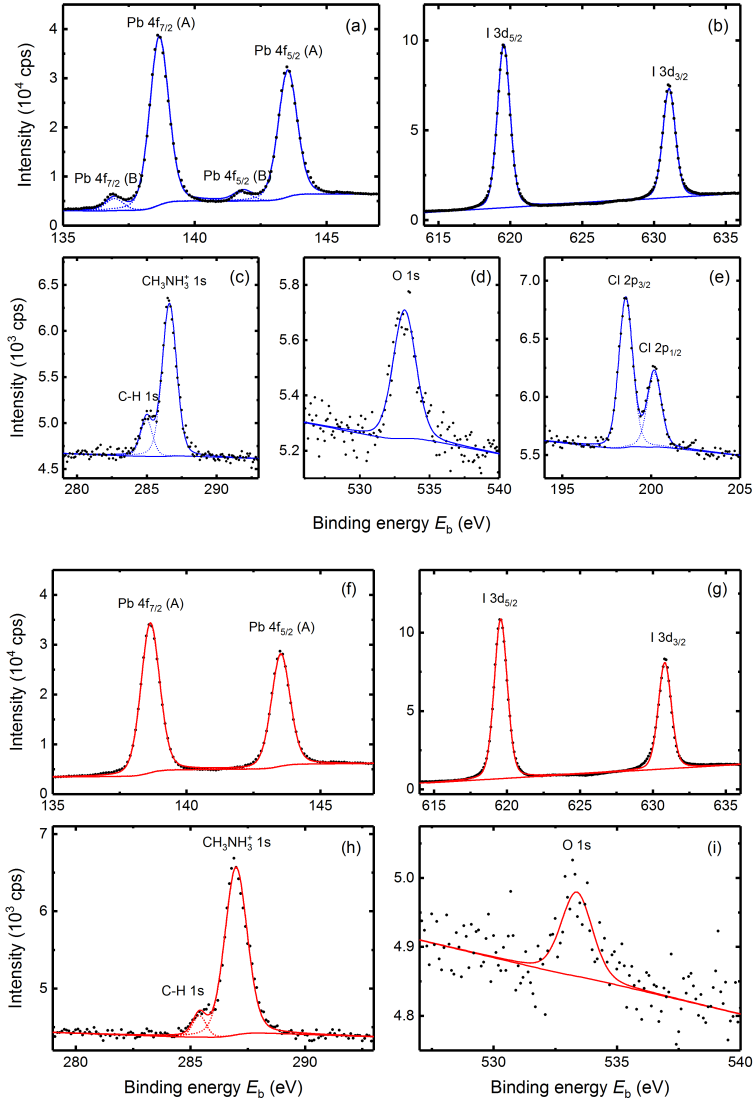
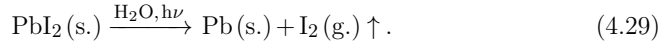


Figure 4.11: High resolution narrow X-ray photoelectron spectroscopy scans (black circles) of selected peaks shown in the survey spectra in Fig. 4.10 for a perovskite film annealed in a moist atmosphere (panels (a) - (e)) and in nitrogen (panels (f) - (i)). Additionally, diverse fits and background lines are shown as solid and dotted lines.

4 Time-resolved photoluminescence from perovskite thin films

137.0eV and $E_b \approx 141.8\text{eV}$, respectively. These positions are in excellent agreement with those of elemental lead [158, 159]. Pb^{2+} cations in halide compounds can be reduced in a humid environment or upon illumination when undergoing the reaction [157]



Thus, after a two-step degradation process (Eq. 4.28 and 4.29), lead can be present at the surface in its elemental form. Charge-carrier quenching at elemental lead is apparently not a relevant issue as the minority-charge carrier lifetime increases with prolonged exposure time of perovskite to moisture (see Tab. 4.3).

After having highlighted the need and the successful realization of surface passivation, I will give estimations of the attainable surface lifetimes and recombination velocities in the following. The perovskite film has two interfaces, where the front surface is in touch with the surrounding atmosphere (i. e. nitrogen during the photoluminescence measurements) and the rear side finishes with the glass substrate. If I assume that the perovskite/glass interface is perfectly passivated (rear surface recombination velocity $S_r = 0$) and the perovskite/ N_2 interface still exhibits surface defects due to inadequate passivation, a non-zero surface recombination velocity $S_f = S$ is found at the front. In this case, the resulting surface lifetime τ_s is well approximated in the case of an electrical field free volume by the relation [160]

$$\tau_s \cong \frac{d}{S} + \frac{4}{D} \left(\frac{d}{\pi} \right)^2. \quad (4.30)$$

Figure 4.12 (a) illustrates which values of the surface recombination velocity S fulfill Eq. 4.30 for various layer thicknesses d and surface lifetimes τ_s . Due to the high values of diffusion constants determined for perovskite materials, the attainable surface lifetime for thin films with a thickness of some hundreds of nanometers is limited by the recombination velocity at the surfaces (first term in Eq. 4.30). For single crystals with $d \gg 1\mu\text{m}$, τ_s detaches from its influence by the surface recombination velocity S to an increasing extent as the diffusive transport of charge carriers from the bulk towards the surfaces becomes the limiting process (second term in Eq. 4.30). Under the assumption that the volume of the absorber would be

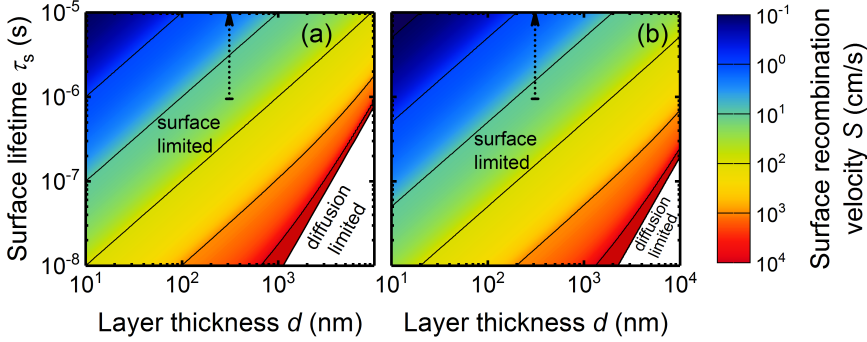


Figure 4.12: Surface lifetimes τ_s , which can be expected for different layer thicknesses d and a given mobility of $20\text{cm}^2\text{V}^{-1}\text{s}^{-1}$, as a function of (a) surface recombination velocities S , which are different at the front and back interfaces, namely $S_f = 0$, $S_b = S$. In panel (b), equal surface recombination velocities are assumed ($S = S_f = S_b$). The blank area in the lower right corners cannot be addressed even by extreme high S values as charge-carrier diffusion towards the surfaces becomes the limiting process in this region and, thus, is defining the boundary. The dotted black line indicates the possible surface lifetimes for the observed layer thickness of $d = 311\text{nm}$. The marked origin reflects the lower limit in the case of non-existing defect-related recombination in the bulk, when τ_s is simply given by the obtained SRH lifetime $\tau_s \approx 950\text{ns}$ upon one-sun illumination. Adapted with permission from [102]. Copyrighted by the American Physical Society, 2016.

completely free of defects as a matter of fact ($\tau_{\text{SRH}} \rightarrow \infty$), the observed trap-assisted recombination would exclusively occur at the surfaces implying that the surface lifetime τ_s is identical with the effective Shockley-Read-Hall lifetime $\tau_{\text{eff,SRH}} \approx 950\text{ns}$ derived under one sun illumination conditions. Consequently, I find a low upper limit for the surface recombination velocity of $S \lesssim 33\text{cm/s}$, which is indicated as the onset of the arrow in Fig. 4.12 (a). Similar values are reported for passivated Si wafers [161,162] indicating that perovskite surfaces are exceptionally well passivated even when attributing the observed trap-assisted recombination to the surfaces alone.

Analogously, for the case that both perovskite interfaces are actually equal in terms of the surface recombination velocity $S_f = S_r = S$, the surface lifetime is derived as [160]

$$\tau_s \cong \frac{d}{2S} + \frac{1}{D} \left(\frac{d}{\pi} \right)^2. \quad (4.31)$$

Consequently, the upper limit of the surface recombination velocity becomes smaller with $S \lesssim 16 \text{ cm/s}$. The corresponding situation according to Eq. 4.31 is illustrated in Fig. 4.12 (b). In the scenario of allocating the Shockley-Read-Hall recombination both to the surfaces and the bulk, the actual surface recombination velocity S will become even lower (following the dotted arrow in Fig. 4.12 (a) and (b)). Typical charge-carrier lifetimes of hundreds of nanoseconds found in the literature for thin films correspond to surface recombination velocities of about 100 cm/s and less and indicate that defects at the sample surfaces are necessarily neutralized by (partially unintentional) surface passivation processes. On the contrary, a surface recombination velocity of 3400 cm/s is obtained for unpassivated surfaces of perovskite single crystals [163]. This finding emphasizes the need for effective perovskite surface passivation.

4.7 Fundamental semiconductor properties

Proceeding from the deduced internal radiative recombination coefficient $k_{\text{rad}}^{\text{int}}$, I derive further intrinsic semiconductor properties, which are listed in Tab. 4.4. For the following inferences, I rely on the principle of detailed balance. Based on the correlation that the radiative recombination rate at thermal equilibrium matches the generation rate of electron-hole pairs by thermal radiation, van Roosbroeck and Shockley derived in 1954 the relation [20]

$$k_{\text{rad}}^{\text{int}} n_i^2 = \int_0^\infty 4\pi n_r^2(E) \alpha(E) \phi_{\text{bb}}(E) dE. \quad (4.32)$$

Equation 4.32 thus connects diverse internal semiconductor properties, namely the internal radiative recombination coefficient $k_{\text{rad}}^{\text{int}}$, the intrinsic charge-carrier concentration n_i , the refractive index n_r and the absorption coefficient α . As the value of the internal radiative recombination coefficient is deduced from the radiative fraction κ of the total internal bimolecular recombination coefficient, the intrinsic charge-carrier concentration n_i itself is correlated to κ as I show in Fig. 4.13. Based

Table 4.4: List of fundamental semiconductor properties of $\text{CH}_3\text{NH}_3\text{PbI}_3$ perovskite for a band gap of $E_g = 1.6\text{eV}$ when assuming a radiative fraction of the internal bimolecular recombination coefficient of $\kappa = 0.66$. The intrinsic charge-carrier concentration n_i , product of densities of states $N_c N_v$ in the conduction and valence bands, and the joint charge-carrier mass m_j^* in terms of the electron rest mass are derived by means of the van Roosbroeck-Shockley relation (Eq. 4.32) at room temperature ($T = 300\text{K}$). Additionally, a prediction of the open-circuit voltage V_{oc} upon one sun illumination is provided.

n_i (cm^{-3})	$N_c N_v$ (cm^{-6})	m_j^*	V_{oc} (V)
$(2.62 \pm 0.12) \times 10^5$	$(5.2 \pm 3.2) \times 10^{37}$	0.435 ± 0.075	1.22 ± 0.02

on the already deduced material properties, I find an intrinsic charge-carrier concentration of $n_i = (2.62 \pm 0.12) \times 10^5 \text{cm}^{-3}$ for $\kappa = 0.66$ at room temperature ($T = 300\text{K}$) from the van Roosbroeck-Shockley relation.

Furthermore, by applying the law of mass action [164]

$$n_i^2 = N_c N_v e^{-E_g/(k_B T)}, \quad (4.33)$$

I provide values of the product of the densities of states $N_c N_v$ in the valence and conduction band (see Tab. 4.4). In doing so, I rely on band gap energy of $E_g = 1.60\text{eV}$ for $\text{CH}_3\text{NH}_3\text{PbI}_3$ perovskites. Because the share of each density of states in the product $N_c N_v$ cannot be separated, I am not able to determine effective masses for each charge-carrier type but rather state a "joint" effective mass m_j according to the relation [164]

$$\sqrt{N_c N_v} = 2 \left(\frac{2\pi m_j k_B T}{h^2} \right)^{3/2}. \quad (4.34)$$

Nevertheless, effective electron and hole masses are reported in the literature to be quite similar with $m_{\text{eff}}^* \approx 0.1 - 0.3$ [70–72], which also hints at similar density of states N_c and N_v and allows the direct comparison with the here derived joint effective mass $m_j = 0.435 \pm 0.075$. Apparently, m_j is slightly higher than literature values of m_{eff}^* . Due to the exponential dependence of the product of the densities of states $N_c N_v$ in the valence and conduction band on the band gap energy E_g (see Eq. 4.33), already small variations in E_g change the deduced $N_c N_v$ and the joint

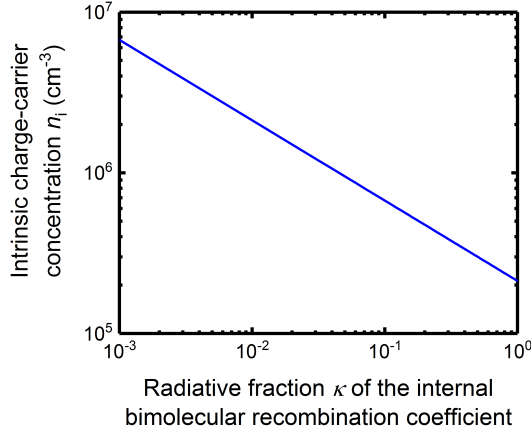


Figure 4.13: Intrinsic charge-carrier concentration n_i as a function of the radiative fraction κ of the internal bimolecular recombination coefficient based on the van Roosbroeck-Shockley relation.

effective mass m_j tremendously. As the band gap of $\text{CH}_3\text{NH}_3\text{PbI}_3$ may vary in the range of $E_g \approx (1.55 - 1.60)$ eV [165], for the lower limit of E_g , I find a significantly decreased joint effective mass of $m_j = 0.235$, which is within the range of literature values.

4.8 Prediction of the implied open-circuit voltage

Upon illumination at open-circuit conditions, all photo-generated charge carriers have to recombine eventually as they will not be extracted as current. Thus, the open-circuit voltage V_{oc} is a suitable physical property which addresses recombination losses of different kinds. In the following, I show the prediction of the implied open-circuit voltage V_{oc} based on findings from time-resolved photoluminescence measurements. This estimation represents a simply way to quantify the quality of any absorbing material and its applicability in photovoltaic devices. As I investigate here the bulk absorber quality, I fortunately do not have to consider possible influences of surrounding transport layers on the perovskite interfaces like in a complete device, for instance, in the form of charge-carrier quenching, interface states and/or

4.8 Prediction of the implied open-circuit voltage

dipoles and band bending. Due to the exceptionally low surface recombination velocities, I assume well passivated and nearly defect-free perovskite surfaces, where any form of charge-carrier recombination takes place in the bulk only.

The maximum attainable open-circuit voltage V_{oc}^{rad} is given for the radiative limit, when the only present recombination loss mechanism is spontaneous radiative recombination, which can not be avoided from a thermodynamic consideration due to the principle of detailed balance. Exchanging the ideal step-like absorption in the approach of Shockley and Queisser [166] by absorption values in more realistic scenarios $A(E)$ [21, 22], V_{oc}^{rad} is obtained as

$$V_{oc}^{rad} = \frac{k_B T}{q} \ln \left(\frac{J_{sc}}{J_0^{rad}} \right) = \frac{k_B T}{q} \ln \left(\frac{\int_0^\infty \varepsilon_{in} A(E) \phi_{sun}(E) dE}{\int_0^\infty \varepsilon_{out} A(E) \phi_{bb}(E) dE} \right), \quad (4.35)$$

where J_{sc} is the short-circuit current density, J_0^{rad} is the radiative saturation current density and ϕ_{sun} is the solar spectrum. The étendue of outgoing and incident light is denoted as ε_{out} and ε_{in} , respectively. I calculate the absorptance $A(E)$ of the 311 nm-thin $\text{CH}_3\text{NH}_3\text{PbI}_3$ film embedded in the in the hypothetical solar cell stack depicted in Fig. 4.5 and find a theoretical maximum open-circuit voltage of $V_{oc}^{rad} = (1.32 \pm 0.01)$ V. As an extension to the ideal Shockley-Queisser approach, also non-radiative recombination can be addressed [29–31] in the form of the external LED quantum efficiency Q_e^{LED} [100, 142, 143]

$$V_{oc} = V_{oc}^{rad} + \frac{k_B T}{q} \ln \left(Q_e^{LED} \right), \quad (4.36)$$

whereas the external LED quantum efficiency Q_e^{LED} and the internal luminescence quantum efficiency Q_i^{lum} are linked by the relation [27, 28]

$$Q_e^{LED} = \frac{p_e Q_i^{lum}}{1 - Q_i^{lum} (1 - p_e - p_a)}. \quad (4.37)$$

Here, the term $1 - p_e - p_a$ corresponds to the probability p_r of photon re-absorption by the absorber layer (see Eq. 4.13). As the probability p_a of parasitic photon absorption is not easily deduced, I simply set $p_a = 0$ in the following and

4 Time-resolved photoluminescence from perovskite thin films

assume optically transparent transport films. The thus derived Q_e^{LED} and V_{oc} , respectively, represent upper limits. Based on Eq. 4.14, I find for a perovskite solar cell with back reflector an outcoupling efficiency for internally generated photons of $p_e \approx 0.057$. Upon one sun illumination, the internal luminescence quantum efficiency was previously derived as $Q_i^{\text{lum}} \approx 0.27$ in Sec. 4.4. These findings lead to an external LED quantum efficiency of $Q_e^{\text{LED}} \approx 0.020$ according to Eq. 4.37. Equation 4.36 can be expressed according to Eq. 4.35 and 4.37 in the alternative form [28]

$$V_{\text{oc}} = \frac{k_{\text{B}}T}{q} \ln \left(\frac{\int_0^\infty A(E)\phi_{\text{sun}}(E) dE}{\int_0^\infty A(E)\phi_{\text{bb}}(E) dE} \right) + \frac{k_{\text{B}}T}{q} \ln \left(\frac{\varepsilon_{\text{in}}}{\varepsilon_{\text{out}}} \right) + \frac{k_{\text{B}}T}{q} \ln \left(\frac{p_e}{p_e + p_a} \right) \quad (4.38)$$

$$+ \frac{k_{\text{B}}T}{q} \ln \left(\frac{(p_e + p_a)Q_i^{\text{lum}}}{(1 - Q_i^{\text{lum}}) + (p_e + p_a)Q_i^{\text{lum}}} \right),$$

which allows me to discriminate term by term the entropic open-circuit voltage loss processes. The first term corresponds to losses related to imperfect absorption and photon cooling addressing the different temperatures of the incoming and the outgoing photons, which in the present case drops down to a voltage of 1.597 V. Étendue expansion between the incident and the emitted photons accounts for ~ 278 meV for non-concentrated solar cells, as the étendue of incoming sun light is found to be $\varepsilon_{\text{in}} \approx 6.8 \times 10^{-5} S_{\text{cell}}$ due to geometrical considerations [167, 168], while the étendue of outgoing light into a hemisphere of air is given as $\varepsilon_{\text{out}} = \pi S_{\text{cell}}$. As I set $p_a = 0$ for simplicity, the third term describing losses based on parasitic absorption cancels out. Defect-related open-circuit voltage losses sum up by non-radiative recombination in the volume to ~ 100 mV upon illumination of one sun. In comparison, organic solution-processed absorber materials exhibit significantly higher non-radiative open-circuit voltage losses of 0.34 – 0.44 V [143]. Ultimately, the potential open-circuit voltage, which can be realized based on the quality of the investigated perovskite material, becomes $V_{\text{oc}} \approx (1.22 \pm 0.02)$ V. The different voltage loss processes are illustrated as colored domains in Fig. 4.14 as a function of the internal luminescence quantum efficiency Q_i^{lum} . Additionally, the open-circuit voltage can also be predicted based on the relation

4.8 Prediction of the implied open-circuit voltage

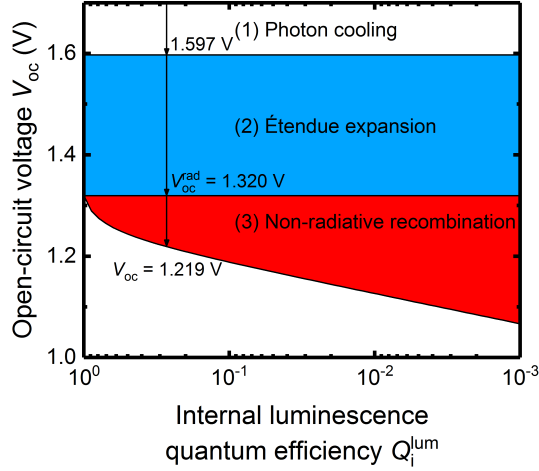


Figure 4.14: Entropic loss processes reducing the open-circuit voltage V_{oc} as a function of the internal luminescence quantum efficiency Q_i^{lum} for a probability of photon outcoupling of $p_e = 0.057$ and neglecting parasitic absorption $p_a = 0$, namely (1) photon cooling, (2) étendue expansion and (3) non-radiative recombination in the volume of the absorber layer. The indicated values and arrows illustrate the situation upon illumination with one sun.

$$V_{oc} = \frac{k_B T}{q} \ln\left(\frac{np}{n_i^2}\right) = \frac{E_g}{q} - \frac{k_B T}{q} \ln\left(\frac{N_c N_v}{np}\right), \quad (4.39)$$

which is an equivalent expression of Eq. 4.36 (see supporting information of Ref. [102]). Together with the semiconductor properties derived in Sec. 4.7, I reveal a similar prediction of $V_{oc} \approx 1.21$ V. Some measured open-circuit voltages of $\text{CH}_3\text{NH}_3\text{PbI}_3$ -based photovoltaic solar cells already exceed 1.15 eV [60]. Slightly different perovskite compositions with a band gap in the vicinity of $E_g \approx 1.6$ eV approach open-circuit voltages of $V_{oc} = 1.2$ V [169] and even surpass this value [61], respectively, due to a better control over material quality and minimal non-radiative recombination losses. Consequently, the implied open-circuit voltage V_{oc} is a realistic approach to estimate the attainable open-circuit voltage of a photovoltaic device based on the material properties of the perovskite absorber layer.

4 Time-resolved photoluminescence from perovskite thin films

As a last step, I quantify the hypothetical impact of photon recycling on the open-circuit voltage upon one sun illumination. In so doing, I assume in a gedanken experiment that I can switch off photon recycling. Consequently, the denominator in Eq. 4.37 will be set to 1 and the external LED quantum efficiency will be linearly linked to the internal luminescence quantum efficiency by $Q_e^{\text{LED}} \approx p_e Q_i^{\text{lum}}$. Thus, the external LED quantum efficiency slightly drops down to $Q_e^{\text{LED}} \approx 0.015$ and the resulting open-circuit voltage will be reduced by $\sim 8\text{mV}$, which can be attributed to the intrinsic voltage gain by recycled photons. This estimate demonstrates that photon recycling is already a relevant process in predicting efficiencies and open-circuit voltages. With improved perovskite material quality, devices will operate closer to the radiative limit and strategies of photon management are becoming more important, i. e. suppression of parasitic absorption and maximizing the amount of recycled photons which will contribute to the photovoltage [13, 170].

5 Time-resolved photoluminescence from single crystals

In this chapter, I study the impact of recombination, reabsorption, photon recycling and charge-carrier diffusion on time-resolved photoluminescence from single perovskite crystals, which is detected in transmission and reflection mode, respectively. Both photon recycling and diffusion have the ability to transport charges within the crystal. However, diffusion is identified to be the dominant transport mechanism and continuously shapes the charge-carrier profiles. Photon recycling rather makes its appearance by its sustaining function of preserving charge carriers. Reabsorption effects modify the photoluminescence spectra and give rise to observed spectral shifts during the measurements.

5.1 Introduction

Beside thin films, single crystals made of organic-inorganic perovskites have been successfully fabricated from the liquid phase, too [90,91,93,171]. Single crystals exhibit reduced defect densities and, therefore, their material quality and carrier transport properties surpass these of thin films (see Tab. 3.1). New potential application in opto-electronics result from the increase in size from hundreds of nanometers (thin films) to several millimeters, e. g. highly narrowband photodetectors [172], x-ray detectors [173], and sensors for environmental gases with high sensitivity [174]. Due to their large thickness and high luminescence quantum yields [12,175], perovskite crystals have become an ideal object of study to investigate reabsorption of luminescence [176–180], charge carrier transport [181,182] and charge carrier recombination [183,184]. In perovskite single crystals, extremely long charge-carrier transport

lengths of some hundred micrometers have been reported [181, 182]. It is still up for debate what underlying transport mechanism causes these long charge-carrier transport lengths as contradictory statements have been made. Some publications report that charge-carrier diffusion in combination with high mobilities and long lifetimes plays the dominant role in carrier transport [178, 180, 185]. Other reports reveal that charge carriers can be efficiently transported over long distances by photon recycling [179, 186–188]. This effect has been observed in perovskite materials and its impact on luminescence properties has been described [102, 186, 188–190]. Only a limited number of physical models [188] exist today which are able to sufficiently disentangle the impact of diffusion and photon recycling and also take the geometry of the sample into account. In the following, I present an approach to understand time-resolved photoluminescence in perovskite single crystals by taking into consideration the interplay of all relevant charge-carrier processes at once; this model [191] includes radiative and non-radiative charge-carrier recombination in the bulk, recombination via defects at the crystal surfaces, and charge-carrier transport by diffusion as well as photon recycling. The latter effect describes the (multiple) conversion processes of excited states into photons and vice versa. After radiative recombination of charge carriers at locations x_r , charges might be re-generated by absorption of radiation at quite different locations x_g . The radiative interaction between different positions is described in detail in Sec. A.3. By modeling experimental findings, I reveal that the relevant charge-carrier transport mechanism in thick perovskite crystals during a transient spectroscopy measurement is charge-carrier diffusion.

5.2 PDS absorptance of perovskite single crystals

In order to investigate the quality in respect of purity and structural order of perovskite single crystals, the absorption onset dynamics of perovskite single crystals were investigated by photothermal deflection spectroscopy (PDS). The normalized PDS absorptance A is depicted in Fig. 5.1 for a $\text{CH}_3\text{NH}_3\text{PbBr}_3$ crystal as orange curve. The steep increase in normalized absorptance at about 2.25 eV marks the band gap of the perovskite material. As seen before in Fig. 3.4, the band gap of

5.2 PDS absorptance of perovskite single crystals

perovskites can be significantly altered by the choice of halide elements in these compounds. Bromine incorporation results therefore in a wider band gap as seen for iodine in Sec. 3.6. For photon energies below $E \sim 2.15$ eV, the absorptance signal drops exponentially, but considerably less pronounced than for the band gap region. Sub-band gap absorption is characteristic for disorder and shallow defect states. The appearance of a significant amount of defects seems to be unusual for a highly ordered system like a single crystal. However, these defects are located at and near the crystal surface, respectively, as it can be deduced from the phase information φ between the modulated excitation signal and the deflected probe signal observed during the PDS measurement (black dashed line in Fig 5.1). Let us first consider the phase in the situation of full absorption ($E \gtrsim 2.25$ eV). High energy photons are typically absorbed close to the surface and, therefore, the phase remains at a constant level. While the absorption coefficient drastically decreases for photons with energies around the band gap, the absorption profile flattens and photons are progressively absorbed in the bulk to a higher extent. As heat generated by recombination in the bulk needs now in average more time to be transported to the surface, where it causes the deflection of the probe beam, the phase changes relatively in comparison to the situation of full absorption. Going towards lower photon energies $E \lesssim 2.15$ eV (entering the sub-band gap region), the phase in Fig. 5.1 returns now to the same value observed for full absorption of high energy photons. Consequently, the sub-band gap absorption occurs mainly in regions very close to the surface. Thus, I identify a significant amount of defects which are present at the crystal surface while the bulk seems to be less affected by sub-band gap states. Such surface-near defects can simply arise for example due to a lack of binding partners for lattice components at the sample edges. Additionally, due to the fabrication process from the liquid phase, solvent residues can remain on the surfaces and act as charge-carrier traps. Furthermore, decomposition and degradation will be more prominent at the crystal surfaces than in the bulk. Trap states act in general as non-radiative recombination centers for charge carriers. This implication and the fact, that the surface is more prone to the formation of defects than the bulk, is considered in the transient photoluminescence simulations described in Sec. 5.4.1.

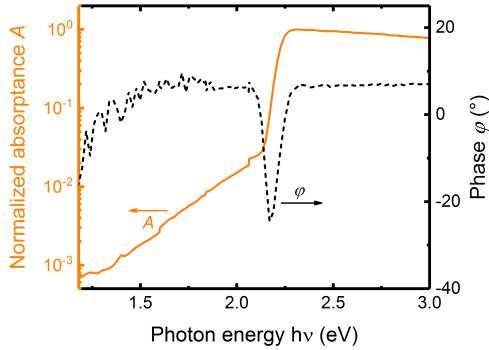


Figure 5.1: Normalized absorbance A of a $\text{CH}_3\text{NH}_3\text{PbBr}_3$ single crystal measured by photothermal deflection spectroscopy (PDS) shown as orange solid line. Additionally, the corresponding phase φ between the modulated excitation signal (pump) and the deflected probe signal is indicated as black dashed line.

5.3 Photoluminescence measurement configurations

For the precise analysis of charge-carrier processes in perovskite crystals, I measured time-resolved photoluminescence in two different measurement configurations as illustrated in Fig. 5.2. In the first configuration, the single crystal is illuminated by the excitation pulse from the front side, which is the same side from which luminescence is detected by the gated camera. This approach, denoted here as front side illumination, was used as a standard for the characterization of perovskite thin films in Chap. 4 and 6. Due to a high absorption coefficient at the photon energy of the excitation source, charge carriers and, subsequently, photoluminescence are mainly generated in close proximity to the sample surface. Therefore, the luminescence has to pass only through marginal segments of the entire crystal before it can be coupled out of the front side of the sample and detected in this configuration. Upon back side illumination on the other side, luminescence is detected in transmission mode. Especially in this configuration, detected luminescence has to traverse the entire thickness while the crystal acts basically as a filter for its own luminescence. Therefore, different photoluminescence spectra in terms of shape, peak position and intensity but also differences in the temporal changes of the mentioned properties can be expected for the two measurement configurations. In the following,

5.3 Photoluminescence measurement configurations

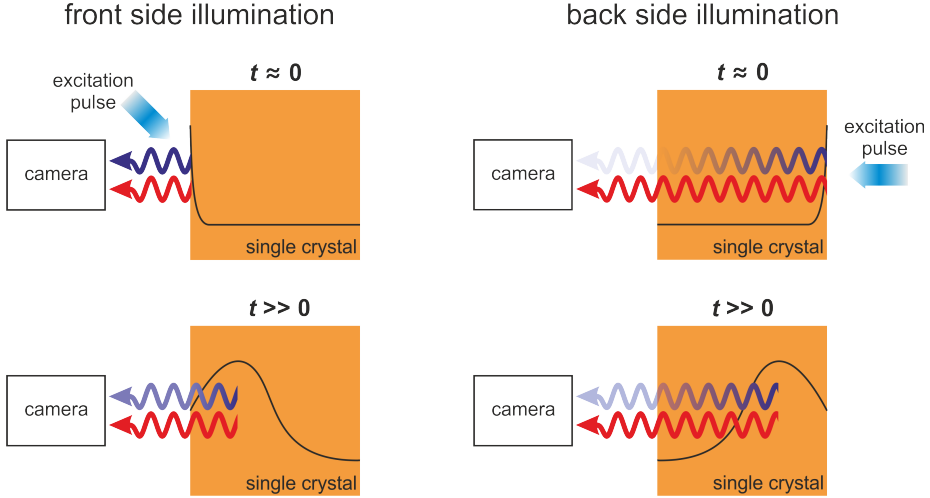


Figure 5.2: Overview of the used measurement configurations. In the left illustrations, pulsed excitation and luminescence detection is implemented at the same side of the sample. I denote this configuration "front side illumination". The observed photoluminescence signal is illustrated here as rays representing high (blue) and low energy photons (red). On the right side of this depiction, the back side of the sample is illuminated and, consequently, luminescence traverses the crystal in order to be detected by the camera. The upper row illustrates the respective initial situations at $t \approx 0$, when the pump pulse excites the sample and, thus, generates an excess charge carrier profile (black lines). Transport and recombination mechanisms reshape the carrier profile over time ($t \gg 0$) leading to spectral changes of the photoluminescence signal, as shown in the lower row. Please note that the charge-carrier profiles in all schemes are not precise and shall only present a rough qualitative carrier distribution.

I exclusively investigate time-resolved photoluminescence of a $\text{CH}_3\text{NH}_3\text{PbBr}_3$ single crystal as the reproducibility of transient data of pure iodine-containing perovskite ($\text{CH}_3\text{NH}_3\text{PbI}_3$) crystals could not be maintained presumably due to degradation or material instability during the measurement. Figure 5.3 shows the initial normalized photoluminescence spectra of a 0.17 cm-thick $\text{CH}_3\text{NH}_3\text{PbBr}_3$ crystal upon front (blue triangles) and back side illumination (red triangles). Due to severe re-absorption of photoluminescence, the high energy part (i. e. where the absorption coefficient α is sufficiently high) of the spectrum recorded upon back side illumi-

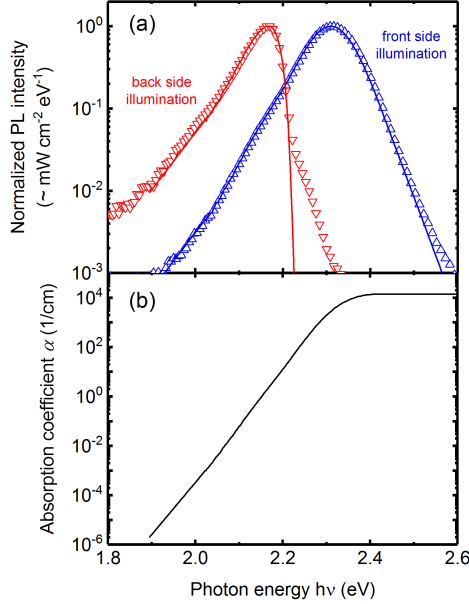


Figure 5.3: (a) Initial photoluminescence spectra of a $\text{CH}_3\text{NH}_3\text{PbBr}_3$ single crystal, which is excited with a photon density of $\phi_{\text{phot}} = 2.9 \times 10^{14} \text{ cm}^{-2}$ and a photon energy of $E = 3.07 \text{ eV}$. Here, the spectra (triangles) are recorded in two different measurement configurations (see also Fig. 5.2), denoted as front side illumination (blue) and back side illumination (red). Additionally, simulated spectra are shown as solid lines. (b) Absorption coefficient α derived from modeling the photoluminescence spectra shown in panel (a).

nation is abruptly cut off. Thus, the corresponding peak shows a significant red shift of $\sim 150 \text{ meV}$. Furthermore, a weak shoulder in the falling edge of the spectra detected for back side illumination is apparent in measurement. This feature could not be reproduced by simulations (solid lines) and its cause is not completely clarified. I suspect that either luminescence generated in domains away from the optical axis or scattered at a rough sample surface is coupled into the spectrometer at angles $\theta \gg 0$ and, eventually, impinges after diffraction on the camera at different locations as expected for a certain wavelength. As a consequence, such an off-axis signal could be falsely interpreted as the appearance of a spectral feature, which is actually absent.

5.4 Simulations and fundamentals

5.4.1 Simulating photoluminescence decays

In order to understand the experimental time-resolved photoluminescence findings, which are presented in the following, I will first cover some fundamentals regarding simulations of transient photoluminescence from single crystals. The assumption that the charge-carrier profile along the sample thickness is always constant at a given time after pulsed optical excitation (see Sec. 4.5) is not valid for "thick" samples anymore. Therefore, in the simulations I have to consider the individual charge-carrier concentrations $n(x, t)$ at each position x in the sample and at a given time t (or in vector notation $\mathbf{n}(t)$). Then the continuity equation reads in linear matrix notation

$$\frac{\partial \mathbf{n}}{\partial t} = \mathbf{G}^{\text{ext}}(t) + (\underline{T} - \underline{R} + \underline{G}^{\text{int}}) \mathbf{n}, \quad (5.1)$$

where $\mathbf{G}^{\text{ext}}(t)$ represents the generation vector due to pulsed excitation and is therefore limited to a short time only. Additionally, \underline{T} , \underline{R} and $\underline{G}^{\text{int}}$ are linear matrix operators for charge-carrier transport, recombination and internal generation, which affect the spatial charge-carrier concentration $\mathbf{n}(t)$ and are explained in Appendix A in more detail. Photoluminescence spectra contain information on the depth-dependent charge-carrier density as the sample will reabsorb its own emission. In case of an exponential (re-)absorption profile based on the Lambert-Beer law, the photoluminescence flux $\phi_{\text{PL}}(E, t)$ signal reads

$$\phi_{\text{PL,fsi}}(E, t) \propto \int_0^d \alpha(E) \phi_{\text{bb}}(E) n(x, t) p(x, t) \exp(-\alpha(E)x) dx \quad (5.2)$$

upon front side illumination and

$$\phi_{\text{PL,bsi}}(E, t) \propto \int_0^d \alpha(E) \phi_{\text{bb}}(E) n(x, t) p(x, t) \exp(-\alpha(E)(d-x)) dx \quad (5.3)$$

when photoluminescence has to traverse the entire crystal upon back side illumination before it can be detected. The only difference in the photon fluxes between

5 Time-resolved photoluminescence from single crystals

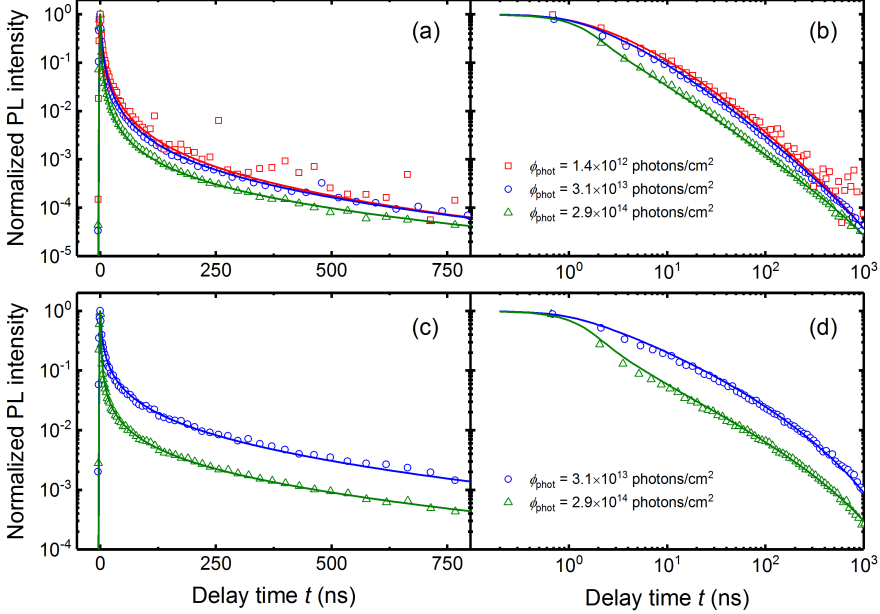


Figure 5.4: Normalized photoluminescence decays from measurements (open symbols) of a $\text{CH}_3\text{NH}_3\text{PbBr}_3$ single crystal for different applied photon densities ϕ_{phot} . Panels (a) and (b) represent the same time-resolved photoluminescence data recorded upon front side illumination on different scales, while panels (c) and (d) show the same photoluminescence data upon back side illumination, respectively. Simulated photoluminescence decays are indicated as solid lines.

front (Eq. 5.2) and back side illumination (Eq. 5.3) is a different exponent in the reabsorption term. As perovskite single crystals are found to be intrinsic semiconductors [192], I assume that hole $p(x)$ and electron concentrations $n(x)$ are equal at each position x and also that the hole μ_p and electron mobilities μ_n are similar $\mu = \mu_n = \mu_p$.

The transient photoluminescence signal $I_{\text{PL}}(t)$ can now be calculated by integrating the respective emitted photon flux $\phi_{\text{PL}}(E, t)$ over photon energy E . Figure 5.4 shows the normalized photoluminescence decays $I_{\text{PL, norm}}(t)$ obtained by measurement in open symbols as a function of time for different applied excitation densities ϕ_{phot} . Upon front side illumination (a, b), even for two orders of magnitude

Table 5.1: Transport and recombination parameters applied and derived from modeling transient photoluminescence data of a $\text{CH}_3\text{NH}_3\text{PbBr}_3$ perovskite single crystal.

Auger recombination coefficient C	$5.0 \times 10^{-28} \text{ cm}^6 \text{ s}^{-1}$
internal radiative recombination coefficient $k_{\text{rad}}^{\text{int}}$	$5.5 \times 10^{-11} \text{ cm}^3 \text{ s}^{-1}$
bulk Shockley-Read-Hall lifetime τ_{SRH}	$2.5 \mu\text{s}$
charge carrier mobility μ	$15 \text{ cm}^2 \text{ V}^{-1} \text{ s}^{-1}$
front surface recombination velocity S_{f}	6700 cm s^{-1}
back surface recombination velocity S_{r}	1100 cm s^{-1}
crystal thickness d	0.17 cm

difference in excitation density ϕ_{phot} , only a moderate change in decay behavior is found. All curves exhibit a strong initial decay (\sim three orders of magnitude decrease in normalized signal strength until $\sim 100 - 200$ ns) followed by a rather moderate decay. Transient photoluminescence data recorded upon back side illumination (c, d) show a more pronounced diversification of the recorded signals for different excitation densities. A good conformity between experiment and simulation can be achieved. Table 5.1 lists the parameters used in both simulations for front and back side illumination, respectively. From simulation, a charge-carrier mobility of $\mu = 15 \text{ cm}^2 \text{ V}^{-1} \text{ s}^{-1}$ is found. OOTP experiments performed by Hannes Hempel from Helmholtz Zentrum Berlin reveal a value of the combined electron and hole mobilities of $\Sigma\mu = 28 \text{ cm}^2 \text{ V}^{-1} \text{ s}^{-1}$. When assuming a balanced transport of electrons and holes, the mobility values from experiment and simulation are in good agreement. Consequently, time-resolved photoluminescence can also be applied as tool to estimate charge-carrier mobilities and surface recombination velocities in single crystals and thick films. In order to cover especially the different dynamic ranges of the photoluminescence transients upon front and back side illumination, different values of the surface recombination velocity have to be assumed at the front side ($S_{\text{f}} = 6700 \text{ cm/s}$) and the back side of the single crystal ($S_{\text{r}} = 1100 \text{ cm/s}$). During crystal growth from the liquid phase, the different surface orientations might be prone to the formation of defects to varying extent and could give rise to the observed difference in the recombination velocities between front and back side.

5 Time-resolved photoluminescence from single crystals

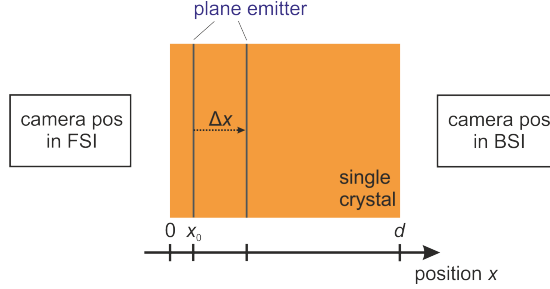


Figure 5.5: Illustration of a plane, which emits luminescence, moving inside a single crystal (thickness d) from its initial position x_0 by the distance Δx . In the chosen depiction, the two luminescence detection configurations, i. e. upon front (FSI) and back side illumination (BSI), are achieved here by different camera positions as indicated.

5.4.2 Simulating time-resolved spectral shifts

Let us now continue with discussing spectral photoluminescence changes over time in more detail. Due to the quadratic dependency on the charge-carrier concentration $n(x, t)$, the measured photoluminescence flux will predominantly originate from regions, where the charge-carrier concentrations are locally the highest (region is also denoted as charge-carrier front in the following) and surface-near regions. This charge-carrier front steadily moves towards the bulk due to diffusion. In the following, I discuss here a simplified approach that allows to explain spectral luminescence shifts. This approach is valid when recombination is assumed to be highly localized and limited in the following to only a single plane, which emits luminescence and acts as the charge-carrier front. Additionally, this emitter plane shall initially (at $t = 0$) be positioned at x_0 close to a surface and travel a distance of Δx towards the bulk after time t (see also Fig. 5.5). Changes in the luminescence intensity over time are neglected here for simplicity. With the notation depicted in Fig. 5.5, the photoluminescence spectrum upon front side illumination $\phi_{\text{PL,fsi}}(E, t)$ emitted by the plane located at position $x(t)$ is found to be

$$\phi_{\text{PL,fsi}}(E, t) \propto \alpha(E)\phi_{\text{bb}}(E)\exp(-\alpha(E)x(t)). \quad (5.4)$$

Upon back side illumination, only the exponential reabsorption term differs com-

pared to Eq. 5.4 and the corresponding photon flux $\phi_{\text{PL,bsi}}(E, x)$ becomes

$$\phi_{\text{PL,bsi}}(E, t) \propto \alpha(E)\phi_{\text{bb}}(E) \exp(-\alpha(E)(d - x(t))). \quad (5.5)$$

In order to calculate the spectral photoluminescence shift, the spectrum at time t (emitter plane has moved to position $x_0 + \Delta x(t)$) is normalized to the initial spectrum (emitter plane is located at x_0). Consequently, the following spectral shifts can be expected upon front side illumination

$$\begin{aligned} I_{\text{PL,norm,fsi}}(E, t) &= \frac{\phi_{\text{PL,fsi}}(E, x_0 + \Delta x(t))}{\phi_{\text{PL,fsi}}(E, x_0)} \propto \frac{\exp(-\alpha(E)(x_0 + \Delta x(t)))}{\exp(-\alpha(E)x_0)} \\ &\propto \exp(-\alpha(E)\Delta x(t)). \end{aligned} \quad (5.6)$$

Upon front side illumination, the internally emitted luminescence emitted has to cover an increasing distance ($x_0 + \Delta x(t)$) to the front surface over time before it can leave the crystal. At the same time, high energy photons are more likely to be reabsorbed by the crystal itself than low energy photons based on the different spectral values of the absorption coefficient $\alpha(E)$. Therefore, the high energy part of the recorded luminescence spectra is attenuated to a greater extent compared to the low energy part as charge carriers move into the bulk. The spectral trend upon back side illumination

$$\begin{aligned} I_{\text{PL,norm,bsi}}(E, t) &= \frac{\phi_{\text{PL,bsi}}(E, x_0 + \Delta x(t))}{\phi_{\text{PL,bsi}}(E, x_0)} \propto \frac{\exp(\alpha(E)(x_0 + \Delta x(t)))}{\exp(\alpha(E)x_0)} \\ &\propto \exp(\alpha(E)\Delta x(t)) \end{aligned} \quad (5.7)$$

is expected to be reversed as the reabsorption distance will in this configuration decrease over time ($d - x_0 - \Delta x(t)$) resulting in an apparent slower decay of high energy photons than low energy photons.

Apparently, the outcomes of Eq. 5.6 and Eq. 5.7 are each other reciprocals. In the range of low photon energies, when $\alpha(E)\Delta x \ll 1$, both $I_{\text{PL,norm,fsi}}$ and $I_{\text{PL,norm,bsi}}$ become 1 and in both cases no spectral changes are expected. At high photon energies ($\alpha(E)\Delta x > 1$), the expression for front side illumination tends towards zero leading to a strong attenuation of the photoluminescence intensity. On

the contrary, a reverse trend is expected for back side illumination as the expression tends now towards infinity resulting here in a high amplification of the photoluminescence intensity. Spectral photoluminescence shifts will therefore become apparent in the transition range between low and high photon energies and a reverse trend is expected among the two different luminescence measurement configurations.

5.5 Time-resolved photoluminescence spectra

5.5.1 Findings from modeling experimental data

First, I will discuss the findings for spectral photoluminescence changes over time. Figure 5.6 compares the normalized initial photoluminescence spectra (at $t = 0$; cycles) with the corresponding normalized spectra after an exemplary delay time of $t = 100$ ns (squares) for front side illumination (panel (a)) and back side illumination (panel (b)). While the spectrum upon front side illumination has clearly shifted towards lower photon energies over time, the two spectra upon back side illumination still resemble each other in shape. Figure 5.7, which displays the photoluminescence

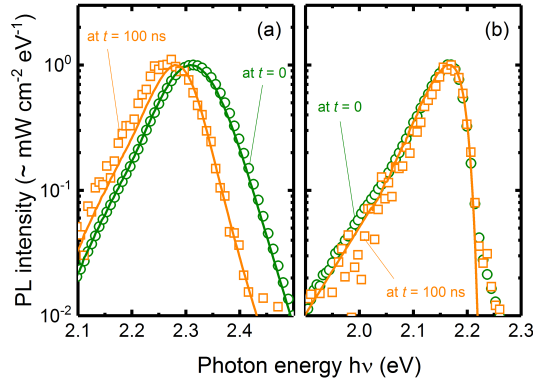


Figure 5.6: Normalized measured photoluminescence spectra at delay times of $t = 0$ (green cycles) and $t = 100$ ns (orange squares) upon (a) front side illumination and (b) back side illumination with a photon density of $\phi_{\text{phot}} = 2.9 \times 10^{14} \text{ cm}^{-2}$ each. Solid represent the respective simulated spectra.

5.5 Time-resolved photoluminescence spectra

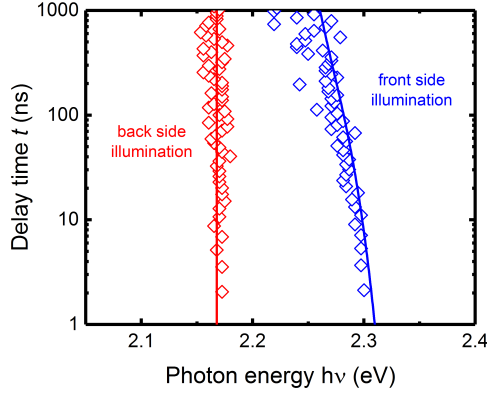


Figure 5.7: Spectral shift of the photoluminescence peak positions over time upon front side illumination (in blue) and back side illumination (in red) with a photon density of $\phi_{\text{phot}} = 2.9 \times 10^{14} \text{ cm}^{-2}$ each. Open symbols represent experimental data while solid lines indicate findings from simulations.

peak positions over time, shows only a spectral change upon front side illumination (blue diamonds) while no remarkable change is seen upon back side illumination (red diamonds). Furthermore, while the normalized decay dynamics at exemplary photon energies clearly differ from each other upon front side (see Fig. 5.8 (a): decay

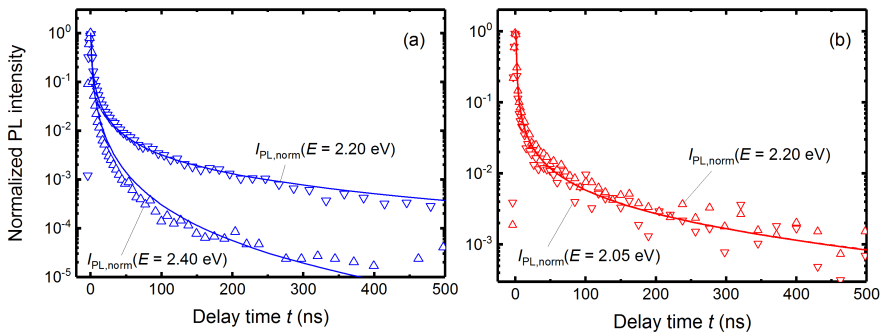


Figure 5.8: Normalized photoluminescence transients at exemplary photon energies as indicated upon (a) front side illumination and (b) back side illumination. Triangles represent the results from measurement and solid lines indicate simulations, respectively.

5 Time-resolved photoluminescence from single crystals

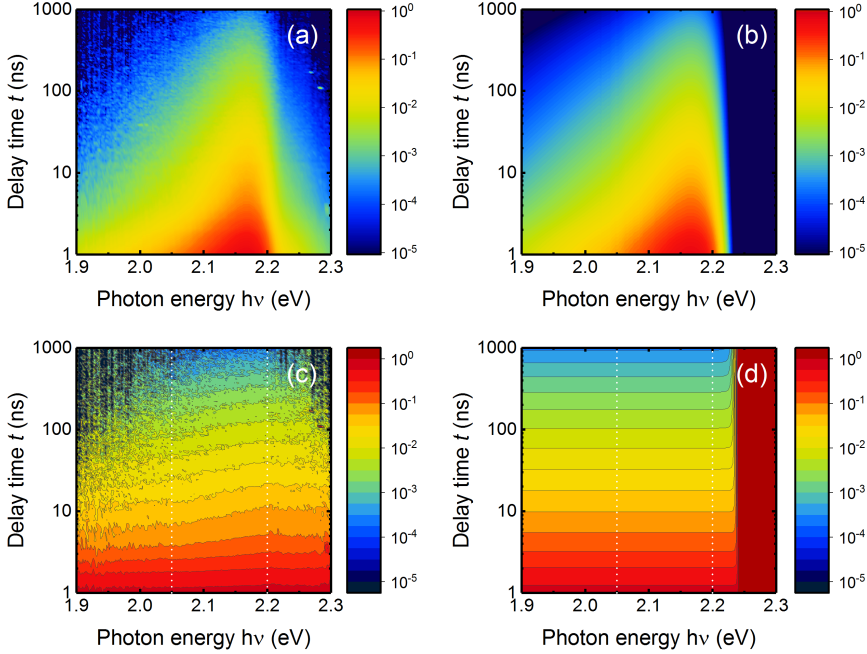


Figure 5.9: Differently normalized spectral photoluminescence decays of a perovskite single crystal illuminated by a photon density of $\phi_{\text{phot}} = 2.9 \times 10^{14} \text{ cm}^{-2}$ in **back side** measurement configuration. The depicted normalizations follow the same procedure as in Fig. 5.11: All data points in (a) and (b) are normalized to the peak value of the initial spectrum (at $t = 0$) exhibiting the highest intensity: $I_{\text{PL, norm}}(E, t) = \phi_{\text{PL}}(E, t) / \max(\phi_{\text{PL}}(E, 0))$. The data in (c) and (d) are spectrally normalized to the respective intensity values of the initial spectrum: $I_{\text{PL, norm}}(E, t) = \phi_{\text{PL}}(E, t) / \phi_{\text{PL}}(E, 0)$. The white dotted lines highlight the exemplary photoluminescence decays, which are presented in Fig. 5.8 (b), at the photon energies $E = 2.05 \text{ eV}$ and $E = 2.20 \text{ eV}$. Panel (a) and (c) are the data obtained from measurement, while panel (b) and (d) show the respective results from simulations.

of high energy photons is faster than for low energy photons), only slight differences in the decay dynamics at times $t \lesssim 200 \text{ ns}$ are seen upon back side illumination (Fig. 5.8 (b)).

The absence of a significant spectral shift upon back side illumination seems to be in contradiction to the prediction by the simplified theoretical approach from

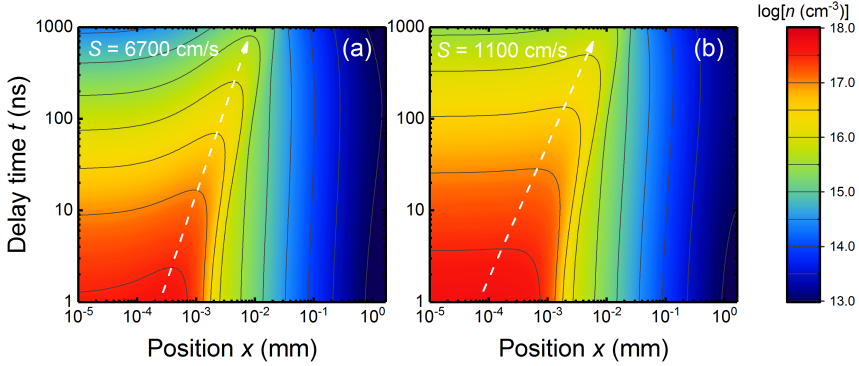


Figure 5.10: Simulated charge carrier profiles $n(x,t)$ within a perovskite single crystal as a function of time upon (a) front side illumination and (b) back side illumination, respectively. Please note that for better comparison the coordinate system in panel (b) has been changed that the position $x = 0$ indicates here the back side and $x = d$ the front side of the crystal. The white dashed arrows approximately mark the respective progression of the charge-carrier front, i. e. the highest spatial concentration over time. The applied values of the surface recombination velocity S differ at front side ($S_f = 6700$ cm/s) and back side ($S_r = 1100$ cm/s) in the simulations in order to fit the measured photoluminescence transients.

the previous Sec. 5.4. Figure 5.9, which shows the spectral photoluminescence decays of a $\text{CH}_3\text{NH}_3\text{PbBr}_3$ crystal illuminated with a photon density of $\phi_{\text{phot}} = 2.9 \times 10^{14} \text{ cm}^{-2}$ at the back side, helps to better understand the deviations. The upper row compares the spectral photoluminescence decays from experiment (panel (a)) and simulation (panel (b)). The data is normalized in both cases to the peak value of the initial spectrum (at $t = 0$), which exhibits the highest intensity ($I_{\text{PL, norm}}(E, t) = \phi_{\text{PL}}(E, t) / \max(\phi_{\text{PL}}(E, 0))$). Deviations are identified at high energy photons, which are discussed after having a closer look at the differently normalized spectral findings displayed in the lower row of Fig. 5.9. Panel (c) shows the measured spectral decays, which are normalized to the initial spectrum according to $I_{\text{PL, norm}}(E, t) = \phi_{\text{PL}}(E, t) / \phi_{\text{PL}}(E, 0)$, while panel (d) reveals the respective results from simulation based on Eq. 5.1 and 5.3. Mainly two energy regions with different spectral behavior are identified in simulations (see Fig. 5.9 (d)). For photons with energies $E \lesssim 2.22$ eV

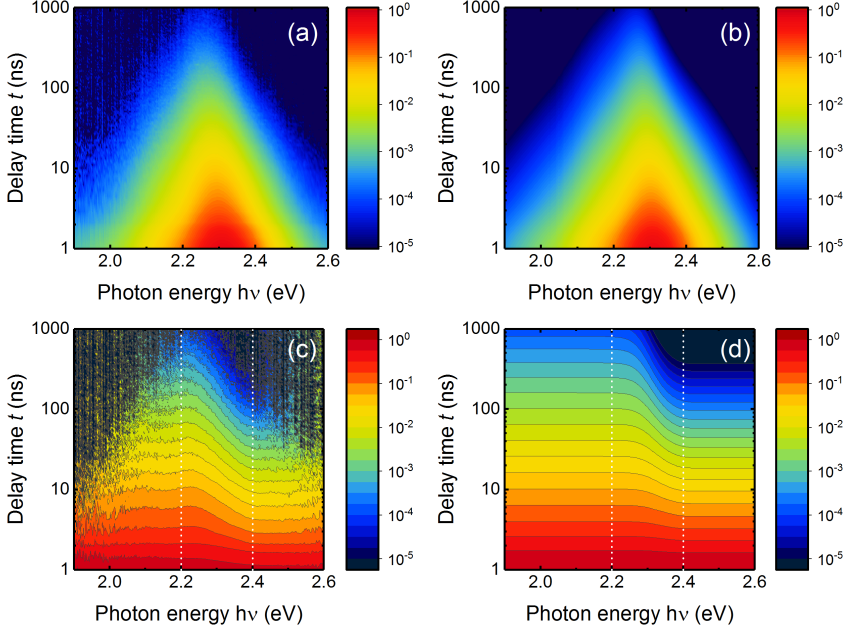


Figure 5.11: Differently normalized spectral photoluminescence decays of a perovskite single crystal illuminated by a photon density of $\phi_{\text{phot}} = 2.9 \times 10^{14} \text{ cm}^{-2}$ in **front side** measurement configuration. All data points in (a) and (b) are normalized to the peak value of the initial spectrum (at $t = 0$) exhibiting the highest intensity: $I_{\text{PL, norm}}(E, t) = \phi_{\text{PL}}(E, t) / \max(\phi_{\text{PL}}(E, 0))$. The data in (c) and (d) are spectrally normalized to the respective intensity values of the initial spectrum: $I_{\text{PL, norm}}(E, t) = \phi_{\text{PL}}(E, t) / \phi_{\text{PL}}(E, 0)$. The white dotted lines highlight the exemplary photoluminescence decays, which are presented in Fig. 5.8 (a), at the photon energies $E = 2.20 \text{ eV}$ and $E = 2.40 \text{ eV}$. Panel (a) and (c) are the data obtained from measurement, while panel (b) and (d) show the respective results from simulations.

no spectral shift is observed (horizontal colored bars), while for photon energies $E \gtrsim 2.24 \text{ eV}$ the normalized photoluminescence intensity first even increases by a factor of about 20 until a delay time of $t \approx 250 \text{ ns}$, before it starts to decrease again but still stays above 1 during the entire simulation. Please note that the color code in Fig. 5.9 is limited to display a maximum value of 1. Strong spectral changes will only occur within the small energy interval $2.22 \text{ eV} \lesssim E \lesssim 2.24 \text{ eV}$. Consequently, the

5.5 Time-resolved photoluminescence spectra

simulation follows in principle the proposed spectral trend of the simplified approach in Sec. 5.4 upon back side illumination, i. e. $\propto \exp(\alpha(E)\Delta x)$. Consequently, the spectral shift becomes relevant at high values of the absorption coefficient $\alpha(E)$, but the photoluminescence signal at high photon energies can hardly be detected upon back side illumination because of efficient reabsorption. In contrast for low values of $\alpha(E)$ (i. e. low energy photons), photoluminescence is detectable, but no spectral shift will appear as $\alpha(E)\Delta x \rightarrow 0$. However, photon recycling within the single crystal will amplify the formation of any spectral shift (see also Sec. 5.5.2.3). Vast domains in the bulk are slightly populated with charge carriers by photon recycling. One effect thereof is that especially the high energy edge of the spectra, where the photoluminescence intensities are initially extremely low, becomes significantly intensified over time as seen in Fig. 5.9 (d). Please note that in this spectral region, the photoluminescence intensities will be still too low (less than 10^{-5} of the photoluminescence peak value, see Fig. 5.9 (b)) to be detected in experiment. Another consequence of photon recycling in very thick samples is that it extremely narrows down the energy interval of the resulting strong spectral shift (here: $2.22 \text{ eV} \lesssim E \lesssim 2.24 \text{ eV}$). However, already the narrow spectral shift occurs at too low photoluminescence intensities in order to be able to be adequately measured in experiment. As already discussed in Sec. 5.3, an overlaying high photon energy shoulder is detected in experiments upon back side illumination (see also Fig. 5.9 (a)), which is assumed to originate from scattered light. Thus, this presumable artifact masks the spectral shift observed in simulations and as a result no significant spectral changes are observed in experiment upon back side illumination (see Fig. 5.9 (c)).

The respective spectral findings upon front side illumination are presented in Fig. 5.11. As expected in Sec. 5.4, a pronounced spectral shift upon front side illumination is found by experiment (see panel (c)), which can accurately be modeled (see panel (d)). The higher value of the surface recombination velocity at the front side with $S_f = 6700 \text{ cm/s}$ causes a more efficient capture with subsequent non-radiative recombination of charge carriers at the front surface than at the back surface of the sample upon back side illumination ($S_b = 1100 \text{ cm/s}$) and, consequently, upon front side illumination, a more pronounced charge-carrier front establishes as seen in Fig. 5.10 (a) and, thus, a distinct spectral shift is observed. Different values for the

5 Time-resolved photoluminescence from single crystals

surface recombination velocities S_f and S_b arise as a result of modeling all measured photoluminescence transients upon front as well as back side illumination with the same set of bulk recombination parameters.

In the following sections, possible influences on the formation and severity of the spectral shift like the surface recombination velocity S , the charge-carrier mobility μ and the occurrence of photon recycling are discussed.

5.5.2 Impacts on spectral time-resolved photoluminescence and transients

Beside the diverse bulk recombination mechanisms, this section covers how surface recombination, charge-carrier mobility and photon recycling affect the characteristic of the spectral photoluminescence shift but also influence the shape of photoluminescence transients.

5.5.2.1 Surface recombination

Figure 5.12 depicts the simulated charge-carrier concentrations as a function of space and time for the highest applied photon density of $\phi_{\text{phot}} = 2.9 \times 10^{14}$ photons/cm² exemplarily for different surface recombination velocities of (a) $S = 0$ cm/s, (b)

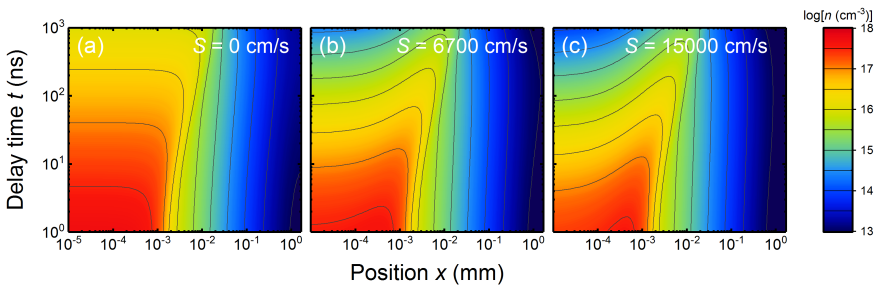


Figure 5.12: Comparison of simulated charge carrier profiles $n(x,t)$ within a perovskite single crystal for different surface recombination velocities: (a) $S = 0$ cm/s, (b) $S = 6700$ cm/s and (c) $S = 15000$ cm/s. All simulations were carried out for a charge-carrier mobility of $\mu = 15$ cm²/(Vs).

5.5 Time-resolved photoluminescence spectra

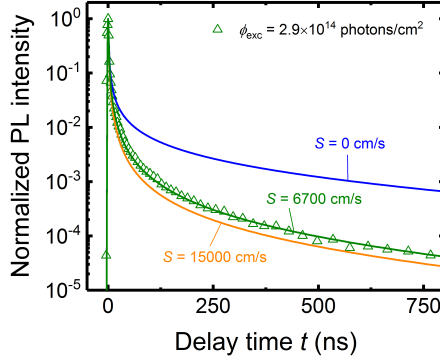


Figure 5.13: Comparison of simulated transient photoluminescence decays for different surface recombination velocities $S = 0$ cm/s (blue line), $S = 6700$ cm/s (green line) and $S = 15000$ cm/s (orange line).

$S = 6700$ cm/s and (c) $S = 15000$ cm/s. The value of the charge-carrier mobility is fixed to $\mu = 15$ cm²/(Vs) and the same bulk recombination parameters (displayed in Tab. 5.1) are used in all simulations. When surface defects exhibit lower capture and non-radiative annihilation rates of charge carriers than in the bulk (see panel (a) for $S = 0$ cm/s), a homogeneous carrier profile starts to form at the surface-near region. Obviously, charge-carrier diffusion and high-order bulk recombination mechanisms (Auger and radiative recombination) reshapes the initial exponential carrier profile photo-generated by Lambert-Beer absorption efficiently at already very short times. The span of the homogeneous distribution starts to extend towards the bulk over time driven by diffusion. With a more severe amount of surface-near defects and higher values of the recombination velocity, the continuous non-radiative surface recombination pulls the concentration $n(t)$ near the surface faster down than in the bulk (see panels (b) and (c)). As a consequence, a charge-carrier front (globally highest charge-carrier concentration at a given time) establishes and continuously moves away from the surface and into the bulk over time mainly due to diffusion. Photon recycling shows no significant impact on the progression of the charge-carrier front as later revealed in Sec. 5.5.2.3.

With a high value of the surface recombination velocity, charge carriers are also

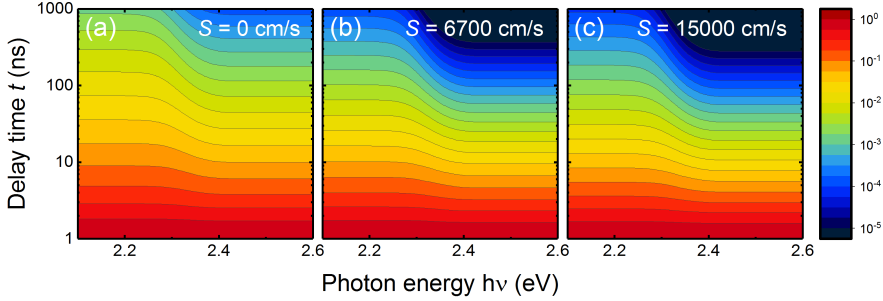


Figure 5.14: Comparison of simulated, normalized spectral photoluminescence decays $I_{\text{PL,norm}}(E, t) = \phi_{\text{PL}}(E, t)/\phi_{\text{PL}}(E, 0)$ upon front side illumination for different surface recombination velocities: (a) $S_f = 0$ cm/s, (b) $S_f = 6700$ cm/s and (c) $S_f = 15000$ cm/s. All simulations were carried out for a charge-carrier mobility of $\mu = 15$ cm²/(Vs).

more efficiently extracted from the bulk and captured at the surface. Consequently, the charge-carrier concentration at the surface but also in the bulk decreases more rapidly. According to Eq. 5.2 and 5.3, the strength of the transient photoluminescence signals depends quadratically on the spatial and temporal charge-carrier concentration values $n(x, t)$. Surface recombination affects therefore the dynamic

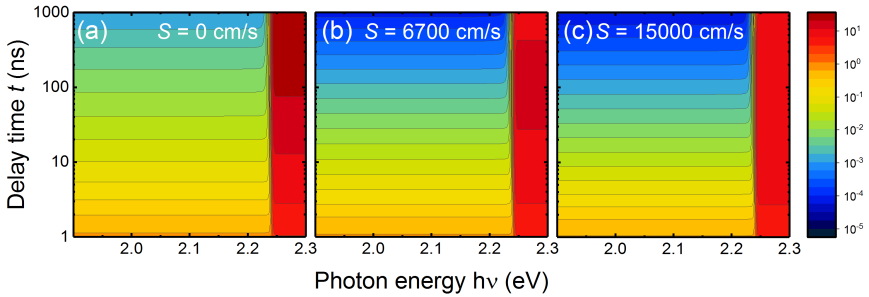


Figure 5.15: Comparison of simulated, normalized spectral photoluminescence decays $I_{\text{PL,norm}}(E, t) = \phi_{\text{PL}}(E, t)/\phi_{\text{PL}}(E, 0)$ upon back side illumination for different surface recombination velocities: (a) $S_b = 0$ cm/s, (b) $S_b = 6700$ cm/s and (c) $S_b = 15000$ cm/s. All simulations were carried out for a charge-carrier mobility of $\mu = 15$ cm²/(Vs). Please note that the scale of the color bar is here slightly different compared to other similar figures in order to illustrate normalized intensities exceeding 1 in this particular figure.

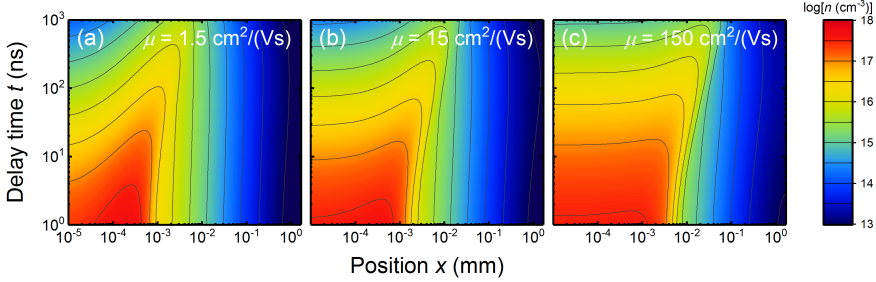


Figure 5.16: Comparison of simulated charge carrier profiles $n(x,t)$ within a perovskite single crystal for different charge-carrier mobilities: (a) $\mu = 1.5 \text{ cm}^2/(\text{Vs})$, (b) $\mu = 15 \text{ cm}^2/(\text{Vs})$ and (c) $\mu = 150 \text{ cm}^2/(\text{Vs})$. All simulations were carried out for a surface recombination velocity of $S = 6700 \text{ cm/s}$.

range of the time-resolved photoluminescence decays as seen in Fig. 5.13 exemplarily upon front side illumination. The simulated spectral decays upon front side illumination for different surface recombination velocities are presented in Fig. 5.14. With increasing S -values, the photoluminescence intensity at all photon energies decays faster and independent of the photon energy. Upon back side illumination, the surface recombination velocity does also not significantly affect spectral shifts as displayed in Fig. 5.15. For higher values of the surface recombination velocity, the decay at low photon energies $E < 2.24 \text{ eV}$ becomes faster while the effective intensity increase at high photon energies $E > 2.24 \text{ eV}$ becomes less pronounced. Please note that the scale of the color bar is adapted here in order to display also changes for normalized intensities above 1. Overall, surface recombination does not impact the formation and characteristic of spectral photoluminescence shifts. The following section will show that charge-carrier transport and the progression of the charge-carrier front are the main drivers for observing spectral shifts in the luminescence.

5.5.2.2 Charge-carrier mobility

In this section, the impact of charge-carrier mobility on photoluminescence transients and spectral shifts is revealed. Figure 5.16 shows the simulated charge-carrier profiles $n(x,t)$ for different charge-carrier mobilities (a) $\mu = 1.5 \text{ cm}^2/(\text{Vs})$, (b) $\mu = 15 \text{ cm}^2/(\text{Vs})$ and (c) $\mu = 150 \text{ cm}^2/(\text{Vs})$, while the same surface recombina-

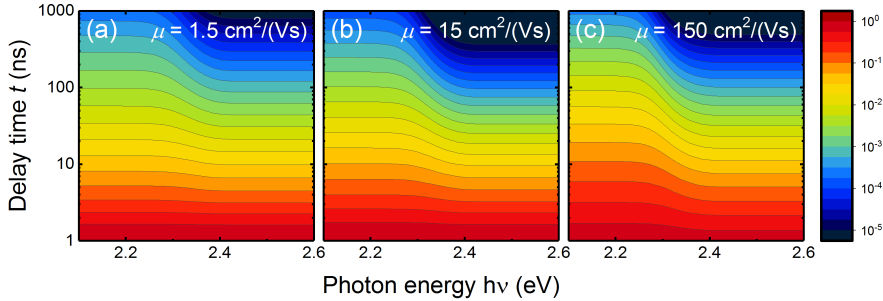


Figure 5.17: Comparison of simulated, normalized spectral photoluminescence decays $I_{\text{PL, norm}}(E, t) = \phi_{\text{PL}}(E, t)/\phi_{\text{PL}}(E, 0)$ upon front side illumination for different charge-carrier mobilities: (a) $\mu = 1.5 \text{ cm}^2/(\text{Vs})$, (b) $\mu = 15 \text{ cm}^2/(\text{Vs})$ and (c) $\mu = 150 \text{ cm}^2/(\text{Vs})$. Spectral differences in the decay dynamics become more pronounced with increasing value of the charge-carrier mobility. All simulations were carried out for a surface recombination velocity of $S_f = 6700 \text{ cm/s}$.

tion velocity of $S = 6700 \text{ cm/s}$ and the same set of bulk recombination parameters (see Tab. 5.1) are applied in the simulations. The progression of the charge-carrier front is obviously linked to the magnitude of the charge-carrier mobility μ . Furthermore, the less mobile charge carriers are, the more efficiently they are captured by surface defects already at short times. Thus, the charge-carrier concentration near the surface is heavily drawn down for low mobilities (see panel (a)). Under these circumstances, the internal emission is highly localized at the temporal position of the charge-carrier front. On the contrary for high charge-carrier mobilities, the influence of surface defects on the profile shape becomes less severe and a rather homogeneous charge-carrier profile will quickly establish and act as a broad source of internal radiation (see panel (c)).

Based on the simulated charge-carrier profiles $n(x, t)$ seen in Fig. 5.16, the spectral shifts in the photoluminescence decays depicted in Fig. 5.17 for front side illumination can be better understood. The strength of the decay for high energy photons is determined by the time-dependent charge-carrier concentrations located near the surface because of strong reabsorption due to high values of the absorption coefficient. Low energy photons on the other hand can be collected from significantly larger depths inside the crystal as they are less likely reabsorbed. Thus, the

5.5 Time-resolved photoluminescence spectra

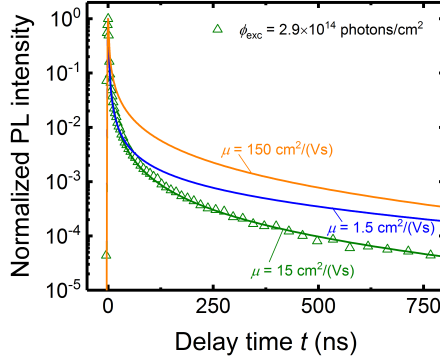


Figure 5.18: Comparison of simulated transient photoluminescence decays for different charge-carrier mobilities $\mu = 1.5 \text{ cm}^2/(\text{Vs})$ (blue line), $\mu = 15 \text{ cm}^2/(\text{Vs})$ (green line) and $\mu = 150 \text{ cm}^2/(\text{Vs})$ (orange line).

decay for low energy photons depends on the magnitude of charge-carrier concentrations throughout the crystal. With increasing value of the charge-carrier mobility, the spectral shift in decay dynamics becomes more pronounced as charge carriers are able to migrate deeper into the crystal and reabsorption effects become more significant. Especially the low energy part ($E \lesssim 2.25 \text{ eV}$) of the spectral luminescence decay is affected by varying the mobility values. Panel (a) with the lowest mobility is highly influenced by surface recombination. At very short times, the rather immobile carriers are already efficiently captured at the surface, where they annihilate. Thus, a strong initial decay for both the high and low energy photons is found. Eventually, some carriers still manage to escape the drain area near the surface and the decay becomes moderate at later times. A pronounced charge-carrier front establishes which only slowly moves towards the bulk (see Fig. 5.16 (a)) and charge carriers predominantly recombine by bulk recombination events. The slow progression of the carrier front into the bulk implies that internally emitted photons have to pass only a slightly larger distance before they are coupled out of the crystal. Consequently, the normalized spectral decay for high energy photons is actually moderate for a low value of the charge-carrier mobility compared to higher values. Spectral differences in the photoluminescence decay upon front side illumination are a result of increasing reabsorption distances over time. Hence, low charge-carrier

5 Time-resolved photoluminescence from single crystals

mobilities cause less pronounced spectral luminescence shifts than higher mobilities. Considering the moderate value of the mobility ($\mu = 15 \text{ cm}^2/(\text{Vs})$) in panel (b), carriers are rather homogeneously distributed over a wider distance but the dip in the carrier profiles due to heavy carrier loss at the surface is not fully compensated yet. The distinct delocalization of carriers causes here a slower decay of the low energy photoluminescence part and at the same time a faster decay of the high energy part. For the highest investigated charge-carrier mobility $\mu = 150 \text{ cm}^2/(\text{Vs})$ (see panel (c) in Fig. 5.16 and 5.17), the charge carrier profile at short times is already rather flat compared to the initial exponential profile due to quick redistribution. Furthermore, carriers are widely spread. As a consequence, the normalized decay at low photon energies is most attenuated for the highest mobility. The severe carrier depletion at the surface due to surface recombination is now inhibited by a fast compensation of highly mobile carriers from the bulk. Remarkably, the relatively persistent, homogeneous charge-carrier distribution near the surface leads to the situation that the high energy part of the normalized luminescence decays actually a bit slower than for the moderate mobility value. Overall, the normalized spectral decay dynamics still show the most deviation for the highest mobility due to the widely and homogeneously distributed charge carriers.

With the above findings, differences in the time-resolved photoluminescence decays simulated for different charge-carrier mobilities can be better understood. Figure 5.18 shows the respective normalized photoluminescence transients simulated for front side illumination and the highest applied photon density of $\phi_{\text{exc}} = 2.9 \times 10^{14} \text{ photons/cm}^2$ for charge-carrier mobilities of $\mu = 1.5 \text{ cm}^2/(\text{Vs})$ (blue line), $\mu = 15 \text{ cm}^2/(\text{Vs})$ (green line) and $\mu = 150 \text{ cm}^2/(\text{Vs})$ (orange line). Apparently, the charge-carrier mobility can significantly modify the long- and short-term decay. A strong initial decay is found for the lowest mobility due to surface recombination and also high order recombination events. Due to the low mobility, charge carriers will not quickly redistribute and local high concentrations are consequently extremely prone to high-order recombination mechanisms like Auger and radiative recombination. Eventually, these previous high concentrations will be significantly reduced in a short time. Additionally, a protected region establishes where charge carriers are beyond the reach of surface defects. These protected carriers are only reduced by bulk recombination processes. Thus, the observed stable long-term photoluminescence

5.5 Time-resolved photoluminescence spectra

decay (blue line) is only shaped by bulk Shockley-Read-Hall recombination. The photoluminescence transient for the moderate mobility of $\mu = 15 \text{ cm}^2/(\text{Vs})$ shows a similar decay at short times as for the lowest mobility; i. e. a high impact by high order mechanisms as well as surface recombination. However, an ongoing surface recombination current evolves as a result of the higher charge-carrier mobility which leads to a faster photoluminescence decay at long times because trap-assisted recombination at the surface is more severe than in the bulk.

In summary, charge-carrier mobility has an crucial impact on the short- and long-term characteristics of photoluminescence decays from perovskite single crystals. The normalized decay for the medium value of the mobility (green line) shows the fastest decay. Considering now the findings for the highest mobility of $\mu = 150 \text{ cm}^2/(\text{Vs})$, the corresponding normalized photoluminescence transient shows the weakest short-term decay. The fast flattening of the initial high charge-carrier concentrations near the surface and the redistribution over a wide distance reduces the otherwise high impact of high order recombination mechanisms at short times. The long-term decay is again dominated by an ongoing non-radiative recombination at the surface.

5.5.2.3 Photon recycling

Lastly, the effect of reabsorption in single perovskite crystals is investigated in more detail. Figure 5.19 (a) and (b) show the comparison of the simulated charge-carrier profiles $n(x, t)$ when considering photon recycling and neglecting it, respectively. Apparently, photon recycling does not significantly affect the progression of the charge-carrier front (marked as white dashed arrows) within the single crystal. Therefore, diffusion is identified as the main driver of charge-carrier transport in the investigated $\text{CH}_3\text{NH}_3\text{PbBr}_3$ single perovskite crystal.

To investigate photon recycling regarding its effect of carrier transportation, a self absorption length L_{PR} is introduced as the mean distance between the position of a radiative recombination event and the position of its reabsorption event. Therefore, L_{PR} acts basically as a measure for the distance a charge-carrier has "traveled" after an average photon was reabsorbed. For practical reasons, the inverted absorption coefficient $\alpha^{-1}(E)$, which marks the distance at which the spectral luminescence

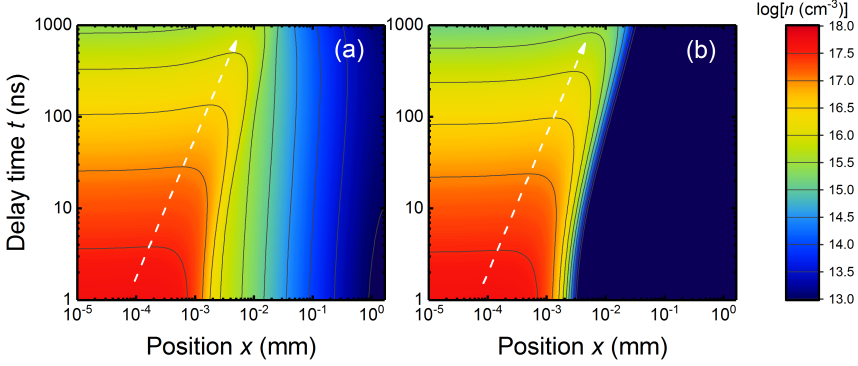


Figure 5.19: Simulated charge-carrier profiles $n(x,t)$ within a perovskite single crystal as a function of time. While panel (a) includes photon recycling, panel (b) neglects reabsorption but apart from that applies the same recombination conditions as in panel (a). The white dashed arrows approximately mark the respective progression of the charge-carrier front, i. e. the highest spatial concentration over time.

intensity drops to e^{-1} of its initial value, is used to compute the self absorption length L_{PR} . Furthermore, I consider emission into the solid angle 2π of a half space and weight $\alpha^{-1}(E)$ with the photon distribution $\alpha(E)\phi_{\text{bb}}(E)$. Projecting the three-dimensional emission on the x -axis results in

$$\begin{aligned}
 L_{\text{PR}} &= \frac{\int_0^{2\pi} d\varphi \int_0^{\pi/2} \sin(\theta) \cos(\theta) d\theta \int_0^\infty \alpha(E)\phi_{\text{bb}}(E) dE}{2\pi \int_0^\infty \alpha^2(E)\phi_{\text{bb}}(E) dE} \\
 &= \frac{\int_0^\infty \alpha(E)\phi_{\text{bb}}(E) dE}{2 \int_0^\infty \alpha^2(E)\phi_{\text{bb}}(E) dE} \approx 1.1\mu\text{m}.
 \end{aligned} \tag{5.8}$$

With the absorption coefficient shown in Fig. 5.3 (b), the self absorption length is found to be $L_{\text{PR}} \approx 1.1\mu\text{m}$. Compared to the crystal dimensions, photons are basically reabsorbed in the vicinity of their recombination location. An arbitrary diffusive charge carrier can cover the distance of $1.1\mu\text{m}$ on average in about 30 ns for a mobility of $\mu = 15 \text{ cm}^2/(\text{Vs})$. If I take this time period as the radiative life-

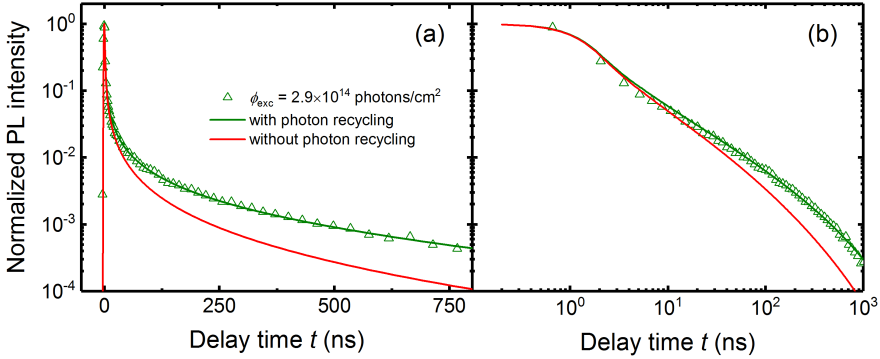


Figure 5.20: Comparison of the normalized photoluminescence transients simulated with the effect of photon recycling (green line) and without photon recycling (red line), while all other recombination and transport properties are kept the same for both simulations. The green open triangles represent the transient data from measurement under back side illumination. Panel (a) shows the same data as in panel (b) but on different scales.

time, it corresponds to a charge-carrier concentration of $n \approx 6 \times 10^{17} \text{ cm}^{-3}$ based on the revealed internal radiative recombination coefficient $k_{\text{rad}}^{\text{int}} = 5.5 \times 10^{-11} \text{ cm}^3 \text{ s}^{-1}$. Thus, for concentrations above this limit, the radiative lifetime will be shorter than 30 ns and photon recycling will be the faster transport phenomena while for lower concentrations, diffusion will provide a more efficient way of carrier transportation. In Fig. 5.19 (a), the concentration has dropped down to $n \approx 6 \times 10^{17} \text{ cm}^{-3}$ already after 3 ns due to strong surface recombination and high order recombination mechanisms like Auger and radiative recombination itself. Except for very short times, charge-carrier diffusion surpasses photon recycling as the dominant transport mechanism in single crystals in the course of the transient measurement. Consequently, photon recycling does not affect the progression of the charge-carrier front significantly in materials providing a sharp absorption onset and adequately mobile charge carriers. The dominant effect of photon recycling in single crystals is to "preserve" the local charge-carrier concentration by reabsorbing photons in the vicinity of the location where the radiative recombination event took place. Seemingly when taking photon recycling into account, a lower recombination rate is perceived. Thus, the photoluminescence signal will decay slower as seen by the comparison of the respec-

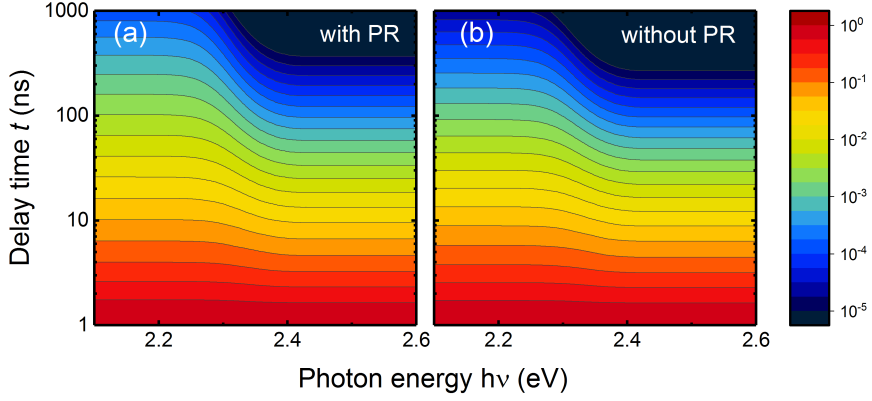


Figure 5.21: Comparison of simulated, normalized spectral photoluminescence decays $I_{\text{PL, norm}}(E, t) = \phi_{\text{PL}}(E, t)/\phi_{\text{PL}}(E, 0)$ upon front side illumination for a charge-carrier mobility of $\mu = 15 \text{ cm}^2/(\text{Vs})$ and a surface recombination velocity of $S = 6700 \text{ cm/s}$. Panel (a) shows the findings from simulations when taking photon recycling (PR) into account. Photon recycling is neglected in the simulation of panel (b).

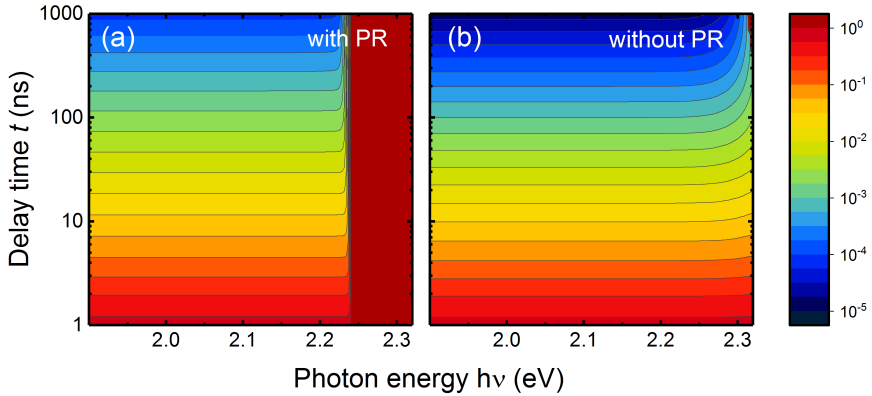


Figure 5.22: Comparison of simulated, normalized spectral photoluminescence decays $I_{\text{PL, norm}}(E, t) = \phi_{\text{PL}}(E, t)/\phi_{\text{PL}}(E, 0)$ upon back side illumination for a charge-carrier mobility of $\mu = 15 \text{ cm}^2/(\text{Vs})$ and a surface recombination velocity of $S_b = 6700 \text{ cm/s}$. Panel (a) shows the findings from simulations when taking photon recycling (PR) into account. Photon recycling is neglected in the simulation of panel (b).

tive simulations in Fig. 5.20 including photon recycling (green line) and neglecting photon recycling (red line).

When comparing the spectral photoluminescence decays with and without the impact of photon recycling, only a slightly stronger spectral shift upon front side illumination is found when photon recycling is taken into account as Fig. 5.21 shows. The simulation with photon recycling (panel (a)) indicates that the decays are consistently slower over the spectral range than without photon recycling (panel (b)), which is in agreement to the previous discussed preservation effect by photon recycling. Upon back side illumination, the spectral photoluminescence shifts clearly differ when photon recycling is switched on or off in the simulations (see also explanations in Sec. 5.5.1). When taking photon recycling into account (see Fig. 5.22), vast domains at the opposite side of the crystal (at positions $x \gtrsim 10 \mu\text{m}$) become slightly populated already at short times by charge carriers based on self-absorption of these low energy photons. This carrier population in the bulk is even quite stable over time because its concentration is quite low and, consequently, also the recombination rates are low, too. The charge carrier concentration in the bulk is also too low to significantly alter the overall measured luminescence signal. However, in the transmission configuration (back side illumination), these carriers cause a significant difference in the simulated spectral shifts. In simulations including the effects of photon recycling, the increased bulk carrier concentrations cause an increased normalized photoluminescence signal at high photon energies over time. Furthermore, photon recycling shifts the onset of the spectral shift towards lower photon energies. It is mentioned here once more, that the spectral luminescence shift upon back side illumination is expected at very high photon energies where the initial photoluminescence intensities are already extremely low due to efficient reabsorption and cannot be detected anymore. Additionally, photon recycling causes a stronger spectral shift over a smaller energetic transition range. Without the impact of photon recycling, carriers can populate the bulk only by diffusion over time. As this process is significantly slower than with the support by photon recycling, the spectral shift starts to establish at later times. Moreover, the shift without photon recycling is rather moderate over a larger photon energy range and also occurs at higher photon energies.

5 Time-resolved photoluminescence from single crystals

In conclusion, spectral changes observed during the photoluminescence measurements are a result of charge-carrier diffusion, because the reabsorption characteristics change over time as the emission zone gradually expands into the bulk over time. Photon recycling modifies slightly the shape of the charge-carrier profile but shows minor impact on the migration of the charge-carrier front, which is identified as the main contributor to the overall photoluminescence intensity when strong surface recombination is present. The dominant feature of photon recycling in thick single crystals is an enhancement of the apparent charge-carrier lifetime that slows down photoluminescence decay dynamics. Due to the sharp absorption onset, photon recycling is not considered to be an efficient charge-carrier transport mechanism in thick perovskite crystals. However, for a reduced crystal thickness and low values of the charge-carrier mobility, carrier transportation by photon recycling will become more important.

6 Photon recycling investigated by time-resolved photoluminescence

As discussed in Sec. 4.3, reabsorption of originally emitted photons in the course of radiative recombination is denoted as photon recycling and implies a prolonged radiative recombination rate. In this chapter, I demonstrate that photon recycling probabilities and, consequently, radiative decay rates in perovskite thin films can be controlled by the optical design of samples alone. Furthermore, I identify a severe limitation of the radiative efficiency, which in turn will reduce the maximum attainable efficiency of perovskite solar cells.

6.1 Introduction

In Sec. 4.3, I have shown that photon recycling modifies the obtained radiative recombination rate in organic inorganic perovskite thin films. As I can manipulate the amount of photon recycling in the films by control over the optical design of a chosen layer structure, differences in recombination kinetics should be observed. To quantify the impact by photon recycling, I model photoluminescence decays and perform optical simulations. These findings allow me to draw more detailed conclusions about fundamental radiative recombination processes. By comparing differently designed samples, I reveal a severe non-radiative bimolecular recombination channel. Its existence becomes essential when evaluating the photovoltaic potential of organic inorganic perovskites.

First, I will introduce the applied sample designs and discuss the observed morphology of the perovskite top layers. After analyzing the transient photoluminescence decay curves, I present optical simulations, which help me to determine

the different photon probabilities and, finally, the radiative fraction of bimolecular recombination.

6.2 Experimental design

In order to investigate reabsorption phenomena of varying degree by time-resolved photoluminescence, I applied the following layer stacks: silicon dioxide layers of distinct thicknesses (2.3 nm and 200 nm, respectively) were thermally grown on crystalline silicon wafers and perovskite layers were formed on top following the procedure described in Sec. 3.4.1. The experimental design of the stacks is shown in Fig. 6.1. The low refractive 200 nm-thick SiO₂ layer causes total internal reflection of the photoluminescence in the high refractive perovskite film (corresponding refractive indices in the energy range $\sim (1.4 - 1.9)$ eV of photoluminescence: $n_{r,\text{SiO}_2} \approx 1.5$ [97], $n_{r,\text{pero}} \approx 2.6$, see Fig. 4.6). Based on Snells' law, a critical angle θ_c of total internal reflection at the interface of a high refractive medium $n_{r,1}$ towards a lower refractive medium $n_{r,2}$ is given by

$$\theta_c = \arcsin \frac{n_{r,2}}{n_{r,1}}. \quad (6.1)$$

Only photons which are emitted under angles $\theta < \theta_c \approx 35^\circ$ can leave the absorber layer through the escape cone (red circular segment in Fig. 6.1 (a)) via the SiO₂ film and are parasitically absorbed when eventually entering the adjacent c-Si wafer. The corresponding solid angle Ω_c is derived as

$$\Omega_c = \int_0^{2\pi} \int_0^{\theta_c} \sin \theta \, d\theta \, d\varphi = 2\pi(1 - \cos \theta_c). \quad (6.2)$$

On the contrary, photons emitted under angles $\theta > \theta_c \approx 35^\circ$ will never leave the absorber layer because total internal reflection at each interface keeps the photons trapped inside the perovskite film, where they are eventually reabsorbed. Such waveguide modes have been observed in similar stack designs [193].

The optical conditions inside the stack change significantly when reducing the SiO₂ thickness from 200 nm to 2.3 nm. Specular light reflection at the perovskite/SiO₂ interface is strongly suppressed in the case of the 2.3 nm-thin SiO₂ layer due to

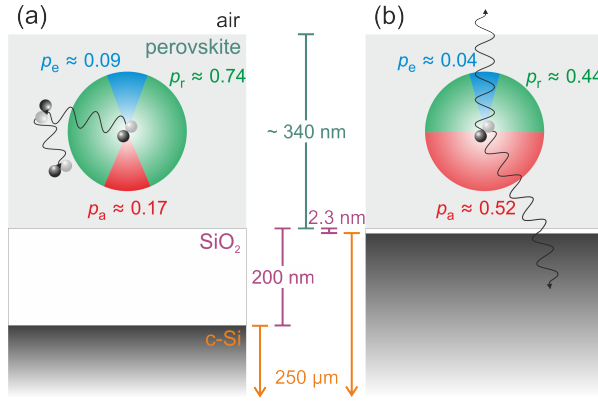


Figure 6.1: Schematic depiction of the experimental stack designs that enable manipulation of reabsorption by modifying parasitic absorption. Isotropic photon emission arising from radiative electron-hole annihilation inside the perovskite layers is indicated as a circle. The colored circular segments illustrate various emission cones, which facilitate photon outcoupling (blue), parasitic photon absorption (red) by entering the crystalline silicon wafer, and photon reabsorption (green), respectively. By significantly changing the thickness of the low-refractive silicon dioxide layer embedded between perovskite and c-Si from 200 nm in (a) to 2.3 nm in (b), the probabilities of parasitic absorption (p_a), outcoupling (p_e), as well as photon recycling (p_r) are tuned. The corresponding values derived from optical simulations are stated. Reprinted with permission from [190]. Copyright 2017 American Chemical Society.

evanescent light coupling. Consequently, luminescence is efficiently coupled into the high-refractive Si wafer ($n_{r,\text{Si}} \approx 3.7$ [97]), where photons are parasitically absorbed. I depend on a thin residual layer of SiO₂ in order to achieve sufficient wetting of the substrate by the perovskite precursor solution. Bare silicon substrates are not applicable for the formation of solution-processed perovskites due to inadequate adhesion. Additionally, an electrically insulating SiO₂ interlayer prevents charge transfer from perovskite into silicon. Charge quenching and transfer processes are difficult to disentangle from recombination kinetics [194–197] and would unnecessarily hamper the analysis of photoluminescence transients in the present case. Furthermore, as SiO₂ is employed as substrate for the growth of perovskite in both stack designs, the formation of crystalline perovskite with comparable quality can be achieved, as

6 Photon recycling investigated by time-resolved photoluminescence

I will confirm in the following Sec. 6.3 and 6.4. Thus in the case of the 2.3 nm-thin SiO₂ layer, parasitic absorption applies to roughly most photons emitted into the hemisphere pointing towards the silicon wafer (see Fig. 6.1 (b)). Therefore, I expect significant differences in the probabilities p_a of parasitic absorption between the two sample designs.

Both layer structures finish with a perovskite film and have the interface with a surrounding medium in common. During transient photoluminescence spectroscopy, the samples are measured in nitrogen atmosphere. For optical simulations, I assume a non-absorbing medium with $n_{r,\text{air}} = 1$, which I denote here as air. Only if light is radiated into the escape cone (blue circular segment in Fig. 6.1) facing towards the perovskite/air interface, light can be outcoupled. The opening angle of the escape cone can be approximated by the critical angle of total internal reflection of $\theta_c \approx 23^\circ$ in both samples.

For future calculations, I assume that radiative recombination inside the absorber material is isotropic, i. e. emission into a solid angle of $\Omega = 4\pi$. Based on the solid angles Ω_c (see Eq. 6.2) of the respective escape cones, I can roughly estimate the probabilities of parasitic absorption and outcoupling by $p_{a,e} = \Omega_c/(4\pi)$. It has to be noted, that this geometrical estimate relies on some additional assumptions: first, (multiple) reflections between interfaces are not considered here. Moreover, especially high energy photons might be reabsorbed before they reach an interface, even though they are on their way leaving the perovskite layer through an escape cone. Furthermore, roughness at the interfaces and scattering are both not taken into account.

Knowing that all photon probabilities have to add up to one, I find the probability p_r of photon recycling to be

$$p_r = 1 - p_e - p_a. \quad (6.3)$$

Based on the derived substantially different values p_a of parasitic absorption, I find quite distinct reabsorption probabilities for the two SiO₂ thicknesses: $p_{r,2} \approx 46\%$ in the case of the 2.3 nm-thin SiO₂ layer and almost doubled for the stack with the 200 nm-thick SiO₂ layer, where $p_{r,200} \approx 86\%$. This simple but rough estimate shall only highlight that the amount of photon recycling can indeed be significantly

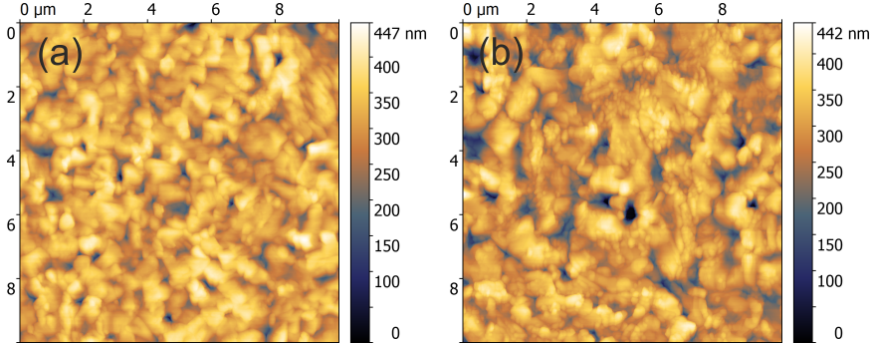


Figure 6.2: Atomic force microscopy (AFM) surface images of perovskite films coated on top of (a) a 200 nm-thick, and (b) a 2.3 nm-thin silicon dioxide layer.

modified only by the optical design. Precise optical simulations are provided in Sec. 6.5. Before I address the implication of different reabsorption probabilities on the transient photoluminescence, I investigate the surface morphology of the perovskite top layers in order to ensure that the perovskite quality is the same for the different stacks.

6.3 Morphology of perovskite top layers

The surface morphology of the perovskite top layers is examined by atomic force microscopy (AFM) and scanning electron microscopy (SEM). From the measured surface topographies by AFM shown in Fig. 6.2, I calculate the corresponding root-mean-square surface roughnesses R_{rms} for each layer stack, which are found to be similar with $R_{\text{rms},200} = 45 \text{ nm}$ and $R_{\text{rms},2} = 51 \text{ nm}$. Here and in the following, the indices "200" and "2" of stated physical quantities correspond to the layer stacks exhibiting the 200 nm-thick and the 2.3 nm-thin silicon dioxide layer, respectively. SEM images displayed in Fig. 6.3 illustrate the crystalline structures at the perovskite surfaces. The shown perovskite morphologies slightly differ among the two samples mainly in the form of varying crystal sizes. It is therefore conceivable that the material quality in terms of defects would not be exactly identical for both stacks as perovskite grain boundaries are present to different extents. However, in

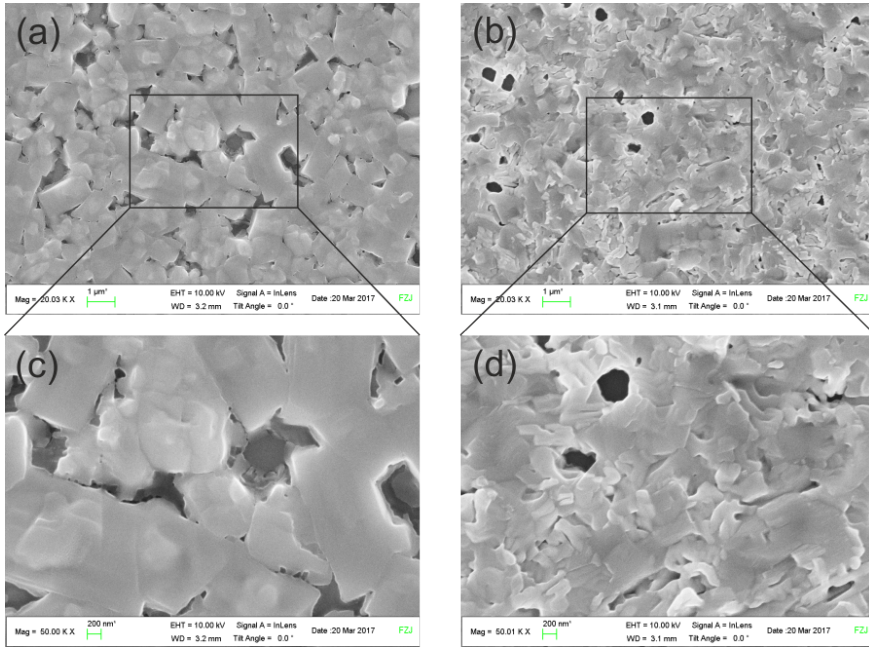


Figure 6.3: Scanning electron microscopy (SEM) surface images of perovskite films coated on top of (a) a 200 nm-thick, and (b) a 2.3 nm-thin silicon dioxide layer. The framed image details are shown in the enlarged panels (c) and (d), respectively.

the upcoming Sec. 6.4, I identify equal defect-related Shockley-Read-Hall lifetimes for both samples. Therefore, the same impact of trap-assisted recombination on the respective charge-carrier dynamics is accomplished and a similar perovskite material quality is assured despite the obvious changes in morphology.

In order to exclude that light guiding in terms of scattering is differently affected by the surface morphologies, I apply a calculation routine to obtain the internally reflected scattering distribution [198]. This approach relies only on surface profiles like AFM images and the refractive indices of the two materials adjacent to the corresponding interface. It is apparent from Fig. 6.4 that in both cases light impinging under normal incidence is primarily scattered (polar angles $\theta > 0$) instead of being specularly reflected ($\theta = 0$). Additionally, the scattering characteristics are similar, which enables me to apply the same optical simulation model for

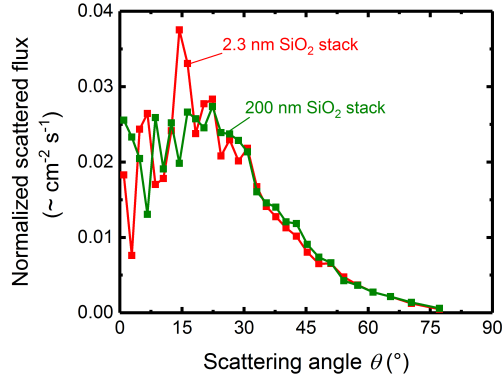


Figure 6.4: Normalized photon flux distribution scattered into the polar angles θ derived from analyzing atomic force microscopy topography images.

both stacks. Based on these findings, I conclude that the observed slightly different morphologies do not matter significantly for the following comparison.

6.4 Time-resolved photoluminescence

Figure 6.5 compares the spectral photoluminescence decays of the two samples for an initial excitation fluence of $15 \mu\text{J}/\text{cm}^2$. The panels (a) and (b) display the spectral components of the photoluminescence transients normalized to the corresponding maximum absolute intensities. A shift of the photoluminescence peak positions between the samples is visible. Furthermore, the spectral photoluminescence decreases in panel (b) faster than in panel (a) in accordance to Fig. 6.7. Both observations will be extensively discussed later on. In the panels (c) and (d), the data is spectrally normalized to the corresponding values of the spectrum at the delay time $t = 0$, which exhibits the highest overall intensity. In this depiction, the observed straight horizontal lines indicate that no spectral changes occur during the measurements. As a result, the photoluminescence decay for both stacks can be investigated being spectrally independent when integrating the spectra over photon energy.

Figure 6.6 shows the measured total time-resolved photoluminescence decays

6 Photon recycling investigated by time-resolved photoluminescence

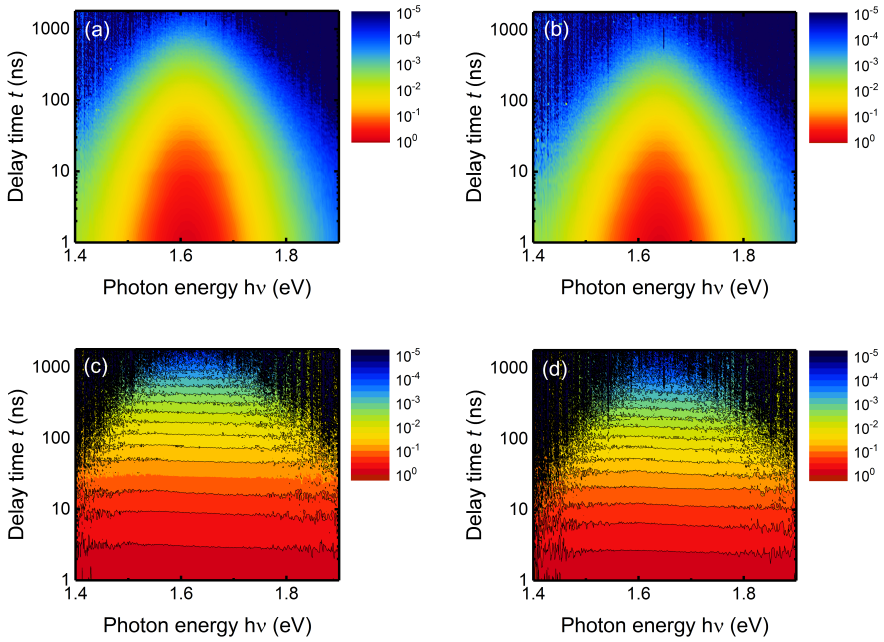


Figure 6.5: Comparison of spectral photoluminescence decays of perovskite thin films on top of (a, c) a 200 nm-thick silicon dioxide layer and (b, d) a 2.3 nm-thin silicon dioxide layer for an excitation fluence of $15 \mu\text{J}/\text{cm}^2$. While every value in (a) and (b) is normalized to the one value exhibiting the maximum absolute photoluminescence intensity, the data in (c) and (d) are spectrally normalized to the corresponding values of the one photoluminescence spectrum showing the highest overall intensity (at delay time $t = 0$).

of the samples when applying the same initial excitation fluences for the individual stacks (squares: $15 \mu\text{J}/\text{cm}^2$, triangles: $1.2 \mu\text{J}/\text{cm}^2$, circles: $0.12 \mu\text{J}/\text{cm}^2$). It is already apparent from Fig. 6.6 that the photoluminescence signals from the stack with the thicker SiO_2 layer are not only initially higher in all cases but also the higher order decay is less pronounced as for the counterpart with the thin SiO_2 layer. Figure 6.7 shows the same experimental data but normalized. The decay dynamics at low excitation fluences ($0.12 \mu\text{J}/\text{cm}^2$) are equal for the two samples. As trap-assisted Shockley-Read-Hall mechanisms govern recombination upon low level injection conditions (see Sec. 4.1), the two stacks are best comparable concerning the influence

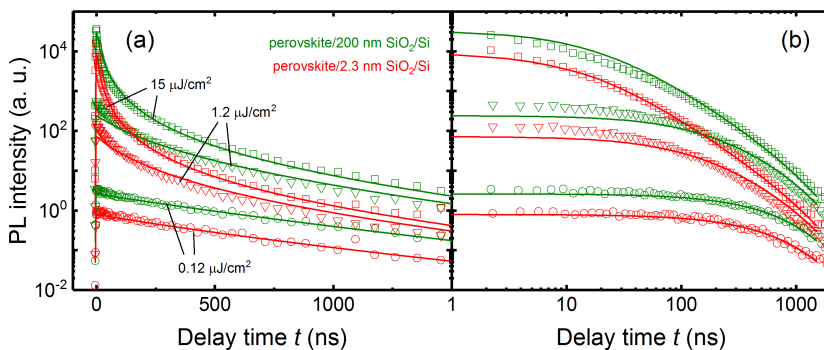


Figure 6.6: Measured time-resolved photoluminescence decays of perovskite films on top of two layer stacks with different silicon dioxide thicknesses: perovskite/200 nm SiO₂/Si (green symbols) and perovskite/2.3 nm SiO₂/Si (red symbols). For each stack, several excitation fluences are applied: 15 μJ/cm² (squares), 1.2 μJ/cm² (triangles) and 0.12 μJ/cm² (circles). The solid lines represent fitted photoluminescence transients. While the data is shown in panel (a) on a semilogarithmic scale, panel (b) displays the same data on a double-logarithmic scale for better visibility. Adapted with permission from [190]. Copyright 2017 American Chemical Society.

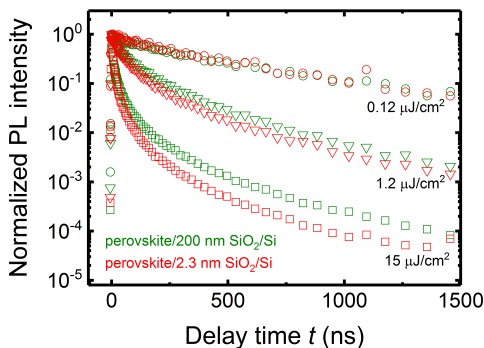


Figure 6.7: Normalized photoluminescence transients of perovskite films coated on top of silicon dioxide layers of different thicknesses (see Fig. 6.6 for non-normalized data). Reprinted with permission from [190]. Copyright 2017 American Chemical Society.

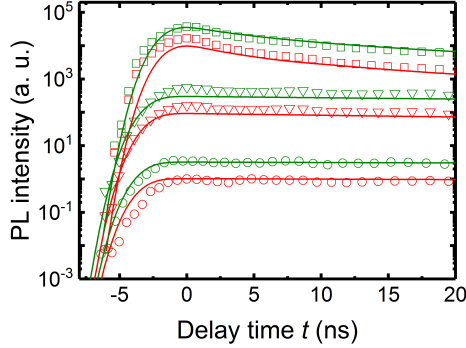


Figure 6.8: Zoom in of the time-resolved photoluminescence decays shown in Fig. 6.6 (a) in order to demonstrate the conformity of the rise dynamics between the experimental data (open symbols) and the corresponding simulated photoluminescence signals (solid lines).

of defects within the perovskite films. When applying increasingly higher excitation fluences, the photoluminescence transients of the two stacks clearly diverge in Fig. 6.7. This finding can be explained by differences in high order recombination kinetics as one would expect from the experimental design. In order to quantify these observations, the experimental decay curves are globally fitted by the recombination model described in Sec. 4.1 with some slight modifications. As the studied organic inorganic perovskite is rather low doped as revealed in Sec. 3.7.1, I neglect here the impact of doping, which leads to a simplified Shockley-Read-Hall model with one specific lifetime τ_{SRH} . Moreover, the careful determination of the higher-order recombination parameters is of uttermost importance in the course of investigating photon recycling. In order to gain a more comprehensive recombination picture, I take here the relative changes between transients for the different excitation fluences as well as the photoluminescence rise dynamics into account. Within the temporal length of the excitation pulses, photogenerated charge carriers might already begin to recombine. Instead of defining the excitation source as an infinitesimal short pulse by a Dirac delta function, I rather assume Gaussian-shaped pulses with a full width half maximum of 2.5 ns. Additionally, I consider the integration time of 2 ns for each spectrum in the simulations. A good conformity of the globally simulated

Table 6.1: Recombination parameters (Auger recombination coefficient C , external bimolecular recombination coefficient k^{ext} and Shockley-Read-Hall lifetime τ_{SRH}) derived from global fits of the respective time-resolved decays obtained from two samples of the same layer sequence perovskite/SiO₂/Si but with different silicon dioxide thicknesses, namely 200 nm and 2.3 nm.

SiO ₂ thickness	C (cm ⁶ s ⁻¹)	k^{ext} (cm ³ s ⁻¹)	τ_{SRH} (ns)
200 nm	$(8.0 \pm 2.1) \times 10^{-29}$	$(4.6 \pm 0.2) \times 10^{-11}$	870 ± 140
2.3 nm	$(9.7 \pm 1.4) \times 10^{-29}$	$(6.3 \pm 0.3) \times 10^{-11}$	990 ± 150

photoluminescence transients with the experimental data is found during the decay (see Fig. 6.6) as well as during the initial rise (see Fig. 6.8). The recombination parameters obtained from the fits are reported in Tab. 6.1. While the Shockley-Read-Hall lifetimes $\tau_{\text{SRH}} \approx 930$ ns as well as the Auger recombination coefficients $C \approx 8.9 \times 10^{-29}$ cm⁶s⁻¹ turn out to be similar for both stacks within their error margins, the external bimolecular recombination coefficients k vary significantly by a factor of $k_{\text{ratio}}^{\text{ext}} = k_2^{\text{ext}}/k_{200}^{\text{ext}} \approx 1.4$. By modeling time-resolved photoluminescence decays, the externally measured bimolecular recombination coefficient k^{ext} is revealed, which is drastically reduced with respect to the internal radiative bimolecular recombination coefficient $k_{\text{rad}}^{\text{int}}$ due to photon recycling events (see Eq. 4.12 and Sec. 4.1). In addition, Richter *et al.* [189] combined transient absorption measurements with findings from photoluminescence quantum efficiency measurements and concluded the presence of a non-radiative bimolecular component k_{nrad} thereof. With the chosen experimental design and the findings from solely steady-state and time-resolved photoluminescence measurements, I am able to verify the existence of a non-radiative bimolecular recombination channel in organic inorganic perovskite thin films. In doing so, the externally measured bimolecular recombination coefficient k^{ext} is composed of a non-radiative contribution k_{nrad} beside the external radiative part $k_{\text{rad}}^{\text{ext}}$. Therefore, I can express the ratio of the obtained k^{ext} values as

$$k_{\text{ratio}}^{\text{ext}} = \frac{k_2^{\text{ext}}}{k_{200}^{\text{ext}}} = \frac{k_{\text{rad},2}^{\text{ext}} + k_{\text{nrad}}}{k_{\text{rad},200}^{\text{ext}} + k_{\text{nrad}}} = \frac{(1 - p_{r,2})k_{\text{rad}}^{\text{int}} + k_{\text{nrad}}}{(1 - p_{r,200})k_{\text{rad}}^{\text{int}} + k_{\text{nrad}}}. \quad (6.4)$$

Here, I make use of Eq. 4.12, which relates the internal radiative coefficient $k_{\text{rad}}^{\text{int}}$

6 Photon recycling investigated by time-resolved photoluminescence

to its external expression $k_{\text{rad}}^{\text{ext}}$. Due to differently pronounced probabilities of photon recycling p_r in the particular stack designs, $k_{\text{rad}}^{\text{ext}}$ is supposed to change accordingly in each case, while $k_{\text{rad}}^{\text{int}}$ is assumed to be an intrinsic property and as such identical in both stacks. It is unclear whether k_{nrad} can be treated as a material-specific, intrinsic parameter, as it could be related to trap-assisted recombination in the sample. However if the latter scenario applies, similar obtained Shockley-Read-Hall lifetimes indicate that also k_{nrad} should be equal in both samples. In the next step, I define the radiative fraction κ of the internal bimolecular recombination coefficient $k^{\text{int}} = k_{\text{rad}}^{\text{int}} + k_{\text{nrad}}$ as

$$\kappa = \frac{k_{\text{rad}}^{\text{int}}}{k_{\text{rad}}^{\text{int}} + k_{\text{nrad}}}. \quad (6.5)$$

Applying Eq. 6.5 to Eq. 6.4 leads to

$$k_{\text{ratio}}^{\text{ext}} = \frac{(1 - p_{r,2})\kappa + 1 - \kappa}{(1 - p_{r,200})\kappa + 1 - \kappa} = \frac{1 - p_{r,2}\kappa}{1 - p_{r,200}\kappa}. \quad (6.6)$$

Solving Eq. 6.6 now for κ results in

$$\kappa = \frac{k_{\text{ratio}}^{\text{ext}} - 1}{p_{r,200}k_{\text{ratio}}^{\text{ext}} - p_{r,2}}. \quad (6.7)$$

Apart from the already determined $k_{\text{ratio}}^{\text{ext}} \approx 1.4$, p_r values for the particular samples have to be derived in order to calculate κ . Based on Eq. 6.7, Fig. 6.9 illustrates which radiative fraction κ can be expected for a matrix of possible photon recycling probabilities $p_{r,2}$ and $p_{r,200}$. A pure radiative k_{int} with $k_{\text{nrad}} = 0$ is realized if the photon recycling probabilities would be linked by the relation $p_{r,200} = 1 - (1 - p_{r,2})/k_{\text{ratio}}^{\text{ext}}$. The simple geometrical approach introduced in Sec. 6.2 leads to $p_{r,2} \approx 0.46$ and $p_{r,200} \approx 0.86$. As a consequence, a radiative fraction of $\kappa \approx 0.54$ (see pink sphere in Fig. 6.9) is found as a simple reference. However, in order to obtain precise photon recycling probabilities, I perform optical simulations, which are discussed in the following section.

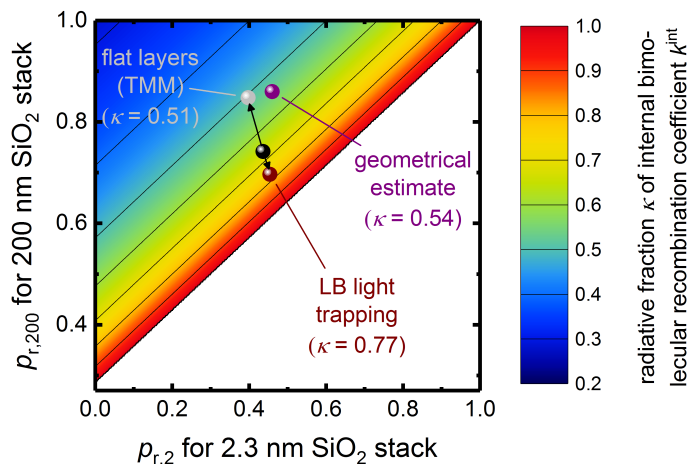


Figure 6.9: Simulated radiative fraction κ of the bimolecular recombination coefficient k^{int} according to Eq. 6.7 (with $k_{\text{ratio}} = 1.4$) for a matrix of photon recycling probabilities p_r of the two layer stacks with different silicon dioxide thicknesses of 200 nm and 2.3 nm, respectively. The pink sphere represents an estimate based on geometrical considerations ($\kappa = 0.54$). The brown sphere marks the result from a transfer matrix method (TMM) when all layers are perfectly flat ($p_{\text{diff}} = 0$, $\kappa = 0.51$). When assuming ideal lambertian (LB) light trapping at an rough air/perovskite interface ($p_{\text{diff}} = 1$), an increased κ of 0.77 is found (purple sphere). The black double arrow indicates the range of transition situations, when the nature of internal reflection changes from specular to diffuse or vice versa. Adapted with permission from [190]. Copyright 2017 American Chemical Society.

6.5 Optical simulations

The direct determination of the probabilities for photon recycling is rather complex. Therefore, it is simpler to approach p_r by first calculating the probabilities for outcoupling p_e and parasitic absorption p_a and finally derive p_r according to $p_r = 1 - p_e - p_a$ (Eq. 6.3). As previously shown in Sec. 4.3 by Eq. 4.14, the outcoupling probability is calculated as the ratio of the outgoing photon flux to the internal radiative recombination inside the absorber layer [28]

6 Photon recycling investigated by time-resolved photoluminescence

$$p_e = \frac{d\varepsilon_{\text{out}} \int_0^\infty A_{\text{fsi}}(E) \phi_{\text{bb}}(E) dE}{dS \int_0^\infty 4n_{\text{r,pero}}^2 \pi d\alpha(E) \phi_{\text{bb}}(E) dE}, \quad (6.8)$$

where the absorptance $A_{\text{fsi}}(E)$ of the perovskite layer is defined for illumination from the air side, here denoted as front side illumination.

Photon emission into the hemisphere of air requires an outgoing étendue of $d\varepsilon_{\text{out}} = \pi dS$ and Eq. 6.8 becomes

$$p_e = \frac{\int_0^\infty A_{\text{fsi}}(E) \phi_{\text{bb}}(E) dE}{\int_0^\infty 4n_{\text{r,pero}}^2 d\alpha(E) \phi_{\text{bb}}(E) dE}. \quad (6.9)$$

On the other hand, the probability of parasitic absorption p_a is rather difficult to calculate in a general case. Due to the specific experimental design, parasitic absorption is dominated here by light coupling into the Si substrate. Therefore, I can calculate p_a in analogy to Eq. 6.8 by considering the emission into the Si wafer and I obtain

$$p_a = \frac{\int_0^\infty n_{\text{r,Si}}^2 A_{\text{bsi}}(E) \phi_{\text{bb}}(E) dE}{\int_0^\infty 4n_{\text{r,pero}}^2 d\alpha(E) \phi_{\text{bb}}(E) dE}. \quad (6.10)$$

In this specific case, the absorptance A_{bsi} has to be simulated for radiation coupled into the perovskite film from the silicon halfspace, i. e. upon back side illumination. As the three distinct photon probabilities have to add up to one, I ultimately derive the probability p_r of photon recycling from the probabilities p_e and p_a , which are obtained from simulations.

It should be noted that I assume the internal emission of radiation inside the absorber layer to be isotropic. As the absorptivity is linked to the emissivity by detailed balance arguments, I have to simulate angle-dependent absorptances $A(E, \theta)$ for a variety of incident polar angles $0 \leq \theta \leq \pi/2$ and after weighting according to

$$A(E) = \frac{\int_0^{\pi/2} A(E, \theta) \sin \theta \cos \theta d\theta}{\int_0^{\pi/2} \sin \theta \cos \theta d\theta}, \quad (6.11)$$

I can apply the derived absorptances to Eq. 6.8, 6.9 and 6.10. In order to derive the absorptances, I combine findings from a coherent transfer matrix method (TMM), which is valid for simulating flat layer stacks, with findings from an incoherent light trapping (LT) approach based on analytical expressions derived by Green [199]. By the use of the latter optical model, I take ideal Lambertian light scattering at the rough perovskite/air interface into account. All other interfaces are considered to be flat. More details about the simulations and models can be found in Appendix B. The topography of the perovskite layers is discussed in more detail in Sec 6.3.

As I assume that both specular and diffuse internal reflection at the perovskite/air interface shape the absorptance in the perovskite layer, I weight the absorptances obtained from the individual optical models (LT and TMM, see Fig. B.2 in Appendix B) by introducing a haze factor p_{diff} according to

$$A(p_{\text{diff}}) = p_{\text{diff}}A_{\text{LT}} + (1 - p_{\text{diff}})A_{\text{TMM}}. \quad (6.12)$$

Haze parameters are commonly applied to describe scattering properties of e. g. textured glass/transparent and conductive oxides substrates [200,201]. In order to derive the relevant diffuse amount p_{diff} in the present samples, I rely on the measured spectral photoluminescence. In so doing, I adjust p_{diff} , and consequently also the simulated absorptance A_{fsi} upon front side illumination, such that the simulated emitted photon fluxes $\phi_{\text{PL}}(E)$ according to

$$\phi_{\text{PL}}(E) \propto A_{\text{fsi}}(E)E^2 \exp[-E/(k_{\text{B}}T)] \quad (6.13)$$

(see Sec. 3.6.2) match the measured photoluminescence spectra. When assuming that the absorptances saturates towards higher photon energies, I am able to determine the sample temperatures by fitting the high photon energy shoulder of the corresponding photoluminescence spectra based on Eq. 6.13. Therefore, I find that

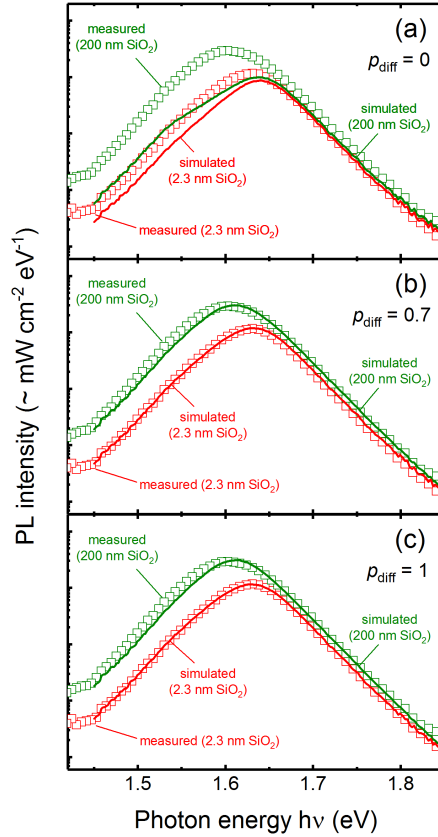


Figure 6.10: Measured steady-state photoluminescence spectra of perovskite films coated on top of a 200 nm-thick (green squares) and a 2.3 nm-thin silicon dioxide layer (red squares). The solid lines represent simulations of the spectra assuming different amounts p_{diff} of internal diffuse light scattering at the air/perovskite interface: (a) $p_{\text{diff}} = 0$, (b) $p_{\text{diff}} = 0.7$ and (c) $p_{\text{diff}} = 1$.

the temperatures of the samples during the steady state photoluminescence measurements are both $T \approx 310\text{K}$, which are needed for simulating emission spectra.

Measured steady-state photoluminescence spectra of both samples are shown in Fig. 6.10 as open squares in green for the sample with the 200 nm-thick SiO_2 layer

6.6 Photon probabilities and radiative fraction of bimolecular recombination

and in red for the sample with the 2.3 nm-thin SiO₂ layer, respectively. While a shift in peak positions of ~ 28 meV is identified, the total photoluminescence intensities differ by a factor of $PL_{200}/PL_2 \approx 2.5$, which is also visible as an offset in the transient photoluminescence data at $t = 0$ in Fig. 6.6. Both mentioned findings can be explained by variations in the absorption onsets between the two layer stacks. As the black body radiation flux is exponentially decreasing toward higher photon energies, already seemingly marginal differences in absorptances in the small photon energy range cause therefore tremendous variations in the intensity and shape of the resulting emission fluxes $\phi_{\text{PL}}(E)$ in accordance with Eq. 6.13.

Figure 6.10 shows additionally the comparison of measured steady-state photoluminescence spectra with findings from various optical simulations (solid lines) based on Eq. 6.12 and 6.13 for different haze parameters p_{diff} , i. e. (a) $p_{\text{diff}} = 0$ when applying solely the coherent TMM implying perfectly flat layers, (b) $p_{\text{diff}} = 0.7$, and (c) $p_{\text{diff}} = 1$ when applying ideal Lambertian light trapping at the perovskite/air interface. The best agreement between simulation and experiment is found when assuming a diffuse share of $p_{\text{diff}} = 0.7$. This value is similar to the haze parameter of $p_{\text{diff}} = 0.5$ used in optical simulations by van Eerden *et al.* [202] for a perovskite film exhibiting a comparable surface root-mean-square roughness of $R_{\text{rms}} = 50$ nm. Adjusting the simulated photoluminescence spectra is the best estimate for deriving the absorptances upon both front and back side illumination, which are needed for the calculations of the probabilities p_e , p_a , and p_r of photon outcoupling, parasitic absorption, and photon recycling, respectively.

6.6 Photon probabilities and radiative fraction of bimolecular recombination

The photon probabilities, which are derived in accordance to Eq. 6.9, 6.10 and 6.3, are plotted in Fig. 6.11 (a) as a function of the diffuse amount p_{diff} of internal reflection. Light outcoupling with probability p_e becomes more efficient with increasing impact by light trapping (increasing p_{diff}) based on detailed balance arguments. As the stack embedding the 200 nm-thick SiO₂ layer exhibits a significantly higher back reflectance R_b , this particular stack benefits from light trapping to a greater extent,

which principally results in higher values of $p_{e,200}$ compared to $p_{e,2}$. The stack with the 2.3 nm-thin SiO₂ layer is designed in a way to particularly favor parasitic absorption in contrast to the sample exhibiting the 200 nm-thick SiO₂ layer, leading to $p_{a,2} > p_{a,200}$. As the derived absorptances A_{bsi} vary only slightly among the applied optical models (see Fig. B.2), the relative changes of the probabilities p_a of parasitic absorption are small over the entire range of p_{diff} . As a consequence of the above observations, light trapping in the sample with the 200 nm-thick SiO₂ layer causes a reduction in the probability $p_{r,200}$ of photon recycling, while $p_{r,2}$ is less strongly affected and even slightly rises with increasing p_{diff} . The vertical dotted line in Fig. 6.11 represents the situation of the best fit of the measured photoluminescence spectra when $p_{\text{diff}} = 0.7$. Keeping this value fixed, Fig. 6.12 illustrates the spectral probabilities and their fundamental differences among the stacks with (a) the 200 nm-thick SiO₂ layer, and (b) the 2.3 nm-thin SiO₂ layer, respectively. Based on the absorption coefficient, which is shown as black dotted line, three regions are identified. The first gray highlighted area ($h\nu \lesssim 1.59\text{eV}$) illustrates the limit of weak absorption $\alpha d \ll 1$, where light trapping typically yields in a relatively high absorptance gain if permitted by the stack design. The significant observed difference in the probability of photon outcoupling $p_{e,200} > p_{e,2}$ is the reason for the measured variations of the photoluminescence intensities. Besides, coupling of weakly absorbed light into the Si wafer is significantly different as $p_{a,2} > p_{a,200}$. A transition region in white ($1.59\text{eV} \lesssim h\nu \lesssim 1.66\text{eV}$) marks the rise of the absorption coefficient α , before a grey highlighted saturation region begins for photon energies $h\nu \gtrsim 1.66\text{eV}$. Even in this regime, photon recycling in the stack with the 2.3 nm-thin SiO₂ layer is suppressed in favor of parasitic absorption.

Figure 6.11 (b) illustrates the photoluminescence intensity ratio PL_{200}/PL_2 based on Eq. 6.13 as well as the radiative fraction κ of the internal bimolecular recombination coefficient k^{int} according to Eq. 6.7. For $p_{\text{diff}} = 0.7$ and, thus, $p_{r,200} \approx 0.74$ and $p_{r,200} \approx 0.44$, I finally find a radiative fraction of $\kappa \approx 0.66$ (see also Fig. 6.9). Therefore, a significant attribution of non-radiative recombination to the bimolecular recombination is revealed. Richter *et al.* [189] combined transient spectroscopy measurements with findings from photoluminescence quantum efficiency measurements and were able to state a similar value of $\kappa \approx 0.74$. Currently, there is no clear understanding about the origin of such a non-radiative bimolecular recom-

6.6 Photon probabilities and radiative fraction of bimolecular recombination

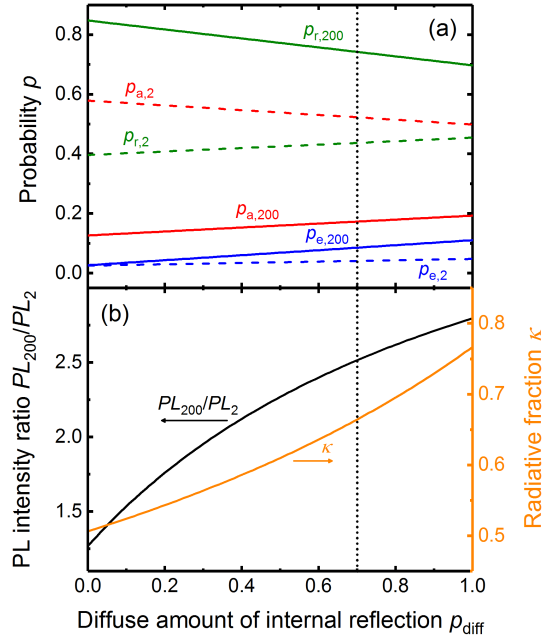


Figure 6.11: (a) Probabilities of photon outcoupling (p_e), parasitic absorption (p_a) and photon reabsorption (p_r) as a function of the diffuse amount of internal reflection p_{diff} at the perovskite/air interface for a perovskite film on top of a 200 nm-thick (solid lines, p_{200}) and a 2.3 nm-thin (dashed lines, p_2) silicon dioxide layer, respectively. (b) Photoluminescence intensity ratio (black line) and radiative fraction κ of the internal bimolecular recombination coefficient k^{int} (right y -axis, orange line) dependent on p_{diff} . The vertical dotted line marks $p_{\text{diff}} = 0.7$, which shows the best agreement between simulation and experiment.

bination channel. The existence of such a non-radiative mechanism is important for photovoltaic research of organic inorganic perovskites as it sets an upper limit of 66% to the internal radiative luminescence quantum efficiency Q_1^{lum} . Consequently, resulting external LED quantum efficiencies Q_e^{LED} are even lower, which in turn affects the maximum attainable solar cell efficiency (see Sec. 4.4 and 4.8). It should be mentioned here that in contrast to the limitation of Q_1^{lum} , laser cooling experiments

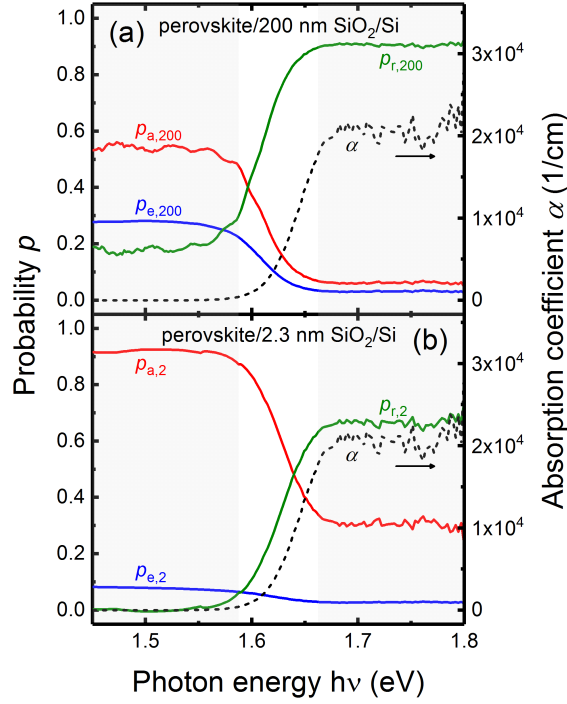


Figure 6.12: Simulated probabilities of internally emitted photons for outcoupling (p_e , blue lines), parasitic absorption (p_a , red lines) and photon recycling (p_r , green lines) in the cases of perovskite films coated on top of (a) a 200 nm-thick and (b) a 2.3 nm-thin silicon dioxide layer, respectively. Here, the diffuse amount of internal reflection at the perovskite/air interface is chosen to be $p_{\text{diff}} = 0.7$. Additionally, the absorption coefficient α is depicted as black dashed line (right y -axis).

performed by Ha *et al.* [175] on perovskite single crystals suggest external radiative quantum efficiencies beyond 90%. These obvious discrepancies could be related to the sample type because e. g. distinctly higher defect concentrations by orders of magnitudes are revealed in thin films compared to single crystals [171, 182, 203, 204]. A possible cause of non-radiative bimolecular recombination is trap-assisted Auger recombination [205–207], which is discussed in the following section.

6.7 Possible origin of non-radiative bimolecular recombination

Trap-assisted Auger recombination involves interactions between two free charge carriers and a trapped electron or an empty trap, respectively. Figure 6.13 illustrates the possible processes, which can be categorized as electron capture events with the corresponding Auger coefficients T_1 and T_2 , and hole capture events with T_3 and T_4 . Here, the coefficients T are derived from Bloch and hydrogen-like wave functions calculations [205]. From those coefficients, an effective trap-assisted Auger recombination rate

$$R_{\text{TA}} = \frac{(np - n_1 p_1)(T_1 n + T_2 p)(T_3 n + T_4 p) N_t}{T_1(n^2 + n n_1) + T_2(np + n_1 p) + T_3(np + n p_1) + T_4(p^2 + p p_1)} \quad (6.14)$$

is found [208], where N_t denotes the trap density, $n = n_0 + \Delta n$ and $p = p_0 + \Delta n$

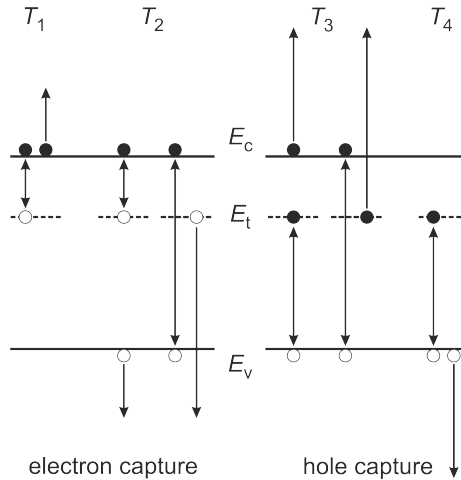


Figure 6.13: Illustration of various interactions between free charge carriers and defect states resulting in electron capture (with coefficients T_1 , T_2) and hole capture (T_3 , T_4), respectively. Please note that the processes 2 and 3 consist two possible interactions each. The energy levels of the valence and conduction band are here denoted as E_v and E_c , respectively. Furthermore, E_t marks the imperfection level (trap depth).

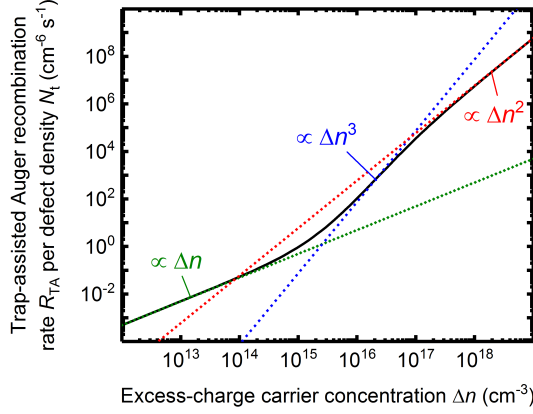


Figure 6.14: Trap-assisted Auger recombination rate R_{TA} per defect density N_t as a function of the excess-charge carrier concentration Δn as black solid line. For the simulation, defects are assumed to be located at a distance of $E_t = 0.116 \text{ eV}$ from the conduction band, which is the case for lead vacancies. Furthermore, I consider here a p -type doping density of $p_0 = 3 \times 10^{15} \text{ cm}^{-3}$. Colorful dotted lines indicate regimes of predominant monomolecular ($R_{TA} \propto \Delta n$), bimolecular ($R_{TA} \propto \Delta n^2$) and trimolecular ($R_{TA} \propto \Delta n^3$) recombination.

are the electron and hole concentrations, respectively. Here, Δn represents the excess-charge carrier concentration and n_0 and p_0 are the respective equilibrium concentrations. Furthermore, the concentrations $n_1 = N_c \exp[-E_t/k_B T]$ and $p_1 = N_v \exp[-(E_g - E_t)/k_B T]$ correspond to the values of n and p , respectively, when the Fermi level lies at the trap depth E_t , defined here with respect to the conduction band edge E_c . Furthermore, the trap density is given by N_t . Figure 6.14 illustrates Eq. 6.14 as a function of the excess-charge carrier concentration Δn , while I consider p -type doping of concentration $p_0 = 3 \times 10^{15} \text{ cm}^{-3}$ and effective densities of states in the conduction and valence bands of $N_c = N_v = 7 \times 10^{18} \text{ cm}^{-3}$ based on the findings in Tab. 4.4. Additionally, I assume a trap depth of $E_t = 0.116 \text{ eV}$, which corresponds to a lead vacancy in the perovskite structure (see Fig. 3.3). The rate of Auger recombination involving interaction with defect states exhibits three regimes with different dependencies on the excess-charge carrier concentration Δn . In the saturation region, i. e. $\Delta n \gg n_1, p_0, \dots$, the effective trap-assisted Auger

6.7 Possible origin of non-radiative bimolecular recombination

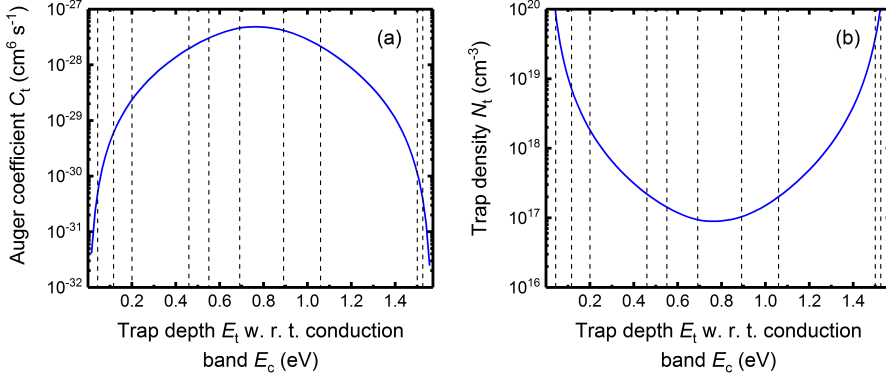


Figure 6.15: (a) Coefficient C_t of trap-assisted Auger recombination as a function of the trap depth E_t with respect to the conduction band edge E_c . Vertical dashed lines represent trap depths of various intrinsic defects according to Ref. [82, 83] (see also Fig. 3.3). (b) Trap density N_t for given trap depths E_t that would be needed to provide a non-radiative contribution to the internal bimolecular recombination coefficient resulting in a radiative fraction of only $\kappa = 0.66$.

recombination rate stated in Eq. 6.14 simplifies

$$R_{TA} = \frac{(T_1 + T_2)(T_3 + T_4)N_t\Delta n^2}{T_1 + T_2 + T_3 + T_4} = C_t N_t \Delta n^2. \quad (6.15)$$

Ultimately, Auger recombination dynamics appear bimolecular and, thus, provide a non-radiative contribution. In order to quantify the amount of non-radiative bimolecular recombination, Fig. 6.15 (a) illustrates the effective Auger coefficient C_t as defined in Eq. 6.15 as a function of trap depth E_t . As it is valid for Shockley-Read-Hall statistics, also the Auger recombination rate via defects shows its maximum for mid-gap traps, when detrapping of captured charge carriers is least likely. The vertical dashed lines represent intrinsic defect levels according to Fig. 3.3. In the next step, I evaluate the defect density N_t , which has to be present in the samples in order to provide a reduced radiative fraction of the internal bimolecular recombination coefficient of $\kappa = 0.66$, i. e. $C_t N_t = (1 - \kappa)k^{\text{int}}$. It is apparent from Fig. 6.15 (b) that a minimum trap density of $N_t \approx 9 \times 10^{16} \text{ cm}^{-3}$ is needed to fulfill the above relation. However, lower trap densities of $N_t \sim 10^{16} \text{ cm}^{-3}$ are reported in the litera-

ture [203,204] for perovskite thin films. Additionally, as the formation energies for deep intrinsic defects are rather high (see Fig. 3.3), the formation of shallow defect states becomes more likely in organic inorganic perovskites. In the context that even higher densities are required for shallow traps to provide a substantial non-radiative contribution to bimolecular recombination (see Fig. 6.15 (b)), trap-assisted Auger recombination might not be the only reason why a radiative fraction of $\kappa < 1$ is observed. Therefore, I find two possible scenarios. Either the approximations of the transition coefficients T derived by Landsberg *et al.* [205] might not be applicable to organic inorganic perovskites and, as a consequence, trap-assisted Auger coefficients are somehow underestimated by orders of magnitudes, or there has to be an additional, yet unknown cause which is mainly accountable for the limitation of κ . However, further investigations are needed to unveil and quantify non-radiative bimolecular recombination mechanisms in order to understand current limitations of perovskite solar cells and develop strategies to circumvent eventual constraints.

7 Conclusion and outlook

High luminescence quantum yields and long charge-carrier lifetimes make the emerging material class of metal halide perovskites an ideal system to apply time-resolved photoluminescence. This non-destructive method measures the decay of (spectral or overall) photoluminescence intensity emitted by the sample over time after temporary photo-generation of excess-charge carriers by a short laser pulse. In the course of the measurement, charge carriers undergo separation and diverse recombination processes leading to a continuous decrease in charge-carrier concentration, which is reflected in the time-dependent intensity of the luminescence signal. Beside radiative recombination, several non-radiative recombination processes are revealed in perovskites: intrinsic, high-order mechanisms like radiative recombination and Auger recombination exhibit the highest recombination rates for high carrier concentrations (e. g. at short times after the excitation pulse). Consequently, a strong initial photoluminescence decay is typically observed. On the contrary, extrinsic, low-order trap-assisted Shockley-Read-Hall recombination is predominant when carrier concentrations are low and the photoluminescence decay becomes rather moderate at longer times. Therefore, the photoluminescence decay changes over becoming moderate at longer times.

Beside unraveling various recombination mechanisms that shape the photoluminescence transients, I have focused in this thesis on the investigation of the so called photon recycling effect by time-resolved photoluminescence. Photon recycling refers to the self-absorption of photons, which have been generated by radiative recombination of excited states, within the absorber material itself. As photon recycling is directly linked with the radiative recombination process, the observed radiative recombination rate in thin-film perovskites is actually the result of a delayed internal radiative recombination rate modified by the mean number of photon recy-

7 Conclusion and outlook

cling events an average photon will experience before it is statistically out-coupled and can leave the absorber. I was able to prove the existence of photon recycling in thin-film perovskites as the observed apparent radiative recombination rate can be manipulated by modifying only the optical design of the sample stack; i. e. enhancing or lowering the probability of photon reabsorption in the absorber layer by altering the light management in the stacks by means of the chosen surrounding layers and their optical properties.

Like radiative and non-radiative recombination processes, also photon recycling affects the open-circuit voltage of solar cells. Based only on the findings from time-resolved photoluminescence, I have demonstrated how it is in general possible to already predict the attainable open-circuit voltage, which the investigated perovskite absorber layer embedded in a solar cell stack could ideally provide. This approach helps to estimate the photovoltaic potential of any absorber layer based on its material quality without the need of fabricating an entire solar cell first. Additionally, I have revealed by simulating the optical findings that the bimolecular recombination channel in thin-film perovskites is not 100 % radiative as previously assumed. I was already able to exclude trap-assisted Auger recombination as possible physical cause of this severe non-radiative contribution. However, the origin remains still unclear and should be subject of future research as it implies a limitation of the photovoltaic potential of perovskite solar cells.

Perovskite single crystals have been investigated in this thesis by time-resolved photoluminescence as a paramount system to study the relevance of photon recycling as charge-carrier transport mechanism in more detail. As the reabsorption event will be typically located at a different position within the thick sample compared to the spot of the original radiative recombination event, photon recycling enables charge-carrier transportation. I have detected spectrally narrow luminescence peaks and sharp absorption onsets in perovskites indicating that an internally emitted photons will travel on average only $\sim 1 \mu\text{m}$ before it is reabsorbed. Therefore, photon recycling rather supports preserving charge carriers locally than actually transporting them. I have identified diffusion as the dominant carrier transport mechanism, which continuously tries to flatten the charge-carrier profiles. As the the recombination zone expands over time mainly due to diffusion as quantified by

simulation, reabsorption effects increasingly modify the recorded photoluminescence spectra and cause spectral shifts during the transient measurements.

Within this thesis, I have demonstrated that time-resolved photoluminescence obtained from metal halide perovskites can be applied to not only determine charge-carrier lifetimes but also to identify and reveal fundamental charge-carrier processes like recombination, photon recycling and separation. These processes are essential for the operation of photovoltaic and light-emitting devices and can indicate efficiency limitations of perovskite devices.

A Appendix: Calculating charge-carrier profiles in single crystals

In order to simulate the time-resolved photoluminescence from perovskite single crystals, the time-dependent charge-carrier profiles $\mathbf{n}(t)$ have to be calculated first. The continuity equation

$$\frac{\partial \mathbf{n}}{\partial t} = \mathbf{G}^{\text{ext}}(t) + (\underline{T} - \underline{R} + \underline{G}^{\text{int}}) \mathbf{n}, \quad (\text{A.1})$$

can be solved for $\mathbf{n}(t)$, when the external charge-carrier generation $\mathbf{G}^{\text{ext}}(t)$ and the matrix operators for charge-carrier transport \underline{T} , recombination \underline{R} and photon recycling $\underline{G}^{\text{int}}$ are known. Their computation is explained in the following sections.

A.1 Charge-carrier generation due to pulsed excitation

The generation of charge carriers by an external source is taken into account by introducing the time-dependent generation vector $\mathbf{G}^{\text{ext}}(t)$. In general, the overall spatial charge-carrier concentration $n_{\text{ini}}(x)$ can be derived from the total photon density ϕ_{phot} of the pulsed laser light impinging on the sample. While I assume that absorption obeys the Lambert-Beer law and, additionally, every incident photon eventually generates an electron-hole pair, the excess charge-carrier concentration $n_{\text{ini}}(x)$ can be computed at the center x_{mk} of each interval $x_k - x_{k-1}$ as

A Appendix: Calculating charge-carrier profiles in single crystals

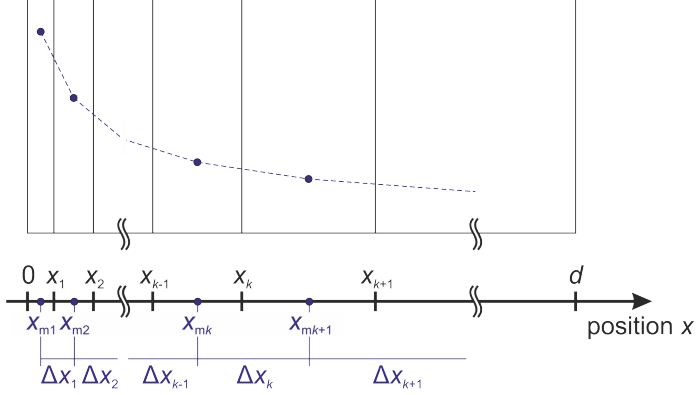


Figure A.1: Schematics of the non-linear discretization of the crystal with thickness d . The position $x = 0$ marks the side of the crystal, which is illuminated. The locations x_k are donated here as interval boundaries with x_{mk} being the middle of the interval $x_k - x_{k-1}$. The charge-carrier concentration within each interval is assumed to be constant for simplicity. Here, an exponential carrier profile is shown as example. The distance between integral centers x_{mk} and x_{mk+1} is defined as Δx_k .

$$n_{\text{ini}}(x)|_{x=x_{mk}} = \phi_{\text{phot}} \frac{\exp(-\alpha_0 x_{k-1}) - \exp(-\alpha_0 x_k)}{x_k - x_{k-1}}. \quad (\text{A.2})$$

Here, the absorption coefficient α_0 of the monochromatic light source ($E = 3.07 \text{ eV}$) is $\alpha_0 = 1.25 \times 10^5 \text{ cm}^{-1}$. For simplification reasons, Eq. A.2 treats the charge-carrier concentration as a constant inside each interval. I divide the sample thickness d into intervals of non-uniform sizes. This logarithmic spacing allows a proper resolution in the regions of interest (near the surface, where charges are generated) while the spacing becomes progressively larger towards the bulk. Figure A.1 illustrates the grid spacing together with the chosen notation.

In reality, the applied excitation pulse is not infinitesimally short. Therefore, I rather assume the pulse to follow a Gaussian distribution in time instead of a Dirac delta function, and $\mathbf{G}^{\text{ext}}(t)$ becomes

$$\mathbf{G}^{\text{ext}}(t) = \frac{\mathbf{n}_{\text{ini}}}{\sqrt{2\pi\sigma^2}} \exp\left(-\frac{(t-t_0)^2}{2\sigma^2}\right), \quad (\text{A.3})$$

with σ being the standard deviation and t_0 the time at which the peak intensity is reached. As a matter of fact, t_0 can be chosen arbitrarily as I adjust the time scale that the highest photoluminescence intensity is observed at $t = 0$. By comparing transient photoluminescence experiments with simulations, I find a full width at half maximum of the peak, which is linked to the standard deviation by $FWHM = 2\sqrt{2\ln 2}\sigma$, of $FWHM \approx 2$ ns.

A.2 Diffusive transport and surface recombination

Diffusion of charge carriers was previously discussed in Sec. 4.5 for the situation in perovskite thin films. Diffusive transport becomes even more important in single crystals as the previous assumption of a homogeneous carrier profile in the course of the experiment becomes more and more invalid when the sample thickness is increased from hundreds of nanometers (thin films) up to millimeters (single crystals). One-dimensional diffusion is defined according to Fick's second law by

$$\frac{\partial n}{\partial t} = D \frac{\partial^2 n}{\partial x^2}. \quad (\text{A.4})$$

The specific diffusion coefficient D is proportional to the charge-carrier mobility μ based on the Einstein equation (see Eq. 4.23). For a linear spacing ($\Delta x = \text{const.}$), the transport operator \underline{T} in linear matrix notation shows the form

$$\underline{T} = \frac{D}{\Delta x^2} \begin{pmatrix} -2 & 1 & 0 & \dots & 0 \\ 1 & -2 & 1 & \dots & 0 \\ 0 & 1 & -2 & \dots & 0 \\ \vdots & \vdots & \vdots & \ddots & \vdots \\ 0 & 0 & 0 & \dots & -2 \end{pmatrix}. \quad (\text{A.5})$$

Here, the consistency error of discretization is on the order of $\mathcal{O}(\Delta x)$. For non-uniform (logarithmic) spacing $\Delta x_{k+1} = r\Delta x_k$, the transport operator becomes

A Appendix: Calculating charge-carrier profiles in single crystals

$$D \frac{\partial^2 n(x)}{\partial x^2} \Big|_{x=x_{mk}>1} = D \left[\frac{2n(x_{mk-1})}{(\Delta x_k + \Delta x_{k-1}) \Delta x_{k-1}} - \frac{2n(x_{mk})}{\Delta x_k \Delta x_{k-1}} + \frac{2n(x_{mk+1})}{(\Delta x_k + \Delta x_{k-1}) \Delta x_k} \right] \quad (\text{A.6})$$

For r being not much larger than one, the approximation retains first-order accuracy $\mathcal{O}(\Delta x^2)$ as for equidistant grids [209].

Additionally, I apply surface recombination conditions at the sample boundaries ($x = x_{m1}$, $x = x_{mN}$) by establishing a recombination current. This current equals the first (space) derivative of the charge-carrier concentration n at the surfaces times diffusion coefficient D , and is proportional to the respective local charge-carrier concentration $n(x = x_{m1}, x_{mN})$ while the constant of proportionality is denoted as surface recombination velocity S . For instance at the front side (surface which is illuminated), the boundary condition reads

$$D \frac{\partial n(x)}{\partial x} \Big|_{x=x_{m1}} = D \frac{n(x_{m1}) - n(x_{m0})}{\Delta x_0} = S n(x_{m1}). \quad (\text{A.7})$$

By mirroring the sample at the boundary $x = 0$ due to reflecting conditions, it becomes apparent that Δx_0 will equal Δx_1 . The occurring concentration $n(x_{m0})$ in Eq. A.7 can be eliminated in the second order derivative. Consequently, the transport operator becomes

$$D \frac{\partial^2 n(x)}{\partial x^2} \Big|_{x=x_{m1}} = \frac{-(S \Delta x_1 + D) 2n(x_{m1}) + 2Dn(x_{m2})}{(\Delta x_1 + \Delta x_0) \Delta x_1}, \quad (\text{A.8})$$

while charges which do not recombine at the front side will be reflected at the surface. Thus for $S = 0$, the boundary condition becomes entirely reflecting.

A.3 Photon recycling scheme

A formalism that is able to describe photon recycling quantitatively in a linearly spaced system was previously derived by Julian Mattheis [210]. The fundamentals of the formalism are briefly explained in the following, which I adapt for a non-uniform spacing. First, we have to find an expression for the internal generation

A.3 Photon recycling scheme

rate $\delta g_{\text{int}}(E, x_{\text{g}})$ at a fixed position x_{g} caused by radiative recombination with a rate $r(E, x_{\text{r}})$ at another fixed position x_{r} . When charge carriers recombine radiatively, they emit photons isotropically into all directions, i. e. into a solid angle of $\Omega = 4\pi$. The three-dimensional problem can easily be treated by a one-dimensional approach. Utilizing the spherical symmetry of radiation with the radius ρ defined as $\rho = |x_{\text{g}} - x_{\text{r}}|/\cos(\theta)$, the photon flux $\delta\phi_{\text{PL}}$ per solid angle interval $d\Omega$ emitted by a thin layer with thickness δx_{r} at position x_{r} into direction θ is derived as

$$\delta\phi_{\text{PL}}(E, x_{\text{r}}, \rho) = \frac{r(E, x_{\text{r}})}{4\pi} \delta\rho. \quad (\text{A.9})$$

As radiation is exponentially attenuated according to the Lambert-Beer law, the generation rate $\delta g_{\text{int}}(E, x_{\text{g}}, \rho)$ reads as

$$\delta g_{\text{int}}(E, x_{\text{g}}, \rho) = \frac{\alpha(E)r(E, x_{\text{r}})}{4\pi} \exp(-\alpha(E)\rho)\delta\rho. \quad (\text{A.10})$$

The recombination rate $r(E, x_{\text{r}})$ in Eq. A.9 and A.10 can be expressed in terms of the spectral radiative recombination rate $r_0(E)$ in thermodynamic equilibrium from the van Roosbroeck-Shockley relation (Eq. 4.32) as

$$r(E, x_{\text{r}}) = r_0(E) \frac{n(x_{\text{r}})p(x_{\text{r}})}{n_{\text{i}}^2} = 4\pi n_{\text{r}}^2(E) \alpha(E) \phi_{\text{bb}}(E) \frac{n(x_{\text{r}})p(x_{\text{r}})}{n_{\text{i}}^2}. \quad (\text{A.11})$$

In the next step, the spherical coordinates are transformed into cylinder coordinates and, additionally, the perspective is changed as the point of generation x_{g} is now put into the center of the system. In order to obtain the total generation rate $\delta G_{\text{int}}(x_{\text{g}}, x_{\text{r}})$ at which carriers are generated at point x_{g} by radiative recombination between x_{r} and $x_{\text{r}} + \delta x_{\text{r}}$, one has to integrate over all angles θ and φ , as well as over all photon energies E . By making use of $\delta\rho = \delta x_{\text{r}}/\cos(\theta)$, $\delta G_{\text{int}}(x_{\text{g}}, x_{\text{r}})$ reads

$$\begin{aligned} \delta G_{\text{int}}(x_{\text{g}}, x_{\text{r}}) = & \int_0^\infty \frac{\alpha(E)r_0(E)}{4\pi} \frac{n(x_{\text{r}})p(x_{\text{r}})}{n_{\text{i}}^2} \int_0^{2\pi} d\varphi \int_0^{\pi/2} \exp\left(\frac{-\alpha(E)|x_{\text{g}} - x_{\text{r}}|}{\cos(\theta)}\right) \\ & \times \frac{\sin(\theta)}{\cos(\theta)} d\theta dE \delta x_{\text{r}}. \end{aligned} \quad (\text{A.12})$$

A Appendix: Calculating charge-carrier profiles in single crystals

Now we consider internal generation in a finite interval between $x_g = x_{i-1}$ and $x_g = x_i$ caused by radiative recombination within a second finite interval between $x_r = x_{j-1}$ and $x_r = x_j$. By considering radiative interaction between two finite intervals instead of between two discrete locations, the formalism becomes self-consistent and ensures the conservation of photons and charge carriers. Eventually, to obtain the total internal generation rate inside the center x_{mi} of a particular interval from recombination in the whole sample, the contributions from each single recombination interval between x_{j-1} and x_j have to be summed up:

$$G_{\text{int}}(x_{mi}) = \sum_{j=1}^N \frac{r_0}{2|x_j - x_{j-1}|} \frac{n(x_{mj})p(x_{mj})}{n_i^2} \int_0^\infty \int_0^{\pi/2} \int_{x_g=x_{i-1}}^{x_g=x_i} \int_{x_r=x_{j-1}}^{x_r=x_j} \alpha(E) \times \exp\left(\frac{-\alpha(E)\Delta x(x_g, x_r)}{\cos(\theta)}\right) \frac{\sin(\theta)}{\cos(\theta)} dx_r dx_g d\theta dE. \quad (\text{A.13})$$

Here, the charge-carrier concentrations n and p are computed in the middle (index m) of each interval between x_{j-1} and x_j , and are assumed to be constant within each interval for simplicity. The path of light $\Delta x(x_g, x_r)$ can either be a direct or a reflected ray and corresponds to the respective distances between the intervals x_g and x_r . In the simulations, I consider paths of light corresponding up to a maximum of 100 reflections. In doing so, I assume flat crystal surfaces and a reflectance of $R = (n_r - 1)^2 / (n_r + 1)^2 \approx 0.17$ given a refractive index of $n_r = 2.4$ [211]. Additionally, based on Snell's law, I take account of total internal reflection at the surfaces for radiation emitted into angles $\theta \geq \arcsin(1/n_r) \approx 24.6^\circ$. For solving Eq. A.13, the interested reader is referred to the PhD thesis of Julian Mattheis [210]. With this formalism, the amount of re-absorbed charge carriers in each sample segment due to radiative recombination in the whole sample can be computed provided the spatial charge-carrier profile is known. Eventually, the internal generation matrix $\underline{G}^{\text{int}}$ reads

$$\underline{G}^{\text{int}} = \frac{1}{4\pi\tau_{\text{rad}}} \begin{pmatrix} f_{11} & f_{12} & \cdots & f_{1N} \\ f_{21} & f_{22} & \cdots & f_{2N} \\ \vdots & \vdots & \ddots & \vdots \\ f_{N1} & f_{N2} & \cdots & f_{NN} \end{pmatrix}, \quad (\text{A.14})$$

where f_{ij} are the respective radiative interaction functions between the recomb-

nation intervals and generation intervals and τ_{rad} is the radiative lifetime in the respective recombination intervals.

It should be noted here that the one-dimensional treatment of the photon recycling process is an idealized approach. In reality, the excitation area is not infinitely large and photons internally emitted in lateral directions are able to exit the probed spot without ever entering it again. Therefore, the photon recycling effect could be overestimated by simulations and the derived value of the internal radiative recombination coefficient $k_{\text{rad}}^{\text{int}} = 5.5 \times 10^{-11} \text{ cm}^3\text{s}^{-1}$ stated in Tab. 5.1 should be considered as a lower limit.

A.4 Bulk recombination

In single crystals, I also take bulk recombination processes into account. As previously described in Sec. 4.1, these consist of trap-assisted Shockley-Read-Hall, radiative and Auger recombination. The effective bulk lifetime τ_{bulk} defines the overall impact of bulk recombination on the excess-charge carrier concentration (see Eq. 4.19). The bulk recombination operator \underline{R} is an identity operator and, therefore, maps a function (here: $\mathbf{n}(t)$) onto itself and reads

$$\underline{R} = \frac{1}{\tau_{\text{bulk}}} \begin{pmatrix} 1 & 0 & \dots & 0 \\ 0 & 1 & \dots & 0 \\ \vdots & \vdots & \ddots & \vdots \\ 0 & 0 & \dots & 1 \end{pmatrix}. \quad (\text{A.15})$$

B Appendix: Optical simulation of thin layer stacks

Optical simulations were performed to derive absorptances of the thin layer stacks described in Chap. 6. Here, I used two approaches: 1) A coherent transfer matrix method (TMM), which is valid for simulating flat layer stacks and 2) an incoherent light trapping (LT) model based on analytical expressions derived by Green [199]. By the use of the latter optical model, I take ideal Lambertian light scattering at the rough perovskite/air interface into account. All other interfaces are considered to be flat.

The optical data, namely the refractive indices n_r and the extinction coefficients k , of the materials used in the optical simulations are depicted in Fig. B.1. Here, silicon dioxide is assumed to be a non-absorbing material ($k_{\text{SiO}_2} = 0$). Please note that for the simulations of the absorptance A_{bsi} upon back side illumination (from the Si halfspace), I have to set the extinction coefficient of Si to zero.

B.1 Coherent simulation of flat layer stacks

For the calculation of absorptances of flat layer stacks as illustrated in Fig. 6.1, I use the TMM Python software package [212]. Figure B.2 shows the resulting absorptances of the perovskite layers as solid lines. Internal specular reflection at the perovskite/air interface does not enhance the effective light path and slight changes in the absorptances in the low energy region as seen in Fig. B.2 (a) upon front side illumination are mainly attributed to the modified back reflection when changing the SiO₂ layer thickness. Upon back side illumination, light is more efficiently coupled into the perovskite film when the thickness of the intermediate, low refractive SiO₂

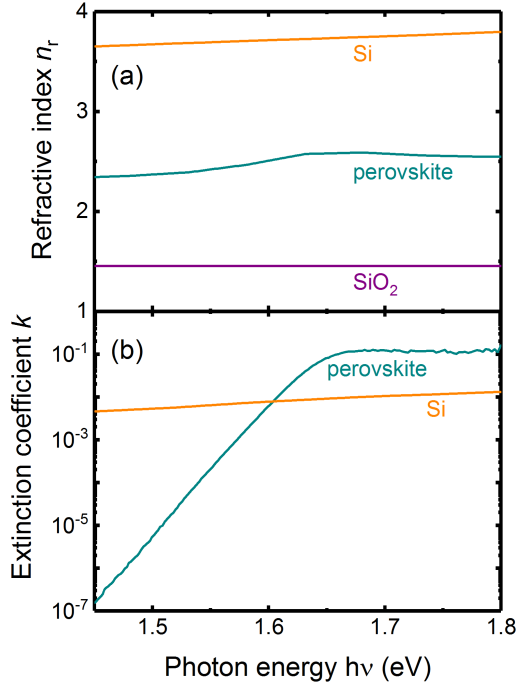


Figure B.1: Optical parameters, i. e. (a) refractive index n_r and (b) extinction coefficient k , of silicon [97] (orange lines), perovskite (cyan lines) and silicon dioxide [97] (purple line) used for the simulations. Silicon dioxide is assumed to be optically transparent ($k_{\text{SiO}_2} = 0$).

layer is drastically reduced. Therefore, the absolute absorptance values in saturation differ significantly in Fig. B.2 (a). Furthermore, highly resonant modes are identified in the absorptance A_{200} due to the embedding of the high refractive perovskite layer between two adjacent media (air and SiO_2) each with a lower refractive index. At the photon energies of these observed spikes, the spectral probabilities $p_a(E)$ of parasitic absorption reach values above one. In reality, flat perovskite layers are not achieved by spin coating (see Sec. 6.3), which are a prerequisite for the formation of waveguides. Small surface roughnesses can lead to a significant attenuation of resonant modes. For this reason, I determine the baseline of A_{200} by smoothing, which is shown as green dashed line in Fig. B.2 (b). That way, simulated resonant

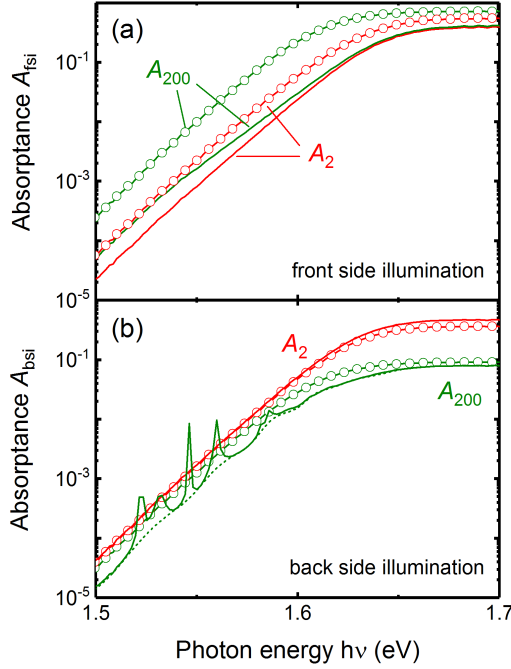


Figure B.2: Simulated absorbances A for perovskite films coated on top of a 200 nm-thick SiO_2 layer (A_{200} , green lines) and a 2.3 nm-thin SiO_2 layer (A_2 , red lines) upon (a) front side illumination and (b) back side illumination. The solid lines represent simulations according to a coherent transfer matrix method, while the lines with the open circles mark simulations including incoherent light trapping. The green dashed line in (b) indicates the baseline of the green solid line.

modes are suppressed and spectral values of $p_a(E) > 1$ are avoided. This procedure reduces the overall probability p_a of parasitic absorption by a total of only ~ 0.025 .

B.2 Incoherent Lambertian light scattering

In the following, I take Lambertian light scattering at the rough perovskite/air interface (see Sec. 6.3 for perovskite surface morphologies) into account. Thus, the

B Appendix: Optical simulation of thin layer stacks

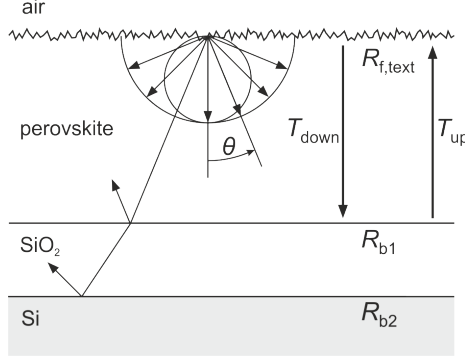


Figure B.3: Schematic depiction of Lambertian light trapping at the rough perovskite/air interface with internal reflectance $R_{f,\text{text}}$. The depicted circle illustrates the scattering rate into different polar angles θ . Due to Lambert's cosine law, the scattered intensity is a function of $\cos\theta$. The respective reflectances at the perovskite/SiO₂ and the SiO₂/Si interfaces are marked as R_{b1} and R_{b2} . The transmittance of a downward hemispherical photon flux through the perovskite absorber is denoted as T_{down} , while T_{up} corresponds to the upward analogue.

orientation of light rays is randomized each time when being reflected at this particular interface. As the scattering distribution obeys Lambert's cosine law, the scattered flux is weighted by $\cos\theta$. While Lambertian light trapping implies diffuse reflection, the reflection at all other interfaces is treated to be specular. Here, I rely on an incoherent approach to describe light trapping based on analytical relations derived by Green [199]. The notation is illustrated in Fig. B.3 for the sample including the 200 nm-thick SiO₂ layer. In the case of the stack with the only 2.3 nm-thin SiO₂ layer, I presuppose the formation of an effective perovskite/Si interface by neglecting the SiO₂ layer, which simplifies the optical simulation tremendously. When considering multiple (infinite) reflection events, the absorptance obtained upon front side illumination is found for the particular samples as

$$A_{\text{fsi}} = \frac{(1 - R_f) [1 - T_{\text{down}} + (1 - T_{\text{up}}) T_{\text{down}} R_b]}{1 - T_{\text{down}} R_b T_{\text{up}} R_{f,\text{text}}}. \quad (\text{B.1})$$

Here, R_f denotes the reflectance at the front surface and the internal reflectance $R_{f,\text{text}}$ is given by

B.2 Incoherent Lambertian light scattering

$$R_{f,\text{text}} = 1 - \frac{\int_0^{\pi/2} [1 - R_f(\theta)] \cos \theta \sin \theta \, d\theta}{\int_0^{\pi/2} \cos \theta \sin \theta \, d\theta}, \quad (\text{B.2})$$

when weighting over all polar angles $0 \leq \theta \leq \pi/2$. R_b is the effective back reflectance, which is simply the reflectance at the perovskite/Si interface in the case of the layer stack with the 2.3 nm-thin SiO₂ layer. On the other hand for the stack with the 200 nm-thick SiO₂ layer, the back reflectance is calculated as

$$R_b(\theta) = R_{b1}(\theta) + \frac{[1 - R_{b1}(\theta)] R_{b2}(\theta_2) [1 - R_{b1}(\theta_2)]}{1 - R_{b1}(\theta_2) R_{b2}(\theta_2)}, \quad (\text{B.3})$$

where θ_2 is the respective angle of refractive light rays in medium 2 (SiO₂) according to Snell's law. For the definitions of the reflectances $R_{b,1}$ and $R_{b,2}$, the reader is guided to the illustration of Fig. B.3. Reflectances at any interface are calculated based on the assumption of an equal mixture of *s*-polarized and *p*-polarized light following the Fresnel equations

$$R_{s\text{-pol}}(\theta) = \left(\frac{n_{r,1} \cos \theta - n_{r,2} \cos \theta_2}{n_{r,1} \cos \theta + n_{r,2} \cos \theta_2} \right)^2 \quad (\text{B.4})$$

$$R_{p\text{-pol}}(\theta) = \left(\frac{n_{r,2} \cos \theta - n_{r,1} \cos \theta_2}{n_{r,2} \cos \theta + n_{r,1} \cos \theta_2} \right)^2. \quad (\text{B.5})$$

The total back reflectance R_b is appropriately weighted by [199]

$$R_b = \frac{\int_0^{\pi/2} R_b(\theta) \exp(-\alpha d / \cos \theta) \cos \theta \sin \theta \, d\theta}{\int_0^{\pi/2} \exp(-\alpha d / \cos \theta) \cos \theta \sin \theta \, d\theta}. \quad (\text{B.6})$$

Here, α and d represent the absorption coefficient of perovskite and the layer thickness, respectively. Upon front side illumination under the incident angle θ , light rays are randomly scattered while entering the perovskite film. Therefore, the transmittances of the downward (T_{down}) and the upward (T_{up}) hemispherical photon flux are given by [199]

B Appendix: Optical simulation of thin layer stacks

$$T_{\text{down}} = \frac{\int_0^{\pi/2} \exp(-\alpha d / \cos \theta) \cos \theta \sin \theta \, d\theta}{\int_0^{\pi/2} \cos \theta \sin \theta \, d\theta} \quad (\text{B.7})$$

$$T_{\text{up}} = \frac{\int_0^{\pi/2} R_{\text{b}}(\theta) \exp(-2\alpha d / \cos \theta) \cos \theta \sin \theta \, d\theta}{\int_0^{\pi/2} R_{\text{b}}(\theta) \exp(-\alpha d / \cos \theta) \cos \theta \sin \theta \, d\theta}. \quad (\text{B.8})$$

Now I address the calculation of the absorptance A_{bsi} upon back side illumination. Please note that light is scattered for the first at the front surface only after being coupled from the Si wafer into the perovskite layer ($1 - R_{\text{b,I}}$) and after being transmitted according to the first upward directed transmission process ($T_{\text{up,I}}$). Therefore, the absorptance A_{bsi} reads

$$A_{\text{bsi}} = (1 - R_{\text{b,I}})(1 - T_{\text{up,I}}) + \frac{(1 - R_{\text{b,I}})T_{\text{up,I}}R_{\text{f,text}} [1 - T_{\text{down}} + T_{\text{down}}R_{\text{b}}(1 - T_{\text{up}})]}{1 - T_{\text{up}}R_{\text{f,text}}T_{\text{down}}R_{\text{b}}}, \quad (\text{B.9})$$

where the respective back reflectances $R_{\text{b,I}}$ and R_{b} are taken into account for the two different samples.

The simulated absorptances according to Eq. B.1 and B.9 are shown in Fig. B.2 as lines with open circles. Light trapping improves light incoupling and, as a consequence, the absorptance A_{fsi} upon front side illumination is increased in the saturation region compared to the simulation results based on the flat layer approach. The absorption onset of A_{200} compared to A_2 is significantly shifted towards lower photon energies, because the stack with the 200 nm-thick SiO_2 layer benefits from the light trapping effect to a higher extend than the other stack embedding the 2.3 nm-thin SiO_2 layer. To understand this finding, I show the corresponding internal reflectances in Fig. B.4. A textured surface causes a high internal reflectance for diffuse light with values of $R_{\text{f,text}} > 0.8$. While the back reflectance $R_{\text{b},200}$ is considerably higher than $R_{\text{b},2}$ due to the different optical design of the stacks, incident light is more efficiently trapped inside the stack with the 200 nm-thick SiO_2 layer resulting in an increased absorptance in the low absorbing region and, thus, a red-

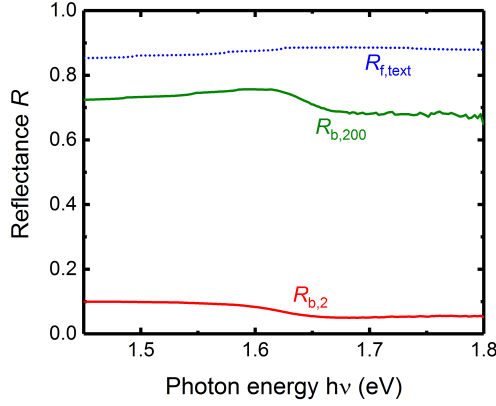


Figure B.4: Spectral internal reflectances at different interfaces: diffuse reflectance $R_{f,ext}$ (blue dotted line) at the rough perovskite/air interface, total specular back reflectance $R_{b,200}$ (green solid line) taking a 200 nm-thick SiO_2 layer into account, and specular back reflectance $R_{b,2}$ (red solid line) at an effective perovskite/Si interface when neglecting the 2.3 nm-thin SiO_2 layer in the optical simulations.

shift of the absorption onset. The absorptances A_{bsi} upon back side illumination (see Fig. B.2) are similar for the two optical models, because light scattering and as a consequence thereof light path enhancement are just realized after the first transition process through the entire layer stacks. The lower back reflectance $R_{b,2}$ (red line in Fig. B.4) facilitates efficient light coupling into the perovskite film leading to a higher saturated absorptance A_2 than A_{200} at high photon energies.

Abbreviations and symbols

α	Absorption coefficient
Γ	Gamma function
Δn	Excess-charge carrier concentration
Δn_s	Excess-charge carrier concentration at the surface
$\Delta\mu$	Quasi-Fermi level splitting
ε_{in}	Étendue of incident light
ε_{out}	Étendue of outgoing light
η	Energy conversion efficiency
θ	Polar angle; also diffraction angle
θ_c	Critical angle of total internal reflection
κ	Radiative fraction of the internal bimolecular recombination coefficient k^{int}
λ	Wavelength
μ	Charge-carrier mobility
μ^*	Reduced Fermi energy
μ_n	Electron mobility
μ_p	Hole mobility
σ	Electrical conductivity; also hybrid orbital
τ	Charge-carrier lifetime
τ_{bulk}	Bulk lifetime
τ_{eff}	Effective lifetime
τ_{mono}	Lifetime extracted from the monoexponential photoluminescence decay
τ_n	Electron lifetime in the Shockley-Read-Hall model
τ_{nrad}	Non-radiative lifetime

Abbreviations and symbols

τ_p	Hole lifetime in the Shockley-Read-Hall model
τ_{rad}	Radiative lifetime
τ_s	Surface lifetime
τ_{SRH}	Shockley-Read-Hall lifetime
$\tau_{\text{SRH,eff}}$	Effective Shockley-Read-Hall lifetime
ϕ_{em}	Emitted photon flux
ϕ_{exc}	Excitation fluence
ϕ_{in}	Incident photon flux
ϕ_{bb}	Black body radiation
ϕ_{phot}	Photon density
ϕ_{PL}	Spectral photoluminescence flux
$\phi_{\text{PL,bsi}}$	Spectral photoluminescence flux upon back side illumination
$\phi_{\text{PL,fsi}}$	Spectral photoluminescence flux upon front side illumination
ϕ_{sun}	Solar spectrum
φ	Azimuthal angle; also phase
ψ	Wave function
Ω	Solid angle
A	Absorptance
c	Speed of light in vacuum: $2.9979 \times 10^8 \text{ ms}^{-1}$
C	Sum of individual Auger recombination coefficients: $C = C_n + C_p$
C_n	Auger recombination coefficient for electrons
C_p	Auger recombination coefficient for holes
C_t	Effective trap-assisted Auger recombination coefficient
d	Thickness
d_{hkl}	Atomic plane distance with respect to the Miller indices hkl
D	Diffusion constant
$D(E)$	Density of states
E	Energy
E_{act}	Activation energy
E_b	Binding energy
E_c	Energy level of conduction band
E_g	Band gap energy

E_{gs}	Ground state energy
E_{phon}	Phonon energy
E_{t}	Trap depth
E_{trap}	Defect level
E_{v}	Energy level of valence band
E_0	Urbach energy
f	Frequency
F_j	Fermi-Dirac integral
FF	Fill factor
G^{ext}	External generation rate
\mathbf{G}^{ext}	External generation vector
G^{int}	Internal generation rate
$\underline{G}^{\text{int}}$	Internal generation operator
h	Planck constant: $4.1357 \times 10^{-15} \text{ eVs}$
H	Hamiltonian
H'_{if}	Transition matrix element
\hbar	Reduced Planck constant $\hbar = h/(2\pi)$
$I_{\text{PL}}(t)$	Photoluminescence intensity over time
$I_{\text{PL,norm}}(t)$	Normalized photoluminescence intensity over time
j	Current density
J_0^{rad}	Radiative saturation current density
J_{sc}	Short-circuit current density
k	Extinction coefficient; also wave vector and bimolecular recombination coefficient
k_{B}	Boltzmann constant: $8.6173 \times 10^{-5} \text{ eVK}^{-1}$
k^{ext}	External bimolecular recombination coefficient; the sum of $k_{\text{rad}}^{\text{ext}}$ and k_{nrad}
$k_{\text{rad}}^{\text{ext}}$	External radiative recombination coefficient; the modification of $k_{\text{rad}}^{\text{int}}$ by photon recycling
k^{int}	Internal bimolecular recombination coefficient; the sum of $k_{\text{rad}}^{\text{int}}$ and k_{nrad}
$k_{\text{rad}}^{\text{int}}$	Internal radiative recombination coefficient
k_{nrad}	Non-radiative bimolecular recombination coefficient

Abbreviations and symbols

L_d	Diffusion length
L_{PR}	Self-absorption length
m_j	Joint effective mass
m_j^*	Joint effective mass in terms of the electron rest mass
m_0	Electron rest mass: 9.1095×10^{-31} kg
n	Electron concentration
\mathbf{n}	Charge-carrier profile
n_i	Intrinsic charge-carrier concentration
n_r	Refractive index
n_0	Equilibrium electron concentration
N_c	Effective density of states in the conduction band
N_t	Trap density
N_v	Effective density of states in the valence band
p	Hole concentration
p_a	Probability of absorbing a photon parasitically
p_{diff}	Haze factor
p_e	Photon outcoupling probability
p_r	Probability of reabsorbing a photon
p_0	Equilibrium hole concentration
P_{max}	Maximum attainable power density of a solar cell
P_0	Irradiated power per unit area
q	Elementary charge: 1.6022×10^{-19} C
Q_e^{LED}	External LED quantum efficiency
Q_i^{lum}	Internal luminescence quantum efficiency
r	Ion radius
\mathbf{r}	Position vector
R	Recombination rate; also reflectance
\underline{R}	Recombination operator
R_{nrad}	Non-radiative recombination rate
R_{rad}	Radiative recombination rate
R_0^{rad}	Internal radiative recombination rate
R_{rms}	Root-mean-square roughness
R_s	Volume-related Shockley-Read-Hall recombination rate

\tilde{R}_s	Shockley-Read-Hall recombination rate at the surface
R_{TA}	Trap-assisted Auger recombination rate
RH	Relative humidity
S	Surface recombination velocity
S_f	Front surface recombination velocity
S_n	Surface recombination velocity for electrons
S_p	Surface recombination velocity for holes
S_r	Rear surface recombination velocity
$S(T)$	Seebeck coefficient
S_{cell}	Active cell area
t	Time; also Goldschmidt tolerance factor
t_{pump}	Delay time after pump pulse in OPTP
T	Temperature
\underline{T}	Transport operator
V	Voltage
V_{oc}	Open-circuit voltage
V_{oc}^{rad}	Radiative limit of the open-circuit voltage
w_{if}	Transition rate between two energy levels (initial and final state)
x	Position
x_g	Position of charge-carrier generation event
x_r	Position of radiative recombination event
AFM	Atomic force microscopy
ASA	Advanced semiconductor analysis; device simulating software
CIGS	Copper indium gallium selenide; solar cell material
CW	Continuous wave
DMF	Dimethylformamide; polar solvent
DPS	Diphenylstilbene; dye used for lasing purposes
FC-75	Fluorocarbon derivate of tetrahydrofuran; solution used for PDS
FWHM	Full width at half maximum
GBA	γ -butyrolactone; solvent
HLI	High level injection
ICCD	Intensified charge-coupled device

Abbreviations and symbols

ITO	Indium tin oxide; transparent and conductive electrode material
LED	Light emitting device
LLI	Low level injection
LT	Light trapping
MAI	Methylammonium iodide; precursor for the fabrication of perovskites
MAPI	Methylammonium lead iodide; perovskite material
MCP	Microchannel plate
OPTP	Optical pump terahertz probe
PCBM	[6,6]-phenyl-C ₆₁ -butyric acid methyl ester; electron transport material
PDS	Photothermal deflection spectroscopy
PEDOT	Poly(3,4-ethylenedioxythiophene); hole transport polymer
PL	Photoluminescence
PR	Photon recycling
SEM	Scanning electron microscope
Spiro-OMeTAD	2,2',7,7'-tetrakis-(N,N-di-4-methoxyphenylamino)-9,9'-spirobifluorene; hole transport material
SQ	Thermodynamic device limit named after Shockley-Queisser
SRH	Non-radiative recombination mechanism named after Shockley-Read-Hall
TMM	Transfer matrix method
TRPL	Time-resolved photoluminescence
UV	Ultraviolet
XPS	X-ray photo-electron spectroscopy
XRD	X-ray diffraction
ZnO-NP	Zinc oxide nanoparticles; electron transport material

References

- [1] M. A. Green, A. Ho-Baillie, and H. J. Snaith, “The Emergence of Perovskite Solar Cells,” *Nature Photonics*, vol. 8, pp. 506–514, 2014.
- [2] B. R. Sutherland and E. H. Sargent, “Perovskite Photonic Sources,” *Nature Photonics*, vol. 10, pp. 295–302, 2016.
- [3] J. H. Noh, S. H. Im, J. H. Heo, T. N. Mandal, and S. I. Seok, “Chemical Management for Colorful, Efficient, and Stable Inorganic-Organic Hybrid Nanostructured Solar Cells,” *Nano Letters*, vol. 13, no. 4, pp. 1764–1769, 2013.
- [4] E. T. Hoke, D. J. Slotcavage, E. R. Dohner, A. R. Bowring, H. I. Karunadasa, and M. D. McGehee, “Reversible Photo-Induced Trap Formation in Mixed-Halide Hybrid Perovskites for Photovoltaics,” *Chemical Science*, vol. 6, pp. 613–617, 2015.
- [5] S. Albrecht, M. Saliba, J. P. Correa Baena, F. Lang, L. Kegelmann, M. Mews, L. Steier, A. Abate, J. Rappich, L. Korte, R. Schlattmann, M. K. Nazeeruddin, A. Hagfeldt, M. Grätzel, and B. Rech, “Monolithic Perovskite/Silicon-Heterojunction Tandem Solar Cells Processed at Low Temperature,” *Energy & Environmental Science*, vol. 9, no. 1, pp. 81–88, 2016.
- [6] D. P. McMeekin, G. Sadoughi, W. Rehman, G. E. Eperon, M. Saliba, M. T. Hörantner, A. Haghighirad, N. Sakai, L. Korte, B. Rech, M. B. Johnston, L. M. Herz, and H. J. Snaith, “A Mixed-Cation Lead Mixed-Halide Perovskite Absorber for Tandem Solar Cells,” *Science*, vol. 351, no. 6269, pp. 151–155, 2016.
- [7] T. Kirchartz, S. Korgitzsch, J. Hüpkens, C. O. R. Quiroz, and C. J. Brabec, “Performance Evaluation of Semitransparent Perovskite Solar Cells for Application in Four-Terminal Tandem Cells,” *ACS Energy Letters*, vol. 3, no. 8,

References

- pp. 1861–1867, 2018.
- [8] S. De Wolf, J. Holovsky, S.-J. Moon, P. Löper, B. Niesen, M. Ledinsky, F.-J. Haug, J.-H. Yum, and C. Ballif, “Organometallic Halide Perovskites: Sharp Optical Absorption Edge and Its Relation to Photovoltaic Performance,” *The Journal of Physical Chemistry Letters*, vol. 5, no. 6, pp. 1035–1039, 2014.
- [9] J. You, Z. Hong, Y. M. Yang, Q. Chen, M. Cai, T.-B. Song, C.-C. Chen, S. Lu, Y. Liu, H. Zhou, and Y. Yang, “Low-Temperature Solution-Processed Perovskite Solar Cells with High Efficiency and Flexibility,” *ACS Nano*, vol. 8, no. 2, pp. 1674–1680, 2014.
- [10] W. Nie, H. Tsai, R. Asadpour, J.-C. Blancon, A. J. Neukirch, G. Gupta, J. J. Crochet, M. Chhowalla, S. Tretiak, M. A. Alam, H.-L. Wang, and A. D. Mohite, “High-Efficiency Solution-Processed Perovskite Solar Cells with Millimeter-Scale Grains,” *Science*, vol. 347, no. 6221, pp. 522–525, 2015.
- [11] D. W. deQuilettes, S. Koch, S. Burke, R. K. Paranjli, A. J. Shropshire, M. E. Ziffer, and D. S. Ginger, “Photoluminescence Lifetimes Exceeding 8 μ s and Quantum Yields Exceeding 30% in Hybrid Perovskite Thin Films by Ligand Passivation,” *ACS Energy Letters*, vol. 1, no. 2, pp. 438–444, 2016.
- [12] F. Deschler, M. Price, S. Pathak, L. E. Klintberg, D.-D. Jarausch, R. Higler, S. Hüttner, T. Leijtens, S. D. Stranks, H. J. Snaith, M. Atatüre, R. T. Phillips, and R. H. Friend, “High Photoluminescence Efficiency and Optically Pumped Lasing in Solution-Processed Mixed Halide Perovskite Semiconductors,” *The Journal of Physical Chemistry Letters*, vol. 5, no. 8, pp. 1421–1426, 2014.
- [13] T. Kirchartz, F. Staub, and U. Rau, “Impact of Photon Recycling on the Open-Circuit Voltage of Metal Halide Perovskite Solar Cells,” *ACS Energy Letters*, vol. 1, no. 4, pp. 731–739, 2016.
- [14] P. Würfel, *Physik der Solarzellen*. Heidelberg: Spektrum Akademischer Verlag, 2nd ed., 2000.
- [15] J. Nelson, *The Physics of Solar Cells*. London: Imperial College Press, 2003.
- [16] C. F. Klingshirn, *Semiconductor Optics*. Berlin Heidelberg New York: Springer-Verlag, 3rd ed., 2007.
- [17] P. Y. Yu and M. Cardona, “6.3 Excitons,” in *Fundamentals of Semiconductors*:

- Physics and Materials Properties*, pp. 276–279, Heidelberg: Springer, 4th ed., 2010.
- [18] T. Kirchartz, *Generalized Detailed Balance Theory of Solar Cells*. PhD thesis, RWTH Aachen, 2009.
- [19] G. Kirchhoff, “Ueber das Verhältniss zwischen dem Emissionsvermögen und dem Absorptionsvermögen der Körper für Wärme und Licht,” *Annalen der Physik*, vol. 185, no. 2, pp. 275–301, 1860.
- [20] W. van Roosbroeck and W. Shockley, “Photon-Radiative Recombination of Electrons and Holes in Germanium,” *Physical Review*, vol. 94, no. 6, pp. 1558–1560, 1954.
- [21] T. Tiedje, E. Yablonovitch, G. D. Cody, and B. G. Brooks, “Limiting Efficiency of Silicon Solar Cells,” *IEEE Transactions of Electron Devices*, vol. 31, no. 5, pp. 711–716, 1984.
- [22] U. Rau and J. H. Werner, “Radiative Efficiency Limits of Solar Cells with Lateral Band-Gap Fluctuations,” *Applied Physics Letters*, vol. 84, no. 19, pp. 3735–3737, 2004.
- [23] I. Pelant and J. Valenta, *Luminescence Spectroscopy of Semiconductors*. Oxford: Oxford University Press, 2012.
- [24] W. Shockley and W. T. Read Jr., “Statistics of the Recombinations of Holes and Electrons,” *Physical Review*, vol. 87, no. 5, pp. 835–842, 1952.
- [25] R. N. Hall, “Electron-Hole Recombination in Germanium,” *Physical Review*, vol. 87, 1952.
- [26] T. Kirchartz, T. Markvart, U. Rau, and D. A. Egger, “Impact of Small Phonon Energies on the Charge-Carrier Lifetimes in Metal-Halide Perovskites,” *The Journal of Physical Chemistry Letters*, vol. 9, no. 5, pp. 939–946, 2018.
- [27] U. Rau and T. Kirchartz, “On the Thermodynamics of Light Trapping in Solar Cells,” *Nature Materials*, vol. 13, no. 2, pp. 103–104, 2014.
- [28] U. Rau, U. W. Paetzold, and T. Kirchartz, “Thermodynamics of Light Management in Photovoltaic Devices,” *Physical Review B*, vol. 90, no. 3, p. 035211, 2014.

References

- [29] R. T. Ross, "Some Thermodynamics of Photochemical Systems," *The Journal of Chemical Physics*, vol. 46, no. 12, pp. 4590–4593, 1967.
- [30] G. Smestad and H. Ries, "Luminescence and Current-Voltage Characteristics of Solar Cells and Optoelectronic Devices," *Solar Energy Materials and Solar Cells*, vol. 25, no. 1, pp. 51–71, 1992.
- [31] U. Rau, "Reciprocity Relation between Photovoltaic Quantum Efficiency and Electroluminescent Emission of Solar Cells," *Physical Review B*, vol. 76, no. 8, p. 085303, 2007.
- [32] U. Brackmann, *Lambdachrome Laser Dyes*. Göttingen: Lambda Physik, 2nd revised ed., 1997.
- [33] D. E. Gray (ed.), *American Institute of Physics Handbook*. New York: McGraw-Hill, 3rd ed., 1982 reissue.
- [34] M. R. Nuys, *Characterization and Modification of Copper and Iron Oxide Nanoparticles for Application as Absorber Material in Silicon Based Thin Film Solar Cells*. PhD thesis, RWTH Aachen, 2015.
- [35] J. Flohre, *Charakterisierung und Modifizierung von Kupferoxid- und Kupfersulfid-Nanopartikeln für Dünnschichtsolarzellen*. PhD thesis, RWTH Aachen, 2017.
- [36] W. B. Jackson, N. M. Amer, A. C. Boccara, and D. Fournier, "Photothermal Deflection Spectroscopy and Detection," *Applied Optics*, vol. 20, no. 8, pp. 1333–1344, 1981.
- [37] J. von Richthofen, *Photothermische Deflektionsspektroskopie an Dünnschichtsolarzellen aus amorphem Silizium*. diploma thesis, RWTH Aachen, 1995.
- [38] T. C. M. Müller and T. Kirchartz, "Absorption and Photocurrent Spectroscopy with High Dynamic Range," in *Advanced Characterization Techniques for Thin Film Solar Cells*, ed. D. Abou-Ras, T. Kirchartz, and U. Rau, pp. 189–214, Weinheim: Wiley-VCH, 2nd ed., 2016. DOI: 10.1002/9783527699025.ch8.
- [39] C. W. H. Sellmer, *Untersuchung der Ladungsträgerkonzentration und -beweglichkeit in mikrokrystallinen Siliziumlegierungen mit Hall-Effekt und Thermokraft*. PhD thesis, RWTH Aachen, 2011.

- [40] J. P. Mock, *Fehlstellendotierung von Eisenoxid- und Bismutsulfid-Nanopartikeln*. PhD thesis, RWTH Aachen, 2017.
- [41] F. Köhler, *Zur Mikrostruktur siliziumbasierter Dünnschichten für die Photovoltaik*. PhD thesis, RWTH Aachen, 2012.
- [42] S. Olthof and K. Meerholz, “Substrate-Dependent Electronic Structure and Film Formation of MAPbI₃ Perovskites,” *Scientific Reports*, vol. 7, p. 40267, 2017.
- [43] H.-R. Wenk and A. Bulakh, *Minerals: Their Constitution and Origin*. Cambridge: Cambridge University Press, 2004.
- [44] G. Rose, “I. De perowskite, fossili novo,” in *De novis quibusdam fossilibus quae in montibus Uraliis inveniuntur*, pp. 3–5, 1839.
- [45] W. Li, Z. Wang, F. Deschler, S. Gao, R. H. Friend, and A. K. Cheetham, “Chemically Diverse and Multifunctional Hybrid Organic-Inorganic Perovskites,” *Nature Reviews Materials*, vol. 2, no. 3, p. 16099, 2017.
- [46] V. M. Goldschmidt, “Die Gesetze der Krystallochemie,” *Naturwissenschaften*, vol. 14, no. 21, pp. 477–485, 1926.
- [47] K. Momma and F. Izumi, “VESTA 3 for Three-Dimensional Visualization of Crystal, Volumetric and Morphology Data,” *Journal of Applied Crystallography*, vol. 44, no. 6, pp. 1272–1276, 2011.
- [48] C. J. Howard and H. T. Stokes, “Group-Theoretical Analysis of Octahedral Tilting in Perovskites,” *Acta Crystallographica Section B*, vol. 54, no. 6, pp. 782–789, 1998.
- [49] H. T. Stokes, E. H. Kisi, D. M. Hatch, and C. J. Howard, “Group-Theoretical Analysis of Octahedral Tilting in Ferroelectric Perovskites,” *Acta Crystallographica Section B*, vol. 58, no. 6, pp. 934–938, 2002.
- [50] P. S. Whitfield, N. Herron, W. E. Guise, K. Page, Y. Q. Cheng, I. Milas, and M. K. Crawford, “Structures, Phase Transitions and Tricritical Behavior of the Hybrid Perovskite Methyl Ammonium Lead Iodide,” *Scientific Reports*, vol. 6, p. 35685, 2016.
- [51] D. Weber, “CH₃NH₃PbX₃, ein Pb(II)-System mit kubischer Perowskitstruktur

References

- tur,” *Zeitschrift für Naturforschung B*, vol. 33, no. 12, pp. 1443–1445, 1978.
- [52] D. B. Mitzi, C. A. Feild, W. T. A. Harrison, and A. M. Guloy, “Conducting Tin Halides with a Layered Organic-Based Perovskite Structure,” *Nature*, vol. 369, no. 6480, pp. 467–469, 1994.
- [53] D. B. Mitzi, S. Wang, C. A. Feild, C. A. Chess, and A. M. Guloy, “Conducting Layered Organic-Inorganic Halides Containing (100)-Oriented Perovskite Sheets,” *Science*, vol. 267, no. 5203, pp. 1473–1476, 1995.
- [54] C. R. Kagan, D. B. Mitzi, and C. D. Dimitrakopoulos, “Organic-Inorganic Hybrid Materials as Semiconducting Channels in Thin-Film Field-Effect Transistors,” *Science*, vol. 286, no. 5441, pp. 945–947, 1999.
- [55] A. Kojima, K. Teshima, Y. Shirai, and T. Miyasaka, “Organometal Halide Perovskites as Visible-Light Sensitizers for Photovoltaic Cells,” *Journal of the American Chemical Society*, vol. 131, no. 17, pp. 6050–6051, 2009.
- [56] M. M. Lee, J. Teuscher, T. Miyasaka, T. N. Murakami, and H. J. Snaith, “Efficient Hybrid Solar Cells Based on Meso-Superstructured Organometal Halide Perovskites,” *Science*, vol. 338, no. 6107, pp. 643–647, 2012.
- [57] M. Liu, M. B. Johnston, and H. J. Snaith, “Efficient Planar Heterojunction Perovskite Solar Cells by Vapour Deposition,” *Nature*, vol. 501, no. 7467, pp. 395–398, 2013.
- [58] M. A. Green, K. Emery, Y. Hishikawa, W. Warta, E. D. Dunlop, D. H. Levi, and A. W. Y. Ho-Baillie, “Solar Cell Efficiency Tables (Version 49),” *Progress in Photovoltaics: Research and Applications*, vol. 25, no. 1, pp. 3–13, 2017.
- [59] H. Zhou, Q. Chen, G. Li, S. Luo, T.-b. Song, H.-S. Duan, Z. Hong, J. You, Y. Liu, and Y. Yang, “Interface Engineering of Highly Efficient Perovskite Solar Cells,” *Science*, vol. 345, no. 6196, pp. 542–546, 2014.
- [60] F. Jiang, Y. Rong, H. Liu, T. Liu, L. Mao, W. Meng, F. Qin, Y. Jiang, B. Luo, S. Xiong, J. Tong, Y. Liu, Z. Li, H. Han, and Y. Zhou, “Synergistic Effect of PbI_2 Passivation and Chlorine Inclusion Yielding High Open-Circuit Voltage Exceeding 1.15 V in Both Mesoscopic and Inverted Planar $\text{CH}_3\text{NH}_3\text{PbI}_3(\text{Cl})$ -Based Perovskite Solar Cells,” *Advanced Functional Materials*, vol. 26, no. 44, pp. 8119–8127, 2016.

- [61] J.-P. Correa-Baena, W. Tress, K. Domanski, E. H. Anaraki, S.-H. Turren-Cruz, B. Roose, P. P. Boix, M. Grätzel, M. Saliba, A. Abate, and A. Hagfeldt, “Identifying and Suppressing Interfacial Recombination to Achieve High Open-Circuit Voltage in Perovskite Solar Cells,” *Energy & Environmental Science*, vol. 10, no. 5, pp. 1207–1212, 2017.
- [62] L. Meng, J. You, T.-F. Guo, and Y. Yang, “Recent Advances in the Inverted Planar Structure of Perovskite Solar Cells,” *Accounts of Chemical Research*, vol. 49, no. 1, pp. 155–165, 2016.
- [63] J. Yin, J. Cao, X. He, S. Yuan, S. Sun, J. Li, N. Zheng, and L. Lin, “Improved Stability of Perovskite Solar Cells in Ambient Air by Controlling the Mesoporous Layer,” *Journal of Materials Chemistry A*, vol. 3, pp. 16860–16866, 2015.
- [64] J. Yang, K. M. Fransishyn, and T. L. Kelly, “Comparing the Effect of Mesoporous and Planar Metal Oxides on the Stability of Methylammonium Lead Iodide Thin Films,” *Chemistry of Materials*, vol. 28, no. 20, pp. 7344–7352, 2016.
- [65] E. L. Unger, E. T. Hoke, C. D. Bailie, W. H. Nguyen, A. R. Bowring, T. Heumüller, M. G. Christoforo, and M. D. McGehee, “Hysteresis and Transient Behavior in Current-Voltage Measurements of Hybrid-Perovskite Absorber Solar Cells,” *Energy & Environmental Science*, vol. 7, no. 11, pp. 3690–3698, 2014.
- [66] H.-S. Kim and N.-G. Park, “Parameters Affecting I - V Hysteresis of $\text{CH}_3\text{NH}_3\text{PbI}_3$ Perovskite Solar Cells: Effects of Perovskite Crystal Size and Mesoporous TiO_2 Layer,” *The Journal of Physical Chemistry Letters*, vol. 5, no. 17, pp. 2927–2934, 2014.
- [67] X. Yin, M. Que, Y. Xing, and W. Que, “High Efficiency Hysteresis-Less Inverted Planar Heterojunction Perovskite Solar Cells with a Solution-Derived NiO_x Hole Contact Layer,” *Journal of Materials Chemistry A*, vol. 3, pp. 24495–24503, 2015.
- [68] P.-Y. Gu, N. Wang, C. Wang, Y. Zhou, G. Long, M. Tian, W. Chen, X. W. Sun, M. G. Kanatzidis, and Q. Zhang, “Pushing Up the Efficiency of Planar

References

- Perovskite Solar Cells to 18.2 % with Organic Small Molecules as the Electron Transport Layer,” *Journal of Materials Chemistry A*, vol. 5, no. 16, pp. 7339–7344, 2017.
- [69] T. M. Brenner, D. A. Egger, L. Kronik, G. Hodes, and D. Cahen, “Hybrid Organic-Inorganic Perovskites: Low-Cost Semiconductors with Intriguing Charge-Transport Properties,” *Nature Reviews Materials*, vol. 1, p. 15007, 2016.
- [70] G. Giorgi, J.-I. Fujisawa, H. Segawa, and K. Yamashita, “Small Photocarrier Effective Masses Featuring Ambipolar Transport in Methylammonium Lead Iodide Perovskite: A Density Functional Analysis,” *The Journal of Physical Chemistry Letters*, vol. 4, no. 24, pp. 4213–4216, 2013.
- [71] K. Galkowski, A. Mitioglu, A. Miyata, P. Plochocka, O. Portugall, G. E. Eperon, J. T.-W. Wang, T. Stergiopoulos, S. D. Stranks, H. J. Snaith, and R. J. Nicholas, “Determination of the Exciton Binding Energy and Effective Masses for Methylammonium and Formamidinium Lead Tri-Halide Perovskite Semiconductors,” *Energy & Environmental Science*, vol. 9, pp. 962–970, 2016.
- [72] F. Brivio, K. T. Butler, A. Walsh, and M. van Schilfhaarde, “Relativistic Quasiparticle Self-Consistent Electronic Structure of Hybrid Halide Perovskite Photovoltaic Absorbers,” *Physical Review B*, vol. 89, no. 15, p. 155204, 2014.
- [73] D. A. Jenny, J. J. Loferski, and P. Rappaport, “Photovoltaic Effect in GaAs *p-n* Junctions and Solar Energy Conversion,” *Physical Review*, vol. 101, no. 3, pp. 1208–1209, 1956.
- [74] B. Saparov and D. B. Mitzi, “Organic-Inorganic Perovskites: Structural Versatility for Functional Materials Design,” *Chemical Reviews*, vol. 116, no. 7, pp. 4558–4596, 2016.
- [75] E. R. Cohen and B. N. Taylor, “The 1973 Least-Squares Adjustment of the Fundamental Constants,” *Journal of Physical and Chemical Reference Data*, vol. 2, no. 4, pp. 663–734, 1973.
- [76] T. Umebayashi, K. Asai, T. Kondo, and A. Nakao, “Electronic Structures of Lead Iodide Based Low-Dimensional Crystals,” *Physical Review B*, vol. 67, no. 15, p. 155405, 2003.

- [77] F. Brivio, A. B. Walker, and A. Walsh, “Structural and Electronic Properties of Hybrid Perovskites for High-Efficiency Thin-Film Photovoltaics from First-Principles,” *APL Materials*, vol. 1, no. 4, p. 042111, 2013.
- [78] J. M. Frost, K. T. Butler, F. Brivio, C. H. Hendon, M. van Schilfgaarde, and A. Walsh, “Atomistic Origins of High-Performance in Hybrid Halide Perovskite Solar Cells,” *Nano Letters*, vol. 14, no. 5, pp. 2584–2590, 2014.
- [79] Y. H. Chang, C. H. Park, and K. Matsuishi, “First-Principles Study of the Structural and the Electronic Properties of the Lead-Halide-Based Inorganic-Organic Perovskites $(\text{CH}_3\text{NH}_3)\text{PbX}_3$ and CsPbX_3 ($X = \text{Cl}, \text{Br}, \text{I}$),” *Journal of the Korean Physical Society*, vol. 44, no. 4, pp. 889–893, 2004.
- [80] Q. Chen, N. De Marco, Y. M. Yang, T.-B. Song, C.-C. Chen, H. Zhao, Z. Hong, H. Zhou, and Y. Yang, “Under the Spotlight: The Organic-Inorganic Hybrid Halide Perovskite for Optoelectronic Applications,” *Nano Today*, vol. 10, no. 3, pp. 355–396, 2015.
- [81] R. E. Brandt, V. Stevanović, D. S. Ginley, and T. Buonassisi, “Identifying Defect-Tolerant Semiconductors with High Minority-Carrier Lifetimes: Beyond Hybrid Lead Halide Perovskites,” *MRS Communications*, vol. 5, no. 2, pp. 265–275, 2015.
- [82] W.-J. Yin, T. Shi, and Y. Yan, “Unusual Defect Physics in $\text{CH}_3\text{NH}_3\text{PbI}_3$ Perovskite Solar Cell Absorber,” *Applied Physics Letters*, vol. 104, no. 6, p. 063903, 2014.
- [83] W.-J. Yin, T. Shi, and Y. Yan, “Unique Properties of Halide Perovskites as Possible Origins of the Superior Solar Cell Performance,” *Advanced Materials*, vol. 26, no. 27, pp. 4653–4658, 2014.
- [84] A. Zakutayev, C. M. Caskey, A. N. Fioretti, D. S. Ginley, J. Vidal, V. Stevanovic, E. Tea, and S. Lany, “Defect Tolerant Semiconductors for Solar Energy Conversion,” *The Journal of Physical Chemistry Letters*, vol. 5, no. 7, pp. 1117–1125, 2014.
- [85] B. Wang, K. Y. Wong, X. Xiao, and T. Chen, “Elucidating the Reaction Pathways in the Synthesis of Organolead Trihalide Perovskite for High-Performance Solar Cells,” *Scientific Reports*, vol. 5, p. 10557, 2015.

References

- [86] S. T. Williams, F. Zuo, C.-C. Chueh, C.-Y. Liao, P.-W. Liang, and A. K.-Y. Jen, "Role of Chloride in the Morphological Evolution of Organo-Lead Halide Perovskite Thin Films," *ACS Nano*, vol. 8, no. 10, pp. 10640–10654, 2014.
- [87] Q. Chen, H. Zhou, Y. Fang, A. Z. Stieg, T.-B. Song, H.-H. Wang, X. Xu, Y. Liu, S. Lu, J. You, P. Sun, J. McKay, M. S. Goorsky, and Y. Yang, "The Optoelectronic Role of Chlorine in $\text{CH}_3\text{NH}_3\text{PbI}_3(\text{Cl})$ -Based Perovskite Solar Cells," *Nature Communications*, vol. 6, p. 7269, 2015.
- [88] J. Chae, Q. Dong, J. Huang, and A. Centrone, "Chloride Incorporation Process in $\text{CH}_3\text{NH}_3\text{PbI}_{3-x}\text{Cl}_x$ Perovskites via Nanoscale Bandgap Maps," *Nano Letters*, vol. 15, no. 12, pp. 8114–8121, 2015.
- [89] S. Colella, E. Mosconi, P. Fedeli, A. Listorti, F. Gazza, F. Orlandi, P. Ferro, T. Besagni, A. Rizzo, G. Calestani, G. Gigli, F. De Angelis, and R. Mosca, "MAPbI_{3-x}Cl_x Mixed Halide Perovskite for Hybrid Solar Cells: The Role of Chloride as Dopant on the Transport and Structural Properties," *Chemistry of Materials*, vol. 25, no. 22, pp. 4613–4618, 2013.
- [90] J.-H. Im, C.-R. Lee, J.-W. Lee, S.-W. Park, and N.-G. Park, "6.5 % Efficient Perovskite Quantum-Dot-Sensitized Solar Cell," *Nanoscale*, vol. 3, pp. 4088–4093, 2011.
- [91] Y. Liu, Z. Yang, D. Cui, X. Ren, J. Sun, X. Liu, J. Zhang, Q. Wei, H. Fan, F. Yu, X. Zhang, C. Zhao, and S. F. Liu, "Two-Inch-Sized Perovskite $\text{CH}_3\text{NH}_3\text{PbX}_3$ (X = Cl, Br, I) Crystals: Growth and Characterization," *Advanced Materials*, vol. 27, no. 35, pp. 5176–5183, 2015.
- [92] Y. Chen, M. He, J. Peng, Y. Sun, and Z. Liang, "Structure and Growth Control of Organic-Inorganic Halide Perovskites for Optoelectronics: From Polycrystalline Films to Single Crystals," *Advanced Science*, vol. 3, no. 4, p. 1500392, 2016.
- [93] T. Baikie, Y. Fang, J. M. Kadro, M. Schreyer, F. Wei, S. G. Mhaisalkar, M. Grätzel, and T. J. White, "Synthesis and Crystal Chemistry of the Hybrid Perovskite $(\text{CH}_3\text{NH}_3)\text{PbI}_3$ for Solid-State Sensitised Solar Cell Applications," *Journal of Materials Chemistry A*, vol. 1, no. 18, pp. 5628–5641, 2013.
- [94] E. D. Palik (ed.), *Handbook of Optical Constants of Solids*. San Diego: Aca-

- demic Press, 1998.
- [95] S. Minoura, K. Kodera, T. Maekawa, K. Miyazaki, S. Niki, and H. Fujiwara, “Dielectric Function of Cu(In, Ga)Se₂-Based Polycrystalline Materials,” *Journal of Applied Physics*, vol. 113, no. 6, p. 063505, 2013.
- [96] M. A. Green, “Self-Consistent Optical Parameters of Intrinsic Silicon at 300 K Including Temperature Coefficients,” *Solar Energy Materials and Solar Cells*, vol. 92, no. 11, pp. 1305–1310, 2008.
- [97] W. Theiss, “SCOUT Software Package, <http://www.wtheiss.com>.”
- [98] C. Wehrenfennig, M. Liu, H. J. Snaith, M. B. Johnston, and L. M. Herz, “Homogeneous Emission Line Broadening in the Organo Lead Halide Perovskite CH₃NH₃PbI_{3-x}Cl_x,” *The Journal of Physical Chemistry Letters*, vol. 5, no. 8, pp. 1300–1306, 2014.
- [99] S. D. Stranks, G. E. Eperon, G. Grancini, C. Menelaou, M. J. P. Alcocer, T. Leijtens, L. M. Herz, A. Petrozza, and H. J. Snaith, “Electron-Hole Diffusion Lengths Exceeding 1 Micrometer in an Organometal Trihalide Perovskite Absorber,” *Science*, vol. 342, no. 6156, pp. 341–344, 2013.
- [100] K. Tvingstedt, O. Malinkiewicz, A. Baumann, C. Deibel, H. J. Snaith, V. Dyakonov, and H. J. Bolink, “Radiative Efficiency of Lead Iodide Based Perovskite Solar Cells,” *Scientific Reports*, vol. 4, p. 6071, 2014.
- [101] P. Würfel, “The Chemical Potential of Radiation,” *Journal of Physics C: Solid State Physics*, vol. 15, no. 18, pp. 3967–3985, 1982.
- [102] F. Staub, H. Hempel, J.-C. Hebig, J. Mock, U. W. Paetzold, U. Rau, T. Unold, and T. Kirchartz, “Beyond Bulk Lifetimes: Insights into Lead Halide Perovskite Films from Time-Resolved Photoluminescence,” *Physical Review Applied*, vol. 6, no. 4, p. 044017, 2016.
- [103] T. Trupke, E. Daub, and P. Würfel, “Absorptivity of Silicon Solar Cells Obtained from Luminescence,” *Solar Energy Materials and Solar Cells*, vol. 53, no. 1, pp. 103–114, 1998.
- [104] C. Barugkin, J. Cong, T. Duong, S. Rahman, H. T. Nguyen, D. Macdonald, T. P. White, and K. R. Catchpole, “Ultralow Absorption Coefficient and Temperature Dependence of Radiative Recombination of CH₃NH₃PbI₃ Perovskite

References

- from Photoluminescence,” *The Journal of Physical Chemistry Letters*, vol. 6, no. 5, pp. 767–772, 2015.
- [105] O. Stenzel, *The Physics of Thin Film Optical Spectra: An Introduction*. No. 44 in Springer series in surface sciences, Berlin Heidelberg New York: Springer-Verlag, 2005.
- [106] M. Sendner, P. K. Nayak, D. A. Egger, S. Beck, C. Müller, B. Epping, W. Kowalsky, L. Kronik, H. J. Snaith, A. Pucci, and R. Lovrinčić, “Optical Phonons in Methylammonium Lead Halide Perovskites and Implications for Charge Transport,” *Materials Horizons*, vol. 3, no. 6, pp. 613–620, 2016.
- [107] A. D. Wright, C. Verdi, R. L. Milot, G. E. Eperon, M. A. Pérez-Osorio, H. J. Snaith, F. Giustino, M. B. Johnston, and L. M. Herz, “Electron-Phonon Coupling in Hybrid Lead Halide Perovskites,” *Nature Communications*, vol. 7, p. 11755, 2016.
- [108] T. Wang, B. Daiber, J. M. Frost, S. A. Mann, E. C. Garnett, A. Walsh, and B. Ehrler, “Indirect to Direct Bandgap Transition in Methylammonium Lead Halide Perovskite,” *Energy & Environmental Science*, vol. 10, no. 2, pp. 509–515, 2017.
- [109] T. Kirchartz and U. Rau, “Decreasing Radiative Recombination Coefficients via an Indirect Band Gap in Lead Halide Perovskites,” *The Journal of Physical Chemistry Letters*, vol. 8, no. 6, pp. 1265–1271, 2017.
- [110] M. V. Kurik, “Urbach Rule,” *physica status solidi (a)*, vol. 8, no. 9, pp. 9–45, 1971.
- [111] G. D. Cody, T. Tiedje, B. Abeles, B. Brooks, and Y. Goldstein, “Disorder and the Optical-Absorption Edge of Hydrogenated Amorphous Silicon,” *Physical Review Letters*, vol. 47, no. 20, pp. 1480–1483, 1981.
- [112] S. M. Wasim, G. Marín, C. Rincón, and G. Sánchez Pérez, “Urbach-Martienssen’s Tail in the Absorption Spectra of the Ordered Vacancy Compound CuIn_3Se_5 ,” *Journal of Applied Physics*, vol. 84, no. 10, pp. 5823–5825, 1998.
- [113] S. D. Stranks and H. J. Snaith, “Metal-Halide Perovskites for Photovoltaic and Light-Emitting Devices,” *Nature Nanotechnology*, vol. 10, no. 5, pp. 391–402,

- 2015.
- [114] E. M. Hutter, M. C. Gélvez-Rueda, A. Osherov, V. Bulović, F. C. Grozema, S. D. Stranks, and T. J. Savenije, “Direct-Indirect Character of the Bandgap in Methylammonium Lead Iodide Perovskite,” *Nature Materials*, vol. 16, no. 1, pp. 115–120, 2017.
- [115] S. Liu, S. Srinivasan, J. Tao, M. C. Grady, M. Soroush, and A. M. Rappe, “Modeling Spin-Forbidden Monomer Self-Initiation Reactions in Spontaneous Free-Radical Polymerization of Acrylates and Methacrylates,” *The Journal of Physical Chemistry A*, vol. 118, no. 40, pp. 9310–9318, 2014.
- [116] C. Motta, F. El-Mellouhi, S. Kais, N. Tabet, F. Alharbi, and S. Sanvito, “Revealing the Role of Organic Cations in Hybrid Halide Perovskite $\text{CH}_3\text{NH}_3\text{PbI}_3$,” *Nature Communications*, vol. 6, p. 7026, 2015.
- [117] P. Azarhoosh, S. McKechnie, J. M. Frost, A. Walsh, and M. van Schilfgaarde, “Research Update: Relativistic Origin of Slow Electron-Hole Recombination in Hybrid Halide Perovskite Solar Cells,” *APL Materials*, vol. 4, no. 9, p. 091501, 2016.
- [118] F. Zheng, L. Z. Tan, S. Liu, and A. M. Rappe, “Rashba Spin-Orbit Coupling Enhanced Carrier Lifetime in $\text{CH}_3\text{NH}_3\text{PbI}_3$,” *Nano Letters*, vol. 15, no. 12, pp. 7794–7800, 2015.
- [119] Z.-G. Yu, “Rashba Effect and Carrier Mobility in Hybrid Organic-Inorganic Perovskites,” *The Journal of Physical Chemistry Letters*, vol. 7, no. 16, pp. 3078–3083, 2016.
- [120] T. Etienne, E. Mosconi, and F. De Angelis, “Dynamical Origin of the Rashba Effect in Organohalide Lead Perovskites: A Key to Suppressed Carrier Recombination in Perovskite Solar Cells?,” *The Journal of Physical Chemistry Letters*, vol. 7, no. 9, pp. 1638–1645, 2016.
- [121] A. Filippetti, P. Delugas, and A. Mattoni, “Radiative Recombination and Photoconversion of Methylammonium Lead Iodide Perovskite by First Principles: Properties of an Inorganic Semiconductor within a Hybrid Body,” *The Journal of Physical Chemistry C*, vol. 118, no. 43, pp. 24843–24853, 2014.
- [122] H. Kawai, G. Giorgi, A. Marini, and K. Yamashita, “The Mechanism of Slow

References

- Hot-Hole Cooling in Lead-Iodide Perovskite: First-Principles Calculation on Carrier Lifetime from Electron-Phonon Interaction,” *Nano Letters*, vol. 15, no. 5, pp. 3103–3108, 2015.
- [123] J.-E. Moser, “Perovskite Photovoltaics: Slow Recombination Unveiled,” *Nature Materials*, vol. 16, no. 1, pp. 4–6, 2017.
- [124] A. Buin, P. Pietsch, J. Xu, O. Voznyy, A. H. Ip, R. Comin, and E. H. Sargent, “Materials Processing Routes to Trap-Free Halide Perovskites,” *Nano Letters*, vol. 14, no. 11, pp. 6281–6286, 2014.
- [125] Q. Wang, Y. Shao, H. Xie, L. Lyu, X. Liu, Y. Gao, and J. Huang, “Qualifying Composition Dependent p and n Self-Doping in $\text{CH}_3\text{NH}_3\text{PbI}_3$,” *Applied Physics Letters*, vol. 105, no. 16, p. 163508, 2014.
- [126] R. A. Street, *Hydrogenated Amorphous Silicon*. Cambridge: Cambridge University Press, 1991.
- [127] W. Beyer and H. Overhof, “Doping Effects in a-Si:H,” in *Semiconductors and Semimetals* (J. I. Pankove, ed.), pp. 257–307, New York: Elsevier, 1984.
- [128] E. Edri, S. Kirmayer, S. Mukhopadhyay, K. Gartsman, G. Hodes, and D. Cahen, “Elucidating the Charge Carrier Separation and Working Mechanism of $\text{CH}_3\text{NH}_3\text{PbI}_{3-x}\text{Cl}_x$ Perovskite Solar Cells,” *Nature Communications*, vol. 5, p. 3461, 2014.
- [129] L. L. Baranowski, K. McLaughlin, P. Zawadzki, S. Lany, A. Norman, H. Hempel, R. Eichberger, T. Unold, E. S. Toberer, and A. Zakutayev, “Effects of Disorder on Carrier Transport in Cu_2SnS_3 ,” *Physical Review Applied*, vol. 4, no. 4, p. 044017, 2015.
- [130] G. W. Guglietta, K. R. Choudhury, J. V. Caspar, and J. B. Baxter, “Employing Time-Resolved Terahertz Spectroscopy to Analyze Carrier Dynamics in Thin-Film $\text{Cu}_2\text{ZnSn}(\text{S},\text{Se})_4$ Absorber Layers,” *Applied Physics Letters*, vol. 104, no. 25, p. 253901, 2014.
- [131] P. U. Jepsen, W. Schairer, I. H. Libon, U. Lemmer, N. E. Hecker, M. Birkholz, K. Lips, and M. Schall, “Ultrafast Carrier Trapping in Microcrystalline Silicon Observed in Optical Pump-Terahertz Probe Measurements,” *Applied Physics Letters*, vol. 79, no. 9, pp. 1291–1293, 2001.

- [132] C. Wehrenfennig, M. Liu, H. J. Snaith, M. B. Johnston, and L. M. Herz, “Charge-Carrier Dynamics in Vapour-Deposited Films of the Organolead Halide Perovskite $\text{CH}_3\text{NH}_3\text{PbI}_{3-x}\text{Cl}_x$,” *Energy & Environmental Science*, vol. 7, no. 7, pp. 2269–2275, 2014.
- [133] C. Wehrenfennig, G. E. Eperon, M. B. Johnston, H. J. Snaith, and L. M. Herz, “High Charge Carrier Mobilities and Lifetimes in Organolead Trihalide Perovskites,” *Advanced Materials*, vol. 26, no. 10, pp. 1584–1589, 2014.
- [134] Y. Shirota, “Photo- and Electroactive Amorphous Molecular Materials – Molecular Design, Syntheses, Reactions, Properties, and Applications,” *Journal of Material Chemistry*, vol. 15, no. 1, pp. 75–93, 2005.
- [135] V. Coropceanu, J. Cornil, D. A. da Silva Filho, Y. Olivier, R. Silbey, and J.-L. Brédas, “Charge Transport in Organic Semiconductors,” *Chemical Reviews*, vol. 107, no. 4, pp. 926–952, 2007.
- [136] T. M. Brenner, D. A. Egger, A. M. Rappe, L. Kronik, G. Hodes, and D. Cahen, “Are Mobilities in Hybrid Organic-Inorganic Halide Perovskites Actually “High”?,” *The Journal of Physical Chemistry Letters*, vol. 6, no. 23, pp. 4754–4757, 2015.
- [137] Q. Lin, A. Armin, R. C. R. Nagiri, P. L. Burn, and P. Meredith, “Electro-Optics of Perovskite Solar Cells,” *Nature Photonics*, vol. 9, no. 2, pp. 106–112, 2014.
- [138] Y. Yang, D. P. Ostrowski, R. M. France, K. Zhu, J. van de Lagemaat, J. M. Luther, and M. C. Beard, “Observation of a Hot-Phonon Bottleneck in Lead-Iodide Perovskites,” *Nature Photonics*, vol. 10, no. 1, pp. 53–59, 2015.
- [139] A. Miyata, A. Mitioglu, P. Plochocka, O. Portugall, J. T.-W. Wang, S. D. Stranks, H. J. Snaith, and R. J. Nicholas, “Direct Measurement of the Exciton Binding Energy and Effective Masses for Charge Carriers in Organic-Inorganic Tri-Halide Perovskites,” *Nature Physics*, vol. 11, no. 7, pp. 582–587, 2015.
- [140] Y. Yamada, T. Nakamura, M. Endo, A. Wakamiya, and Y. Kanemitsu, “Photocarrier Recombination Dynamics in Perovskite $\text{CH}_3\text{NH}_3\text{PbI}_3$ for Solar Cell Applications,” *Journal of the American Chemical Society*, vol. 136, no. 33, pp. 11610–11613, 2014.

References

- [141] Y. Yang, M. Yang, Z. Li, R. Crisp, K. Zhu, and M. C. Beard, "Comparison of Recombination Dynamics in $\text{CH}_3\text{NH}_3\text{PbBr}_3$ and $\text{CH}_3\text{NH}_3\text{PbI}_3$ Perovskite Films: Influence of Exciton Binding Energy," *The Journal of Physical Chemistry Letters*, vol. 6, no. 23, pp. 4688–4692, 2015.
- [142] W. Tress, N. Marinova, O. Inganäs, M. K. Nazeeruddin, S. M. Zakeeruddin, and M. Grätzel, "Predicting the Open-Circuit Voltage of $\text{CH}_3\text{NH}_3\text{PbI}_3$ Perovskite Solar Cells Using Electroluminescence and Photovoltaic Quantum Efficiency Spectra: The Role of Radiative and Non-Radiative Recombination," *Advanced Energy Materials*, vol. 5, no. 3, p. 1400812, 2015.
- [143] J. Yao, T. Kirchartz, M. S. Vezie, M. A. Faist, W. Gong, Z. He, H. Wu, J. Troughton, T. Watson, D. Bryant, and J. Nelson, "Quantifying Losses in Open-Circuit Voltage in Solution-Processable Solar Cells," *Physical Review Applied*, vol. 4, no. 1, p. 014020, 2015.
- [144] P. Asbeck, "Self-Absorption Effects on the Radiative Lifetime in GaAs-GaAlAs Double Heterostructures," *Journal of Applied Physics*, vol. 48, no. 2, pp. 820–822, 1977.
- [145] B. E. Pieters, J. Krč, and M. Zeman, "Advanced Numerical Simulation Tool for Solar Cells - ASA5," in *Proceedings of the 4th WCPEC*, (Waikoloa, Hawaii), pp. 1513–1516, May 2006.
- [146] M. Maiberg and R. Scheer, "Theoretical Study of Time-Resolved Luminescence in Semiconductors. I. Decay from the Steady State," *Journal of Applied Physics*, vol. 116, no. 12, p. 123710, 2014.
- [147] A. G. Aberle, "Surface Passivation of Crystalline Silicon Solar Cells: A Review," *Progress in Photovoltaics: Research and Applications*, vol. 8, no. 5, pp. 473–487, 2000.
- [148] A. M. Munro, I. Jen-La Plante, M. S. Ng, and D. S. Ginger, "Quantitative Study of the Effects of Surface Ligand Concentration on CdSe Nanocrystal Photoluminescence," *The Journal of Physical Chemistry C*, vol. 111, no. 17, pp. 6220–6227, 2007.
- [149] J. Tang, K. W. Kemp, S. Hoogland, K. S. Jeong, H. Liu, L. Levina, M. Furukawa, X. Wang, R. Debnath, D. Cha, K. W. Chou, A. Fischer, A. Amassian,

- J. B. Asbury, and E. H. Sargent, "Colloidal-Quantum-Dot Photovoltaics Using Atomic-Ligand Passivation," *Nature Materials*, vol. 10, no. 10, pp. 765–771, 2011.
- [150] M. T. Sheldon, C. N. Eisler, and H. A. Atwater, "GaAs Passivation with Trioctylphosphine Sulfide for Enhanced Solar Cell Efficiency and Durability," *Advanced Energy Materials*, vol. 2, no. 3, pp. 339–344, 2012.
- [151] G. E. Eperon, S. N. Habisreutinger, T. Leijtens, B. J. Bruijnaers, J. J. van Franeker, D. W. deQuilettes, S. Pathak, R. J. Sutton, G. Grancini, D. S. Ginger, R. A. J. Janssen, A. Petrozza, and H. J. Snaith, "The Importance of Moisture in Hybrid Lead Halide Perovskite Thin Film Fabrication," *ACS Nano*, vol. 9, no. 9, pp. 9380–9393, 2015.
- [152] J. You, Y. M. Yang, Z. Hong, T.-B. Song, L. Meng, Y. Liu, C. Jiang, H. Zhou, W.-H. Chang, G. Li, and Y. Yang, "Moisture Assisted Perovskite Film Growth for High Performance Solar Cells," *Applied Physics Letters*, vol. 105, no. 18, p. 183902, 2014.
- [153] Q. Chen, H. Zhou, T.-B. Song, S. Luo, Z. Hong, H.-S. Duan, L. Dou, Y. Liu, and Y. Yang, "Controllable Self-Induced Passivation of Hybrid Lead Iodide Perovskites toward High Performance Solar Cells," *Nano Letters*, vol. 14, no. 7, pp. 4158–4163, 2014.
- [154] N. K. Noel, A. Abate, S. D. Stranks, E. S. Parrott, V. M. Burlakov, A. Goriely, and H. J. Snaith, "Enhanced Photoluminescence and Solar Cell Performance via Lewis Base Passivation of Organic-Inorganic Lead Halide Perovskites," *ACS Nano*, vol. 8, no. 10, pp. 9815–9821, 2014.
- [155] D. W. de Quilettes, S. M. Vorpahl, S. D. Stranks, H. Nagaoka, G. E. Eperon, M. E. Ziffer, H. J. Snaith, and D. S. Ginger, "Impact of Microstructure on Local Carrier Lifetime in Perovskite Solar Cells," *Science*, vol. 348, no. 6235, pp. 683–686, 2015.
- [156] Y. Li, X. Xu, C. Wang, C. Wang, F. Xie, J. Yang, and Y. Gao, "Degradation by Exposure of Coevaporated $\text{CH}_3\text{NH}_3\text{PbI}_3$ Thin Films," *The Journal of Physical Chemistry C*, vol. 119, no. 42, pp. 23996–24002, 2015.
- [157] J. Chun-Ren Ke, A. S. Walton, D. J. Lewis, A. Tedstone, P. O'Brien,

References

- A. G. Thomas, and W. R. Flavell, “*In Situ* Investigation of Degradation at Organometal Halide Perovskite Surfaces by X-Ray Photoelectron Spectroscopy at Realistic Water Vapour Pressure,” *Chemical Communications*, vol. 53, no. 37, pp. 5231–5234, 2017.
- [158] R. I. Hegde, S. R. Sainkar, S. Badrinarayanan, and A. P. B. Sinha, “A Study of Dilute Tin Alloys by X-Ray Photoelectron Spectroscopy,” *Journal of Electron Spectroscopy and Related Phenomena*, vol. 24, no. 1, pp. 19–25, 1981.
- [159] M. J. Bozack and K. W. Bryant, “Elemental Lead by XPS,” *Surface Science Spectra*, vol. 1, no. 3, pp. 324–327, 1992.
- [160] A. B. Sproul, “Dimensionless Solution of the Equation Describing the Effect of Surface Recombination on Carrier Decay in Semiconductors,” *Journal of Applied Physics*, vol. 76, no. 5, pp. 2851–2854, 1994.
- [161] B. Hoex, S. B. S. Heil, E. Langereis, M. C. M. van de Sanden, and W. M. M. Kessels, “Ultralow Surface Recombination of *c*-Si Substrates Passivated by Plasma-Assisted Atomic Layer Deposited Al₂O₃,” *Applied Physics Letters*, vol. 89, no. 4, p. 042112, 2006.
- [162] G. Agostinelli, A. Delabie, P. Vitanov, Z. Alexieva, H. Dekkers, S. De Wolf, and G. Beaucarne, “Very Low Surface Recombination Velocities on *p*-Type Silicon Wafers Passivated with a Dielectric with Fixed Negative Charge,” *Solar Energy Materials and Solar Cells*, vol. 90, no. 18, pp. 3438–3443, 2006.
- [163] Y. Yang, Y. Yan, M. Yang, S. Choi, K. Zhu, J. M. Luther, and M. C. Beard, “Low Surface Recombination Velocity in Solution-Grown CH₃NH₃PbBr₃ Perovskite Single Crystal,” *Nature Communications*, vol. 6, p. 7961, 2015.
- [164] N. W. Ashcroft and N. D. Mermin, *Chapter 28 Homogeneous Semiconductors*. Belmont: Brooks/Cole, Cengage Learning, 1976.
- [165] W. Tress, “Maximum Efficiency and Open-Circuit Voltage of Perovskite Solar Cells,” in *Organic-Inorganic Halide Perovskite Photovoltaics. From Fundamentals to Device Architectures* (N.-G. Park, M. Grätzel, and T. Miyasaka, eds.), p. 62, Cham: Springer, 2016.
- [166] W. Shockley and H. J. Queisser, “Detailed Balance Limit of Efficiency of *p-n* Junction Solar Cells,” *Journal of Applied Physics*, vol. 32, no. 3, pp. 510–519,

- 1961.
- [167] A. Rabl, “Solar Geometry,” in *Active Solar Collectors and Their Applications*, pp. 28–47, New York: Oxford University Press, 1985.
- [168] Z. R. Abrams, *Thermodynamics, Entropy, Information and the Efficiency of Solar Cells*. PhD thesis, University of California, Berkeley, 2012.
- [169] D. Bi, W. Tress, M. I. Dar, P. Gao, J. Luo, C. Renevier, K. Schenk, A. Abate, F. Giordano, J.-P. Correa Baena, J.-D. Decoppet, S. M. Zakeeruddin, M. K. Nazeeruddin, M. Grätzel, and A. Hagfeldt, “Efficient Luminescent Solar Cells Based on Tailored Mixed-Cation Perovskites,” *Science Advances*, vol. 2, no. 1, 2016.
- [170] O. D. Miller, E. Yablonovitch, and S. R. Kurtz, “Strong Internal and External Luminescence as Solar Cells Approach the Shockley-Queisser Limit,” *IEEE Journal of Photovoltaics*, vol. 2, no. 3, pp. 303–311, 2012.
- [171] M. I. Saidaminov, A. L. Abdelhady, B. Murali, E. Alarousu, V. M. Burlakov, W. Peng, I. Dursun, L. Wang, Y. He, G. Maculan, A. Goriely, T. Wu, O. F. Mohammed, and O. M. Bakr, “High-Quality Bulk Hybrid Perovskite Single Crystals within Minutes by Inverse Temperature Crystallization,” *Nature Communications*, vol. 6, p. 7586, 2015.
- [172] Y. Fang, Q. Dong, Y. Shao, Y. Yuan, and J. Huang, “Highly Narrowband Perovskite Single-Crystal Photodetectors Enabled by Surface-Charge Recombination,” *Nature Photonics*, vol. 9, no. 10, pp. 679–686, 2015.
- [173] H. Wei, Y. Fang, P. Mulligan, W. Chuirazzi, H.-H. Fang, C. Wang, B. R. Ecker, Y. Gao, M. A. Loi, L. Cao, and J. Huang, “Sensitive X-Ray Detectors Made of Methylammonium Lead Tribromide Perovskite Single Crystals,” *Nature Photonics*, vol. 10, no. 5, pp. 333–339, 2016.
- [174] H.-H. Fang, S. Adjokatse, H. Wei, J. Yang, G. R. Blake, J. Huang, J. Even, and M. A. Loi, “Ultrahigh Sensitivity of Methylammonium Lead Tribromide Perovskite Single Crystals to Environmental Gases,” *Science Advances*, vol. 2, no. 7, 2016.
- [175] S.-T. Ha, C. Shen, J. Zhang, and Q. Xiong, “Laser Cooling of Organic-Inorganic Lead Halide Perovskites,” *Nature Photonics*, vol. 10, no. 2, pp. 115–

References

- 121, 2015.
- [176] T. Yamada, Y. Yamada, H. Nishimura, Y. Nakaike, A. Wakamiya, Y. Murata, and Y. Kanemitsu, “Fast Free-Carrier Diffusion in $\text{CH}_3\text{NH}_3\text{PbBr}_3$ Single Crystals Revealed by Time-Resolved One- and Two-Photon Excitation Photoluminescence Spectroscopy,” *Advanced Electronic Materials*, vol. 2, no. 3, p. 1500290, 2016.
- [177] T. Yamada, Y. Yamada, Y. Nakaike, A. Wakamiya, and Y. Kanemitsu, “Photon Emission and Reabsorption Processes in $\text{CH}_3\text{NH}_3\text{PbBr}_3$ Single Crystals Revealed by Time-Resolved Two-Photon-Excitation Photoluminescence Microscopy,” *Physical Review Applied*, vol. 7, no. 1, p. 014001, 2017.
- [178] Y. Fang, H. Wei, Q. Dong, and J. Huang, “Quantification of Re-Absorption and Re-Emission Processes to Determine Photon Recycling Efficiency in Perovskite Single Crystals,” *Nature Communications*, vol. 8, p. 14417, 2017.
- [179] H. Diab, C. Arnold, F. Lédée, G. Trippé-Allard, G. Delport, C. Vilar, F. Bretenaker, J. Barjon, J.-S. Lauret, E. Deleporte, and D. Garrot, “Impact of Re-absorption on the Emission Spectra and Recombination Dynamics of Hybrid Perovskite Single Crystals,” *The Journal of Physical Chemistry Letters*, vol. 8, no. 13, pp. 2977–2983, 2017.
- [180] B. Wenger, P. K. Nayak, X. Wen, S. V. Kesava, N. K. Noel, and H. J. Snaith, “Consolidation of the Optoelectronic Properties of $\text{CH}_3\text{NH}_3\text{PbBr}_3$ Perovskite Single Crystals,” *Nature Communications*, vol. 8, p. 590, 2017.
- [181] Q. Dong, Y. Fang, Y. Shao, P. Mulligan, J. Qiu, L. Cao, and J. Huang, “Electron-Hole Diffusion Lengths $> 175 \mu\text{m}$ in Solution-Grown $\text{CH}_3\text{NH}_3\text{PbI}_3$ Single Crystals,” *Science*, vol. 347, no. 6225, pp. 967–970, 2015.
- [182] D. Shi, V. Adinolfi, R. Comin, M. Yuan, E. Alarousu, A. Buin, Y. Chen, S. Hoogland, A. Rothenberger, K. Katsiev, Y. Losovyj, X. Zhang, P. A. Dowben, O. F. Mohammed, E. H. Sargent, and O. M. Bakr, “Low Trap-State Density and Long Carrier Diffusion in Organolead Trihalide Perovskite Single Crystals,” *Science*, vol. 347, no. 6221, pp. 519–522, 2015.
- [183] H.-H. Fang, R. Raissa, M. Abdu-Aguye, S. Adjokatse, G. R. Blake, J. Even, and M. A. Loi, “Photophysics of Organic-Inorganic Hybrid Lead Iodide Per-

- ovskite Single Crystals,” *Advanced Functional Materials*, vol. 25, no. 16, pp. 2378–2385, 2015.
- [184] B. Wu, H. T. Nguyen, Z. Ku, G. Han, D. Giovanni, N. Mathews, H. J. Fan, and T. C. Sum, “Discerning the Surface and Bulk Recombination Kinetics of Organic-Inorganic Halide Perovskite Single Crystals,” *Advanced Energy Materials*, vol. 6, no. 14, p. 1600551, 2016.
- [185] Y. Yamada, T. Yamada, L. Q. Phuong, N. Maruyama, H. Nishimura, A. Wakamiya, Y. Murata, and Y. Kanemitsu, “Dynamic Optical Properties of $\text{CH}_3\text{NH}_3\text{PbI}_3$ Single Crystals As Revealed by One- and Two-Photon Excited Photoluminescence Measurements,” *Journal of the American Chemical Society*, vol. 137, no. 33, pp. 10456–10459, 2015.
- [186] L. M. Pazos-Outón, M. Szumilo, R. Lamboll, J. M. Richter, M. Crespo-Quesada, M. Abdi-Jalebi, H. J. Beeson, M. Vrućinić, M. Alsari, H. J. Snaith, B. Ehrler, R. H. Friend, and F. Deschler, “Photon Recycling in Lead Iodide Perovskite Solar Cells,” *Science*, vol. 351, no. 6280, pp. 1430–1433, 2016.
- [187] I. Dursun, Y. Zheng, T. Guo, M. De Bastiani, B. Turedi, L. Sinatra, M. A. Haque, B. Sun, A. A. Zhumekenov, M. I. Saidaminov, F. P. García de Arquer, E. H. Sargent, T. Wu, Y. N. Gartstein, O. M. Bakr, O. F. Mohammed, and A. V. Malko, “Efficient Photon Recycling and Radiation Trapping in Cesium Lead Halide Perovskite Waveguides,” *ACS Energy Letters*, vol. 3, no. 7, pp. 1492–1498, 2018.
- [188] M. Ansari-Rad and J. Bisquert, “Insight into photon recycling in perovskite semiconductors from the concept of photon diffusion,” *Physical Review Applied*, vol. 10, p. 034062, 2018.
- [189] J. M. Richter, M. Abdi-Jalebi, A. Sadhanala, M. Tabachnyk, J. P. Rivett, L. M. Pazos-Outón, K. C. Gödel, M. Price, F. Deschler, and R. H. Friend, “Enhancing Photoluminescence Yields in Lead Halide Perovskites by Photon Recycling and Light Out-Coupling,” *Nature Communications*, vol. 7, p. 13941, 2016.
- [190] F. Staub, T. Kirchartz, K. Bittkau, and U. Rau, “Manipulating the Net Radiative Recombination Rate in Lead Halide Perovskite Films by Modification of

References

- Light Outcoupling,” *The Journal of Physical Chemistry Letters*, vol. 8, no. 20, pp. 5084–5090, 2017.
- [191] F. Staub, I. Anusca, D. C. Lupascu, U. Rau, and T. Kirchartz, “Effect of Reabsorption and Photon Recycling on Photoluminescence Spectra and Transients in Lead-Halide Perovskite Crystals,” *Journal of Physics: Materials*, vol. 3, no. 2, p. 025003, 2020.
- [192] Y. Liu, Z. Yang, and S. F. Liu, “Recent Progress in Single-Crystalline Perovskite Research Including Crystal Preparation, Property Evaluation, and Applications,” *Advanced Science*, vol. 5, no. 1, p. 1700471, 2018.
- [193] I. Suárez, E. J. Juárez-Pérez, J. Bisquert, I. Mora-Seró, and J. P. Martínez-Pastor, “Polymer/Perovskite Amplifying Waveguides for Active Hybrid Silicon Photonics,” *Advanced Materials*, vol. 27, no. 40, pp. 6157–6162, 2015.
- [194] J. M. Marin-Beloqui, J. P. Hernández, and E. Palomares, “Photo-Induced Charge Recombination Kinetics in MAPbI_{3-x}Cl_x Perovskite-Like Solar Cells Using Low Band-Gap Polymers as Hole Conductors,” *Chemical Communications*, vol. 50, no. 93, pp. 14566–14569, 2014.
- [195] C. S. Ponseca Jr., E. M. Hutter, P. Piatkowski, B. Cohen, T. Pascher, A. Douhal, A. Yartsev, V. Sundström, and T. J. Savenije, “Mechanism of Charge Transfer and Recombination Dynamics in Organo Metal Halide Perovskites and Organic Electrodes, PCBM, and Spiro-OMeTAD: Role of Dark Carriers,” *Journal of the American Chemical Society*, vol. 137, no. 51, pp. 16043–16048, 2015.
- [196] J. C. Brauer, Y. H. Lee, M. K. Nazeeruddin, and N. Banerji, “Charge Transfer Dynamics from Organometal Halide Perovskite to Polymeric Hole Transport Materials in Hybrid Solar Cells,” *The Journal of Physical Chemistry Letters*, vol. 6, no. 18, pp. 3675–3681, 2015.
- [197] B. Krogmeier, F. Staub, D. Grabowski, U. Rau, and T. Kirchartz, “Quantitative Analysis of the Transient Photoluminescence of CH₃NH₃PbI₃/PC₆₁BM Heterojunctions by Numerical Simulations,” *Sustainable Energy Fuels*, vol. 2, no. 5, pp. 1027–1034, 2018.
- [198] D. Dominé, F.-J. Haug, C. Battaglia, and C. Ballif, “Modeling of Light Scat-

- tering from Micro- and Nanotextured Surfaces,” *Journal of Applied Physics*, vol. 107, no. 4, p. 044504, 2010.
- [199] M. A. Green, “Lambertian Light Trapping in Textured Solar Cells and Light-Emitting Diodes: Analytical Solutions,” *Progress in Photovoltaics: Research and Applications*, vol. 10, no. 4, pp. 235–241, 2002.
- [200] M. Zeman, R. A. C. M. M. van Swaaij, J. W. Metselaar, and R. E. I. Schropp, “Optical Modeling of *a*-Si:H Solar Cells with Rough Interfaces: Effect of Back Contact and Interface Roughness,” *Journal of Applied Physics*, vol. 88, no. 11, pp. 6436–6443, 2000.
- [201] J. Krč, M. Zeman, F. Smole, and M. Topič, “Optical Modeling of *a*-Si:H Solar Cells Deposited on Textured Glass/SnO₂ Substrates,” *Journal of Applied Physics*, vol. 92, no. 2, pp. 749–755, 2002.
- [202] M. van Eerden, M. Jaysankar, A. Hadipour, T. Merckx, J. J. Schermer, T. Aernouts, J. Poortmans, and U. W. Paetzold, “Optical Analysis of Planar Multicrystalline Perovskite Solar Cells,” *Advanced Optical Materials*, vol. 5, no. 18, p. 1700151, 2017.
- [203] H.-S. Duan, H. Zhou, Q. Chen, P. Sun, S. Luo, T.-B. Song, B. Bob, and Y. Yang, “The Identification and Characterization of Defect States in Hybrid Organic-Inorganic Perovskite Photovoltaics,” *Physical Chemistry Chemical Physics*, vol. 17, no. 1, pp. 112–116, 2015.
- [204] A. Baumann, S. Văth, P. Rieder, M. C. Heiber, K. Tvingstedt, and V. Dyakonov, “Identification of Trap States in Perovskite Solar Cells,” *The Journal of Physical Chemistry Letters*, vol. 6, no. 12, pp. 2350–2354, 2015.
- [205] P. T. Landsberg, C. Rhys-Roberts, and P. Lal, “Auger Recombination and Impact Ionization Involving Traps in Semiconductors,” *Proceedings of the Physical Society*, vol. 84, no. 6, pp. 915–931, 1964.
- [206] P. T. Landsberg and M. J. Adams, “Radiative and Auger Processes in Semiconductors,” *Journal of Luminescence*, vol. 7, pp. 3–34, 1973.
- [207] A. M. Stoneham, “The Auger Effect and Related Phenomena,” in *Theory of Defects in Solids: Electronic Structure and Defects in Insulators and Semiconductors*, pp. 539–546, Oxford: Clarendon Press, 1975.

References

- [208] F. Staub, U. Rau, and T. Kirchartz, “Statistics of the Auger Recombination of Electrons and Holes via Defect Levels in the Band Gap - Application to Lead-Halide-Perovskites,” *ACS Omega*, vol. 3, no. 7, pp. 8009–8016, 2018.
- [209] T. Kajishima and K. Taira, “Finite-Difference Discretization of the Advection-Diffusion Equation,” in *Computational Fluid Dynamics*, pp. 23–72, Cham: Springer, 2017.
- [210] J. Mattheis, *Mobility and Homogeneity Effects on the Power Conversion Efficiency of Solar Cells*. PhD thesis, University of Stuttgart, 2008.
- [211] J.-S. Park, S. Choi, Y. Yan, Y. Yang, J. M. Luther, S.-H. Wei, P. Parilla, and K. Zhu, “Electronic Structure and Optical Properties of α -CH₃NH₃PbBr₃ Perovskite Single Crystal,” *The Journal of Physical Chemistry Letters*, vol. 6, no. 21, pp. 4304–4308, 2015.
- [212] S. J. Byrnes, “Multilayer Optical Calculations,” *ArXiv e-prints*, 2016. arXiv:1603.02720v2.

Acknowledgments

Many persons have supported me in the course of this thesis. Here, I would like to express my gratitude to:

Forschungszentrum Jülich, IEK-5 Photovoltaics

- Prof. Dr. Thomas Kirchartz for being an excellent supervisor, providing a lot of scientific input and brilliant ideas, and also giving me the freedom to explore
- Prof. Dr. Uwe Rau, head of the institute, for his keen interest in my studies and his excellent ideas
- Prof. Dr. Reinhard Carius for sharing his immense knowledge on physics and optics, and also for the hands-on sessions in the lab
- Dr. Benjamin Klingebiel for versatile help in the chemistry lab, XPS measurements and analysis, and being a reliable contact for anything that was closely related to chemistry
- Dr. Thomas C. M. Müller for any kind of assistance in the optical lab
- Dr. Jan Flohre and Markus Hülsbeck for support with PL and TRPL setups
- Irina Kühn and Jan-Christoph Hebig for assistance with perovskite fabrication
- Dr. Karsten Bittkau for help with optical simulations and models
- Dr. André Hoffmann for optical data and fitting with SCOUT
- Ulrike Gerhards for cutting and cleaning glass substrates
- Dr. Jan Mock for electrical transport measurements
- Josef Klomfaß and Oliver Thimm for PDS measurements and analysis
- Dr. Pascal Kaienburg for SEM images

Acknowledgments

- Dr. Florian Köhler for XRD measurements
- Pascal Foucart for AFM images
- Malte Köhler for preparing silicon wafers
- Lisa Krückemeier for her kind help during the publishing process of this thesis
- The entire Kirchartz research group for fruitful discussions and the enjoyable working atmosphere
- Andrea Mülheims and Petra Lorbach for administrative support
- Dr. Maurice Nuys and the HITEC team for the diverse training opportunities
- My office mates: Dr. Manuel Pomaska, Dr. Alexei Richter, Dr. Florian Lentz and Ali Padidar for an enjoyable and pleasant atmosphere
- Everyone from the "Kicker group"
- The one and only "IEK-5 Photonensturm" soccer team

University of Duisburg-Essen

- Prof. Dr. Gerd Bacher for taking over the responsibility as second assessor
- Dr. Irina Anusca for providing perovskite single crystals
- Marion Bröckels and Nadine Abbing for administrative support

Helmholtz-Zentrum Berlin

- Dr. Thomas Unold and Dr. Hannes Hempel for OPTP spectroscopy measurements and fruitful discussions

Karlsruhe Institute of Technology

- Dr. Ulrich W. Paetzold for providing perovskite samples

Friedrich-Alexander-University Erlangen-Nuremberg

- Dr. Shreetu Shrestha and Dr. Ievgen Levchuk for providing single crystals

Family and friends

- My parents for perpetual support throughout my scientific career
- My wife Dr. Verena Staub for her support and always believing in me
- Anybody I forgot to list here but truly deserves to be mentioned

Many thanks to all of you!

Band / Volume 500

**Mechanical Behavior of Solid Electrolyte Materials
for Lithium-ion Batteries**

G. Yan (2020), x, 139 pp

ISBN: 978-3-95806-484-3

Band / Volume 501

**Retrieval of atmospheric quantities from remote sensing measurements of
nightglow emissions in the MLT region**

Q. Chen (2020), 208 pp

ISBN: 978-3-95806-485-0

Band / Volume 502

Auswirkungen der Energiewende auf das deutsche Gastransportsystem

B. Gillessen (2020), XVII, 186

ISBN: 978-3-95806-487-4

Band / Volume 503

**Lagrangian Simulation of Stratospheric Water Vapour: Impact of Large-
Scale Circulation and Small-Scale Transport Processes**

L. Poshyvailo (2020), 124 pp

ISBN: 978-3-95806-488-1

Band / Volume 504

**Water Management in Automotive Polymer-Electrolyte-Membrane
Fuel Cell Stacks**

S. Asanin (2020), XVIII, 172 pp

ISBN: 978-3-95806-491-1

Band / Volume 505

**Towards a new real-time irrigation scheduling method: observation,
modelling and their integration by data assimilation**

D. Li (2020), viii, 94 pp

ISBN: 978-3-95806-492-8

Band / Volume 506

Modellgestützte Analyse kosteneffizienter CO₂-Reduktionsstrategien

P. M. Lopion (2020), XIV, 269 pp

ISBN: 978-3-95806-493-5

Band / Volume 507

**Integration of Renewable Energy Sources into the Future
European Power System Using a Verified Dispatch Model
with High Spatiotemporal Resolution**

C. Syranidou (2020), VIII, 242 pp

ISBN: 978-3-95806-494-2

Band / Volume 508

Solar driven water electrolysis based on silicon solar cells and earth-abundant catalysts

K. Welter (2020), iv, 165 pp

ISBN: 978-3-95806-495-9

Band / Volume 509

Electric Field Assisted Sintering of Gadolinium-doped Ceria

T. P. Mishra (2020), x, 195 pp

ISBN: 978-3-95806-496-6

Band / Volume 510

Effect of electric field on the sintering of ceria

C. Cao (2020), xix, 143 pp

ISBN: 978-3-95806-497-3

Band / Volume 511

Techno-ökonomische Bewertung von Verfahren zur Herstellung von Kraftstoffen aus H₂ und CO₂

S. Schemme (2020), 360 pp

ISBN: 978-3-95806-499-7

Band / Volume 512

Enhanced crosshole GPR full-waveform inversion to improve aquifer characterization

Z. Zhou (2020), VIII, 136 pp

ISBN: 978-3-95806-500-0

Band / Volume 513

Time-Resolved Photoluminescence on Perovskite Absorber Materials for Photovoltaic Applications

F. Staub (2020), viii, 198 pp

ISBN: 978-3-95806-503-1

Weitere **Schriften des Verlags im Forschungszentrum Jülich** unter
<http://www.zb1.fz-juelich.de/verlagextern1/index.asp>

Energie & Umwelt / Energy & Environment
Band / Volume 513
ISBN 978-3-95806-503-1